

Evaluation of Sorbents for the Cleanup of Coal-Derived Synthesis Gas at Elevated Temperatures

by

David Joseph Couling

B.S., Chemical Engineering
University of Notre Dame (2006)

M.S., Chemical Engineering Practice
Massachusetts Institute of Technology (2008)

Submitted to the Department of Chemical Engineering
in partial fulfillment of the requirements for the degree

DOCTOR OF PHILOSOPHY IN CHEMICAL ENGINEERING


at the

MASSACHUSETTS INSTITUTE OF TECHNOLOGY

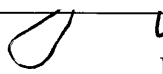
February 2012

© 2012 Massachusetts Institute of Technology. All rights reserved.

Author: _____

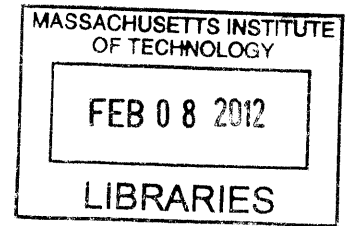
 _____
Department of Chemical Engineering
December 19, 2011

Certified by: _____

 _____
William H. Green
Hoyt C. Hottel Professor of Chemical Engineering
Thesis Supervisor

Accepted by: _____

William M. Deen
Professor of Chemical Engineering
Chairman, Committee for Graduate Students



ARCHIVES

Evaluation of Sorbents for the Cleanup of Coal-Derived Synthesis Gas at Elevated Temperatures

by

David Joseph Couling

Submitted to the Department of Chemical Engineering
on December 19, 2011 in partial fulfillment of the requirements for the degree
Doctor of Philosophy in Chemical Engineering

ABSTRACT

Integrated Gasification Combined Cycle (IGCC) with carbon dioxide capture is a promising technology to produce electricity from coal at a higher efficiency than with traditional subcritical pulverized coal (PC) power plants. As with any coal-based technology, however, it is of critical importance to develop efficient techniques to reduce the emissions of its many environmental pollutants, including not only carbon dioxide, but also sulfur and trace metals such as lead or mercury. One potential method to improve the efficiency for IGCC is through the use of solid sorbents that operate at elevated temperatures. Because many of these technologies are in their infancy and have yet to be commercially demonstrated, a strong desire exists to develop methods to critically evaluate these technologies more rapidly and inexpensively than can be done through experiments alone.

In this thesis we applied computational techniques to investigate the feasibility of sorbents for the warm temperature removal of two key pollutants, carbon dioxide and mercury. We developed pressure swing adsorption models for the removal of carbon dioxide using both metal oxide and metal hydroxide sorbents and incorporated them into IGCC process simulations in Aspen Plus in order to evaluate the energy penalties associated with using these carbon dioxide capture technologies. We identified the optimal properties of CO₂ sorbents for this application. Although warm CO₂ capture using solid sorbents could lead to slight efficiency increases over conventional cold cleanup methods, the potential gains are much smaller than previously estimated.

In addition, we used density functional theory to screen binary metal alloys, metal oxides, and metal sulfides as potential sorbents for mercury capture. We computed the thermochemistry of 40 different potential mercury sorbents to evaluate their affinity for mercury at the low concentrations and elevated temperatures found in the coal gas stream. We also evaluated the tendency of these sorbent materials to react with major components of the gas stream, such as hydrogen or steam. Finally, we tested the mercury adsorption characteristics of three of the most promising materials experimentally. Our experimental observations showed good qualitative agreement with our density functional theory calculations.

Thesis Supervisor: William H. Green, Jr.
Title: Hoyt C. Hottel Professor of Chemical Engineering

Dedication

For my wife, Becky, and my parents, Sid and Kathy.

Acknowledgments

One does not complete a thesis without considerable assistance from others along the way. I would first like to thank my research advisor, Professor William H. Green. I have truly enjoyed my time in his research group. His enthusiasm for tackling difficult problems with wide-reaching impacts was contagious, his door was always open for my many questions during the course of this research project, and his advice that our jobs as researchers should be to find “truth” will stay with me throughout my career. Moreover, his style to advising created a friendly and collaborative environment in our research group. I never felt uncomfortable asking one of my fellow labmates for help, even if our projects were quite different. I hope that Professor Green’s approach to research will be a model for me as I continue my career.

I would also like to thank my committee members, Professor Michael Strano and Professor Gerbrand Ceder. Professor Strano provided very useful advice on the practicality of different sorbent materials and valuable insight on the importance of remembering that cost and safety of promising materials are just as important as their efficiency. His encouragement to continue to deepen my understanding in CO₂ capture technologies was also very appreciated. Professor Ceder was essential in helping to develop the density functional theory screening method for promising Hg sorbents. He also offered much needed information about performing DFT calculations, especially with strategies for correctly dealing with transition metal compounds. I am grateful to both of them for their assistance throughout this thesis.

I am also grateful to many Green, Strano, and Ceder group members, past and present. Dr. Changsik Song in the Strano group offered many helpful discussions on Hg experimental techniques and was always available with a kind word during our research meetings. Chris Fischer and Anubhav Jain in the Ceder group did invaluable work in the screening of pure metals for Hg capture, and this work served as the basis for my own screening calculations. Anubhav also was very generously offered his time in explaining any details about DFT calculations that I did not fully understand.

I would be hard-pressed to find some Green group member who did not help me along the way. In particular I would like to Dr. Seyed-Abdolreza Seyed-Reihani for his critical assistance in

setting up my experimental apparatus and Dr. Ujjal Das for his help with setting up DFT calculations in VASP. Thank you to Dr. Mike Harper for helping me with my many MATLAB questions (as well as forging a path for me by TAing 10.34 the year before I did), and Dr. Wayne Blaylock for many helpful discussions about thermodynamics and for helping me to set up my MATLAB programs on our server. Josh Allen was a great “go-to” reference for Linux questions, Geoff Oxberry provided great advice on programming and presentation style, and Greg Magoon was a great reference for pretty much any ChemE-related question, in addition to being a good lunch and trivia companion. Dr. Huzeifa Ismail and Josh Middaugh provided key help in setting up and troubleshooting my Hg adsorption apparatus. Kshitij Prakash and Zan Liu were great brothers-in-arms for me throughout the course of our work on the BP-MIT Conversion Project. Kshitij developed some great membrane models for CO₂ and H₂ separations and was always there to bounce ideas back and forth with me. Likewise, Zan Liu and I had many enlightening discussions about the value of various CO₂ sorbents and experimental adsorption techniques. He also was very helpful in performing BET measurements for me, in addition to being a great officemate. My two undergraduate researchers were also quite helpful: Steven Alvarez laid the groundwork for the CO₂ separation models we used in Aspen Plus, and Hoang Viet Nguyen helped me perform many of the calculations for the DFT screening of Hg sorbents. I would like to thank Barbara Balkwill for her assistance with all the day-to-day work I encountered during my thesis. She truly helped make this work possible. Finally, I would like to add that the people listed above were invaluable not only for their assistance, but also for their friendship. They helped to make my graduate experience enjoyable.

Of course, the help I received was not limited to people from the above research groups. Randy Field in the MIT Energy Initiative was integral to my work in this thesis. In addition to helping to coordinate our interactions with BP, he generously helped edit papers and posters over the years. He also was one of the principal developers of the base case IGCC model in Aspen Plus, without which I would not have been able to do my own Aspen Plus studies. Similarly, Rob Brasington was also critical in developing the base case IGCC model and was also a great resource for Aspen Plus troubleshooting. Moreover, he played an invaluable role in helping to develop the Aspen Plus model for the RTI sulfur removal process, also helping to make my work possible. I would like to thank Susan Leite and Andy Kalil in the Environmental Health and Safety office for their assistance in setting up my Hg experiments, and Dr. Herui Dou for his

assistance with BET measurements. I would also like to thank Barbara Botros many helpful discussions about steam power cycles, and to Santosh Shanbhogue for helping me troubleshoot MATLAB on the Pharos server. Thank you too to BP for funding, especially to George Huff and David Byard for their helpful comments along the way.

I would like to add a special thank you to my friends and family. The research experience at MIT has been incredible, but the friendships I have developed here are equally unforgettable. I will fondly remember IM sports with Jordi, barbecues with Jerry and CJ, and football wagers with Kevin. My parents deserve a lot of the credit for me making it this far. Not only did they help to instill a fondness for science in me at a young age, they also gave unending love, support, and encouragement for all my many endeavors over the years. I also want to thank them for making the repeated trips out to Boston to visit. Thank you also to my brother, Matt, and my sister, Megan, both of whom were also very supportive along the way and also made the trek out to Boston to get the full MIT experience with me. Even though I was living hundreds of miles away, my family always made me feel like they were near.

Finally, a huge thank you for my wife, Becky. Her decision to “follow a boy” out to MIT in 2007 has meant the world to me. Her love and support over the years have made even my bad days seem better, and I know that this work would have been infinitely harder without her by my side.

Table of Contents

List of Figures	13
List of Tables	17
Chapter 1. Background	19
1.1 Introduction to IGCC	19
1.2 Environmental Impacts of IGCC.....	21
1.3 Current Cleanup Technologies for IGCC.....	24
1.3.1 Acid Gas Removal (Sulfur and Carbon Dioxide).....	25
1.3.2 Nitrogen Removal.....	27
1.3.3 Particulate Matter Removal	27
1.3.4 Lead Removal	27
1.3.5 Mercury Removal	28
1.4 Warm Cleanup Methods for IGCC	28
1.4.1 Sulfur Removal	29
1.4.2 CO ₂ Removal	29
1.4.3 Mercury Removal	31
1.5 Technology Evaluation Using Computational Methods	33
1.5.1 Process Simulations	33
1.5.2 Materials Screening Using Density Functional Theory.....	34
1.6 Goals of Thesis.....	35
Chapter 2. Development of Carbon Dioxide Adsorption Model.....	37
2.1 Introduction.....	37
2.2 Carbon Dioxide Adsorption on Metal Oxides.....	37
2.2.1 Mass Balance in Packed Column.....	38

2.2.2	Energy Balance in a Packed Column.....	42
2.2.3	Evaluation of Governing Equations.....	44
2.2.4	Development of the Pressure Swing Adsorption Cycle.....	45
2.2.5	Validity of Ideal Gas Law.....	52
2.3	Carbon Dioxide Adsorption on Metal Hydroxides	55
2.3.1	Modification of Governing Equations	56
2.3.2	Modifications to Pressure Swing Adsorption Cycle.....	57
2.4	Conclusions	60
Chapter 3.	Process Simulations of IGCC Systems Using CO ₂ Adsorption Models	61
3.1	Introduction	61
3.2	Description of Base Case IGCC Simulation	61
3.3	Description of IGCC Flowsheet with Warm Syngas Cleanup.....	64
3.3.1	RTI Sulfur Removal via ZnO Sorbent.....	65
3.3.2	RTI Direct Sulfur Recovery Process.....	66
3.4	Base Case Metal Oxide Adsorption Model Results	67
3.4.1	Additional Modifications to IGCC Flowsheet.....	67
3.4.2	Efficiency Results of Base Case Adsorption Model.....	69
3.4.3	Sensitivity Study of Key Parameters in Base Case Model	72
3.5	Isothermal Metal Oxide Adsorption Model Results	74
3.6	Nonideal Gas Metal Oxide Adsorption Model Results.....	79
3.7	Metal Oxide with H ₂ Regeneration Results	81
3.8	The Effect of the Linear Driving Force Constant	84
3.9	Metal Hydroxide Adsorption Model Results	86
3.9.1	Additional Modifications to IGCC Flowsheet.....	86
3.9.2	Efficiency Results of General Metal Hydroxide Sorbents.....	87

3.9.3	Hydroxide Materials Identified Using DFT	94
3.10	A Note on Warm Sulfur Removal	95
3.11	Conclusions	97
Chapter 4.	Computational Screening of Hg Adsorbents Using DFT	100
4.1	Introduction	100
4.2	Previous Uses of DFT for Hg Capture	100
4.3	DFT Screening of Pure Metals for Hg Adsorption	102
4.4	DFT Screening of Binary Metal Alloys for Hg Adsorption.....	104
4.4.1	Calculation Details.....	104
4.4.2	Extension of Calculations to Stream Conditions	105
4.4.3	Accuracy of Enthalpy of Formation Calculations	110
4.4.4	Gibbs Energy of Reaction Calculations.....	112
4.5	DFT Screening of Metal Oxides and Metal Sulfides for Hg Adsorption.....	113
4.5.1	Calculation Details.....	113
4.5.2	Extension of Calculations to Stream Conditions	115
4.5.3	Accuracy of Enthalpy of Formation Calculations	118
4.5.4	Gibbs Energy of Reaction Calculations.....	122
4.5.5	Comparison of Hg and H ₂ Reactions Using Experimental Data	125
4.6	Conclusions	126
4.7	Appendix	128
Chapter 5.	Experimental Testing of Promising Sorbents for Hg Capture	133
5.1	Introduction	133
5.2	Construction of Experimental Apparatus.....	133
5.2.1	Previous Investigations of Hg Adsorption.....	133
5.2.2	Experimental Apparatus Design	134

5.2.3	Safety Considerations	137
5.3	Characterization of Experimental Apparatus	138
5.3.1	Hg Detection in the Mass Spectrometer	138
5.3.2	Accounting for Signal Drift	139
5.3.3	Investigation of Detection Limit.....	142
5.4	Breakthrough Analyses of Candidate Materials.....	144
5.4.1	Sorbent Preparation and Safety Considerations.....	144
5.4.2	General Procedure of Breakthrough Experiment.....	145
5.4.3	Potassium Polysulfide.....	148
5.4.4	Barium Peroxide	151
5.4.5	Chromium (IV) Oxide.....	152
5.5	Additional Investigations of Chromium (IV) Oxide.....	157
5.5.1	Cyclic Adsorption of Hg on CrO ₂	157
5.5.2	Estimation of Enthalpy of Adsorption	159
5.6	Conclusions	164
Chapter 6.	Recommendations for Future Work.....	166
6.1	Introduction	166
6.2	Development of Carbon Dioxide Adsorption Model.....	166
6.2.1	Model Equations	166
6.2.2	Modifications to PSA Cycle	167
6.3	Process Simulations of IGCC Systems Using CO ₂ Adsorption Models.....	168
6.4	Computational Screening of Hg Adsorbents Using DFT.....	169
6.4.1	Expansion of Parameter Space.....	169
6.4.2	Expansion of Calculation Methods.....	170
6.5	Experimental Testing of Promising Sorbents for Hg Capture	170

6.5.1	Modifications to Apparatus.....	170
6.5.2	Additional Experiments	171
	Bibliography	173

List of Figures

Figure 1.1 Generic IGCC facility. Polygeneration units to co-produce fuels and chemicals are included[5]. 20

Figure 1.2 Atmospheric concentration of CO₂ measured at the Mauna Loa Observatory[12].... 23

Figure 1.3 Schematic for Acid Gas Removal process. 25

Figure 2.1 Standard discretization for Method of Lines. 44

Figure 2.2 Staggered discretization used in Method of Lines. 45

Figure 2.3 Sample output for average adsorption exit temperature after 150 cycles. 50

Figure 2.4 Comparison of equilibrium bed capacity for adiabatic and isothermal cases. 51

Figure 2.5 Comparison between ideal gas molar volume and *B* parameter..... 54

Figure 3.1 Schematic of base case IGCC flowsheet. 62

Figure 3.2 Schematic of base case CO₂ compression process. 63

Figure 3.3 Overall IGCC flowsheet for warm syngas cleanup processes..... 64

Figure 3.4 Schematic of RTI sulfur removal process. 65

Figure 3.5 Schematic of RTI Direct Sulfur Recovery Process. 66

Figure 3.6 CO₂ removal flowsheet for base case metal oxide sorbent model. 67

Figure 3.7 Schematic of the CO₂ compression process following the CO₂ capture via a metal oxide sorbent..... 68

Figure 3.8 Steam requirement (mole ratio of steam required to CO₂ removed) at $y_{CO_2} = 0.313$ for $T_{feed} = 505$ K..... 70

Figure 3.9 Unburned H₂ as a function of p_{regen} and $|\Delta H_{ads}|$ in the adiabatic model at $T_{feed} = 505$ K, and $y_{CO_2} = 0.313$. Each contour represents the percentage of total H₂ produced that is lost to the CO₂ product stream..... 71

Figure 3.10 HHV thermal efficiency of base case adsorption model as a function of p_{regen} and $|\Delta H_{ads}|$ at $T_{feed} = 505$ K. Each contour represents the HHV thermal efficiency of the IGCC plant (%). 72

Figure 3.11 Sensitivity analysis of perturbing ϵ , $C_{p,solid}$, q^{sat} , and k_{LDF} from their original values of $\epsilon = 0.4$, $C_{p,solid} = 1000$ J/mol-K, $q^{sat} = 9$ mol/kg, and $k_{LDF} = 30$ s⁻¹. 73

Figure 3.12 Steam requirement (mole ratio of steam required to CO ₂ removed) for the isothermal model at $y_{CO_2} = 0.313$ for $T_{feed} =$ a) 480 K and b) 505 K. The color scale is constant between these plots and those in Figure 3.8 for the sake of comparison, but the steam to CO ₂ ratio at 480 K reached as high as 10.	75
Figure 3.13 Working capacity of base case and isothermal models for $p_{regen} = 1$ atm, $T_{feed} = 505$ K and $y_{CO_2} = 0.313$	76
Figure 3.14 HHV thermal efficiency of isothermal adsorption model as a function of p_{regen} and $ \Delta H_{ads} $ at $T_{feed} =$ a) 480 K and b) 505 K. Each contour represents the HHV thermal efficiency of the IGCC plant (%).	77
Figure 3.15 Comparison of results of ideal and nonideal adiabatic adsorption models.	80
Figure 3.16 Comparison of ideal and nonideal isothermal models for a) $T_{feed} = 480$ K and b) $T_{feed} = 505$ K.	81
Figure 3.17 Unburned H ₂ as a function of $ \Delta H_{ads} $ in both the a) adiabatic and b) isothermal metal oxide with H ₂ regeneration models at $T_{feed} = 505$ K, $p_{regen} = 1$ atm, and $y_{CO_2} = 0.313$	82
Figure 3.18 IGCC HHV efficiency for adiabatic and isothermal cases with H ₂ regeneration and $T_{feed} = 505$ K, $p_{regen} = 1$ atm.	83
Figure 3.19 Heat integration for CO ₂ removal with metal hydroxides.	86
Figure 3.20 Steam requirement as a function of enthalpy of adsorption, $y_{CO_2} = 0.31$, $ \Delta S_{ads} = 25$ J/mol-K, $T_{regen} = 550$ K.	87
Figure 3.21 Contour plot of HHV efficiency (%) of metal hydroxide adsorption process, $ \Delta S_{ads} = 25$ J/mol-K, $T_{regen} = 550$ K.	88
Figure 3.22 Comparison between steam requirement for $ \Delta S_{ads} = 25$ and 30 J/mol-K, $y_{CO_2} = 0.31$	91
Figure 3.23 HHV Efficiency at $p_{regen} = 30$ atm for $ \Delta S_{ads} = 30$ J/mol-K, $T_{regen} = 550$ K.	92
Figure 3.24 Calculated working capacity for $ \Delta S_{ads} = 25$ and 30 J/mol-K cases, $T_{regen} = 550$ K.	93
Figure 3.25 IGCC HHV efficiency for materials calculated via DFT with $T_{regen} = 550$ K. The solid line shows the base case Selexol efficiency.	94
Figure 4.1 Comparison of oxide and amalgam formation enthalpies for pure metal sorbents[111].	103

Figure 4.2 Parity plot between experimental and calculated enthalpies of formation at 298 K for binary alloys. The value of EuSn is indicated with a diamond because its experimental value is estimated.	111
Figure 4.3 Gibbs free energy of reaction for Hg adsorption (Equation (4.17)) and steam oxidation (Equation (4.18)) for the conditions shown in Table 4.2. A full description of each reaction is found in Table 4.9 at the end of this chapter.	112
Figure 4.4 Parity plot for enthalpy of formation for Hg species $HgMX_y$ for a) $0 \leq \Delta H_f^0 \leq 500$ kJ/mol and b) $600 \leq \Delta H_f^0 \leq 1100$ kJ/mol. Hg_2WO_4 and Hg_2MoO_4 are indicated with diamonds because the experimental values are estimated.	118
Figure 4.5 Parity plot for enthalpy of formation for MX_y using Equation (4.32) for a) $0 \leq \Delta H_f^0 \leq 550$ kJ/mol and b) $550 \leq \Delta H_f^0 \leq 1600$ kJ/mol. The Ag_2O_2 species indicated with a diamond was calculated using the HSE functional. The error bars shown are from the experimental numbers in Equation (4.32); deviations from the parity line bigger than the error bars are likely due to the DFT calculations.	121
Figure 4.6 Computed Gibbs energy of reaction for Hg adsorption (Equation (4.17)) and H_2 reduction (Equation (4.26)) for the IGCC conditions found in Table 4.4. A full description of each reaction is found at the end of this chapter.	123
Figure 5.1 General schematic of experimental apparatus. The dotted box refers to the portions of the apparatus contained within the ventilated cabinet, as described in Section 5.2.3.	137
Figure 5.2 Drift associated with raw Hg signal in the mass spectrometer.	140
Figure 5.3 Drift reduction using ratio of Hg and Ne signals.	141
Figure 5.4 Investigation of Hg detection limit in MSD.	142
Figure 5.5 Typical form of breakthrough curve.	147
Figure 5.6 Breakthrough experiment of K_2S_x at 170°C of 155 ppbv Hg in 260 SCCM He/Ne.	149
Figure 5.7 Investigation of Hg adsorption on K_2S_x at different temperatures. The red dotted line shows the constant inlet Hg concentration of 155 ppbv.	150
Figure 5.8 Breakthrough experiment of BaO_2 at 200°C of 155 ppbv Hg in 260 SCCM He/Ne.	151
Figure 5.9 Breakthrough experiment of CrO_2 at 200°C of 155 ppbv Hg in 260 SCCM He/Ne.	153
Figure 5.10 Experimental apparatus with modified carrier gas inlet.	154

Figure 5.11 Breakthrough experiment of CrO₂ at 200°C of 155 ppbv Hg in 260 SCCM He/Ne after exposure to 145 SCCM 2% H₂ in Ar at 200°C for 3 hours. The results of the breakthrough experiment for native CrO₂ are shown for comparison. 155

Figure 5.12 Breakthrough experiment of CrO₂ at 200°C of 155 ppbv Hg in 260 SCCM He/Ne after exposure to 145 SCCM 2% H₂ in Ar, 145 SCCM air, and 145 SCCM 5% SO₂ in N₂ at 200°C. The results of the breakthrough experiment for native CrO₂ are shown for comparison. 156

Figure 5.13 Cyclic adsorption of Hg on CrO₂. The regeneration steps were taken at 230°C in 190 SCCM pure He/Ne, and the adsorption steps were taken at 200°C with 155 ppbv Hg in 260 SCCM He/Ne. 158

Figure 5.14 Exponential fit of tail of breakthrough curve for $y_{inlet} = 155$ ppbv Hg, T = 250°C. 160

Figure 5.15 Fitted Langmuir isotherms for the data shown in Table 5.2. The solid lines refer to the model predictions and the colored circles refer to the experimental data at the temperatures corresponding to the colors of the model. 162

Figure 5.16 Fitted Langmuir isobar at $p_{Hg} = 2.1 \times 10^{-7}$ atm for the data shown in Table 5.3. The solid lines refer to the model predictions and the colored circles refer to the experimental data at the temperatures corresponding to the colors of the model. 164

Figure 6.1 Heat exchanger profile for generation of sweep steam in metal hydroxide process simulation. In this example, $|\Delta H_{ads}| = 25$ kJ/mol and $p_{regen} = 23$ atm. 168

List of Tables

Table 1.1 Comparison of IGCC and PC power technologies[10]. 20

Table 1.2 Acceptable concentrations of EPA Criteria Air Pollutants[11]. 21

Table 1.3 Typical concentrations of major species of a gasification-derived syngas stream[3]. 22

Table 1.4 Comparison of different AGR techniques for sulfur removal[4], [9], [10], [21]. 26

Table 2.1 Parameters used in adsorption model. 43

Table 2.2 6-stage PSA system description—steam regeneration. 47

Table 2.3 5-stage PSA system description—H₂ regeneration. 49

Table 2.4 Compressibility factor estimates for major species in IGCC stream. 52

Table 2.5 Critical properties for MATLAB model. 53

Table 2.6 5-stage PSA system description—adsorption on metal hydroxide. 58

Table 2.7 Parameters used in hydroxide adsorption model. 60

Table 3.1 Tabulated values for Excel workbook used in base case adsorption model. 69

Table 3.2 Parameter values investigated in sensitivity analysis. 73

Table 3.3 Efficiency summary for optimal base case (adiabatic) and isothermal models with steam regeneration. 78

Table 3.4 Tabulated parameters for adiabatic and isothermal nonideal gas metal oxide models. The value of 480 K is shown in parentheses because it was simulated for the isothermal model only. 79

Table 3.5 Tabulated values for Excel workbook used in adsorption model with H₂ regeneration. 81

Table 3.6 Efficiency summary for optimal adiabatic and isothermal models with H₂ regeneration in the desorption step. 83

Table 3.7 Results of changing the LDF rate expression in the metal oxide model. The steam requirement is a mole ratio of H₂O to CO₂ removed. 85

Table 3.8 Optimal sorbent performance, $|\Delta S_{ads}| = 25$ J/mol-K. 89

Table 3.9 Calculated thermodynamic parameters for the sorbent materials used in this work. .. 94

Table 3.10 H₂ flow rates for both Selexol cold cleanup and isothermal metal oxides. 95

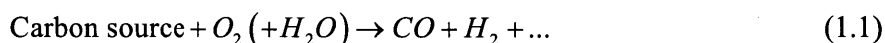
Table 4.1	Convergence of electronic energies at different <i>k</i> -point densities for reactions involving binary alloy sorbents.....	105
Table 4.2	Syngas conditions chosen for binary alloy calculations, including volumetric composition of key species.	106
Table 4.3	Convergence of electronic energies at different <i>k</i> -point densities for reactions involving oxidized sorbents.	115
Table 4.4	Syngas conditions chosen for oxidative sorbent calculations, including volumetric composition of key species.	116
Table 4.5	Comparison of enthalpies of formation calculated using Equations (4.27) and (4.29). The experimentally-determined enthalpy of formation of HgBaO ₂ is -701 kJ/mol[124]......	119
Table 4.6	Comparison of experimental and calculated Gibbs free energies of reaction.	122
Table 4.7	Comparison of metal oxide sorbents at syngas and flue gas conditions. The temperature of both the syngas and the flue gas streams was assumed to be 170°C.....	124
Table 4.8	Comparison of Gibbs energy of sample Hg and H ₂ reactions using experimental data.	126
Table 4.9	Reactions for Hg capture and steam oxidation for the binary alloys investigation. ...	128
Table 4.10	Calculated enthalpy of formation of M _x ¹ M _y ² species. The number indicated with an asterisk(*) is estimated. All values included for the CuTi and CuZr entries are from the same source.	129
Table 4.11	Calculated enthalpy of formation of HgM _x ¹ M _y ² species. The estimated uncertainty is 20 kJ/mol.....	129
Table 4.12	Reactions for Hg capture and H ₂ reduction for the sorbent materials investigation.	130
Table 4.13	Calculated enthalpy of formation for MX _y species.	131
Table 4.14	Calculated enthalpy of formation of HgMX _y species. The asterisks (*) refer to compounds whose experimental enthalpy of formation is estimated.	132
Table 5.1	Natural abundance of stable Hg isotopes.....	138
Table 5.2	Summary of breakthrough experiments performed with exponential fit on the tail of the breakthrough curve.	160
Table 5.3	Summary of desorption experiments based on initial saturation at 250°C.....	163

Chapter 1. Background

1.1 Introduction to IGCC

The gasification of solid carbon-based fuels have become increasingly popular in recent years. These technologies have the potential to increase the liquid fuel supply[1], increase the production of hydrocarbon-based specialty chemicals[2], and increase the efficiency of traditional electricity generation plants[3–6], all while decreasing the dependence on foreign-based fossil fuel products.

All these facets of gasification technology rely on the chemical equation depicted in Equation (1.1).



The carbon source in Equation (1.1) refers to a carbon-rich solid material such as petroleum coke, biomass, or coal. For simplicity we will limit all future discussions to a coal feed. Coal is a highly-abundant fossil fuel that will likely be a large part of the world's energy portfolio for years to come due to its geographic distribution and abundant supply[7], [8]. However, coal also can contribute a large number of environmental pollutants that will be discussed in future sections.

The key difference between coal combustion and gasification technology is the amount of oxygen in Equation (1.1); rather than complete combustion, in which the products of the reaction are mostly carbon dioxide and water, the gasification process is oxygen-starved. Gasification only occurs at high temperature and pressure to drive the reaction forward, and the resulting products (carbon monoxide and hydrogen) are reactive. A growing use of the carbon monoxide and hydrogen mixture, known as synthesis gas, or simply “syngas,” is in electricity production in Integrated Gasification Combined Cycle (IGCC) technology.

A schematic of a generic IGCC facility is shown below.

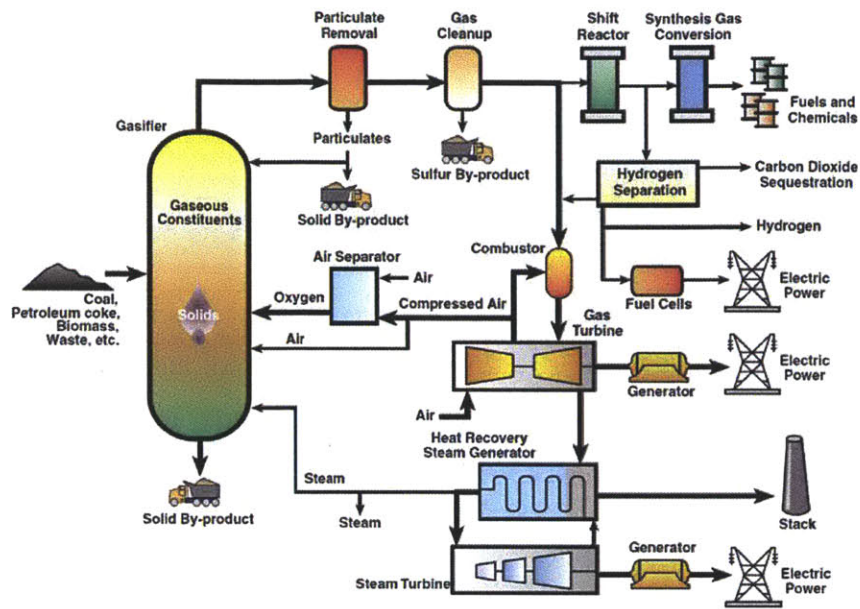


Figure 1.1 Generic IGCC facility. Polygeneration units to co-produce fuels and chemicals are included[5].

The gasifier operates at extreme conditions, with temperatures often exceeding 1000°C and pressures exceeding 50 bar, depending on the gasifier type. At these conditions, the mineral content of the coal tends to melt and fuse into a vitreous product, which is cooled and collected as solid slag at the gasifier outlet. The syngas exiting the gasifier is cooled down to room temperature or below, often through the use of a water quench[9], impurities are removed, and then the gas is reheated and combusted in a turbine, producing electricity via a gas turbine power cycle. The excess heat from the combustion process is used to drive a steam power cycle, thus making two sources of power generation. Some of the advantages and disadvantages of IGCC over conventional pulverized coal (PC) power plants are shown in Table 1.1.

Table 1.1 Comparison of IGCC and PC power technologies[10].

IGCC Advantages	IGCC Disadvantages
1. Increased electricity production efficiency (approximately 40% vs. 32% for PC)	1. High capital and operational cost
2. Increased environmental performance due to easier pollutant control	2. Due to intense operating conditions, gasifiers need repair on a more frequent basis, and spare gasifiers may need to be purchased to ensure plant availability greater than 90%
3. Relatively easy integration with carbon dioxide capture and sequestration	

1.2 Environmental Impacts of IGCC

Unfortunately, environmental issues abound with coal power technology. Coal is predominantly carbon and hydrogen, and this carbon will eventually become CO₂, an important greenhouse gas, regardless of the combustion technique employed. In addition, nitrogen and sulfur compounds can comprise approximately 1% and 3% by weight in coal, respectively, depending on the coal type[10]. When coal is burned in a typical pulverized coal power plant, these elements lead to the formation of hazardous nitrogen oxides (“NO_x”) and sulfur dioxide. Trace metals, such as cadmium, mercury, and lead, are also present in coal and are emitted to the atmosphere upon combustion. Furthermore, the mineral content of coal can become entrained as particulate matter from the coal burner exhaust that is released into the atmosphere. Due to the fact that these pollutants are commonplace and pose significant health risks, they have each been designated as “criteria air pollutants” by the Environmental Protection Agency. A table of the acceptable concentrations of each is shown below.

Table 1.2 Acceptable concentrations of EPA Criteria Air Pollutants[11].

Species	Acceptable Concentration	Average Duration
Carbon Monoxide	9 ppm	8-hour
	35 ppm	1-hour
Lead	0.15 µg/m ³	Rolling 3-month Average
Nitrogen Dioxide	100 µg/m ³	Annual
Particulate Matter		
-PM ₁₀	N/A	Annual
	150 µg/m ³	24-hour
-PM _{2.5}	15 µg/m ³	Annual
	35 µg/m ³	24-hour
Ozone	0.12 ppm	1-hour
	0.075 ppm	8-hour
Sulfur Oxides	0.03 ppm	Annual
	0.14 ppm	24-hour
	0.5 ppm	3-hour

Traditional coal-fired power plants have several technologies implemented in order to reduce these emissions, such as electrostatic precipitators for particulate matter, or “low NO_x” burners to reduce the flame temperature and therefore the NO_x formation[10]. IGCC, however, poses both

new benefits and challenges concerning these criteria air pollutants. As was shown earlier in Equation (1.1), the coal gasification process is oxygen-deficient. This oxygen deficiency causes the gasifier to become a reducing environment. Therefore, instead of the typical pollutants like sulfur dioxide and nitrogen oxides, the reducing environment of the gasifier produces the pollutants hydrogen sulfide (H₂S), carbonyl sulfide (COS), hydrogen cyanide (HCN), and ammonia (NH₃). Although the capture technologies for these pollutants are different from their PC counterparts, the high pressure of the syngas exiting the gasifier causes smaller gas volumes and higher pollutant partial pressures—facilitating an easier capture process. Concentrations of a typical syngas stream are shown below in Table 1.3.

Table 1.3 Typical concentrations of major species of a gasification-derived syngas stream[3].

Compound	Concentration (vol %)
CO	30-60
H ₂	25-30
CO ₂	5-15
H ₂ O	2-30
CH ₄	0-5
H ₂ S	0.2-1
COS	0-0.1
N ₂	0.5-4
Ar	0.2-1
NH ₃ + HCN	0-0.3

The trace metallic species are also present in the syngas stream in the ppm or ppb range. Notice that a significant fraction (often over 50% by volume) of the syngas stream is some form of carbon—virtually all of which is eventually combusted to become CO₂. CO₂, although not a criteria air pollutant, has been the source of significant concern lately due to its role as a greenhouse gas. The atmospheric concentration of CO₂ has increased dramatically over the last several decades, as shown in Figure 1.2.

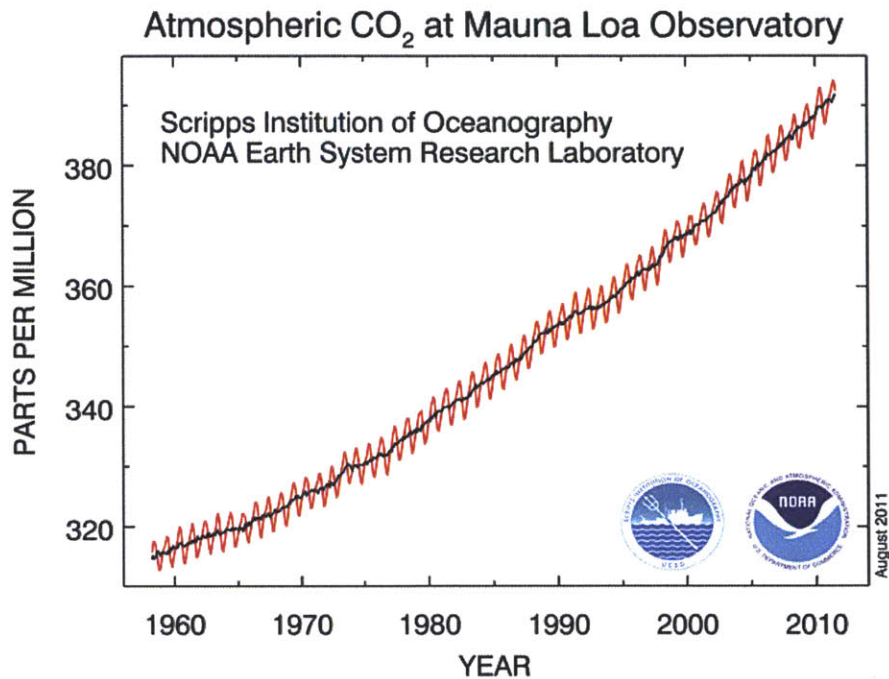


Figure 1.2 Atmospheric concentration of CO₂ measured at the Mauna Loa Observatory[12].

The Intergovernmental Panel on Climate Change (IPCC) predicts that in order to maintain the global average temperature rise at about 3°C or lower from its pre-industrial revolution temperature—an atmospheric concentration of 535 to 590 ppm—the global carbon emissions need to increase by a maximum of 5% by 2050, and preferably decrease by up to 85% if a lower atmospheric concentration is desired[13]. Because coal is likely to be a significant energy source for the near future, especially in the developing world[8], efficient, cost-effective methods of CO₂ capture from IGCC are necessary in order to address the threat posed by climate change.

In addition to the criteria air pollutants, the EPA has designated 188 “hazardous air pollutants” whose emissions are also regulated. Among these hazardous air pollutants are several metal compounds found in trace amounts in coal, such as boron, arsenic, lead, selenium, and mercury. The EPA has since declared mercury to be particularly harmful, and is now in the process of regulating its air emissions even more stringently. The Clean Air Mercury Rule (CAMR), originally issued in March 2005, but vacated in February 2008, planned to cut national mercury emissions from 48 to 15 tons per year[14]. Despite the fact that CAMR was vacated, the number of EPA regulations regarding its release is continuing to increase[15]. Elemental Hg (Hg⁰), a relatively inert Hg species, is expected to be the predominant species of Hg in the reducing

environment of the gasifier[5]. Elemental mercury is one of the only metallic elements without a known beneficial biological role. Its vapor is a potent nerve toxin, and overexposure to mercury can also result in personality changes, weight loss, skin or gum discolorations, stomach pains, or other damages to the heart, kidneys, liver, or brain[16], [17].

Mercury emissions occur from both non-anthropogenic (e.g. volcanic eruptions) and anthropogenic (e.g. emissions from coal-fired power plants and crematoria) sources, and these emissions pose significant risks to the environment. Hg^0 has a residence time in the atmosphere of at least one year, and therefore can disperse significantly from a point source such as a power plant. If the mercury deposits in the oceans, it can be converted by microorganisms to methylmercury (CH_3Hg^+), a very potent poison. Neither the organic nor the elemental forms of mercury are biodegradable, and as a result there is the tendency of mercury to “bioaccumulate” in the food chain[18].

The concentration of mercury in coal varies dramatically, depending on coal source and type, but its average value is approximately 100 parts per billion by weight (ppbw)[19]. Anthropogenic sources from US power plants are thought to contribute only about 1% of the world annual emissions, but because elemental mercury has the potential to be transported thousands of miles before it is eventually deposited, the overall emissions of the entire globe need to be reduced in order to reduce exposure. This includes finding inexpensive methods to reduce mercury emissions in rapidly developing nations, such as China, where at least 10 GW extra capacity from coal-fired power plants is under construction for 2012 alone—about a new 600 MW power plant every 3 weeks[20]!

1.3 Current Cleanup Technologies for IGCC

As was mentioned in Section 1.1, current pollutant removal methods involve decreasing the temperature of the gas stream to room temperature or lower. This temperature reduction is performed because it facilitates the separation process. A gaseous pollutant has a large amount of entropy associated with it, and some of this entropy is lost during the transformation from a free gaseous state to a hindered “captured” state. Because the Gibbs energy of any process

depends on the entropy change multiplied by the temperature, performing these separations at lower temperature minimizes the effect of this entropy loss. A brief description of the techniques used to remove the common pollutants found in coal is given below.

1.3.1 Acid Gas Removal (Sulfur and Carbon Dioxide)

Greater than 99% of the sulfur can be removed using an Acid Gas Removal (AGR) process[5], [10]. The sulfur is then recovered from the stripping solvent, and regenerated to its elemental form. In general, three types of solvents are employed for these separations: chemical, such as methyldiethylamine (MDEA), physical, such as Selexol[®] or Rectisol[®], and hybrid, such as sulfinol. All three types operate under the same general procedure, with a basic flow diagram of this process being shown below.

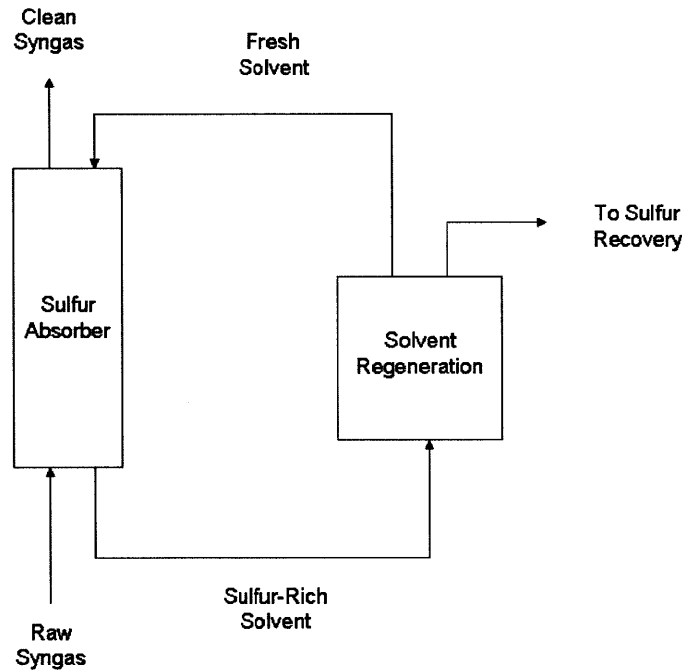


Figure 1.3 Schematic for Acid Gas Removal process.

Table 1.4 presents a brief description of each process and its respective advantages and disadvantages.

Table 1.4 Comparison of different AGR techniques for sulfur removal[4], [9], [10], [21].

Process	Description	Advantages	Disadvantages
MDEA	Chemical absorption using methyldiethylamine solvent	Cheapest of the three options	1) Sulfur removal is greater than 99%, but lower than Selexol and Rectisol 2) COS is not absorbed as well, so a hydrolysis unit is needed to convert COS to H ₂ S
Selexol	Physical absorption using proprietary solvent consisting of polyethylene glycol ethers	1) No refrigeration necessary 2) Greater absorption than MDEA	1) Sulfur removal is lower than Rectisol 2) COS hydrolysis unit needed
Rectisol	Physical absorption using refrigerated methanol	1) Highest sulfur removal percentage 2) Removes COS without hydrolysis unit 3) Removes virtually all impurities, including trace metals	Cryogenic refrigeration is very expensive
Hybrid Solvents	Chemical solvent for high-purity capture at low concentrations, physical solvent for capture at high concentrations	1) Flexible operation 2) Do not require refrigeration	1) COS hydrolysis unit may be needed 2) Solvent cost

CO₂ removal uses many of the same technologies listed above. If the capture of both sulfur and CO₂ is desired, this is typically performed using a two-stage AGR process. Immediately upstream of this, however, the syngas is reacted in a water gas shift (WGS) reactor in order to convert the CO to CO₂. If the WGS were not performed, then the CO in the syngas would not be captured—a problem because this CO is combusted to become CO₂ in the gas turbine power cycle. One of the advantages of MDEA is its selectivity of H₂S over CO₂, and as a result if CO₂ capture is desired the chemical solvent would probably be replaced with one that captures CO₂ also such as diisopropanolamine (DIPA)[9]. In many cases the type of AGR unit selected depends on the remainder of the chemical process. For example, Eastman Chemical selected the

Rectisol process for the removal of its sulfur and CO₂ because the desired purity of the syngas downstream is extremely high[22].

1.3.2 Nitrogen Removal

The predominant forms of nitrogen impurities created in the reducing environment of the gasifier are hydrogen cyanide and ammonia. Initial analyses show that the majority of these compounds originate from the nitrogen already bound in the fuel, not from the molecular nitrogen gas, which has strong chemical bonds[4]. Although these compounds are formed in relatively small quantities, they still pose significant problems due to their health hazards. In addition, hydrogen cyanide can act as a catalyst poison to several processes downstream of gasification, such as Fischer-Tropsch synthesis[4]. Because of their high solubilities in water, these compounds are currently removed using water scrubbers. The nitrogen species (including molecular N₂) that do remain after the water scrubbers continue into the gas turbine. A diluent is used to keep the flame temperature in the turbine low in order to reduce the formation of NO_x species[9].

1.3.3 Particulate Matter Removal

Like PC plants, gasification of coal results in much of the mineral ash being entrained by the syngas exiting the gasifier. This particulate matter is removed through the use of dry candle filters that can remove all solids from the gas at temperatures between 300 and 500°C[4]. Because the temperature of the syngas exiting the gasifier is approximately 900°C, this requires significant stream temperature reduction. This temperature reduction is necessary, however, because at temperatures greater than 500°C, alkali compounds can pass through the candle filters in significant amounts and cause corrosion of the downstream turbine blades[4], [10].

1.3.4 Lead Removal

In general, a separate lead removal unit is not necessary for IGCC systems. Lead is not a highly volatile metal, and as such much of it remains in the slag that collects at the bottom of the gasifier[10]. Much of the lead also ends up in the process water associated with the various cleanup technologies. In general, only about 5% of what is originally present in the coal tends to be emitted in the gas phase, which satisfies its air pollution constraints[10].

1.3.5 Mercury Removal

Not all current gasification systems attempt to remove mercury. In fact, some of the mercury is seemingly removed unintentionally within other chemical processes throughout the system, as only approximately 65% of the mercury vapor exiting the gasifier can be accounted for[5]. It has been suggested that the remaining mercury partitions to solvents in the AGR systems, or possibly to the sulfur in the sulfur recovery units. Current plants that do not have separate mercury removal systems release mercury on the order of 60×10^{-6} lb/MWh. The companies that do have separate mercury removal systems tend to use sulfided or brominated activated carbon. Eastman Chemical, for example, uses brominated activated carbon at 86°F and 900 psig. The advantage of activated carbon is that it is inexpensive; a typical price of activated carbon is approximately \$6.40/lb[19], which is only slightly higher than an inexpensive metal such as copper (\$4/lb) and significantly lower than a more precious metal such as silver (\$43/lb)[23]. The savings of activated carbon are increased even more in the high pressure environment of an IGCC gas stream—mercury removal with activated carbon in an IGCC plant has been estimated to cost less than 10% of what it would cost in a PC plant[19].

Because activated carbons are inexpensive, it is not economically viable to attempt to regenerate them. However, their disposal as hazardous waste may pose problems for the future. In part because land releases of mercury, such as those occurring from mining activities, are steadily increasing, the EPA has dramatically increased the number of companies who need to report their mercury production[15]. As a result, it is quite possible that because regulations concerning air and water releases are becoming more stringent, equivalent regulations on land releases will not be far behind.

1.4 Warm Cleanup Methods for IGCC

As was mentioned in Section 1.3, all current cleanup methods in IGCC are performed at or below room temperature. Although these low temperatures allow for easier separations, they increase capital expenditures due to the need for large heat exchangers, and they decrease the overall efficiency of the IGCC plant due to a loss in availability. Eastman Chemical and the

Research Triangle Institute (RTI) predict that for the case of no CO₂ capture, the overall efficiency of the plant can increase by as much as 3.6 percentage points HHV if the sulfur were removed by some high-temperature method[24]. We detail the most promising technologies for the warm temperature removal of the key pollutants sulfur, CO₂, and Hg below.

1.4.1 Sulfur Removal

A high temperature ZnO-based adsorbent process has been developed by RTI[25] for the removal of H₂S and COS from the syngas. The H₂S and COS react with ZnO to form ZnS and release a gaseous effluent (H₂O and CO₂, respectively). The sorbent is regenerated by oxidation in a stream of O₂ supplied from the Air Separation Unit (ASU) shown in Figure 1.1 to form SO₂, which is reacted with a slip stream of syngas to yield elemental sulfur. Eastman Chemical and RTI are currently performing demonstration plant tests for this process.

1.4.2 CO₂ Removal

There are several methods currently being developed for warm temperature CO₂ removal. The first such method is membrane separation. Because the “syngas” at this point is predominantly a mixture of H₂, H₂O, and CO₂ at this point in the cleanup process, there are essentially two design strategies with membrane separation: H₂ permeability or CO₂ permeability. Perhaps the most promising H₂-permeable membranes are Pd-alloy membranes. With these membranes, a thin Pd alloy layer is placed on a porous support. The H₂ dissociates on the surface of the Pd alloy, diffuses through the membrane, and recombines on the permeate side[26]. Because the permeation mechanism involves dissociation of the H₂, the membrane is essentially impermeable to the other syngas components, making its selectivity virtually infinite. H₂ permeabilities have been reported in the literature ranging from about 7.1×10^{-10} mol/m-s-Pa^{0.5} for a Pd-Ni membrane[27] and up to about 2.6×10^{-8} mol/m-s-Pa^{0.5} for a Pd-Cu membrane[28], although there have been possible reductions in permeability reported for H₂ in the presence of CO, H₂O, or H₂S[29–31]. A clear disadvantage of these membranes is their cost, estimated to be anywhere from \$2000-\$4500 per m²[32], [33]. In addition, their infinite selectivity also means that the separation is *too* good; the combustible components that are still present in the gas stream, such as CO or CH₄, remain with the retentate stream. These species, although low in concentration,

contribute a significant heating value upon combustion, and a technique such as catalytic oxidation needs to be employed if their heating value is to be recovered[34].

An alternative type of H₂ permeable membrane is a polymeric or ceramic membrane, whose mechanism is essentially one of size exclusion. Of these, one of the most promising is a composite polybenzimidazole (PBI)-based membrane that has shown stability up to 400°C[35]. Unfortunately, although these membranes are undoubtedly cheaper than their Pd alloy counterparts (recent estimates for polymeric membranes are approximately \$10 to \$30 per m²[36]), their H₂/CO₂ selectivities are approximately 40 at 250°C[35], making it much less likely that all of the H₂ can be recovered while still capturing 90% of the CO₂—a common benchmark in a carbon-rich fuel such as coal.

The separation of CO₂ and H₂ can also be performed using CO₂-permeable membranes. In this case, because CO₂ is much larger than H₂, the separation mechanism is one of solution-diffusion: the CO₂ is soluble in the membrane, but the H₂ is not. For example, researchers at the U.S. National Energy Technology Laboratory (NETL) are reported to have recently fabricated and tested a supported ionic liquid membrane that is CO₂ selective and stable at temperatures exceeding 300°C[35], but these membranes are still in their developmental stages. Other CO₂ membranes currently under development have reported CO₂ permeabilities as high as 9710 Barrer (1 Barrer = 10⁻¹¹ cm³-STP-cm/cm²-s-torr, which is about 3.35x10⁻¹⁶ mol/m-s-Pa) and CO₂/H₂ selectivities up to 500[37], [38]. However, these performance data have been reported at low temperatures and high relative humidity conditions, not the conditions of a typical IGCC stream. At higher temperatures, the selectivity and stability of these membranes are much lower[39]. In addition, the steam that is present in the syngas typically is much more permeable than even the CO₂, which is not very desirable for IGCC applications.

The other main technique for CO₂ separation is through the use of solid adsorbents. In general, in order for the sorbent to adsorb CO₂ at elevated temperatures, the enthalpy of adsorption needs to be quite exothermic because there is a significant entropy loss during the adsorption reaction as the gaseous CO₂ adsorbs on the solid phase and has its motion restricted. The effect of the entropy is even greater at higher temperatures because the free energy of the system is related to this entropy change multiplied by the system temperature. The large enthalpy of adsorption can lead to various practical difficulties in running the process on an industrial scale, since the

adsorption and desorption of CO₂ would lead to large temperature swings, potentially decreasing the lifetime of the materials[40]. The temperature swing can be reduced by diluting the sorbent in an inert solid, but this is at the cost of increasing the size of an already huge sorbent bed. There are currently many different types of sorbent under development, including alkali earth metal oxides, hydrotalcites, zeolites, and silicates[41–44], but these materials generally suffer from low capacity at elevated temperatures or large energy penalties associated with their regeneration. Efforts are also underway to develop hydroxide-based solid sorbents, such as sodium hydroxide or magnesium hydroxide[45], [46], in order to overcome the need for highly exothermic adsorption reactions. In this case, the CO₂ would liberate a molecule of H₂O upon adsorption, making the overall entropy change of the reaction significantly smaller.

1.4.3 Mercury Removal

To our knowledge, there are no warm temperature methods for Hg removal currently in commercial operation in industry. However, there are several materials that are currently being investigated for their use in syngas applications. There are several sorbents that can be found in the literature that deal with the removal of mercury at elevated temperatures. NETL has published several papers screening potential metal powders as mercury sorbents[47], [48]. At 288°C, both platinum and palladium remove significant amounts of elemental mercury vapor from a nitrogen carrier gas—100% and 65%, respectively. Because common components of syngas, such as carbon monoxide, water, hydrogen, and hydrogen sulfide, all can interfere with the adsorption of mercury, it is important to test candidate sorbents in this reactive environment. Therefore, these metals were also screened in simulated fuel gases at elevated temperatures. In one simulated fuel gas, only palladium showed significant adsorptive abilities at both 288°C and 371°C. The temperatures with significant mercury adsorption are above the dew point of water (165 - 170°C), indicating that they could be favorable at IGCC conditions. Experimental evidence has suggested that a mercury-palladium amalgam is the product of the reaction, but regeneration data has not been provided. In addition, palladium reacts with sulfur compounds and is subject to hydrogen embrittlement[49], possibly limiting its effectiveness as a mercury sorbent.

TDA Research, Inc. is also currently working high-temperature Hg adsorption[50]. The sorbent they have developed is proprietary, and as a result the specific chemistry of adsorption is

unknown. However, the sorbent has been demonstrated to adsorb approximately 98% of the mercury released at 260°C and be regenerated at 285°C. This sorbent has been tested in a reactive syngas environment, with the gas mixture including hydrogen, carbon monoxide, carbon dioxide, and as much as 10% water. It also has been demonstrated to be inactive to sulfur, but only at concentrations below 20 parts per million by volume (ppmv). The low tolerance for sulfur does not limit the adsorption ability of mercury, but it does limit the mercury removal to occurring after the sulfur removal. In addition, the experimental data shows that it takes at least 30 minutes to achieve the desired outlet concentration, possibly suggesting that the kinetics of its adsorption are too slow to be effective on an industrial scale.

Finally, Eastman Chemical and RTI are currently working to develop sorbents that will not only remove elemental mercury vapor at elevated temperatures, but also arsenic, lead, and other trace metal compounds. These sorbents are proprietary, so very few details are known about them; however, they do plan to have these sorbents be disposable[24]. Several of the materials that they have tested, removing anywhere from 55 to 134% of the inlet Hg (results of over 100% occurred due to measurement limitations in the system)[51], and field testing has shown that both Hg and As have been captured in coal-derived syngas at temperatures around 200°C[52]. This sorbent material is currently undergoing performance testing in the Polk IGCC plant along with the high temperature sulfur removal process[53].

On the flue gas side (i.e., an oxidizing environment rather than the reducing environment of the IGCC syngas), MinPlus, Inc. is developing a high-temperature mercury sorbent intended for use in flue gas streams at temperatures as high as 1100°C[54]. Its design is also proprietary, but it is a disposable sorbent made from the minerals found in paper waste, such as gehlenite[55]. The sorbent is injected in a similar manner to limestone for sulfur emissions. At high injection rates, it is reported to remove 98% of the mercury. MinPlus is appealing from a raw material cost perspective, but much still needs to be known about its use, including the mechanism of adsorption, the product made, and whether it will be as effective in the fuel gas mixture. Additionally, Granite et al. have screened a large number of metal oxides, sulfides, and halogens for their Hg capture potential in flue gas. The majority of materials tested did not capture significant amounts of mercury, but iodine-impregnated activated carbon and MoS₂ both showed potential due to their higher capacities[56]. In summary, the most developed warm Hg cleanup

method to date is the sorbent developed by RTI, but because its composition and material properties are unknown, it is valuable to determine favorable characteristics of other potential sorbent materials.

1.5 Technology Evaluation Using Computational Methods

Clearly, the diversity of the technologies described in Section 1.4 and the fact that many of these technologies are still in their developmental stages illustrate the need for strategies to quickly evaluate these technologies and use the results to help guide future development efforts. Computational methods provide the means to accomplish this goal because processes can be simulated more cheaply and more rapidly than experimental studies alone. The strategies for computational methods can be wide-ranging. A brief overview of examples of two strategies, process simulations and density functional theory (DFT) are given below.

1.5.1 Process Simulations

Process simulations are widely used in industrial processes to predict the mass and energy balances within the plant. Some examples are pressure swing adsorption[57] or distillation[58]. Examples abound for CO₂ removal processes integrated into IGCC plants as well. For CO₂ capture, because CO₂ is a major component of the gas stream, its removal is likely to have a significant impact on the overall efficiency of the IGCC system. This impact can be quantified through the use of process modeling software. A key example of this is illustrated with a study by NETL evaluating the performance of various PC, IGCC, and natural gas combined cycle (NGCC) power plants with and without CO₂ capture[9]. This analysis was performed using existing CO₂ capture technologies in an effort to combine all previous analyses of each technology under one consistent basis.

Process simulations can also be used to evaluate novel technologies. With membrane simulations, a study by Amelio et al.[59], which compared using a Pd-based membrane for CO₂ capture in IGCC against using a conventional physical absorption system suggested a 1.4 percentage point lower heating value (LHV) lower efficiency for the membrane reactor. On the contrary, Chiesa et al.[34] predicted the thermal efficiency of IGCC using a Pd-alloy H₂

membrane reactor for CO₂ capture to be 1.5 higher heating value (HHV) percentage points higher than IGCC with conventional physical absorption for CO₂ capture. Although the source of the discrepancy between the two models is not immediately clear, the Chiesa model does include a greater degree of optimization in the steam cycle and the use of a catalytic oxidation unit to recover heating value from the retentate stream, both of which could be significant. In addition, Grainger and Hägg's techno-economic evaluation of CO₂ selective membranes for carbon capture, based on data published for an operating IGCC plant, concluded an HHV efficiency penalty of 10 percentage points compared to a no-capture case[60]. Process simulations of sorbents in IGCC systems are less common, but an evaluation performed by Ito and Makino estimated a 14.9% reduction in electricity output (or a reduction of 6.2 percentage points of efficiency) using CO₂-removing pressure swing adsorption when compared to a no-capture case[61].

1.5.2 Materials Screening Using Density Functional Theory

DFT calculations are quite useful in identifying favorable properties of materials and chemicals when experimental data is not readily available. Recently, Vasiliu et al. used DFT to predict the thermodynamic properties of compounds derived from the conversion of biomass feedstocks[62]. In addition, Mindrup and Schneider used DFT to identify the locations of different functional groups on amine molecules that would result in a favorable amine-CO₂ reaction stoichiometry[63]. In addition to identifying accurate property data for a select set of compounds, the increase in computational power has given rise to the ability to quickly screen huge numbers of potential materials. Recently, Jain et al. constructed a high-throughput infrastructure so that properties such as enthalpies of formation or phase diagrams of thousands of compounds could be quickly constructed through the use of DFT calculations[64]. In addition, high-throughput screening methods have already been used to help identify high-performance piezoelectric materials[65] or metal hydrides suitable for hydrogen storage[66].

This particular technique is applicable to Hg capture from IGCC streams. Because Hg is a trace species, and the sorbents used for its capture are often disposable, its removal may only have minimal effect on the efficiency of the process, rendering process simulations less useful. In this case, however, because Hg is an inert and toxic species, materials screening using computational

chemistry packages could identify promising materials more safely and cheaply than if such screening were performed experimentally.

1.6 Goals of Thesis

The goals of this thesis are to use the computational and experimental methods described above to evaluate different materials for their potential as warm temperature sorbents for pollutants in an IGCC syngas stream. We limit our focus to two compounds, CO₂ and Hg, because each provides a concrete example of the benefits of different types of computational methodology.

In Chapter 2 we describe the development of the adsorption models created to evaluate metal oxides for their potential as CO₂ sorbents. We describe the assumptions used to create our base case adsorption model, and we also evaluate the effect of different perturbations to from this base case model, including different methods of sorbent regeneration and assuming a nonideal gas during the numerical simulations. We also describe the development of the adsorption models used to evaluate metal hydroxides as CO₂ sorbents. The models can be used to evaluate both real and hypothetical materials in order to discover which are the most favorable.

In Chapter 3 we apply the adsorption models developed in Chapter 2 to an Aspen Plus process simulation of the IGCC plant. We evaluate the effect of these adsorption systems on the overall efficiency of the IGCC plant and compare our results to a base case model in which CO₂ was removed by Selexol, a traditional physical absorption solvent. We use these results to identify favorable characteristics of both metal oxide and metal hydroxide sorbent materials in an effort to direct future sorbent synthesis efforts.

In Chapter 4 we illustrate the methodology used to screen various materials for their ability to capture elemental Hg vapor from an IGCC syngas stream. As part of these calculations we evaluate the favorability of species participating in competing oxidation or reduction reactions with these materials, depending on the material type. We then apply this technique to evaluate a variety of pure metals, binary metal alloys, and a variety of oxidative sorbents including metal oxides and metal sulfides.

In Chapter 5 we apply the results of the DFT screening calculations performed in Chapter 4 to evaluate promising materials experimentally. We describe the experimental apparatus constructed to test these materials, including the analysis method used. We then show results of breakthrough analyses performed for 3 of the most promising materials identified by the DFT calculations.

Finally, in Chapter 6 we present our conclusions from this thesis and put forth our recommendations for further study.

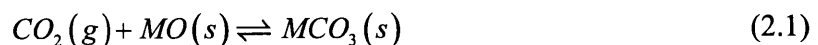
Chapter 2. Development of Carbon Dioxide Adsorption Model

2.1 Introduction

In order to be confident in the results we obtained via process simulation modeling (see Chapter 3), we first needed to develop a model for the CO₂ adsorption system itself. Through the use of this model we can predict the influence of various process parameters (e.g., the enthalpy of adsorption for the sorbent material) on the outlet stream conditions, including composition, temperature, and pressure. In the following sections we overview the development model for the adsorption of CO₂ via a hypothetical metal oxide material. This overview includes both a description of the governing equations describing the CO₂ adsorption and a description of the process cycles selected in order to achieve a cyclic steady state. Modifications to the model via nonideal gas behavior and adsorption of CO₂ via a hypothetical metal hydroxide material are also discussed.

2.2 Carbon Dioxide Adsorption on Metal Oxides

The adsorption of CO₂ onto a metal oxide can be described by the chemical reaction in Equation (2.1).



In the above equation, M can be interpreted to mean any metal in stoichiometric proportions with oxygen, including metals in the +2 oxidation state, such as Ca (CaO), and metals in the +1 oxidation state, such as K (K₂O). It is worth noticing that there is a significant loss of entropy in Equation (2.1) due to the change from one gas-phase molecule on the reactant side to zero gas-phase molecules on the product side. As a result, the enthalpy of adsorption is by necessity relatively large in magnitude and negative in order to overcome this loss of entropy. The effect

of such an exothermic CO₂ adsorption reaction can be significant and will be discussed in subsequent sections. The reactor selected for this model was a fixed-bed reactor due to its wide use in other adsorption models[57], [67], [68] and in practice.

2.2.1 Mass Balance in Packed Column

A common starting point for the component mass balance in the fixed-bed adsorption system is the axial dispersed plug flow model, a one-dimensional model shown below[69].

$$\varepsilon \frac{\partial C_i}{\partial t} + \varepsilon \frac{\partial(uC_i)}{\partial z} = \varepsilon D_L \frac{\partial^2 C_i}{\partial z^2} + (1-\varepsilon) \rho_s \frac{dq_i}{dt} \quad (2.2)$$

In the above equation, q refers to the moles of CO₂ adsorbed on the solid phase per kg of sorbent, D_L is the axial dispersion coefficient, u is the interstitial gas velocity, and ρ_s is the density of the sorbent particles. The parameter ε refers to the void fraction of the column and is equal to the vapor volume of the column divided by the total volume of the column. It is worth noting that this method neglects any radial variations within the column, but this is usually a safe assumption[70]. Furthermore, axial dispersion is generally not important for large industrial units, and as such the axial dispersion term can also be eliminated[70]. This is particularly true in the large volumetric flows characteristic of an IGCC plant, with gas flow rates often being greater than 4000 m³/s[71], and typical gas phase diffusivities being on the order of 10⁻⁵ m²/s, leading to very large Péclet numbers. This simplifying assumption results in a new form of Equation (2.2) shown below.

$$\varepsilon \frac{\partial C_i}{\partial t} = -\varepsilon \frac{\partial(uC_i)}{\partial z} + (1-\varepsilon) \rho_s \frac{dq_i}{dt} \quad (2.3)$$

A common method for further simplification is to assume that the velocity is constant throughout the adsorption column. This method can lead to an analytical solution in the case of a linear isotherm[40], [72] or at least a more stable set of differential equations if the system is solved numerically. However, this method is not implemented in this thesis because it is generally applicable for trace adsorbates[70], and CO₂ is present in quantities often exceeding 30 mol%. In particular, as Equation (2.1) shows, because no gas is evolved as the CO₂ reacts with the metal

oxide the total number of moles of gas in the system is changing as CO₂ adsorbs along the column, necessitating a model that includes axial variations of the velocity.

The adsorption term can be addressed in several ways. A high level of theory would include modeling intraparticle diffusion in order to account for additional mass transfer limitations to adsorption. A sample method is described in Suzuki[73] and a similar method is also implemented in Ribeiro et al[57]. Ribeiro et al. also accounts for the difference between macro- and micropore diffusion. The commonality between these methods is that the $\frac{dq}{dt}$ term is expanded so that the gas phase concentration (C_i) is different from the concentration in the particle phase (C_i^p), which itself has some type of dependence on the particle radius (r'), as shown in Equation (2.4).

$$\frac{\partial C_i^p}{\partial t} = \frac{1}{r'^2} \frac{\partial}{\partial r'} \left(r'^2 \frac{\partial C_i^p}{\partial r'} \right) + \rho_s \frac{dq^p}{dt} \quad (2.4)$$

In Equation (2.4), all variables with the superscript p refer to the variable within the particle phase (macropore or micropore, depending on the model complexity). The $\frac{dq^p}{dt}$ term can be the intrinsic kinetics of the adsorption process, such as those determined in Du et al.[74], but it more often is defined in terms of either some type of mass transfer relationship between the concentration within the particle and the equilibrium amount adsorbed, or it is neglected and fast equilibrium between C_i^p and q is assumed.

Although this description of the adsorption system is mathematically rigorous, the computation time required to simulate such a system is drastically longer due to the added dimension of variables. As a result, a common approximation is to eliminate the intraparticle diffusion and replace it with a single lumped term. One method, the linear driving force (LDF) approximation, is shown in Equation (2.5).

$$\frac{dq}{dt} = k_{LDF} (q_i^* - q_i) \quad (2.5)$$

The variable q_i^* refers to the equilibrium amount of CO₂ adsorbed in mol/kg. This linear driving force approximation is often used for linear isotherms, i.e. $q_i^* = KC_i$, but the early incarnations of this approximation, such as that proposed by Glueckauf, were applicable to more general isotherms[75]. In addition, the LDF model has been used in many different situations with a variety of isotherms and the model continues to be a successful approximation[76], [77]. For our simulations we chose the Langmuir isotherm for q_i^* because it provides a good combination of simplicity and physical meaning. The functional form is shown below in Equation (2.6).

$$\frac{dq_i}{dt} = k_{LDF} \left(\frac{q_i^{sat} K_{eq} (p_i/p_{ref})}{1 + K_{eq} (p_i/p_{ref})} - q_i \right) \quad (2.6)$$

In the above equation, K_{eq} is the adsorption equilibrium constant at reference pressure $p_{ref} = 1$ atm, and q_i^{sat} is the maximum amount of species i that can be adsorbed, also in mol/kg. K_{eq} depends on the enthalpy and entropy of adsorption, where the standard enthalpy at 298 K was given as an input to the simulation. The standard entropy at 298 K was assumed to be a constant value of -160 J/mol-K, regardless of the metal oxide material simulated. This value was chosen based on an average value for chemisorption found in the Handbook of Chemistry and Physics[78] for CO₂ adsorption on Group I and Group II metals. The enthalpies and entropies of the gas-phase species were allowed to vary with temperature, however, and were adjusted to the temperature of interest using the Shomate coefficients found on the NIST Chemistry Webbook[79].

The value of the LDF constant (k_{LDF}) varies depending on the type of system involved. Equations (2.7) and (2.8) show the functional form for k_{LDF} for macropore- and micropore-controlled diffusion resistance, respectively[70].

$$k_{LDF} = \Omega_i \frac{\varepsilon D_e}{R_p^2} \frac{\varepsilon C_0}{(1-\varepsilon)\rho_s q_0} \quad (2.7)$$

$$k_{LDF} = \Omega_i \frac{D_e}{R_c^2} \quad (2.8)$$

In the above equations, R_p and R_c refer to the particle and pore radii, respectively, and D_e is an effective diffusivity. The parameter Ω_i is a constant LDF parameter related to the cycle time of

the PSA process, commonly approximated as 15. In addition to the above functional forms, multiple resistances are sometimes combined into one LDF constant, as is the case below, where external and internal mass transfer resistances are lumped together. Equation (2.9) below shows this simplification, with the external mass transfer resistance included in the first term with the external mass transfer coefficient k_c , and the internal mass transfer resistance included in the second term with Ω_i set at 15. The multiplicative factor is a type of equilibrium constant with the loading q_0 being divided by the gas phase concentration C_0 .

$$\frac{1}{k_{LDF}} = \left(\frac{R_p}{3k_c} + \frac{R_p^2}{15D_p} \right) \frac{(1-\varepsilon)\rho_s q_0}{\varepsilon C_0} \quad (2.9)$$

The equilibrium constant factor is illustrative because it indicates that the rate is expected to be slower when the adsorption is more exothermic (and therefore has a larger equilibrium constant). In addition, previous researchers have developed more complex concentration-dependent factors to include in the k_{LDF} formulation to increase its accuracy in the case of Langmuir adsorption[80].

Thus, the description of the component mass balance is complete. This equation can be summed for all components to yield a total mass balance, which is shown in Equation (2.10).

$$\varepsilon \frac{\partial C}{\partial t} = -\varepsilon \frac{\partial(uC)}{\partial z} - (1-\varepsilon)\rho_s \sum_i \frac{dq_i}{dt} \quad (2.10)$$

The total concentration (C) is simply the sum of the component concentrations (C_i). Although the description of the mass balance is mathematically complete, the presence of the velocity derivative tends to make the numerical integrations of this system unstable. To help alleviate this problem, we eliminate the velocity derivative using the method of Simo et al.[81], where Equation (2.10) is multiplied by the mole fraction y_i and is subtracted from Equation (2.3).

$$\varepsilon \frac{\partial y_i}{\partial t} = \varepsilon u \frac{\partial y_i}{\partial z} - \frac{(1-\varepsilon)\rho_s RT}{p} \frac{dq_i}{dt} - y_i \sum_i \frac{dq_i}{dt} \quad (2.11)$$

Equation (2.11) is also simplified by assuming the system can be described by an ideal gas equation of state. In this situation, the variable of interest changes from the concentration (C_i) to

the mole fraction (y_i). The validity of the ideal gas assumption is investigated further in Section 2.2.5. The summation term in Equation (2.11) can also be eliminated because we assumed the only adsorbing component is CO₂. Therefore, for the other major species present in this model (H₂, H₂O, and N₂ balance), the third term in Equation (2.11) is eliminated. Finally, a relationship between the pressure drop and the velocity in the bed was provided via the Ergun equation[82].

$$\frac{\partial p}{\partial z} = -\frac{150\mu_m(1-\varepsilon)^2 u_0}{\varepsilon^3 d_p^2} - \frac{1.75(1-\varepsilon)\rho_g u_0^2}{\varepsilon^3 d_p} \quad (2.12)$$

It is worth noting that the velocity u_0 in Equation (2.12) refers to the superficial velocity, not the interstitial velocity u . The two are related via the simple relationship $u_0 = \varepsilon u$.

2.2.2 Energy Balance in a Packed Column

By analogy to Equation (2.2), an energy balance in the packed column is shown below in Equation (2.13).

$$\begin{aligned} & \left(\varepsilon\rho_g C_{p,gas} + (1-\varepsilon)\rho_g C_{p,solid} \right) \frac{\partial T}{\partial t} + \varepsilon \frac{\partial(\rho_g C_{p,gas} u T)}{\partial z} = \varepsilon k_{cond} \frac{\partial^2 T}{\partial z^2} \\ & + (1-\varepsilon)\rho_s (-\Delta H_{ads}) \frac{dq}{dt} + \frac{4h}{d_t} (T_w - T) \end{aligned} \quad (2.13)$$

Although this equation makes no assumptions about the influence of axial conduction or the heat transfer via the wall temperature T_w , a key simplification in Equation (2.13) is the assumption that the fluid and solid phases at each axial position in the bed are equilibrated to the same temperature T . This assumption is only valid if the heat transfer between the fluid and solid phases is rapid, but it is commonly made to simplify the governing equations[67], [70], [81].

We neglect the axial conduction in Equation (2.13) as we neglected dispersion in Equation (2.2)—the Péclet number for heat transfer should be just as high as that for mass transfer because the Schmidt number and Prandtl number are both order unity for gases[83]. As a final simplification, we neglect the final term in Equation (2.13), the heat transfer to the wall. Correlations for the heat transfer coefficient (h) have been well studied[84], and heuristics for the heat transfer coefficient are readily available, such as that given in Equation (2.14)[72].

$$h \left([=] \frac{BTU}{hr \cdot ft^2 \cdot ^\circ F} \right) = 0.27 \Delta T \left([=] ^\circ F \right) \quad (2.14)$$

However, large industrial columns, such as those that we hope to simulate in this work, generally operate under near adiabatic conditions[72], and as such we neglect the heat transfer term to arrive at our final model, Equation (2.15).

$$\left(\varepsilon \rho_g C_{p,gas} + (1-\varepsilon) \rho_s C_{p,solid} \right) \frac{\partial T}{\partial t} = - \frac{\partial (\rho_g C_{p,gas} u T)}{\partial z} + (1-\varepsilon) \rho_s (-\Delta H_{ads}) \frac{dq}{dt} \quad (2.15)$$

A summary of the parameters used in the governing equations is given below in Table 2.1.

Table 2.1 Parameters used in adsorption model.

Parameter	Value
ΔS_{ads}	-160 J/mol-K
ε	0.4
d_p	0.01 m
ρ_s	1600 kg/m ³
$C_{p,solid}$	1000 J/kg-K
$q_{CO_2}^{sat}$	9 mol/kg
k_{LDF}	30 s ⁻¹
d_t	3 m
L	3.5 m

The values of ε , $C_{p,solid}$ and $q_{CO_2}^{sat}$ were all chosen based on literature values to represent a porous sorbent dispersed upon a solid support of moderately large heat capacity in order to minimize the temperature fluctuations due to adsorption and desorption. The maximum theoretical CO₂ capacity for pure calcium oxide (a common sorbent) is 17.8 mol/kg, so dispersing this material upon an inert support lowers the theoretical maximum capacity accordingly. In order to simplify the model and to provide a lower bound of the time scale for mass transfer, the k_{LDF} value was specified to be a rather high value of 30 s⁻¹. Depending on the parameters of the packed column and the sorbent particles, the true mass transfer coefficient may be perhaps an order of magnitude smaller. This parameter, along with ε , $C_{p,solid}$, and $q_{CO_2}^{sat}$ was varied within reasonable upper and lower bounds in order to explore the sensitivity of the model to the parameter values. These results are discussed in Chapter 3. In addition, we note that the assumption of constant k_{LDF}

removes any effect of the equilibrium constant or the gas-phase concentrations, described in Equation (2.9), on the value of k_{LDF} . We further explore the effect of this assumption in Chapter 3 as well. The size and dimensions of the adsorption column in all probability can significantly affect the performance of a real adsorption unit. These variables would likely have to be optimized along with the other parameters in order to yield the highest efficiency of the adsorption process. However, in an attempt to reduce the scale of the optimization problem, the varied parameters were limited to the pressure of regeneration (p_{regen}), the standard-state adsorption enthalpy (ΔH_{ads}), and the inlet temperature of the syngas feed (T_{feed}).

2.2.3 Evaluation of Governing Equations

The resulting system of governing equations is a set of nonlinear, partial differential equations and therefore impossible to solve analytically. The governing equations were therefore implemented into MATLAB using the Method of Lines; the discretization was performed in the z direction, and the integration was in the time domain. The number of discretization grid points was varied to find a value that yielded a suitable combination of speed, robustness, and accuracy, where “accuracy” was taken to signify an output that was similar to the output obtained at higher grid point density. In this thesis, the number was chosen to be 65 grid points.

The original discretization scheme was set up using the configuration in Figure 2.1, where all variables were evaluated at each grid point, and the boundary points 0 and $N+1$ (66, in the final model) were not used as variables in the differential equations.

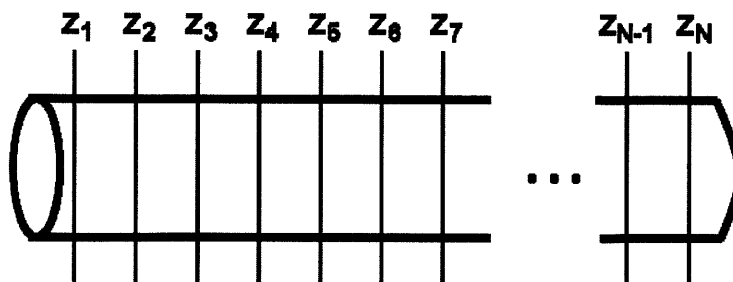


Figure 2.1 Standard discretization for Method of Lines.

This discretization method, while the simplest, unfortunately led to unstable behavior during the numerical integration. Much of this instability was determined to be caused by the pressure and velocity variables being defined at the same grid points.

The errors introduced due to the coupling the pressure and velocity variables have been well studied previously in computational fluid dynamics. The SIMPLE algorithm developed by Patankar and Spalding was one of the first to successfully mitigate this problem[85], and this method was later improved by Patankar to the more robust SIMPLER algorithm[86]. Both methods benefit from separating the pressure and velocity variables using a “staggered grid,” as illustrated in Figure 2.2 below.

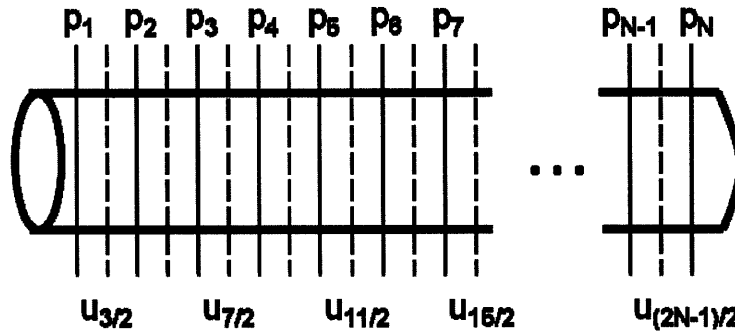


Figure 2.2 Staggered discretization used in Method of Lines.

As shown in the above figure, the pressure variables (along with the species mole fractions (y_i), the sorbent loading (q), and the temperature (T)) are set at the integer grid points, but the velocity is staggered and is at the half-integer grid points. This simple modification greatly improved the stability of the numerical solution of the governing equations.

2.2.4 Development of the Pressure Swing Adsorption Cycle

Pressure swing adsorption cycles generally consist of a series of elementary steps, the most common of which are pressurization, adsorption, depressurization (blowdown), desorption, pressure equalization, and rinse (purge). A general description of each of these steps is as follows[70].

- Pressurization: The adsorption column, initially at the low pressure (p_{low}) is opened and high-pressure gas enters, gradually increasing the pressure to some final pressure (p_{high}).
- Adsorption: The adsorption column, now at high pressure (p_{high}), is exposed to the feed gas. The adsorbate binds to the solid adsorbent, and the adsorbate-lean gas exits the

reactor as a product stream. This step continues until the adsorbate concentration rises to a previously-specified limit.

- **Depressurization:** The reverse of the pressurization step, the adsorption column is opened at one end to the low pressure environment (p_{low}), and the bed gradually decreases in pressure until p_{low} is achieved.
- **Desorption:** The remaining adsorbate is desorbed from the adsorption column at p_{low} , either via a vacuum process or via the flow of a purge gas through the column.
- **Pressure Equalization:** An energy-conserving step used in operations with multiple adsorption columns in which a column at p_{high} and a different column at p_{low} are connected.
- **Rinse:** A separate gas, typically the preferentially-adsorbed species, is fed to the adsorption column after the adsorption step to improve the product purity.

Perhaps the simplest pressure swing adsorption cycle is the Skarstrom cycle in which only the first four of the steps listed above are used: pressurization, adsorption, depressurization, and desorption[70]. True industrial processes, however, quickly increase in complexity, incorporating multiple beds, several pressure equalization steps, and more[68], [70], [87]. In order to limit the complexity of the model, however, our original approach was to model this system with only the four steps of the Skarstrom cycle. Unfortunately, the recovery of the H₂ product was much too low in this configuration, and as a result a rinse step was also added. Although the purge gas for the rinse step is typically the preferentially-adsorbed species, previous studies have shown improved characteristics with the use of a steam purge gas instead[88]. Similarly, the purge gas for the desorption step is typically the non-adsorbing product (H₂, in this case), but in some instances other purge gases, such as steam, have also been used[68]. Based on these previous studies, we decided to create two different cyclic models—one using steam in the desorption step, and the other using the H₂ product stream. Both models used steam as the purge gas in the rinse step because it led to increased numerical stability of the models. However, the disadvantage of using steam in the rinse step is that at the high-pressure conditions of the syngas stream, a pure steam stream at the inlet temperature of approximately 500 K is below its dew point. To overcome this limitation, we first performed a cocurrent depressurization to some intermediate pressure (p_{med}) so that the incoming steam at p_{med} in the

rinse step remained in the vapor phase. This initial desorption step has the added advantage of decreasing the steam requirement for the rinse step, since the depressurization step also serves to displace H₂ from the column. A description of the system with steam regeneration is shown below in Table 2.2.

Table 2.2 6-stage PSA system description—steam regeneration.

Step	Description	Boundary Conditions $z = 0$	Boundary Conditions $z = L$	Integration End Criterion
Pressurization	High- p gas enters at $z = 0$, vessel closed at $z = L$	$y_i = y_{feed}$ $T = T_{feed}$ $p = p_{feed}$	$\frac{\partial y_i}{\partial z} = 0$ $\frac{\partial T}{\partial z} = 0$ $\frac{\partial p}{\partial z} = 0$	$p _{z=L} = 0.99 p _{z=0}$
Adsorption	High- p gas enters at $z = 0$, CO ₂ adsorbed on sorbent	$y_i = y_{feed}$ $T = T_{feed}$ $u = u_{feed}$	$\frac{\partial y_i}{\partial z} = 0$ $\frac{\partial T}{\partial z} = 0$ --	$y_{CO_2} _{z=0.8L} = 0.1 y_{CO_2} _{z=0}$
Cocurrent Depressurization	Vessel closed at $z = 0$, CO ₂ exits at $z = L$	$\frac{\partial T}{\partial z} = 0$ $\frac{\partial p}{\partial z} = 0$	$\frac{\partial T}{\partial z} = 0$ $p = p_{med}$	$p _{z=0} = 1.05 p _{z=L}$
Rinse	Med- p steam enters at $z = 0$, pushes fuel gas out exit	$y_{H_2O} = 1$ $T = T_{feed}$ $p = 1.05 p_{med}$	$\frac{\partial y_i}{\partial z} = 0$ $\frac{\partial T}{\partial z} = 0$ $p = p_{med}$	Cumulative CO ₂ in syngas product is 7.3% of feed
Countercurrent Depressurization	Vessel closed at $z = L$, CO ₂ exits at $z = 0$	$\frac{\partial T}{\partial z} = 0$ $p = p_{regen}$	$\frac{\partial T}{\partial z} = 0$ $\frac{\partial p}{\partial z} = 0$	$p _{z=L} = p _{z=0} + 1 \text{ atm}$
Desorption	Steam enters at $z = L$ and $p = p_{regen} + 1 \text{ atm}$, CO ₂ exits at $z = 0$	$\frac{\partial y_i}{\partial z} = 0$ $\frac{\partial T}{\partial z} = 0$ $p = p_{regen}$	$y_{H_2O} = 1$ $T = T_{regen}$ $p = p_{regen} + 1 \text{ atm}$	Adsorbed CO ₂ remaining is 20% of amount adsorbed in Cycle 1

The integration end criterion for the adsorption step in Table 2.2 was chosen to reduce the amount of H₂ product that is lost to the CO₂ stream. In addition, the rinse step end criterion of 7.3% was selected in order to make the carbon capture percentage of the entire IGCC plant to be 90%. In other words, the PSA model was constructed to capture 92.7% of the CO₂ entering the column so that this CO₂ loss, coupled with the other CO₂ losses in the IGCC plant, would amount to 90% CO₂ capture. Table 2.2 also shows several operational parameters that can be selected in an effort to optimize the adsorption process. For example, if a high regeneration pressure (p_{regen}) were selected in the countercurrent depressurization step, the CO₂ product would be obtained at this higher pressure, decreasing the costs associated with its eventual compression for sequestration. However, a high p_{regen} would also consume more process steam as a diluent for the regeneration of the sorbent bed in the desorption step. Similarly, specifying a 90% capture case in the rinse step could result in a more environmentally-benign process, but may also result in a larger fraction of the product syngas ending up in the CO₂ stream if over 7.3% of the CO₂ is lost before the H₂ is displaced from the column. A similar description of the H₂ regeneration case is shown in Table 2.3.

Table 2.3 5-stage PSA system description—H₂ regeneration.

Step	Description	Boundary Conditions $z = 0$	Boundary Conditions $z = L$	Integration End Criterion
Pressurization	High- p gas enters at $z = 0$, vessel closed at $z = L$	$y_i = y_{feed}$ $T = T_{feed}$ $p = p_{feed}$	$\frac{\partial y_i}{\partial z} = 0$ $\frac{\partial T}{\partial z} = 0$ $\frac{\partial p}{\partial z} = 0$	$p _{z=L} = 0.99 p _{z=0}$
Adsorption	High- p gas enters at $z = 0$, CO ₂ adsorbed on sorbent	$y_i = y_{feed}$ $T = T_{feed}$ $u = u_{feed}$	$\frac{\partial y_i}{\partial z} = 0$ $\frac{\partial T}{\partial z} = 0$ --	$y_{CO_2} _{z=0.75L} = 0.8 y_{CO_2} _{z=0}$
Cocurrent Depressurization	Vessel closed at $z = 0$, CO ₂ exits at $z = L$	$\frac{\partial T}{\partial z} = 0$ $\frac{\partial p}{\partial z} = 0$	$\frac{\partial T}{\partial z} = 0$ $p = p_{med}$	$p _{z=0} = 1.05 p _{z=L}$
Rinse	Med- p steam enters at $z = 0$, pushes fuel gas out exit	$y_{H_2O} = 1$ $T = T_{feed}$ $p = 1.05 p_{med}$	$\frac{\partial y_i}{\partial z} = 0$ $\frac{\partial T}{\partial z} = 0$ $p = p_{med}$	Cumulative CO ₂ in syngas product is 7.3% of feed
Countercurrent Depressurization	Vessel closed at $z = L$, CO ₂ exits at $z = 0$	$\frac{\partial T}{\partial z} = 0$ $p = p_{regen}$	$\frac{\partial T}{\partial z} = 0$ $\frac{\partial p}{\partial z} = 0$	$p _{z=L} = p _{z=0} + 1 \text{ atm}$
Desorption	H ₂ enters at $z = L$ and $p = p_{regen} + 1 \text{ atm}$, CO ₂ exits at $z = 0$	$\frac{\partial y_i}{\partial z} = 0$ $\frac{\partial T}{\partial z} = 0$ $p = p_{regen}$	$y_i = y_{ads,exit}$ $T = T_{regen}$ $p = p_{regen} + 1 \text{ atm}$	$y_{H_2} _{z=0} = 0.18$

The cycle shown in Table 2.3 is almost identical to that in Table 2.2; the main differences are changes in the Integration End Criteria of the adsorption and desorption steps in order to reduce the amount of H₂ lost to the CO₂ product stream. The integration end criterion in the desorption step had to be modified in the isothermal case so that the exit mole fraction of H₂ was 0.3, rather

than 0.18, as is shown in the table above. This adjustment was necessary so that enough CO₂ was purged from the bed during the desorption step; however, it significantly affected the efficiency due to the increased H₂ loss, as will be discussed in Chapter 3.

In both the steam-regenerated and H₂ regenerated cases, the systems of equations were numerically evaluated in MATLAB. Because we were interested in steady-state operation and were not concerned with the transient effects of startup in the adsorption beds, we simulated a large number of cycles (150, in most cases) to approach cyclic steady state. We then fit the trajectory of each output variable using a nonlinear optimization routine within MATLAB to estimate the cyclic steady-state behavior. An example output for the average exit temperature of adsorption is shown below in Figure 2.3.

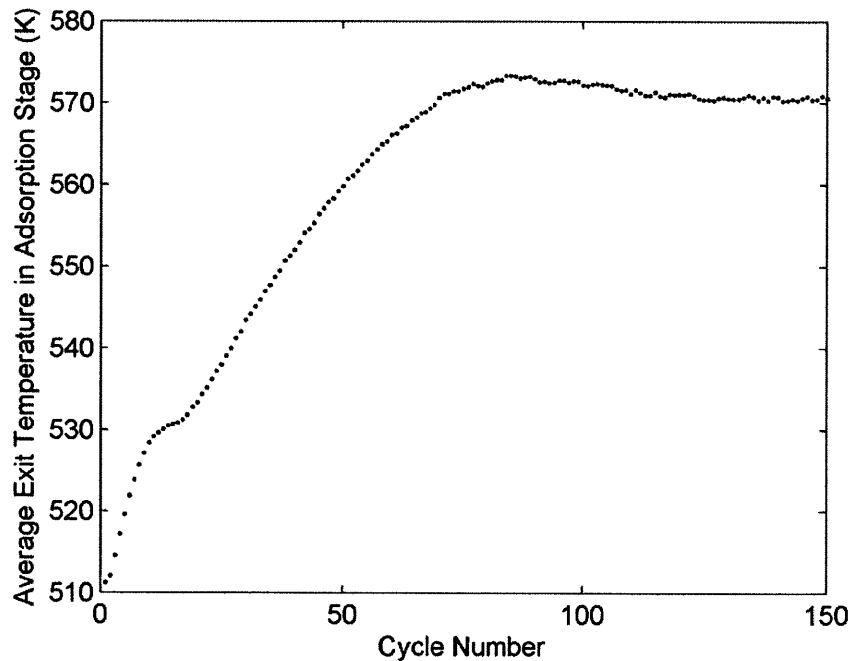


Figure 2.3 Sample output for average adsorption exit temperature after 150 cycles.

An interesting consequence of an adiabatic sorbent model is its effect on the CO₂ capacity of the sorbent. Because the adsorption is exothermic, the bed temperature increases during the adsorption step, inhibiting further adsorption and decreasing the sorbent capacity. This effect is illustrated below in Figure 2.4.

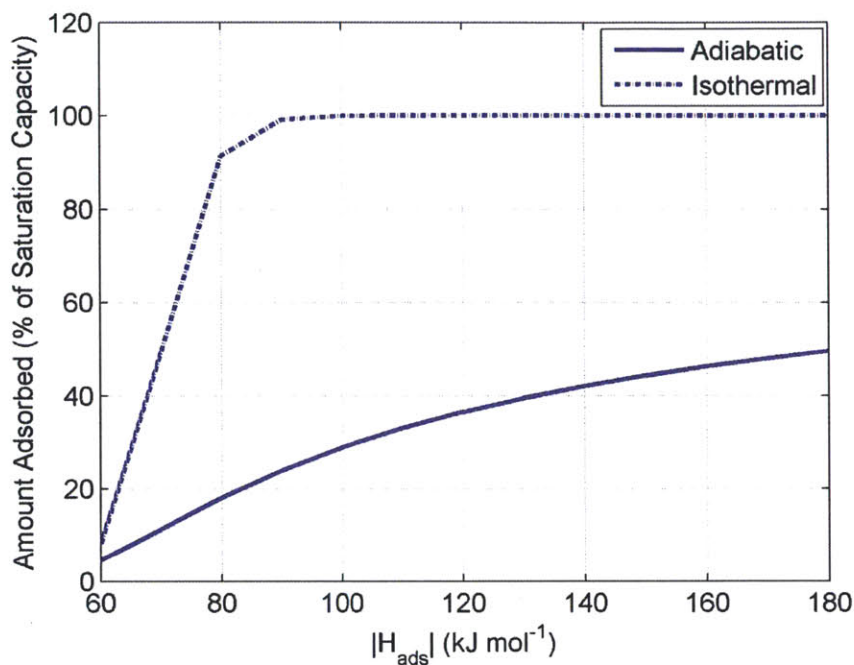


Figure 2.4 Comparison of equilibrium bed capacity for adiabatic and isothermal cases.

Figure 2.4 shows the equilibrium sorbent capacity as a function of the adsorption enthalpy, assuming a constant vapor phase concentration of $y_{CO_2} = 0.313$. Because the temperature does not rise in the isothermal case, the maximum capacity is significantly higher. Therefore, in order to further investigate the effect of temperature variations in the bed, the pressure swing adsorption model was modified and simulated again keeping the temperature constant at the temperature of the inlet syngas. We expect the true bed behavior to be somewhere in between these two extremes (although likely closer to the adiabatic limit due to practical issues regarding heat transfer in fixed-bed systems). However, by modeling both the adiabatic and isothermal limits we are able to effectively create upper and lower bounds for the temperature effects within the bed. In order to mitigate numerical instabilities that arose from the stiffness of this isothermal model, k_{LDF} was reduced to 9 s^{-1} for the isothermal case. However, this value is large enough to still be close the equilibrium limit (i.e., fast mass transfer) in order to provide a reasonable "best case" for the bed performance. Additionally, the desorption step end criterion was altered from the 20% shown for the adiabatic steam regenerated case in Table 2.2 to 10% CO_2 remaining on the bed in the isothermal case (steam regeneration) because the numerical stability of the problem did not allow us to satisfy both the desorption step end criterion and the

overall 90% CO₂ capture criterion. This change likely increased the amount of steam required during the desorption step (and therefore decreased the overall IGCC efficiency). However, the isothermal operation was expected to greatly decrease the amount of steam required in this desorption step. In particular, during adiabatic operation the desorption process is endothermic, and as the temperature lowers the amount of steam required rises because the CO₂ is more stable in the adsorbed state at lower temperatures. By contrast, in the isothermal case the temperature does not decrease during the desorption step, allowing the steam requirement to stay at a relatively low value. Therefore, we expect the slight increase in steam required due to regeneration of the bed to 10% CO₂ remaining to be small compared to this larger effect.

2.2.5 Validity of Ideal Gas Law

As described in Section 2.2.1, the ideal gas law was the equation of state used in the model equations. Although this model is quite useful in its simplicity, its validity needed to be tested. The high total pressure of the feed gas entering the adsorption column is greater than 40 bar, and the presence of significant amounts of traditionally “nonideal” gases such as CO₂ and H₂O indicates that some nonideal behavior may be expected, especially because in our PSA cycle we operate very close to the dew point. As a result we wanted to investigate the effect of this behavior on the overall efficiency of the IGCC plant. We began by computing the compressibility factor (Z) for each gas at the IGCC conditions. The results are shown in Table 2.4.

Table 2.4 Compressibility factor estimates for major species in IGCC stream.

Species	p_i (bar)	T (K)	\underline{V}_i (m ³ /mol)	Z
CO ₂	12	500	3.96×10^{-3a}	1.14
H ₂	16	500	2.62×10^{-3b}	1.01
H ₂ O	10	500	3.87×10^{-3c}	0.93

^aInterpolated from [89].

^bInterpolated from [90].

^cInterpolated from [91].

Because the estimated compressibility factors are no longer equal to unity, as the ideal gas law predicts, the 1st order Virial Equation of State was used to more fully capture the effects of the nonideality. We recognize that other, more detailed equations of state would likely capture the gas phase behavior of our system more accurately. We limited our investigation to the 1st order

Virial equation in order to limit the complexity of our model while still investigating the effect of some nonideality in the system.

$$Z = \frac{pV}{RT} = 1 + \frac{Bp}{RT} \quad (2.16)$$

The parameter B in Equation (2.16) can be calculated for pure gases using the gas critical properties as shown in Equation (2.17)[92].

$$B_i = \frac{RT_{c,i}}{P_{c,i}} \left(B_i^{(0)} + \omega B_i^{(1)} \right) \quad (2.17)$$

The parameters $B^{(0)}$ and $B^{(1)}$ are also calculated from the critical properties as shown in Equation (2.18).

$$\begin{aligned} B_i^{(0)} &= 0.083 - \frac{0.422}{T_r^{1.6}} \\ B_i^{(1)} &= 0.139 - \frac{0.172}{T_r^{4.2}} \end{aligned} \quad (2.18)$$

Equations (2.17) and (2.18) refer to pure component species, so the mixture value of B that was used in the model was simply the pure component parameters weighted by their mass fractions.

$$B = \sum_i y_i B_i \quad (2.19)$$

The critical properties used to calculate B_i for each species in the model are shown in Table 2.5.

Table 2.5 Critical properties for MATLAB model.

Species	p_c (Pa)	T_c (K)	ω
CO ₂	7.382x10 ⁶	304.19	0.228
H ₂	1.313x10 ⁶	33.19	-0.216
H ₂ O	2.2064x10 ⁷	647.10	0.345
N ₂	3.4x10 ⁶	126.20	0.0377

The governing equations for the numerical model as described in Sections 2.2.1 and 2.2.2 were adapted in order to account for this nonideal equation of state. The concentration (C), originally simplified to $p/(RT)$, was kept in its original form in these new equations.

$$\varepsilon \frac{\partial y_i}{\partial t} = \varepsilon u \frac{\partial y_i}{\partial z} - \frac{(1-\varepsilon)\rho_s}{C} \frac{dq_i}{dt} - y_i \frac{dq_{CO_2}}{dt} \quad (2.20)$$

$$\left(\varepsilon \rho_g C_{p,gas} + (1-\varepsilon) C_{p,solid} C\right) \frac{\partial T}{\partial t} = - \frac{\partial (C_{p,gas} u C T)}{\partial z} + (1-\varepsilon) \rho_s (-\Delta H_{ads}) \frac{dq}{dt} \quad (2.21)$$

$$0 = RT - p(\underline{V} - B) = RT - p\left(\frac{1}{C} - B\right) \quad (2.22)$$

As Equation (2.22) shows, the molar volume (\underline{V}) is identically equal to the reciprocal of the concentration (C). As such the molar volume variable was replaced by this form of the total concentration in the model equations.

The expression in Equation (2.22) is particularly enlightening because it shows the effect that the B parameter has on the system of equations; if B is significantly smaller than $1/C$, then $1/C$ is simply equal to RT/p , the ideal gas expression. We compare B with the calculated value of $1/C$ determined by the Virial Equation for three different gas phase concentrations below in Figure 2.5.

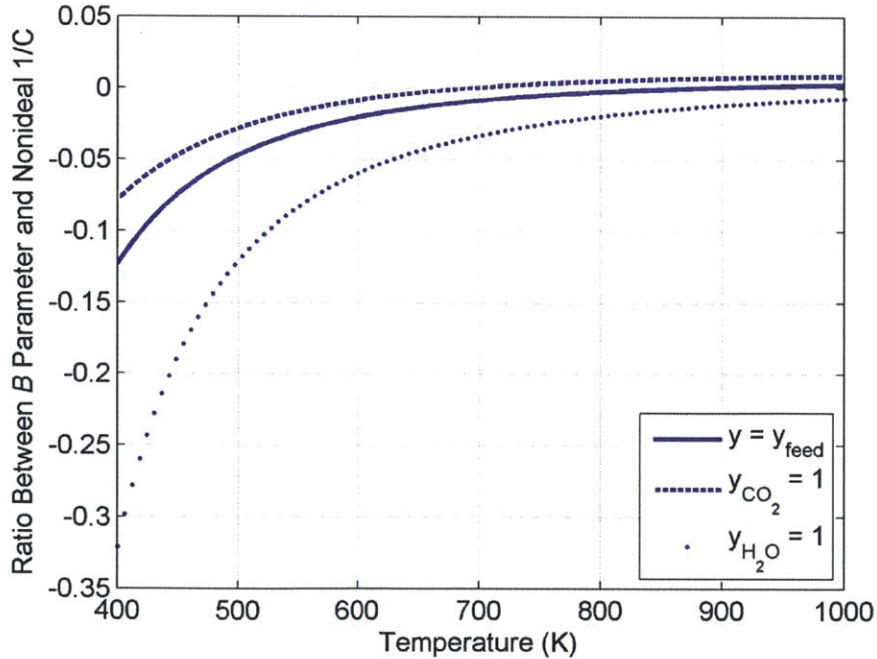
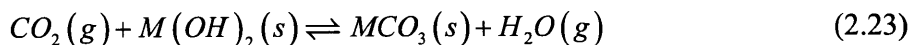


Figure 2.5 Comparison between ideal gas molar volume and B parameter.

The value of y_{feed} in Figure 2.5 is the approximate syngas mole ratio entering the adsorption column, with CO₂ at 30%, H₂ at 40%, H₂O at 25%, and the balance being N₂. The value of $1/C$ was calculated at 4.14 MPa for the syngas feed and CO₂ feed cases in order to show the “worst case” scenario, since the molar volume is the lowest at the highest pressure. The value of $1/C$ was calculated at 2 MPa for the steam feed case because that value is usually above the dew point in that temperature range. Unsurprisingly, the maximum deviation between B and the ideal gas law molar volume occurs at the lowest temperature, 400 K, and the greatest concentration of the nonideal gas H₂O ($y_{H_2O} = 1$). The fact that the magnitude of B is over 20% of the magnitude of $1/C$ signifies that the 1st order Virial equation of state is likely to have a significant effect at these conditions. Even at 500 K, a more realistic representation of the system, the B parameter ratio is about 8% for a steam feed, and a pure steam feed does occur in the rinse step of the PSA cycle (see Table 2.2 and Table 2.3). Therefore, modeling these steps using the Virial equation of state to see its effect on the overall efficiency was warranted.

2.3 Carbon Dioxide Adsorption on Metal Hydroxides

An alternative form of CO₂ sorbent is a metal hydroxide, whose CO₂ capture reaction is shown in Equation (2.23).



As was the case with Equation (2.1), M here refers to any metal that is in stoichiometric proportion with the (OH)₂²⁻ group. As the reaction above shows, two key differences immediately emerge between using metal oxides and metal hydroxides. First, a gas (H₂O) is evolved during the adsorption process, thereby making the overall entropy of reaction much lower in magnitude. This in turn means that the reaction does not need to be as exothermic in order to be favorable. Second, the fact that H₂O is evolved during the adsorption process also means that H₂O needs to be present for the sorbent regeneration process. In other words, a purely “pressure swing” cycle is not sufficient to regenerate the sorbent. In fact, because the total number of moles of gas is constant in this system—one mole of H₂O is produced for every mole of CO₂ that is adsorbed—changing the total pressure of the system has no effect on the

process. This has a profound impact on the equations used to model the system, as shown in the following sections.

2.3.1 Modification of Governing Equations

Assuming the adsorption behavior follows the reaction shown in Equation (2.23), the total number of moles of gas adsorbed on the bed at any one time is constant—each adsorption site is filled with either a molecule of CO₂ or a molecule of H₂O. Mathematically, this means that the sum of the adsorption rates of all species, $\sum_i \frac{dq_i}{dt}$, is equal to zero. This in turn yields a simplification to Equations (2.10) and (2.11), shown below in Equations (2.24) and (2.25).

$$\varepsilon \frac{\partial C}{\partial t} = -\varepsilon \frac{\partial(uC)}{\partial z} \quad (2.24)$$

$$\varepsilon \frac{\partial y_i}{\partial t} = \varepsilon u \frac{\partial y_i}{\partial z} - \frac{(1-\varepsilon)\rho_s RT}{p} \frac{dq_i}{dt} \quad (2.25)$$

Because the total number of species in the system is constant in this hydroxide case, the constant velocity assumption is more valid. However, we continued to allow the velocity to vary here because the system was not necessarily isobaric or isothermal. The constant velocity assumption requires a system that is both[40], and because the adsorption reaction is exothermic and the pressurization and depressurization steps involve large pressure changes, we do not expect either assumption to remain valid.

The rate of adsorption itself also changed in the case of hydroxides, in which we used the linear driving force model described by Seader and Henley[69], in which the driving force is treated as a difference between the gas-phase concentration and the equilibrium concentration (C^*) as shown in Equation (2.26).

$$\frac{dq_{CO_2}}{dt} = k_{LDF} (C_{CO_2} - C_{CO_2}^*) \frac{\varepsilon}{\rho_s (1-\varepsilon)} = k_{LDF} (p_{CO_2} - p_{CO_2}^*) \frac{\varepsilon}{RT \rho_s (1-\varepsilon)} \quad (2.26)$$

The equilibrium partial pressure of CO₂ is related to the loading (q) and the equilibrium partial pressure of H₂O using the Langmuir isotherm and assuming all sites are occupied by either CO₂ or H₂O as shown in Equation (2.27).

$$q_{CO_2} = \frac{q_{CO_2}^{sat} K_{eq} P_{CO_2}^*}{P_{H_2O}^* + K_{eq} P_{CO_2}^*} \quad (2.27)$$

The Langmuir isotherm in Equation (2.27) assumed that no bicarbonates or metal oxides were formed. We related the equilibrium partial pressures (p_i^*) to the bulk partial pressures by assuming the total bulk pressure was equal to the total equilibrium pressure. Rearranging our expression in terms of the equilibrium partial pressure of CO₂, we obtain the final LDF expression shown in Equation (2.28).

$$\frac{dq_{CO_2}}{dt} = k_{LDF} \left(P_{CO_2} - \frac{q_{CO_2} (P_{CO_2} + P_{H_2O})}{q_{CO_2} + K_{eq} (q_{CO_2}^{sat} - q_{CO_2})} \right) \frac{\varepsilon}{RT \rho_s (1 - \varepsilon)} \quad (2.28)$$

The rate of adsorption of H₂O is then just the negative of the above expression. This LDF expression is different from that used in our study of metal oxides, but we felt that this expression provided a logical dependence of the equilibrium constant and the total pressure on the rate of the adsorption process. We note that this mathematical description demonstrates that although the rate is dependent on the total pressure of the system, the relative amount of CO₂ or H₂O adsorbed is independent of the total pressure of the system, since the total pressure can simply be factored out of the difference in Equation (2.28). This pressure independence means that merely changing the pressure of the system will not cause the sorbent to regenerate. This is discussed in greater detail in 2.3.2. The energy balance and the pressure drop (Ergun equation) do not change from the oxide to the hydroxide case.

2.3.2 Modifications to Pressure Swing Adsorption Cycle

The PSA cycle developed for the metal hydroxide case was similar to that of the metal oxide case; however, there were key differences that are worth enumerating. As before, the cycle consisted of 5 key steps: pressurization, adsorption, rinse, depressurization, and desorption. These steps are summarized below in Table 2.6.

Table 2.6 5-stage PSA system description—adsorption on metal hydroxide.

Step	Description	Boundary Conditions $z = 0$	Boundary Conditions $z = L$	Integration End Criterion
Pressurization	High- p gas enters at $z = 0$, vessel closed at $z = L$	$y_i = y_{feed}$ $T = T_{feed}$ $p = p_{feed}$	$\frac{\partial y_i}{\partial z} = 0$ $\frac{\partial T}{\partial z} = 0$ $\frac{\partial p}{\partial z} = 0$	$p _{z=L} = 0.99 p _{z=0}$
Adsorption	High- p gas enters at $z = 0$, CO ₂ adsorbed on sorbent	$y_i = y_{feed}$ $T = T_{feed}$ $u = u_{feed}$	$\frac{\partial y_i}{\partial z} = 0$ $\frac{\partial T}{\partial z} = 0$ --	$y_{CO_2} _{z=0.75L} = 0.8 y_{CO_2} _{z=0}$
Rinse	High- p CO ₂ enters at $z = 0$, pushes fuel gas out exit	$y_{CO_2} = 1$ $T = 91^\circ C$ $u = u_{feed}$	$\frac{\partial y_i}{\partial z} = 0$ $\frac{\partial T}{\partial z} = 0$ --	Cumulative CO ₂ in syngas product is 7.3% of feed
Depressurization	Vessel closed at $z = L$, CO ₂ exits at $z = 0$	$\frac{\partial T}{\partial z} = 0$ $p = p_{regen}$	$\frac{\partial T}{\partial z} = 0$ $\frac{\partial p}{\partial z} = 0$	$p _{z=L} = p _{z=0} + 1 \text{ atm}$
Desorption	Steam enters at $z = L$ and $p = p_{regen} + 1 \text{ atm}$, CO ₂ exits at $z = 0$	$\frac{\partial y_i}{\partial z} = 0$ $\frac{\partial T}{\partial z} = 0$ $p = p_{regen}$	$y_{H_2O} = 1$ $T = T_{regen}$ $p = p_{regen} + 1 \text{ atm}$	Adsorbed CO ₂ remaining is 50% of amount adsorbed in Cycle 1

Unlike the adsorption model for metal oxides, the purge gas used for the rinse step in this case was CO₂. Steam was not used in the rinse step because the presence of steam regenerates the sorbent via the reverse reaction of Equation (2.23), and the CO₂ liberated by this reaction readsorbs farther along the bed, rather than exiting at $z = 0$ as desired. As such, the PSA cycle was 5 steps, rather than the 6 steps of the metal oxide models. The CO₂ used for this regeneration step was taken from the high-pressure CO₂ product stream generated by the IGCC plant (see Chapter 3). The temperature of this stream, while variable in the IGCC process

simulations, was usually approximately 91°C. Because the hydroxide adsorption model was not sensitive to small fluctuations in the temperature of this stream, 91°C was selected as the rinse temperature for all simulations. In addition, because a significant amount of steam is needed for the sorbent regeneration, the desorption step for this cycle was modeled using a pure steam stream.

As was mentioned in Section 2.3.1, the total pressure of the system has no effect on the adsorption isotherm, and as a result the pressurization and depressurization steps do not contribute to the sorbent loading or regeneration. Their function, therefore, is simply to change the system conditions so that the system is physically realizable: namely, it may not be possible or practical to deliver steam for the desorption step at the feed pressure. A more effective method to regenerate the bed could be to use a *temperature* swing rather than a *pressure* swing, and indeed this is a commonly-used method for hydroxide sorbents[45], [46]. Because allowing the temperature to change greatly increases the scope of the optimal parameter space for the problem, we simplified the problem by removing this temperature effect.

Essentially, a tradeoff existed between higher and lower values of T_{regen} . At higher values of T_{regen} , the desorption step was more efficient, and less steam was needed. However, in order to heat this stream to the higher value of T_{regen} , heat needed to be extracted from the high-pressure steam generator, which decreased the overall steam power output, and, correspondingly, the overall HHV efficiency. Therefore, we decided to keep the value of T_{regen} fixed at 550 K, but only regenerate the bed during the desorption step to 50% of the original CO₂ adsorbed (see Table 2.7). By doing this, we kept the value of T_{regen} low enough that lower-pressure steam could be used to heat the stream to the desired temperature, but we decreased the amount of regeneration in order to minimize the steam requirement in the desorption step.

Table 2.7 Parameters used in hydroxide adsorption model.

Parameter	Value
ΔS_{ads}	-25 J/mol-K
ε	0.4
d_p	0.01 m
ρ_s	1600 kg/m ³
$C_{p,s}^{sat}$	96 J/mol-K
$C_{p,s}^{unsat}$	96 J/mol-K
$q_{CO_2}^{sat}$	5 mol/kg
k_{LDF}	100 s ⁻¹
d_t	3 m
L	3.5 m

Many of the above parameters are the same as those in the oxide metal case (see Section 2.2.4). The entropy of adsorption, ΔS_{ads} , was taken as a representative number based on Group I and Group II hydroxide compounds[78]. The saturated and unsaturated heat capacities were simply taken as average values based on the quantum calculations performed by Das and Green[93]. The saturated capacity of the bed of 5 mol/kg is actually lower than what could be found via stoichiometric ratios for typical metal hydroxides. However, to decrease the heat fluctuations within the adsorption column, we assumed that approximately half the column was filled with an inert material such as alumina, which would also be used as a support to increase the surface area. The constant value of k_{LDF} was increased to 100 s⁻¹ to simulate a “fast” (i.e., near equilibrium) adsorption step for this new rate expression.

2.4 Conclusions

In conclusion we have developed numerical PSA models for metal oxides and metal hydroxides. Our base case model was for ideal gas, adiabatic adsorption of CO₂ onto a metal oxide with steam regeneration. We have developed models to test each of these assumptions, allowing the adsorption to be isothermal, nonideal, and regenerated using our H₂ product stream. Finally, we developed similar models for CO₂ adsorption onto a metal hydroxide sorbent. Our next steps will be to use these models in process simulations for IGCC systems to evaluate their effects on the overall efficiency of the IGCC system. We discuss these investigations in Chapter 3.

Chapter 3. Process Simulations of IGCC Systems Using CO₂ Adsorption Models

3.1 Introduction

In this chapter we integrate the pressure swing adsorption models for CO₂ capture that were developed in Chapter 2 with an overall IGCC process simulation flowsheet in Aspen Plus. We use our numerical models of metal oxides to explore the favorable sorbent and process conditions that result in the most efficient process. In addition, we use our models of metal hydroxides to determine the favorable characteristics of hypothetical hydroxide materials. We also apply this information to “real” materials whose thermodynamic parameters were calculated by Dr. Ujjal Das using DFT.

3.2 Description of Base Case IGCC Simulation

The base case simulation used in this work was an Aspen Plus simulation developed by Field and Brasington[94], in turn based on the Cost and Baseline Performance study by NETL in 2010[9]. An overall schematic of the flowsheet is shown below in Figure 3.1.

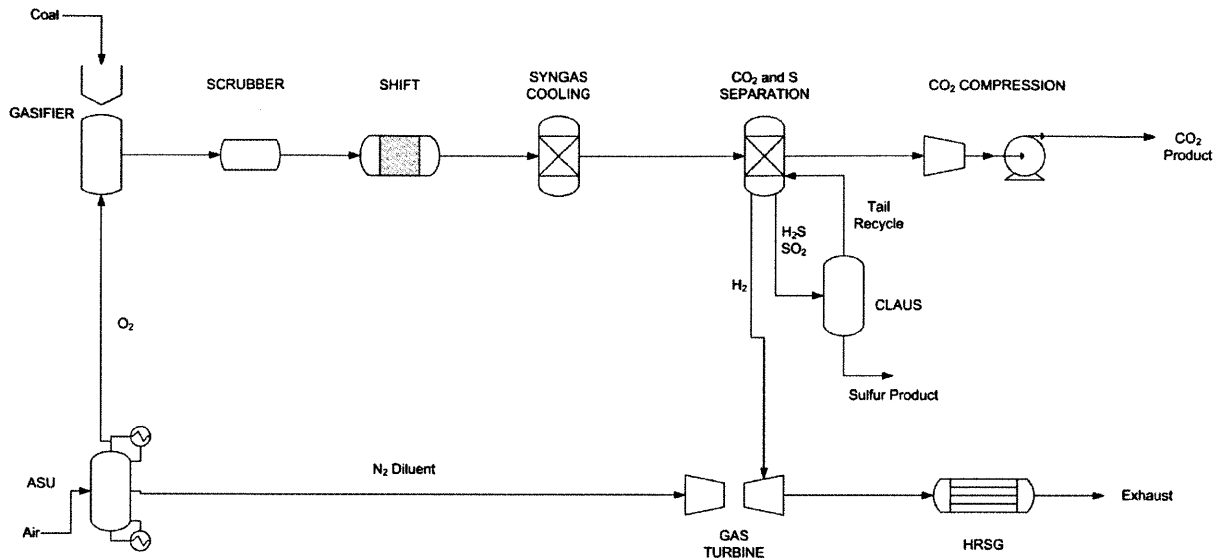


Figure 3.1 Schematic of base case IGCC flowsheet.

Coal was fed to an entrained-flow, oxygen-blown, slurry-fed gasifier whose characteristics reproduced the Texaco-GE Energy gasification technology. The coal slurry and the oxygen reacted in the gasifier at 5.6 MPa (815 psia) and 1643 K to produce syngas. The oxygen for the gasifier was supplied from a cryogenic Air Separation Unit (ASU). The syngas consisted primarily of hydrogen and carbon monoxide, with lesser amounts of water vapor and carbon dioxide, and small amounts of hydrogen sulfide, carbonyl sulfide, methane, argon, and nitrogen. The syngas was cooled from 1643 K to 1033 K in a radiant cooler, and the heat transferred was used to generate high-pressure steam. The raw syngas was then quenched, that is, cooled by direct contact with a large liquid water stream, and saturated with water vapor. It then passed through a scrubber where a water wash was used to remove chlorides and particulate matter.

The syngas exiting the scrubber was adjusted to an $\text{H}_2\text{O}:\text{CO}$ molar ratio of 2:1 by adding high pressure steam prior to the first water gas shift reactor (WGS) reactor, where its temperature increased to 693 K due to the exothermic nature of the reaction. Heat released at this temperature was also used to generate high-pressure saturated steam. A second, cooler stage of WGS was added to achieve higher overall conversion of CO to CO_2 . The WGS catalyst also served to hydrolyze COS, thus eliminating the need for a separate COS hydrolysis reactor (a disadvantage of Selexol mentioned in Chapter 1). To limit the scope of the project, the WGS conversion was held constant throughout the course of this study. However, Bhattacharyya et al.

demonstrated that efficiency improvements of about 1.6 percentage points could be achieved if more global optimizations such as WGS conversion were taken into account[95]. The syngas was then cooled to 312 K, removing most of the water present in the stream, by heating up feed water and generating low pressure steam through a series of heat exchangers and knockout drums. The cooled syngas was fed to a two-stage Selexol process for acid gas removal, where H₂S was removed in the first stage and CO₂ in the second stage of the absorption system. The CO₂-rich stream was obtained at two different pressure levels and compressed to a final pressure of 150 bar for sequestration, while the H₂S stream was sent to the Claus unit for sulfur recovery. A schematic of the CO₂ compression process is shown in Figure 3.2.

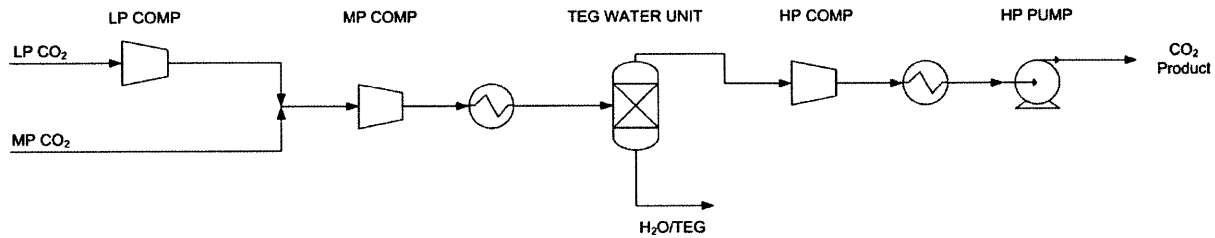


Figure 3.2 Schematic of base case CO₂ compression process.

The decarbonized syngas, composed primarily of H₂, was then run through an expansion turbine to recover energy and bring the pressure down to the delivery pressure of the gas turbine. The clean syngas was diluted with N₂ from the ASU and entered the gas turbine burner. The amount of N₂ diluent to be added was determined by the requirement of maintaining the appropriate lower heating value of the syngas feeding into the gas turbine burner to achieve sufficiently low NO_x emissions (15-35 ppmv at 15% O₂)[96] and to keep the temperature of the gas low enough to avoid blade failure. The decarbonized, diluted fuel underwent combustion and power generation in an advanced GE 7FB class gas turbine. The amount of coal fed to the gasifier was specified so that the power output of the gas turbine was a constant 460 MW. High-temperature flue gas exiting the gas turbine was conveyed through the Heat Recovery Steam Generator (HRSG) to recover the large quantity of thermal energy that remained in the exhaust. The heat exchange between various streams in the HRSG section was modeled in Aspen Plus using two *MHeatX* blocks, which allow heat exchange between multiple process streams. One *MHeatX* block superheated HP and IP steam from the heat from the flue gas above 623 K, while the other block created low pressure (LP) steam from the lower temperature flue gas and the lower quality

heat available in the plant. IP steam was also generated through direct heat exchange with process heat in the IGCC plant. Both *MHeatX* blocks were specified within Aspen Plus to maintain a certain minimum approach temperature (at least 25 K for the HP block, and exactly 12 K for the LP block). The steam exiting the low pressure turbine was condensed and sent to a boiler feedwater mixer, where it was reheated and recycled. Further details about this model can be found in the work of Field and Brasington[94].

3.3 Description of IGCC Flowsheet with Warm Syngas Cleanup

The main difference between the hot syngas cleanup flowsheet, shown below in Figure 3.3, and the base case, described in Section 3.2, is the absence of a cooling section to lower the syngas temperature after the WGS reactors. Since carbon capture and pollutant removal were accomplished using high temperature sorbent processes, no cooling section was needed.

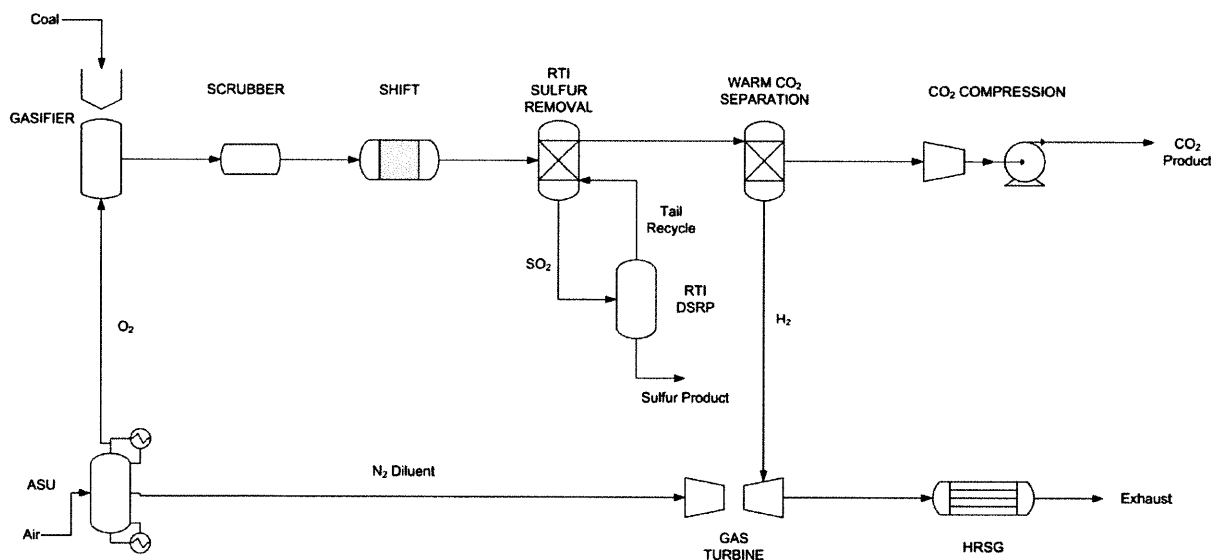


Figure 3.3 Overall IGCC flowsheet for warm syngas cleanup processes.

The sulfur removal process, previously 1 stage of a multistage Selexol process, was replaced with the ZnO sorbent process developed by RTI. Descriptions of both the adsorption and the regeneration processes for the sulfur removal are detailed in the following sections. The operating conditions for this process were estimated using documentation available from Eastman Chemical and RTI[52], [97]. The gasifier, ASU, scrubber, shift, gas turbine, and even

the HRSG sections did not differ considerably from the base case model (with the exception of the rinse and desorption steam streams being removed from the HRSG section for the CO₂ removal process), and as such they will not be described in greater detail here. The warm CO₂ separation process and the CO₂ compression differ not only from the base case Selexol model, they also differ between the metal oxide and metal hydroxide sorbent cases. As such, they will be described specifically in each section.

3.3.1 RTI Sulfur Removal via ZnO Sorbent

A schematic of the RTI sulfur removal process that was implemented in our Aspen Plus simulation is shown below.

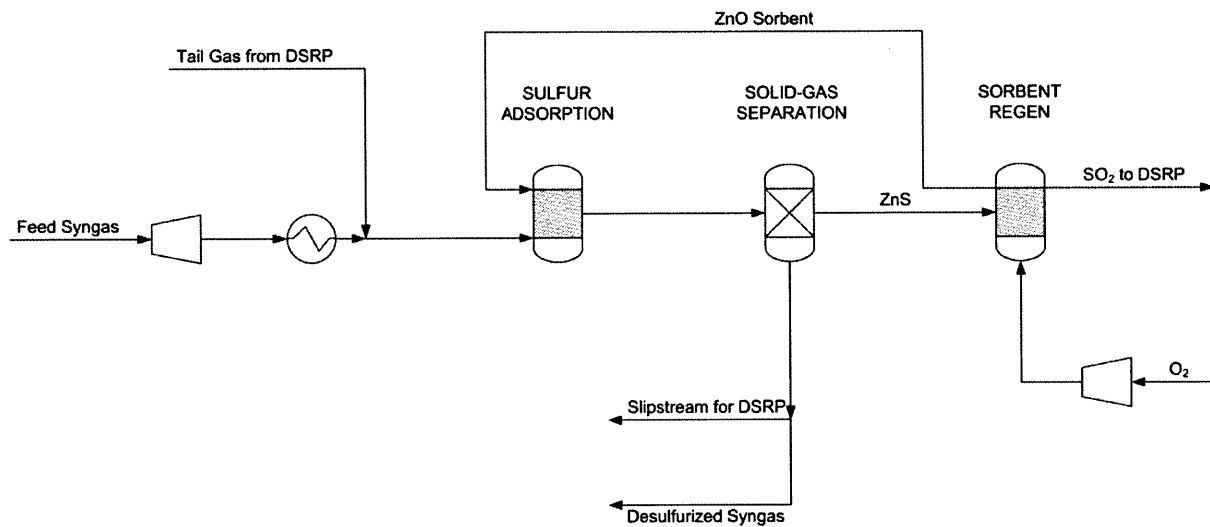


Figure 3.4 Schematic of RTI sulfur removal process.

The syngas first entered an expander which lowers the overall pressure of the syngas stream to 4.14 MPa (600 psia). The syngas then entered a heat exchanger to bring its temperature up to the desired temperature of 320°C. It was then fed to a reactor in which the sulfur components of the syngas reacted with a ZnO sorbent via the reactions shown in Equations (3.1) and (3.2).



The combined gas-solid stream then entered a separator. The desulfurized syngas continued to the CO₂ removal process (minus a slipstream for the SO₂ reduction as described in Section 3.3.2). The solid sorbent, meanwhile, entered a reactor in which it was oxidized according to the following reaction.



The mixture then entered a separator in which the regenerated sorbent was recycled to the adsorption step, and the SO₂ product gas was sent to the Direct Sulfur Recovery Process (DSRP), described in Section 3.3.2.

3.3.2 RTI Direct Sulfur Recovery Process

The DSRP was implemented in our Aspen Plus simulation following the schematic below.

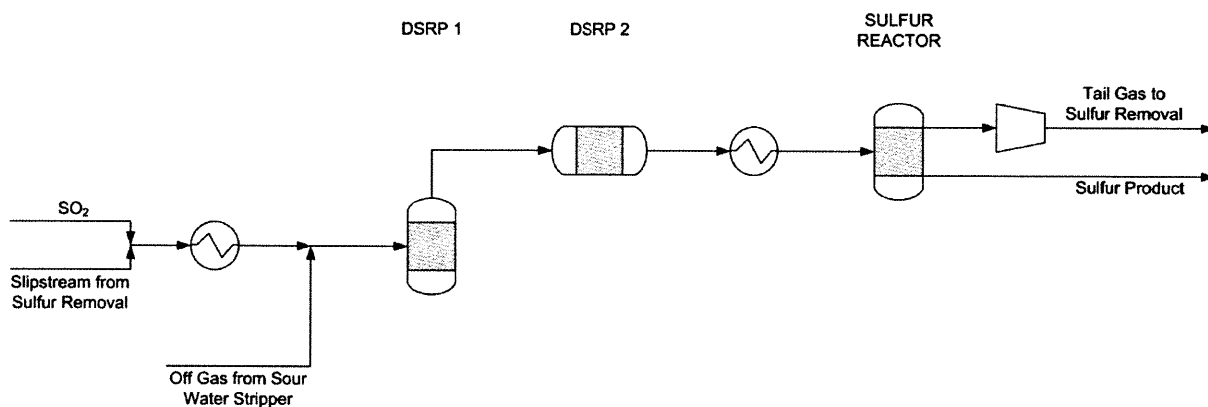


Figure 3.5 Schematic of RTI Direct Sulfur Recovery Process.

The SO₂ product stream combined with the desulfurized slip stream (rich in H₂) and the sulfur-containing off gas from the water scrubbers. These gases were sent to a reactor in which the SO₂ was reduced to elemental sulfur via the reaction below.



The process was modeled in Aspen Plus using two reactors. DSRP 1, the first reactor, was an *REquil* reactor in which the process is allowed to come to equilibrium. The SO₂ concentration was not reduced to the specifications in the literature[97] following these equilibrium reactions,

and as a result the SO_2 was further reduced via an *RStoic* stoichiometric reactor (DSRP 2). Finally, the generic sulfur species, “S,” was then converted via equilibrium data to its relative allotropes: S_2 through S_8 . These species were condensed out of the stream via the final two reactors. The gaseous species, on the other hand, were recycled to the sulfur removal process as a tail gas because small amounts of H_2S were still present in the stream.

3.4 Base Case Metal Oxide Adsorption Model Results

3.4.1 Additional Modifications to IGCC Flowsheet

The PSA process was implemented in Aspen Plus using a *USER2* block, as illustrated in Figure 3.6.

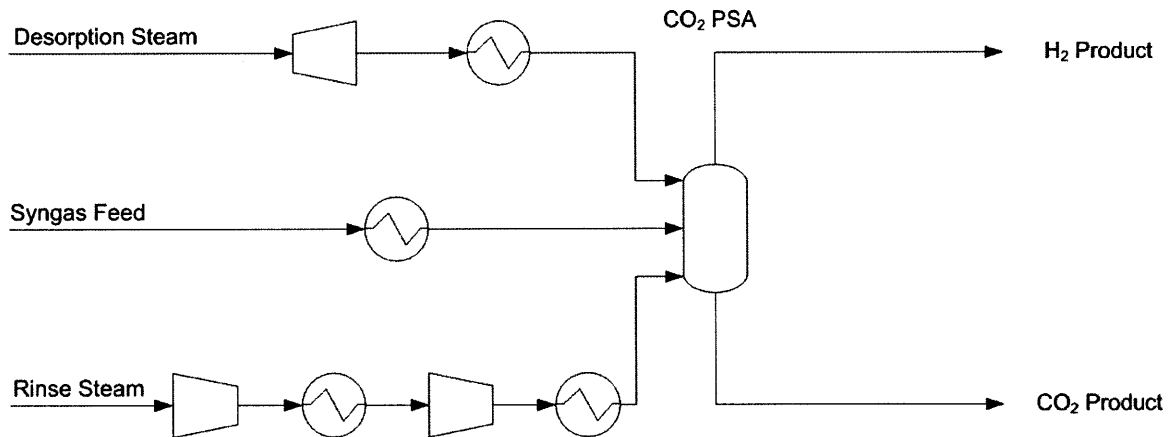


Figure 3.6 CO_2 removal flowsheet for base case metal oxide sorbent model.

The *USER2* block was linked to an Excel Workbook with the PSA model results. Although it was in theory possible to have Aspen Plus communicate back and forth with MATLAB via this Excel interface, the total simulation time for the MATLAB sorbent model was too long (at least 2 hours for one data point) to have simulations of reasonable length. Aspen Plus functions as a sequential modular solver, meaning each iteration for its tear streams and design specifications would require another MATLAB sorbent model simulation—dozens of simulations in all. To overcome this problem, we tabulated output data for a variety of sorbent model parameters in the Excel workbook. The Aspen Plus model then interpolated based on the inlet concentration of

CO₂ for its necessary values of exit composition, temperature, pressure, and flow rate of each stream.

The rinse steam was taken from the HRSG section (see Section 3.2) at about 4 atm and 150°C. The stream was then compressed to the PSA pressure of 18 or 27 atm, depending on the inlet feed temperature of the syngas. Intercooling was used to generate additional low pressure steam and to decrease the energy costs of the steam compression process. The desorption steam was taken from superheated low pressure steam in the HRSG section at about 4 atm and 290°C. The steam was expanded or compressed to the desired regeneration pressure (p_{regen}) + 1 atm (see Table 2.2 in Chapter 2), and a final heat exchanger was used to bring the steam to the appropriate inlet temperature.

The CO₂ compression process was very similar to that of the cold gas cleanup. A flowsheet of the CO₂ compression process for the metal oxide sorbent is shown in Figure 3.7 below.

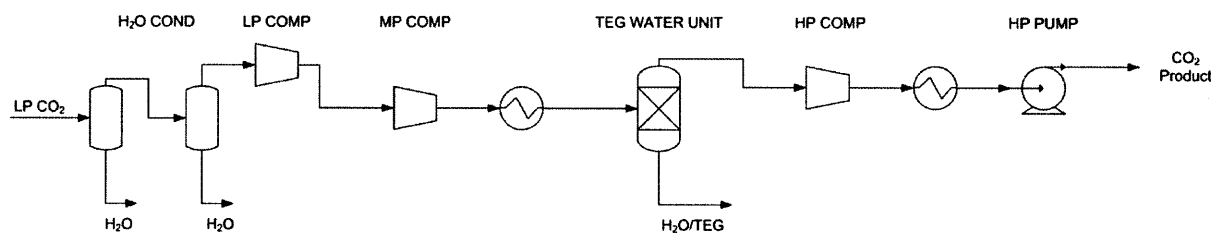


Figure 3.7 Schematic of the CO₂ compression process following the CO₂ capture via a metal oxide sorbent.

The key differences from the cold cleanup Selexol model occurred at the upstream sections of this flowsheet. First, all the CO₂ was produced at the same (low) pressure, rather than a split between medium pressure and low pressure streams of the Selexol process. This led to a slight increase in the CO₂ compression power load over the Selexol process, as described later in this chapter. Second, a H₂O condensing unit was implemented at the beginning of this flowsheet to account for the higher concentration of steam in the CO₂ stream. The first condenser was used to preheat some boiler feed water in the HRSG section or perhaps generate some low pressure steam, depending on the dew point of the stream. The second condenser was unfortunately even lower quality heat and was just extracted to a cooling water system. However, the removal of the remaining steam was necessary in this condenser to reduce the load on the compressors so

that they were not compressing steam along with the CO₂. The remaining sections of the CO₂ compression flowsheet were identical to those of the base case Selexol model.

3.4.2 Efficiency Results of Base Case Adsorption Model

As we described in Section 3.4.1, to decrease the total simulation time of the process flowsheet, the output parameters of the MATLAB adsorption model were tabulated in the Excel workbook. The range of CO₂ concentrations, inlet temperatures, and regeneration pressures surveyed for the base case model are shown in Table 3.1. The rinse stream, which was pure steam, was set at 25 bar and 505 K, which was slightly below the dew pressure of steam at that temperature. We note that because the column operation was adiabatic in this model, the temperature at the inlet of the column could decrease enough that this steam would start to condense in a real column. If this were to occur, the rinse pressure would need to be lowered so that the steam would remain in the vapor phase. In order to limit the variables studied in this thesis, we did not investigate that effect; however, because we would expect the HHV efficiency to decrease with a lower-pressure rinse stream, we expect that the parameters of our system resulted in an upper bound of the efficiency of an adiabatic model.

Table 3.1 Tabulated values for Excel workbook used in base case adsorption model.

Model Variable	Tabulated Values
y_{CO_2}	0.1, 0.2, 0.313
ΔH_{ads} (kJ/mol)	-60, -65, -70, -75, -80
p_{regen} (atm)	1, 2, 3, 4, 5
T_{feed} (K)	505

The syngas inlet temperature (T_{feed}), sorbent binding energy (ΔH_{ads}), and regeneration pressure (p_{regen}) were all specified within the Aspen Plus flowsheet. The model then interpolated the tabulated data based on the inlet mole fraction of CO₂ (y_{CO_2}) to determine the values of the output variables. These variables included the amount of steam needed for the rinse and desorption steps, the amount of H₂ lost to the CO₂ stream, the average temperatures of the fuel gas and CO₂ streams, the outlet pressure of the H₂ stream after the adsorption step, and an estimate of the working capacity of the sorbent, based on the cycle parameters and the saturation

capacity of 9 mol/kg shown in Table 2.1 in Chapter 2. In order to find the properties of the optimal sorbent, the enthalpy of adsorption was varied to predict the amount of steam required for regenerating the bed for a 90% CO₂ capture case.

The overall thermal efficiency of the cyclic process was generally determined by two factors: the amount of steam needed for the rinse and desorption steps, and the amount of H₂ lost into the CO₂ stream after the rinse step. In general, the total amount of steam required by the process increased as $|\Delta H_{ads}|$ or as the sweep gas pressure during the desorption step (p_{regen}) became larger in magnitude, as shown in Figure 3.8. The contours for $|\Delta H_{ads}| = 60$ kJ/mol, $T_{feed} = 505$ K, and $p_{regen} = 1$ atm and 2 atm are slightly different because it was not possible to achieve 90% CO₂ capture in the adsorbent bed with those parameters in the given column geometry. As a result, the cycle parameters were adjusted so that the bed was regenerated in the desorption step to 10% of the CO₂ remaining, rather than the 20% of all the other data points (see the Integration End Criteria in Table 2.2).

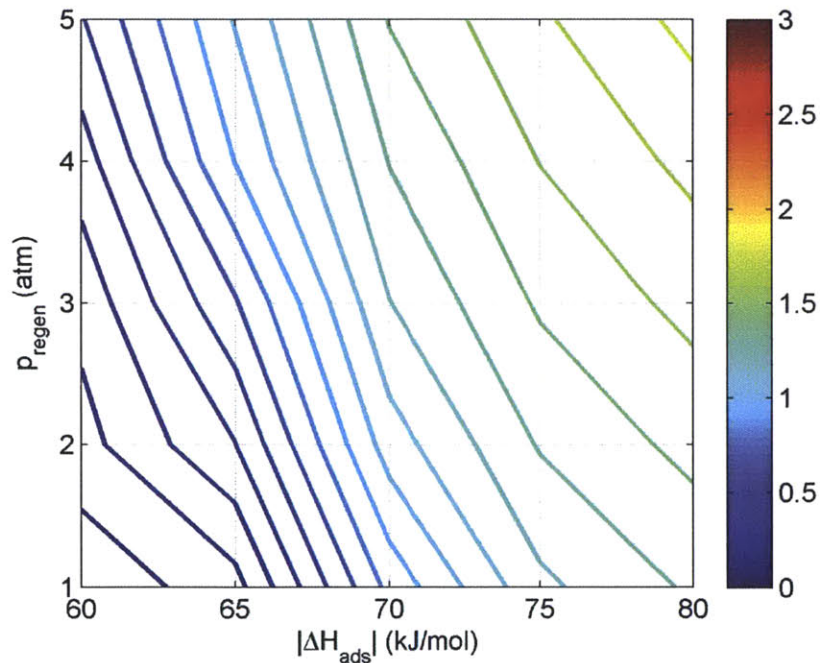


Figure 3.8 Steam requirement (mole ratio of steam required to CO₂ removed) at $y_{CO_2} = 0.313$ for $T_{feed} = 505$ K.

The percentage of H₂ lost to the CO₂ stream (see Figure 3.9) also tended to increase with $|\Delta H_{ads}|$ and p_{regen} . The amount of H₂ lost is likely related to the dispersal of the CO₂ concentration front during the adsorption step. If the concentration front is sharp, meaning that a large fraction of CO₂ is near the outlet of the bed, then the rinse step will be very short in duration, and if this rinse time is shorter than the residence time in the adsorption bed, then some of the H₂ will not be displaced into the desired H₂ product stream. This H₂ remaining in the bed will likely be wasted as a component of the CO₂ sequestration stream. As Figure 3.9 shows, this percentage of H₂ lost tended to hit a minimum at low values of $|\Delta H_{ads}|$, although this value increased at $|\Delta H_{ads}| = 60$ kJ/mol as well—especially for $p_{regen} = 1$ atm and 2 atm, the values where the bed was regenerated to 10%. In all likelihood, the integration end criteria for each step of the PSA cycle detailed in Table 2.2 in Chapter 2 could be optimized for each value of $|\Delta H_{ads}|$ in order to minimize the amount of H₂ lost to the CO₂ stream. Even if this were undertaken, however, the high values of $|\Delta H_{ads}|$ would still be at a disadvantage due to the increased amount of sweep steam required.

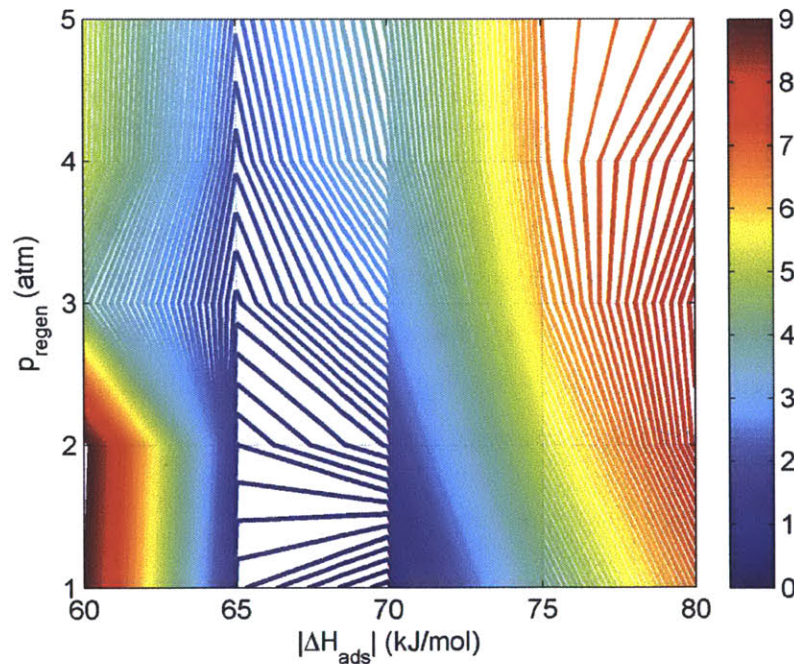


Figure 3.9 Unburned H₂ as a function of p_{regen} and $|\Delta H_{ads}|$ in the adiabatic model at $T_{feed} = 505$ K, and $y_{CO_2} = 0.313$. Each contour represents the percentage of total H₂ produced that is lost to the CO₂ product stream.

The HHV thermal efficiency calculated for each $|\Delta H_{ads}|$ and p_{regen} in the adiabatic case is shown in Figure 3.10.

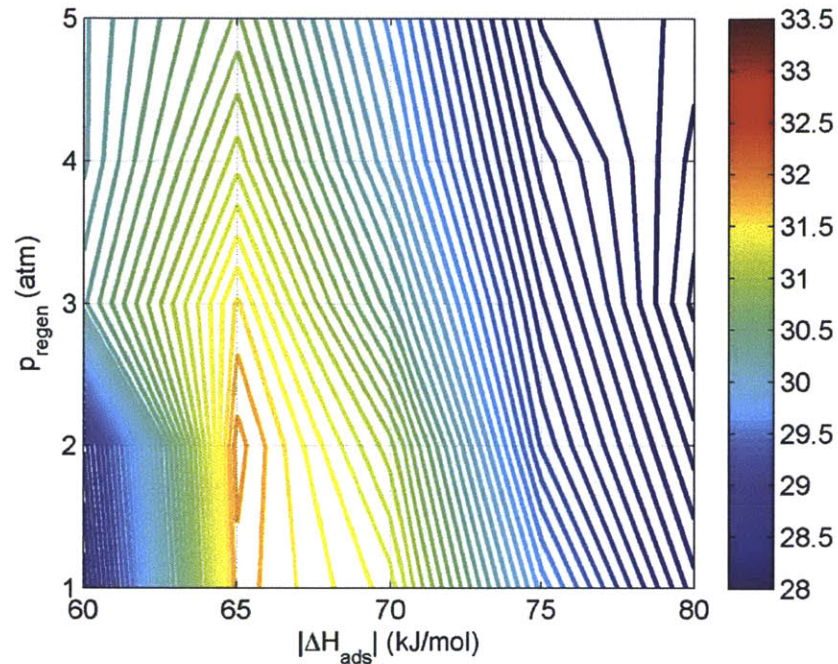


Figure 3.10 HHV thermal efficiency of base case adsorption model as a function of p_{regen} and $|\Delta H_{ads}|$ at $T_{feed} = 505$ K. Each contour represents the HHV thermal efficiency of the IGCC plant (%).

The efficiency tended to decrease with increasing $|\Delta H_{ads}|$ or p_{regen} , although the maximum efficiency was actually achieved at $|\Delta H_{ads}| = 65$ kJ/mol. This is likely due to the increase in H_2 lost to the product stream at $|\Delta H_{ads}| = 60$ kJ/mol, shown in Figure 3.9. The efficiency at $|\Delta H_{ads}| = 65$ kJ/mol was predicted to be 31.9%. We note that this is actually slightly smaller than the efficiency of the cold cleanup Selexol process, which is 32.6%.

3.4.3 Sensitivity Study of Key Parameters in Base Case Model

Several of the parameters chosen for the adsorption model could potentially have a significant effect on the HHV thermal efficiency; for example, a lower heat capacity for the solid would lead to increased temperature fluctuations during the adsorption and desorption cycles, potentially affecting the overall working capacity and the exit temperatures of the process gas streams. In order to attempt to quantify the effect of this and other parameters, we performed a

brief sensitivity study of the effect of changes in void fraction (ε), solid heat capacity ($C_{p,s}$), saturation capacity (q^{sat}), and mass transfer coefficient (k_{LDF}) on the base case sorbent model with $|\Delta H_{ads}| = 65$ kJ/mol, $p_{regen} = 2$ atm, and $T_{feed} = 505$ K. The upper and lower bounds for each parameter varied depending on the amount of uncertainty associated with each one; for example, although it is reasonable to assume that ε is known within 10%, k_{LDF} could easily vary by an order of magnitude. The upper and lower bounds of each parameter are summarized in Table 3.2, and the corresponding efficiency results are in Figure 3.11.

Table 3.2 Parameter values investigated in sensitivity analysis.

Parameter	Lower Bound	Original Value	Upper Bound
ε	0.36	0.40	0.44
$C_{p,s}$	800	1000	1200
q^{sat}	6	9	12
k_{LDF}	3	30	100

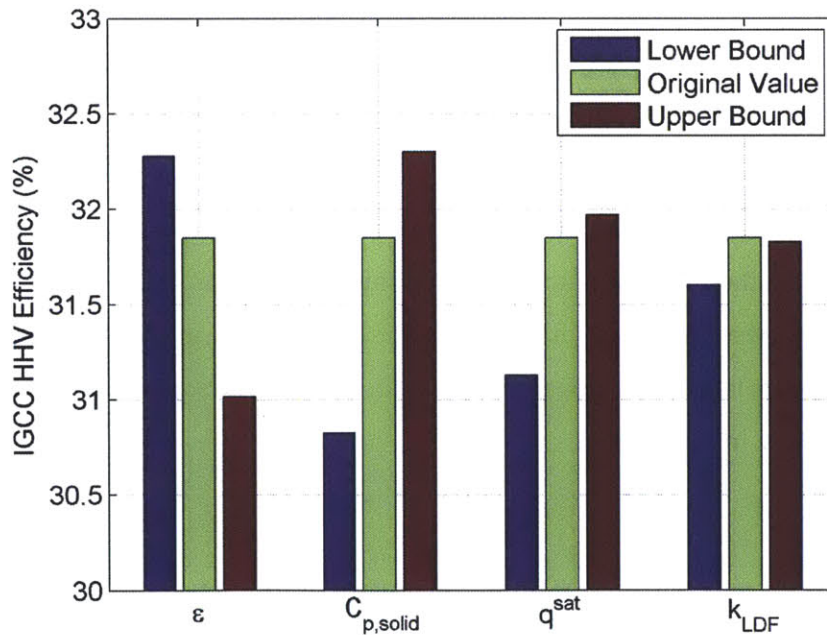


Figure 3.11 Sensitivity analysis of perturbing ε , $C_{p,solid}$, q^{sat} , and k_{LDF} from their original values of $\varepsilon = 0.4$, $C_{p,solid} = 1000$ J/mol-K, $q^{sat} = 9$ mol/kg, and $k_{LDF} = 30$ s⁻¹.

These results show that the effect of changes in each parameter can be fairly large, even greater than 1 percentage point HHV. This indicates the importance of ensuring that these parameters

are well-known. We note, however, that although this sensitivity study is instructive on the importance of the system parameters, these parameters rarely change independently. For example, the saturation capacity (q^{sat}) could be decreased by filling the bed with a high heat capacity solid that is inert to CO₂. In that case, the heat capacity of the bed would rise as the saturation capacity falls, perhaps helping to cancel out the large fluctuations in efficiency in either direction.

3.5 Isothermal Metal Oxide Adsorption Model Results

The isothermal metal oxide model described in Chapter 2 used the same Aspen Plus flowsheet as the base case metal oxide model. The efficiency differences between the two cases, therefore, derived from differences in the adsorption model outputs themselves. The model parameters surveyed for the isothermal model were nearly identical to those for the base case adiabatic model, shown in Table 3.1. However, an additional temperature of 480 K was included in this study because the column temperature would remain constant in all stages of the PSA cycle, ensuring that the rinse steam would not condense within the column. For the same reason, we increased the pressures of the rinse stream to 17 bar and 26 bar for the 480 K and 505 K systems, respectively—even though these temperatures and pressures are very close to the dew point of the rinse steam, the isothermal operation of the column ensured that the steam would remain in the vapor phase. As was the case with the base case adsorption model, the efficiency of the isothermal model was related to its steam requirement. The steam requirement for the isothermal process is shown below in Figure 3.12.

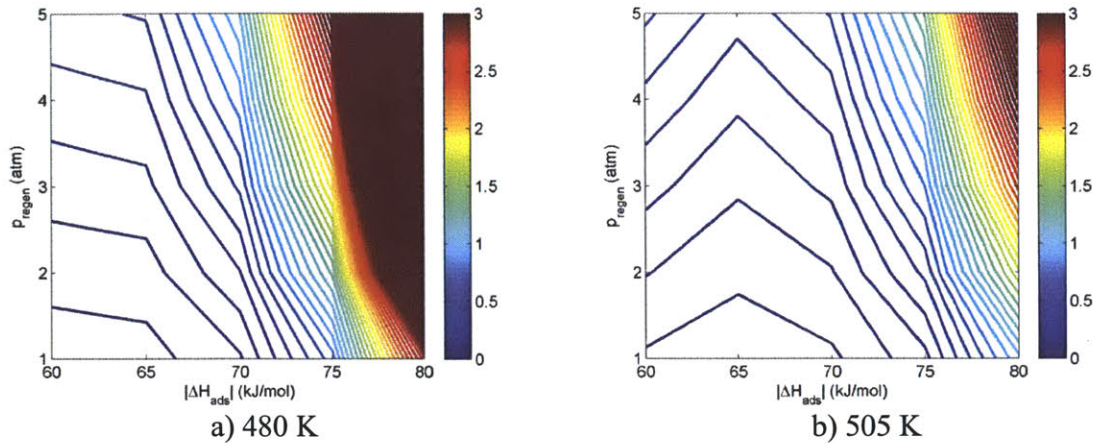


Figure 3.12 Steam requirement (mole ratio of steam required to CO₂ removed) for the isothermal model at $y_{CO_2} = 0.313$ for $T_{feed} =$ a) 480 K and b) 505 K. The color scale is constant between these plots and those in Figure 3.8 for the sake of comparison, but the steam to CO₂ ratio at 480 K reached as high as 10.

As before, the total amount of steam required by the process increased as $|\Delta H_{ads}|$ or p_{regen} became larger in magnitude. Interestingly, the steam requirement also increased at $|\Delta H_{ads}| = 60$ kJ/mol in the isothermal case at $T_{feed} = 505$ K. The fraction of H₂ lost to the CO₂ stream was constant at virtually 0 for the isothermal case, suggesting that the loss of H₂ to the CO₂ stream may be related to temperature affects within the adsorption column.

The working capacities for the adiabatic and isothermal cases were also calculated. A plot of the calculated working capacity as a function of $|\Delta H_{ads}|$ is shown below for both models. The computed numbers are in the usual range. For example, modified CaO is reported to have a working capacity of 6 mol/kg, while hydrotalcite is reported to have a working capacity of 0.8 mol/kg[42], [68].

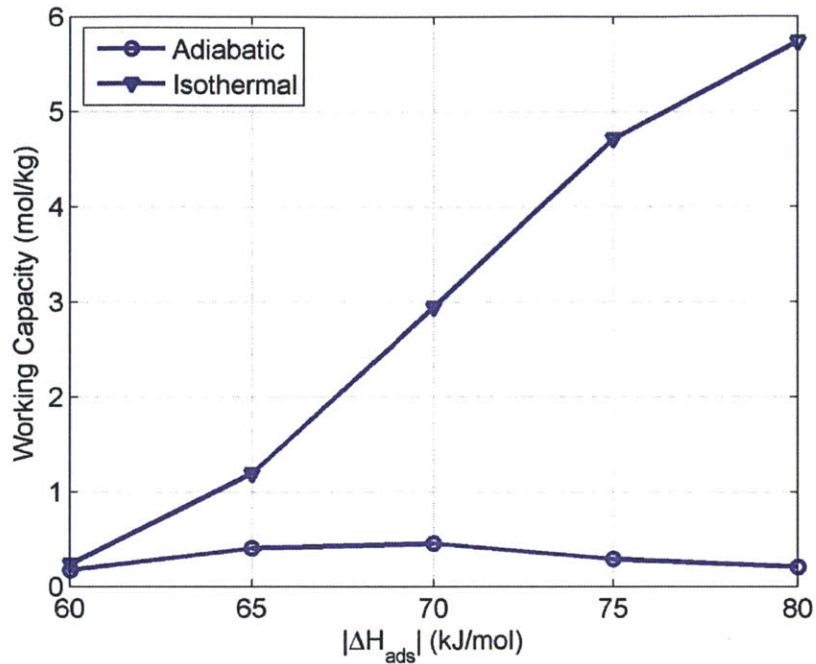


Figure 3.13 Working capacity of base case and isothermal models for $p_{regen} = 1$ atm, $T_{feed} = 505$ K and $y_{CO_2} = 0.313$.

Figure 3.13 proves the claim suggested in Chapter 2 that temperature effects within the bed greatly affect the working capacity. One might expect that the working capacity should increase as $|\Delta H_{ads}|$ becomes larger in magnitude; larger values of $|\Delta H_{ads}|$ translate to more negative values of $|\Delta G_{ads}|$, causing the CO_2 to bind more strongly to the sorbent. This is exactly the behavior that was observed in an isothermal bed. However, although the *initial* capacity of the sorbent markedly increased with $|\Delta H_{ads}|$ in an adiabatic bed, the *working* capacity decreased for large $|\Delta H_{ads}|$. A large binding energy raises the temperature of the bed more upon adsorption, decreasing the equilibrium amount adsorbed. It is also interesting to note that the largest working capacity predicted by the adiabatic model was lower than that reported by Hufton et al. for the SEWGS process[68]; perhaps that process is not perfectly adiabatic, or $|\Delta S_{ads}|$ for hydrotalcite is a bit smaller than the 160 J/mol-K assumed here. It is a great advantage to employ some sort of heat transfer technique to operate the column closer to the isothermal limit—this not only dramatically improves the working capacity, it also improves the thermal efficiency, shown in Figure 3.14.

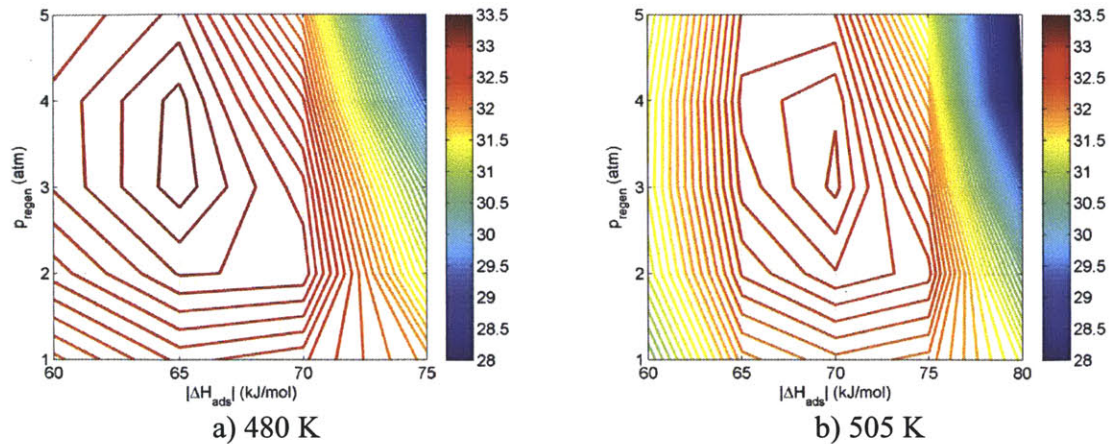


Figure 3.14 HHV thermal efficiency of isothermal adsorption model as a function of p_{regen} and $|\Delta H_{ads}|$ at $T_{feed} =$ a) 480 K and b) 505 K. Each contour represents the HHV thermal efficiency of the IGCC plant (%).

Although the trend of efficiency decreasing with increasing $|\Delta H_{ads}|$ continues somewhat with the isothermal case, the efficiency was much less dependent on p_{regen} . In fact, the maximum HHV efficiency predicted by this model actually occurred at $|\Delta H_{ads}| = 65$ kJ/mol and $p_{regen} = 3$ atm for $T_{feed} = 480$ K. The range of $|\Delta H_{ads}|$ plotted in this isothermal case is slightly smaller than that of the adiabatic case because the amount of steam required increases dramatically at high $|\Delta H_{ads}|$ (see Figure 3.12). The amount of steam required actually increased so much that there was not enough steam generated in the HRSG section to fulfill the regeneration requirement. As a result, those infeasible values of $|\Delta H_{ads}|$ are not plotted here.

A breakdown of the simulation estimate of the IGCC plant efficiency using the optimal conditions for both the adiabatic and isothermal cases is shown in Table 3.3.

Table 3.3 Efficiency summary for optimal base case (adiabatic) and isothermal models with steam regeneration.

Power Summary (MW)	Cold Cleanup Selexol	Steam Regen. Adiabatic	Steam Regen. Isothermal
ΔH_{ads}	--	-65 kJ/mol	-65 kJ/mol
P_{regen}	--	2 atm	3 atm
T_{feed}	--	505 K	480 K
Total Power Generated	737.1	710.8	724.3
<i>Gas Turbine</i>	464.4	462.4	462.2
<i>Steam Turbine</i>	264.5	243.4	256.5
<i>Auxiliary</i>	8.2	5.0	5.6
Total Power Consumed	-187.1	-159.4	-150.9
<i>N₂ Compression</i>	-34.8	-16.4	-14.9
<i>CO₂ Compression</i>	-28.3	-35.2	-29.8
<i>Auxiliary</i>	-124.0	-107.8	-106.2
Net Power Output	550.0	551.4	573.4
Thermal Power Input	1688	1731	1724
Thermal Efficiency (HHV)	32.6%	31.9%	33.3%

It is interesting to note that the total power generated actually decreased from the Selexol case to the two sorbent cases. The reason for this decrease is that some of the steam that is usually used in the HRSG section to generate power was instead used for the rinse and desorption steps in the PSA cycle. In addition, the CO₂ compression costs were slightly higher in the adiabatic adsorbent case than in the Selexol case because the CO₂ stream was produced at low pressure only in the adsorbent cases and the CO₂ is produced at two pressures in the Selexol case, as shown earlier in Figure 3.2 and Figure 3.7. Where the adsorbent cases saw an advantage over Selexol was the decrease in N₂ compression costs. As Figure 3.1 shows, the IGCC process with cold cleanup uses N₂ from the ASU as a diluent in the gas turbine, and this N₂ has to be compressed to the gas turbine delivery pressure of about 31 atm. In the sorbent cases, however, a significant amount of steam was retained with the H₂ stream going into the gas turbine, and this steam could take the place of the N₂, thereby decreasing the N₂ compression costs. The “Auxiliary” power consumption includes the power consumption from all other areas of the plant—for example, the air compressor required for the Air Separation Unit. However, the adsorbent processes also eliminated many of the auxiliary power loads, such as compressors, that are present in the Selexol process. These factors together make the adsorbent processes more competitive with Selexol; Selexol is about 0.7 percentage points more efficient than the adiabatic case and about 0.7 percentage points less efficient than the isothermal case.

3.6 Nonideal Gas Metal Oxide Adsorption Model Results

We simulated the nonideal gas adsorption model in both the adiabatic and isothermal cases. The structure of the Aspen Plus flowsheets was identical to that of the ideal gas models simulated in Sections 3.4 and 3.5. A link between the adsorption model outputs and the IGCC process simulation was again provided via tabulated data in an Excel workbook. We limited our parameter space to a smaller range because we felt this range would adequately capture the effect of the nonideal gas model. The explored parameter space for the adiabatic and isothermal nonideal gas models is shown below.

Table 3.4 Tabulated parameters for adiabatic and isothermal nonideal gas metal oxide models. The value of 480 K is shown in parentheses because it was simulated for the isothermal model only.

Model Variable	Tabulated Values
y_{CO_2}	0.20, 0.313
ΔH_{ads} (kJ/mol)	-65, -75
p_{regen} (atm)	1, 3, 5
T_{feed} (K)	(480), 505

It is worth noting that in order to include the B parameter in the model equations, the structure of the equations needed to be changed slightly. This change led to slight differences in the model parameter outputs as compared to the original base case model, even when the B parameter was set equal to 0, which, as shown in Chapter 2, would change the nonideal gas model back into the ideal gas model. These differences in model parameter outputs led to differences in HHV efficiency as large as 0.3 percentage points HHV at large values of $|\Delta H_{ads}|$, which would undoubtedly affect our comparison between the ideal gas and nonideal gas models. To avoid these numerical difficulties, we chose our comparison to be between the model parameters calculated using the nonideal gas model and the model parameters calculated using the nonideal gas model with B set equal to 0. The latter model parameters therefore took the place of the base case ideal gas adsorption model. We preferred this method because it enabled us to directly see the results that occur when the B parameter is nonzero; however, it is also instructive that the numerical differences in the model can account for efficiency differences as large as 0.3 percentage points HHV at high $|\Delta H_{ads}|$.

A comparison of the adiabatic models is shown in Figure 3.15.

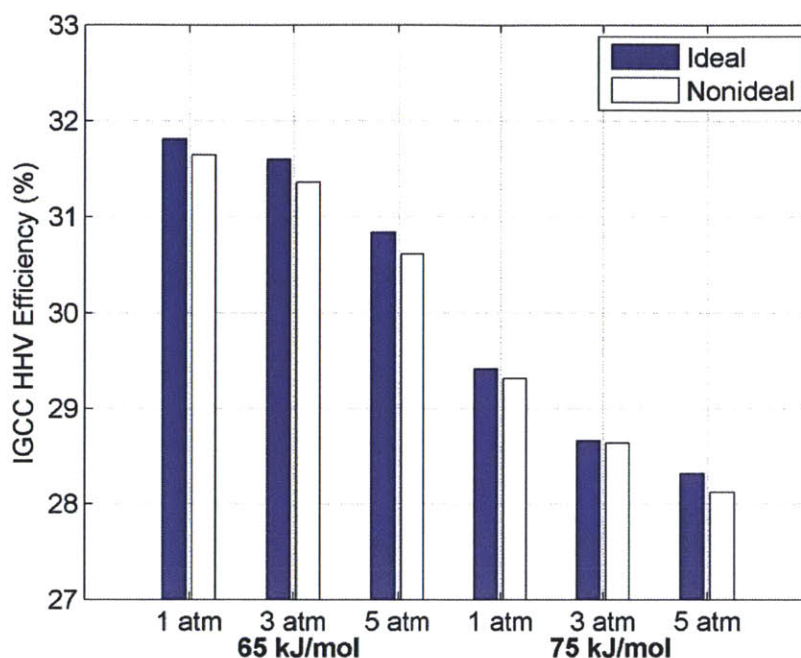


Figure 3.15 Comparison of results of ideal and nonideal adiabatic adsorption models.

The results of Figure 3.15 illustrate a few important points. The efficiency difference between the ideal and nonideal models was slight—a maximum of 0.2 percentage points in the cases investigated. This is not surprising—Figure 2.5 in Chapter 2 showed that the B parameter is small compared to the molar volume for most of the combinations of temperature, pressure, and concentration explored in the PSA cycle, so we would expect the efficiency differences to be correspondingly small. Interestingly, however, the nonideal model was consistently less efficient than the ideal model. This reduction in efficiency was caused by a slight increase in the amount of H_2 lost to the CO_2 stream. As we suggested in Section 3.5, this H_2 loss was likely due to temperature effects within the column. The temperature rise in the column during the adsorption step was slightly larger in the nonideal model than in the ideal model; this in turn made the CO_2 concentration front slightly more diffuse, necessitating a shorter rinse step.

Further evidence that the loss of H_2 product was related to temperature effects in the column is shown below in Figure 3.16, which shows a similar comparison of the ideal and nonideal models

for the isothermal case. As Figure 3.16 shows, there was virtually no difference between the ideal and nonideal models, regardless of the value of T_{feed} .

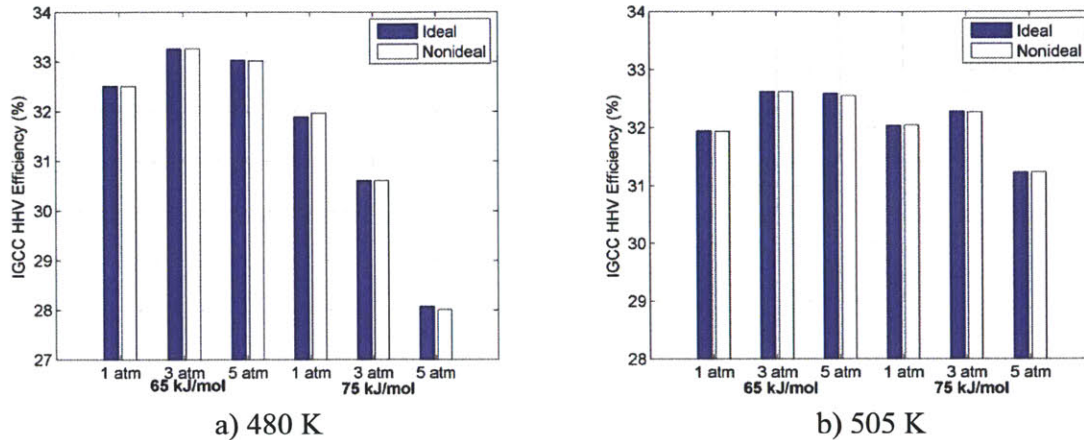


Figure 3.16 Comparison of ideal and nonideal isothermal models for a) $T_{feed} = 480$ K and b) $T_{feed} = 505$ K.

3.7 Metal Oxide with H₂ Regeneration Results

The use of the H₂ product stream as the purge gas in the desorption step did not dramatically change the IGCC flowsheet used in Aspen Plus. The largest change is simply the removal of the “desorption stream” from Figure 3.6—in this case, no desorption steam is needed. The explored parameter space for the H₂ regeneration case, shown in Table 3.5, was reduced compared to the steam regeneration base case due to a decreased numerical robustness in the H₂ regeneration model. However, the parameters chosen were those that tended to minimize the loss of H₂ to the CO₂ stream (see Sections 3.4 and 3.5), so we anticipated that we were limiting the parameter space to those parameters with the most potential.

Table 3.5 Tabulated values for Excel workbook used in adsorption model with H₂ regeneration.

Model Variable	Tabulated Values
y_{CO_2}	0.25, 0.313
ΔH_{ads} (kJ/mol)	-65, -70, -75, -80, -85
p_{regen} (atm)	1
T_{feed} (K)	505

Like the steam regeneration case, the HHV efficiency of the IGCC plant when using H₂ regeneration was determined by the amount of steam required by the process (here, just in the rinse step) and the amount of H₂ lost to the CO₂ product stream. On the one hand, because there is no steam used in the desorption step, we would expect the HHV efficiency to increase. However, in order to conform to the 90% CO₂ capture constraint, more H₂ was lost to the CO₂ product stream than in the steam regeneration case. Figure 3.17 shows the percentage of H₂ lost to the CO₂ product stream at $y_{CO_2} = 0.313$.

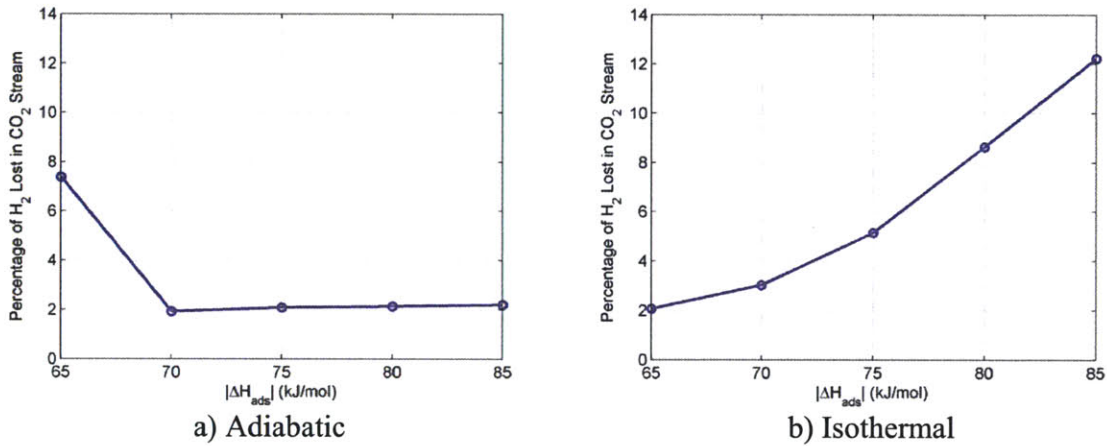


Figure 3.17 Unburned H₂ as a function of $|\Delta H_{ads}|$ in both the a) adiabatic and b) isothermal metal oxide with H₂ regeneration models at $T_{feed} = 505$ K, $p_{regen} = 1$ atm, and $y_{CO_2} = 0.313$.

The shape of the curves in Figure 3.17 is related to the length of the desorption steps. In the adiabatic case, the high temperatures of the column reduced the working capacity, even at high $|\Delta H_{ads}|$. Therefore, a long desorption step was not needed to regenerate the column. By contrast, the working capacity in the isothermal case increased with increasing $|\Delta H_{ads}|$, requiring longer desorption steps. The fraction of unburned H₂ could likely be reduced through further optimization of the pressure swing adsorption cycle for each value of $|\Delta H_{ads}|$; however, it is unlikely to be completely eliminated because the desorption step needs to be long enough in duration for the H₂ sweep gas to displace much of the CO₂ from the vapor phase in the adsorption column. Because the vapor phase in the column also includes some H₂ gas at the beginning of the desorption step, invariably some of this H₂ will be displaced into the CO₂

stream as well. Unfortunately, this lost H₂ had a significant impact on the HHV efficiency of the IGCC process, as illustrated in Figure 3.18.

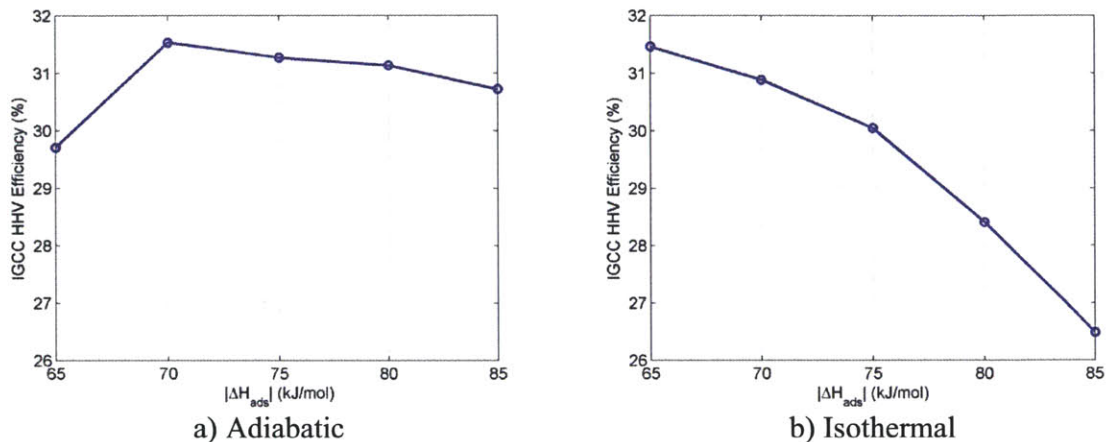


Figure 3.18 IGCC HHV efficiency for adiabatic and isothermal cases with H₂ regeneration and $T_{feed} = 505$ K, $p_{regen} = 1$ atm.

Clearly, the overall IGCC efficiency shown in Figure 3.18 was inversely related to the fraction of H₂ lost to the product stream in Figure 3.17. The isothermal case actually tended to produce lower efficiencies than the adiabatic case, likely due to the requirement of a longer desorption step, resulting in more H₂ lost to the CO₂ stream, especially at large values of $|\Delta H_{ads}|$. A summary of the optimal adiabatic and isothermal cases is shown in Table 3.6.

Table 3.6 Efficiency summary for optimal adiabatic and isothermal models with H₂ regeneration in the desorption step.

Power Summary (MW)	Cold Cleanup Selexol	H ₂ Regen. Adiabatic	H ₂ Regen. Isothermal
ΔH_{ads}	--	-70 kJ/mol	-65 kJ/mol
p_{regen}	--	1 atm	1 atm
Total Power Generated	737.1	724.1	726.8
<i>Gas Turbine</i>	464.4	462.7	462.5
<i>Steam Turbine</i>	264.5	256.5	258.7
<i>Auxiliary</i>	8.2	4.9	5.6
Total Power Consumed	-187.1	-173.8	-175.1
<i>N₂ Compression</i>	-34.8	-17.7	-16.9
<i>CO₂ Compression</i>	-28.3	-45.1	-45.6
<i>Auxiliary</i>	-124.0	-111.0	-112.6
Net Power Output	550.0	550.3	551.7
Thermal Power Input	1688	1745	1754
Thermal Efficiency (HHV)	32.6%	31.5%	31.5%

The H₂ regeneration cases were less efficient than the Selexol cold cleanup case and slightly less efficient than adiabatic operation with steam regeneration in the desorption step. One interesting thing to note, however, is that the tradeoff between H₂O required for regeneration and regeneration pressure that existed in the steam regeneration case does not exist here. Namely, if the adsorption column could be adequately designed to minimize the amount of H₂ lost to the CO₂ stream *and* the column could be regenerated at pressures greater than 1 atm, then the HHV efficiency would increase. We performed a hypothetical example of this in which p_{regen} was raised to 2 atm, but the amount of H₂ lost to the CO₂ stream is maintained at the same level as the optimal isothermal case. In this hypothetical case, the HHV efficiency increased by 0.6 percentage points due to a reduction in the CO₂ compression costs. It is therefore most advantageous with regard to HHV efficiency to design the adsorption column to be regenerated at as high a pressure as possible while keeping the amount of H₂ lost to the CO₂ stream less than 1%.

3.8 The Effect of the Linear Driving Force Constant

In Chapter 2 we described the model equations for the PSA system that included a constant, large value of k_{LDF} . We note that the LDF model for gas adsorption is usually applicable in the regimes where mass transfer resistances dominate; for example, previous researchers have indicated that the LDF model successfully approximates Fickian diffusion[76]. However, in these cases the value of k_{LDF} is typically either multiplied by a factor of the total concentration or divided by the equilibrium constant, suggesting that the rate is limited when the reaction is more exothermic. Furthermore, Seader and Henley suggest that the LDF rate with a constant k_{LDF} is applicable when the LDF rate refers to a difference in gas-phase concentrations[69], as shown in Equation (3.5).

$$\frac{dq_{CO_2}}{dt} = k_{LDF} (C_{CO_2} - C_{CO_2}^*) \frac{\varepsilon}{\rho_s (1 - \varepsilon)} = k_{LDF} \left(p_{CO_2} - \frac{q_{CO_2}}{K_{eq} (q_{CO_2}^{sat} - q_{CO_2})} p_{ref} \right) \frac{\varepsilon}{RT \rho_s (1 - \varepsilon)} \quad (3.5)$$

In this new LDF expression the rate in the desorption step may be slower than that in the adsorption step due to the lower partial pressure of CO₂. Therefore, we also evaluated our

adiabatic and isothermal metal oxide models with this new LDF model. We note that the constant value k_{LDF} was increased to 100 s^{-1} for this test to ensure that the rate during the adsorption step stayed relatively constant between the two LDF expressions.

The largest effect of modifying the LDF expression was to increase the steam requirement for the PSA cycle. This is a logical result; if the mass transfer is slower in the desorption step, the regeneration becomes less efficient, leading to an increase in the amount of steam required to perform the same amount of regeneration. As the results in Table 3.7 show, the effect on the steam requirement was fairly large, with the largest change being over 20%.

Table 3.7 Results of changing the LDF rate expression in the metal oxide model. The steam requirement is a mole ratio of H_2O to CO_2 removed.

Output	Adiabatic Model		Isothermal Model	
	$ \Delta H_{ads} = 65 \text{ kJ/mol}$ $p_{regen} = 3 \text{ atm}$ $T_{feed} = 505 \text{ K}$	$ \Delta H_{ads} = 75 \text{ kJ/mol}$ $p_{regen} = 1 \text{ atm}$ $T_{feed} = 505 \text{ K}$	$ \Delta H_{ads} = 65 \text{ kJ/mol}$ $p_{regen} = 3 \text{ atm}$ $T_{feed} = 480 \text{ K}$	$ \Delta H_{ads} = 75 \text{ kJ/mol}$ $p_{regen} = 1 \text{ atm}$ $T_{feed} = 480 \text{ K}$
Steam Requirement, rate = $k_{LDF}(q^*-q)$	0.73	1.26	0.29	0.76
Steam Requirement, rate = $k_{LDF}(C-C^*)$	0.80	1.45	0.29	0.94
HHV Efficiency rate = $k_{LDF}(q^*-q)$	31.6%	29.8%	33.3%	32.0%
HHV Efficiency, rate = $k_{LDF}(C-C^*)$	31.6%	29.8%	33.2%	31.5%

Interestingly, the relatively large changes in the steam requirement shown in Table 3.7 created correspondingly small changes in HHV efficiency. For the most part, the HHV efficiency was unchanged, although a 0.5 percentage point decrease was observed for the $|\Delta H_{ads}| = 75 \text{ kJ/mol}$ isothermal case. The HHV efficiency was essentially constant between the two rate expressions in the adiabatic case, even though the steam requirement increased. This occurred because the H_2 recovery increased with the new rate expression, and this counteracted the efficiency loss that would have arisen with a higher steam requirement. We can therefore conclude that any changes to the IGCC-CCS efficiency due to the change in LDF rate expression would likely be small. We also note that we would expect a slight increase in the capital cost of the PSA unit using this rate expression, since although we did not observe any significant changes in working capacity, the overall cycle time would increase due to a slightly longer desorption step.

3.9 Metal Hydroxide Adsorption Model Results

3.9.1 Additional Modifications to IGCC Flowsheet

As was the case with the metal oxide adsorption model, the PSA model was implemented in Aspen Plus using a *USER2* block that was linked to an Excel file. The heat integration of the system needed to be significantly modified because the steam requirement in the desorption step was much larger for metal hydroxides than it was for metal oxides. A schematic of this heat integration is shown below.

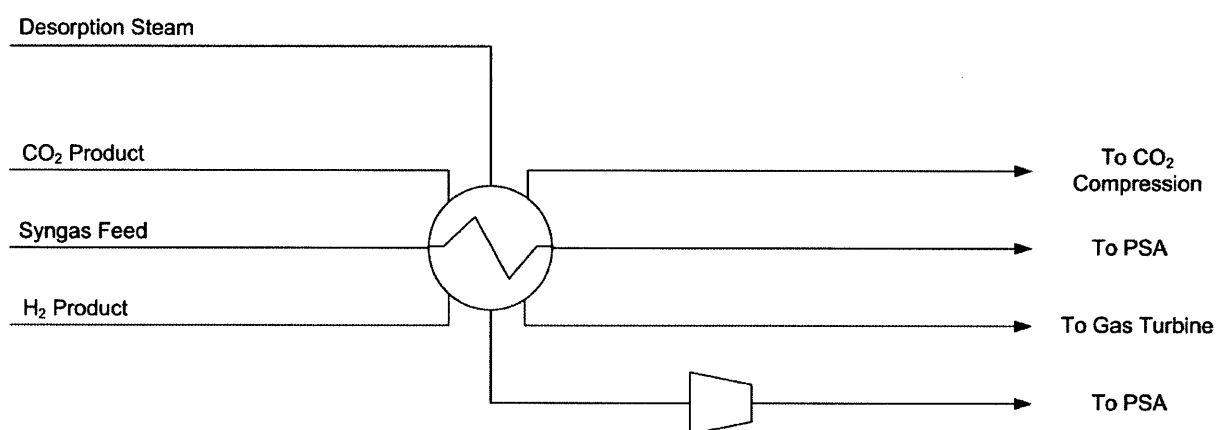


Figure 3.19 Heat integration for CO₂ removal with metal hydroxides.

The desorption steam entered the heat exchanger as boiler feed water that was compressed to some intermediate pressure. The hot syngas feed stream and the two product streams from the PSA process were used to heat this desorption water such that it boiled to become vapor phase. A compressor was used downstream of this heat exchanger to compress the desorption steam to the appropriate final pressure. Figure 3.19 is actually a slight simplification because the desorption steam stream actually consisted of three separate streams, each at a different inlet pressure so that the temperature differences across the heat exchanger could be reduced. In all cases care was taken to ensure the minimum approach temperature was approximately 5-10°C.

Higher-temperature heat streams, such as the exhaust gas exiting the gas turbine, were not used in the heat integration above because it was determined to be more beneficial to generate high pressure steam with those heat streams. In addition, because the dew points of the CO₂ product and H₂ product streams were too low to produce superheated desorption steam at the desired

pressure, additional compression of the superheated desorption steam was required. The use of the compressor provided an additional benefit, however, because it effectively raised the temperature of the sweep gas to the desired temperature of 550 K without requiring additional heat from the steam power cycle.

3.9.2 Efficiency Results of General Metal Hydroxide Sorbents

The main factors contributing to the overall efficiency of the IGCC-CCS process are the amount of steam required for the desorption step and the steam pressure during this step. Additional factors such as the exit temperatures of the H₂ and CO₂ product streams also contributed to the efficiency. A plot of the mole ratio of steam required per mole of CO₂ removed is shown in Figure 3.20.

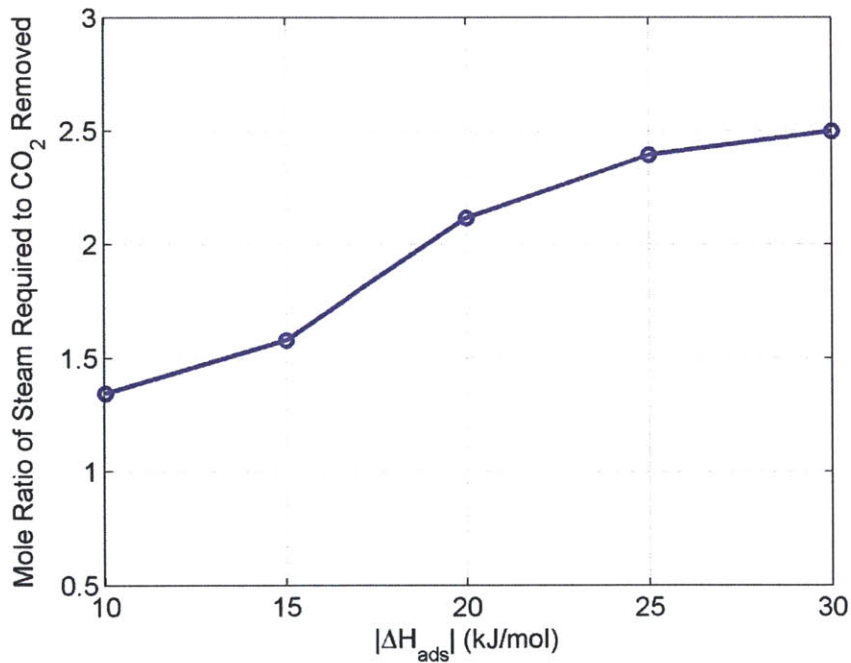


Figure 3.20 Steam requirement as a function of enthalpy of adsorption, $y_{CO_2} = 0.31$, $|\Delta S_{ads}| = 25$ J/mol-K, $T_{regen} = 550$ K.

We note that because the adsorption isotherm is independent of the total system pressure (see Chapter 2), the amount of steam required did not strongly depend on the regeneration pressure over the range of $20 \text{ atm} \leq p_{regen} \leq 30 \text{ atm}$ surveyed in this work. In other words, regeneration at 30 atm required virtually the same amount of steam as regeneration at 20 atm. This is a key

difference of metal hydroxides as compared to metal oxides—because the isotherm is independent of pressure, sorbent regeneration can be achieved at any physically realizable p_{regen} . As such, it is worth noting that unlike in the metal oxide model described earlier, variations in regeneration pressure were not tabulated in our Excel workbook linking the hydroxide simulation results to the Aspen Plus flowsheet and were instead calculated at 20 atm only.

The steam requirement for the desorption step *does* depend on the enthalpy of adsorption, however. As Figure 3.20 shows, the steam requirement increased as the enthalpy of adsorption increased in magnitude. This is a logical result, since a larger enthalpy of adsorption would signify that the CO₂ is adsorbed more strongly, meaning that a larger amount of steam would be needed to remove it.

The HHV efficiency of the IGCC plant is shown in Figure 3.21.

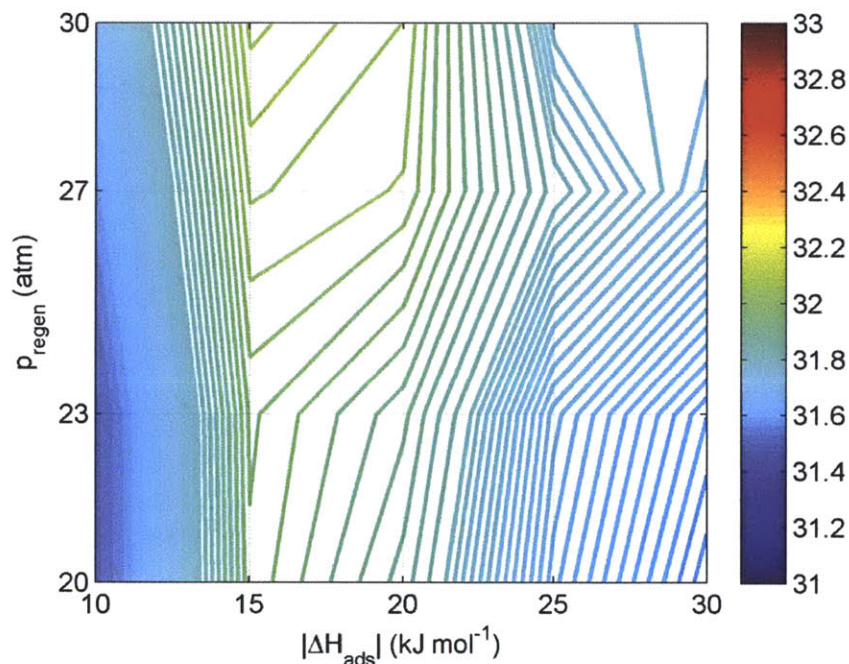


Figure 3.21 Contour plot of HHV efficiency (%) of metal hydroxide adsorption process, $|\Delta S_{ads}| = 25 \text{ J/mol-K}$, $T_{regen} = 550 \text{ K}$.

It is also worth noting that the HHV efficiencies in Figure 3.21 seemed to be maximized in most cases when $p_{regen} = 30 \text{ atm}$, although the variation with respect to pressure was within 0.2 percentage points HHV. Although the regeneration steam compression costs increased with

increasing p_{regen} , a higher p_{regen} allowed for a slight increase in steam turbine output due to the greater amount of usable heat in the high-pressure CO₂ stream and a decrease in the CO₂ compression costs. The pressure was not increased above 30 atm in this study because further increases led to the steam being below its dew point.

In addition, our calculations showed that the overall HHV efficiency was consistently slightly less than that of Selexol, the conventional cold CCS technology. The maximum efficiency achieved was at 15 kJ/mol, which is at first surprising given that its steam requirement is actually larger than that at 10 kJ/mol. However, at 10 kJ/mol, the amount of CO₂ required for the rinse step is larger, leading to slightly larger compression costs for the CO₂ recycle stream. At enthalpy of adsorption values larger than 15 kJ/mol, the efficiency also tended to decrease due to the increased steam requirement for the desorption step (see Figure 3.20). Therefore, 15 kJ/mol and $p_{regen} = 30$ atm seemed to achieve the optimal efficiency of 32.1%. A breakdown of the efficiency in this case is shown in Table 3.8.

Table 3.8 Optimal sorbent performance, $|\Delta S_{ads}| = 25$ J/mol-K.

Power Summary (MW)	Cold Cleanup Selexol	Optimal Sorbent $\Delta H_{ads} = -15$ kJ/mol, $p_{regen} = 30$ atm
Total Power Generated	737.1	725.5
<i>Gas Turbine</i>	464.4	463.5
<i>Steam Turbine</i>	264.5	258.2
<i>Auxiliary</i>	8.2	3.8
Total Power Consumed	-187.1	-169.6
<i>N₂ Compression</i>	-34.8	-20.6
<i>CO₂ Compression</i>	-28.3	-8.6
<i>Auxiliary</i>	-124.0	-140.4
Net Power Output	550.0	555.9
Thermal Power Input	1688	1733
Thermal Efficiency (HHV)	32.6%	32.1%

As Table 3.8 shows, the main areas where the optimal hydroxide sorbent performance exceeded that of the base case Selexol process was in the decrease of N₂ and CO₂ compression costs. The N₂ compression load was decreased because a significant amount of steam was retained in the H₂ product stream, and this steam functioned as the diluent in the gas turbine. Because less N₂ was needed for the gas turbine, the compression costs decreased accordingly. The CO₂ compression

load decreased because the CO₂ is produced at 30 atm, meaning that significantly less compression is needed to bring it to its sequestration pressure of 150 atm. Even though the total power consumed was decreased in the metal hydroxide case, the “Auxiliary” power is actually a little larger. As before, the “Auxiliary” power includes the power consumption from all other areas of the plant—for example, the air compressor required for the Air Separation Unit. However, as described in Section 3.9.1, the steam for the desorption step was produced at pressures below p_{regen} , since not enough high-temperature heat was available to produce the steam at the desired pressure. Therefore, additional compressors had to be added to increase the steam pressure to its desired level. The work for these compressors was routinely greater than 20 MW, and as a result the efficiency was affected accordingly.

We note that we did not optimize the heat integration of the IGCC plant, and as such we recognize that more efficient processes may exist. However, even without optimizing the heat integration we can achieve HHV efficiencies that are greater than 32% for $15 \text{ kJ/mol} \leq |\Delta H_{ads}| \leq 20 \text{ kJ/mol}$. As a result, we conclude that the use of metal hydroxides is at least competitive with Selexol in this enthalpy range.

We also investigated the effect of ΔS_{ads} on this optimal range of enthalpies of adsorption. Figure 3.22 shows a comparison of the steam requirement for the process if $|\Delta S_{ads}|$ were increased to 30 J/mol-K.

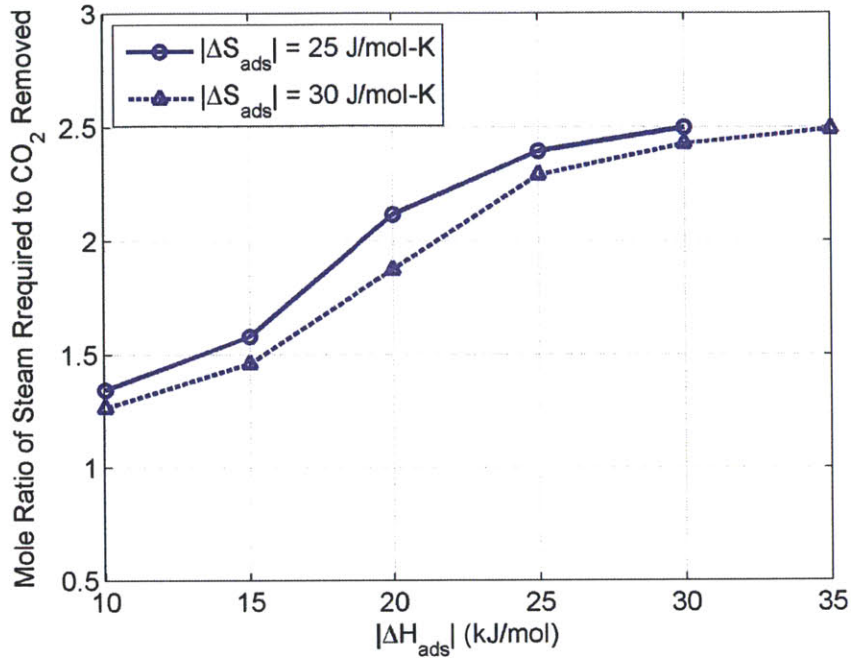


Figure 3.22 Comparison between steam requirement for $|\Delta S_{ads}| = 25$ and 30 J/mol-K, $y_{\text{CO}_2} = 0.31$.

For the most part, the steam requirement was consistently lower for $|\Delta S_{ads}| = 30$ J/mol-K, and the enthalpy of adsorption could be increased to 35 kJ/mol for $|\Delta S_{ads}| = 30$ J/mol-K while still achieving the same steam requirement as 30 kJ/mol for $|\Delta S_{ads}| = 25$ J/mol-K. This is reasonable; the affinity of a given sorbent for CO_2 is determined by its Gibbs free energy of adsorption, not solely its enthalpy of adsorption, so because the entropy of adsorption is larger, the enthalpy of adsorption can be correspondingly larger to obtain the same overall binding strength. The corresponding HHV efficiencies for this 30 J/mol-K case are shown in Figure 3.23. Because Figure 3.21 shows that the efficiencies were usually greatest at 30 atm (with only small variations with respect to pressure), we limited our plot to the efficiencies at 30 atm only.

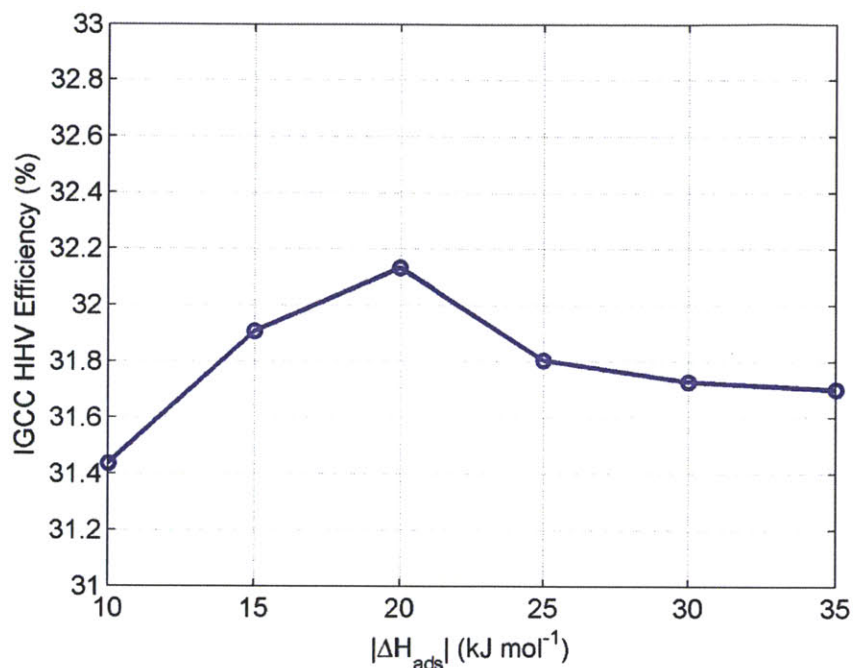


Figure 3.23 HHV Efficiency at $p_{regen} = 30$ atm for $|\Delta S_{ads}| = 30$ J/mol-K, $T_{regen} = 550$ K.

As Figure 3.23 shows, the optimal efficiency shifted slightly to the right (i.e., more exothermic adsorption) when compared to the $|\Delta S_{ads}| = 25$ J/mol-K case, which is logical because a more exothermic reaction would counter the increased entropy change upon adsorption. The shift was slight, however, because the range of favorable enthalpy of adsorption values in which the efficiency is competitive with the cold cleanup Selexol process was still approximately $15 \text{ kJ/mol} \leq |\Delta H_{ads}| \leq 20 \text{ kJ/mol}$. In addition, the maximum efficiency is approximately the same as in the $|\Delta S_{ads}| = 25$ J/mol-K case, with a value of 32.2%, indicating that the value of the maximum efficiency achieved was not dependent on the entropy of adsorption.

As a final note in this general study, we show the computed working capacities in both the $|\Delta S_{ads}| = 25$ J/mol-K and $|\Delta S_{ads}| = 30$ J/mol-K cases, as shown in Figure 3.24.

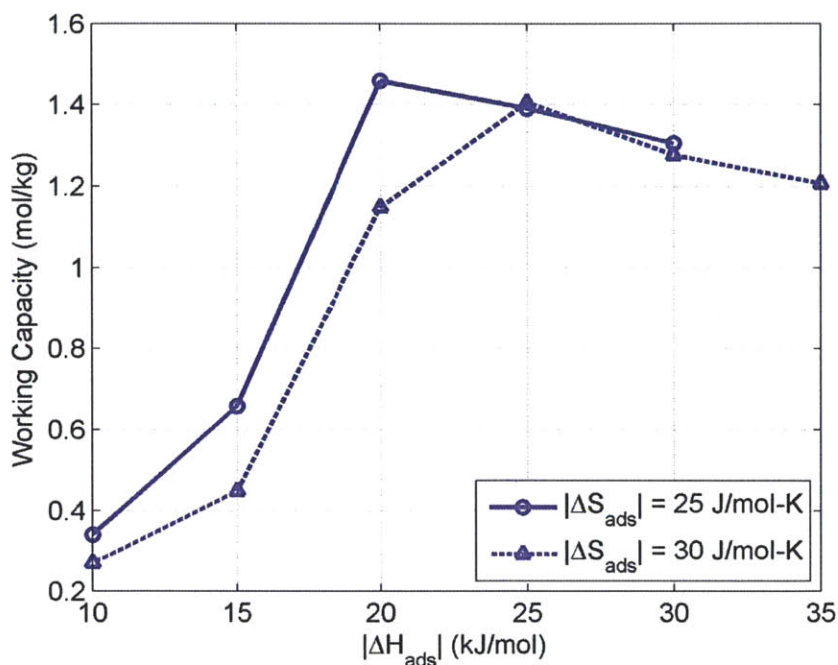


Figure 3.24 Calculated working capacity for $|\Delta S_{ads}| = 25$ and 30 J/mol-K cases, $T_{regen} = 550$ K.

The working capacity reached a maximum value of about 1.4 to 1.5 mol/kg at approximately $|\Delta H_{ads}| = 20$ kJ/mol for both values of the entropy of adsorption. It is worth noting that the capacity dropped by at least a factor of 2 at $|\Delta H_{ads}| = 15$ kJ/mol and lower. This decrease in capacity was due to the fact that the Gibbs energy of adsorption is at its most unfavorable for adsorption (and conversely, most favorable for desorption) at the lowest value of the adsorption enthalpy. Because the calculated efficiencies at $|\Delta H_{ads}| = 15$ kJ/mol and $|\Delta H_{ads}| = 20$ kJ/mol were similar, these working capacities strongly suggest that $|\Delta H_{ads}| = 20$ kJ/mol is a better target enthalpy of adsorption for a general metal hydroxide material.

It is also interesting to note that the working capacity of 1.4 mol/kg is approximately 2-3 times greater than the working capacities calculated for the adiabatic operation of metal oxide materials (see Section 3.5). This capacity difference illustrates a potential benefit of metal hydroxides over metal oxides: a higher working capacity leads to lower sorbent requirement and therefore potentially lower capital costs. The overall capital cost of the PSA process is related to both the working capacity and the cycle time, however, so additional optimizations of the PSA cycle times would need to be performed in order to evaluate more definitively which material would result in the lowest costs.

3.9.3 Hydroxide Materials Identified Using DFT

We conclude our study of hydroxide materials by moving away from a hypothetical “general” sorbent to materials with specific thermodynamic properties. The thermodynamic parameters for the 5 hydroxide materials are given in Table 3.9.

Table 3.9 Calculated thermodynamic parameters for the sorbent materials used in this work.

Material	ΔH_{ads} (kJ/mol)	ΔS_{ads} (J/mol-K)	$C_{p,s}^{sat}$ (J/mol-K)	$C_{p,s}^{unsat}$ (J/mol-K)	q_i^{sat} (mol/kg)
Co(OH) ₂	-31.5	-36.5	98.2	95.8	5.38
Fe(OH) ₂	-26.2	-38.3	93.9	92.3	5.56
Mn(OH) ₂	-52.0	-22.3	99.0	97.1	5.62
Ni(OH) ₂	-28.7	-22.3	97.5	94.2	5.39
Zn(OH) ₂	-33.9	-31.2	96.2	96.2	5.03

We compute their corresponding HHV efficiencies in Figure 3.25.

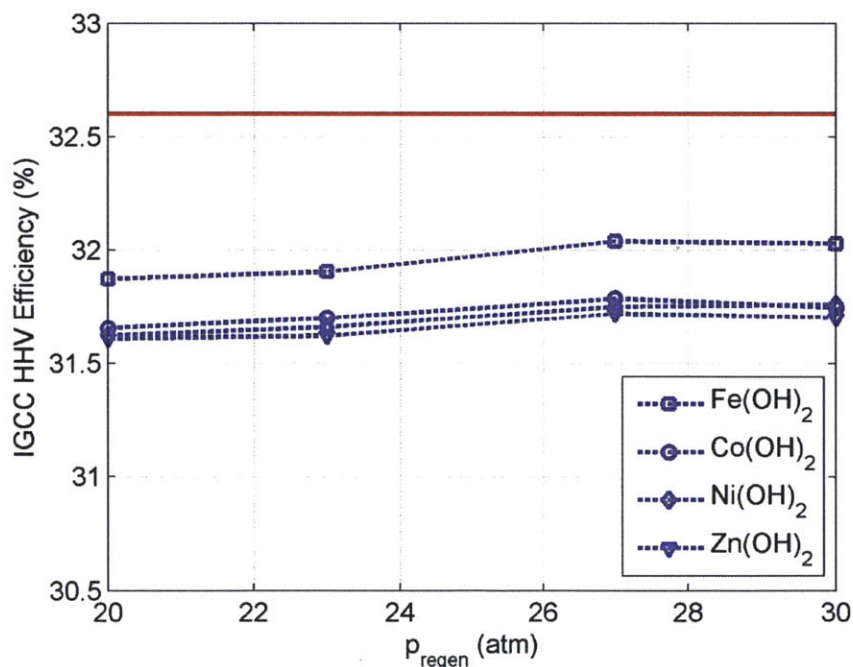


Figure 3.25 IGCC HHV efficiency for materials calculated via DFT with $T_{regen} = 550$ K. The solid line shows the base case Selexol efficiency.

Our calculations show that 4 of the 5 materials, Fe(OH)₂, Ni(OH)₂, Co(OH)₂, and Zn(OH)₂, were within 1 percentage point HHV of the Selexol process, with the most efficient material being

Fe(OH)₂. These results are consistent with those of the general material studied in the previous section, since the thermodynamic parameters of Fe(OH)₂ most closely resemble those determined to be the most favorable. Mn(OH)₂ is not displayed in Figure 3.25 because the steam requirement for that material was much too large. This result is also consistent with our earlier discussion of the general hydroxide sorbents for CO₂ capture, since the calculated enthalpy of adsorption for Mn(OH)₂, -52 kJ/mol, is well outside the favorable range studied.

3.10 A Note on Warm Sulfur Removal

Throughout this work, our evaluation of the various warm CO₂ removal technologies was based upon the sulfur removal technology being developed by RTI and Eastman Chemical, which is described in Sections 3.3.1 and 3.3.2. From an economic perspective, it may be worthwhile to produce elemental sulfur in this manner, since sulfur is a salable byproduct. From an efficiency standpoint, however, the process loses 2 moles of H₂ for every mole of sulfur within the coal, decreasing the power output of the gas turbine. Because we used a relatively high-sulfur coal (approximately 3 wt%), this amount of H₂ was significant. Table 3.10 shows the flow rates of hydrogen exiting the water gas shift reactor and entering the gas turbine for two different cases. The first column shows the flow rates for the cold cleanup Selexol flowsheet; the second column shows the flow rates for the isothermal CO₂ adsorption on metal oxides (with steam regeneration) case, $|\Delta H_{ads}| = 65$ kJ/mol, $T_{feed} = 505$ K, and $p_{regen} = 1$ atm. The latter case was selected to be a suitable representative "warm cleanup" case due to the fact that no H₂ was predicted to be lost in the CO₂ product stream.

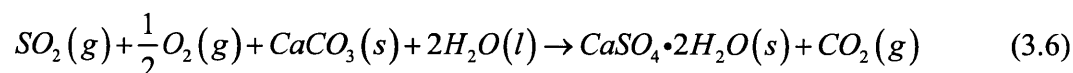
Table 3.10 H₂ flow rates for both Selexol cold cleanup and isothermal metal oxides.

H ₂ Flow Rate (kmol/hr)	Cold Cleanup Selexol	Warm Cleanup Isothermal Metal Oxide
Exiting Water Gas Shift	15800	16100
Entering Gas Turbine	15700	15700

Interestingly, even though the H₂ flow rate entering the gas turbine was approximately the same in each case, the flow rate exiting the WGS unit was approximately 2% higher in the adsorbent case. This decreases the potential HHV efficiency because more coal was needed (i.e., greater

thermal input) to produce the same amount of hydrogen and achieve the same amount of power output.

To overcome this problem, one potential solution is to replace the RTI DSRP step with a simple wet flue gas desulfurization (FGD) step. The pertinent reaction for the FGD process is shown below in Equation (3.6).



The product generated from this FGD reaction is gypsum, which has a small market value due to its use in the manufacture of concrete and drywall. The FGD process, however, is not without its own limitations. Specifically, this process introduces an additional raw material cost in the limestone sorbent ($CaCO_3$). Because the price of gypsum is highly variable, it is often estimated at \$0 per ton for conservative economic analyses. The limestone, meanwhile, can be estimated to cost \$15 per ton[98]. Based on the flow rate of sulfur entering the FGD unit, this translates to an additional operating cost of approximately 0.05 cents per kWh, not counting transportation costs.

Assuming the additional operating cost is acceptable, the FGD process still presents an additional technical challenge in that it produces more CO_2 . In order to maintain an overall CO_2 capture rate of 90%, this CO_2 must be accounted for in some manner. It is worth noting that alternative warm sulfur capture technologies, such as the production of sulfuric acid, do not produce CO_2 as a byproduct and may as a result be more promising than the FGD process. The FGD process is useful as an illustration of a relatively simple alternative to the DSRP process, however, and a result will be the only process described in detail here. We envisioned 4 scenarios in which the additional CO_2 separation could occur.

- Scenario 1: Isothermal adsorbent case with RTI sulfur removal, O_2 -fired ZnS oxidation, and DSRP for sulfur recovery (no FGD)
- Scenario 2: Isothermal adsorbent case with RTI sulfur removal, O_2 -fired ZnS oxidation, and O_2 -fed FGD for sulfur capture. The CO_2 -containing exhaust stream from the FGD unit is fed directly into the CO_2 compression block in the Aspen Plus flowsheet to maintain 90% capture

- Scenario 3: Isothermal adsorbent case with RTI sulfur removal, air-fired ZnS oxidation, and air-fed FGD for sulfur capture. The CO₂-containing exhaust stream from the FGD unit is fed directly into the CO₂ compression block in the Aspen Plus flowsheet to maintain 90% capture
- Scenario 4: Isothermal adsorbent case with RTI sulfur removal, air-fired ZnS oxidation, and air-fed FGD for sulfur capture. The CO₂-containing exhaust stream from the FGD unit is vented to the atmosphere. To compensate, the CO₂ adsorption unit is modified to capture additional CO₂ in the Aspen Plus flowsheet to maintain 90% capture

Each scenario was tested within the Aspen Plus framework in order to evaluate its overall IGCC-CCS efficiency. Scenarios 2 and 4 were feasible; Scenario 3 resulted in the purity of the CO₂ product stream being too low due to the presence of additional N₂. Scenario 4 was deemed to be the most efficient, with an overall efficiency of 33.8%. Therefore, if FGD were used in place of the RTI DSRP process, the potential gain in efficiency is at least another 0.5 percentage points HHV. Based on these favorable results, a careful evaluation of the tradeoff between the additional operating cost of the FGD unit and the gains in efficiency would need to be performed in order to select the proper sulfur recovery technique.

3.11 Conclusions

In this chapter we detailed the results of our process simulations for metal oxide and metal hydroxide sorbents. Prior reports suggest that conducting the separations at high temperature provides a large HHV efficiency advantage. However, we found that conducting the separations at high temperature is only slightly advantageous for metal oxides and potentially metal hydroxides, and to achieve even larger HHV efficiencies, a different sulfur handling technique, such as FGD, is required. In addition, the CO₂ adsorbents only offer a gain in efficiency over the Selexol process for certain combinations of $|\Delta H_{ads}|$ and p_{regen} . We acknowledge that due to the limitations of our numerical models, a lack of optimization of the overall IGCC flowsheet, and some uncertainties surrounding many of the model parameters, the absolute HHV efficiencies of the IGCC processes calculated in this work may be inaccurate by even several percentage points HHV. However, due to the fact that many of these limitations are the same in each model

studied, we feel that the efficiency differences between the different technologies captured within this study are correct.

For metal oxides, a major challenge is reducing the temperature variations within the adsorption column, as evidenced by both the increased HHV efficiency and sorbent working capacity during isothermal operation. If a better sorbent material with more optimal properties is identified, it could provide a promising solution for high temperature CO₂ capture in the near future. A standard state enthalpy change of adsorption of -65 kJ/mol and regeneration pressure of 3 atm was found to yield the highest gain in efficiency relative to Selexol (0.7 percentage points HHV) in isothermal operation. During adiabatic operation this efficiency is reduced relative to Selexol, with the maximum efficiency being 0.7 percentage points below that of Selexol. Only minor reductions in HHV efficiency occurred if the ideal gas law were replaced by the 1st order Virial equation of state (0.2 percentage points HHV or lower). If the sorbent regeneration were performed using H₂ instead of steam, a major process challenge would be reducing the amount of H₂ lost to the CO₂ product stream. However, if a proper adsorption cycle could be developed with regeneration occurring above 1 atm, the gains in efficiency could be significant due to the savings in CO₂ compression costs. Further research should be directed toward synthesizing candidate materials with this binding energy and optimizing the adsorption-desorption cycle in order to improve the working capacity. Testing is required to verify the new sorbents are durable through many adsorption-desorption cycles and that they are not degraded by other components of the IGCC syngas.

For metal hydroxides, the optimal range of adsorption enthalpies varies slightly depending on the entropy of adsorption used, but in general the favorable range is approximately $15 \text{ kJ/mol} \leq |\Delta H_{ads}| \leq 20 \text{ kJ/mol}$. The highest efficiency occurs at $|\Delta H_{ads}| = 15 \text{ kJ/mol}$, with calculated HHV efficiencies being approximately 0.5 percentage points HHV lower than Selexol at the current level of heat integration. The working capacities calculated for metal hydroxides are larger than those corresponding to adiabatic operation of metal oxides, showing that a potentially significant advantage of these materials is their ability to reduce the capital costs of the PSA unit. An important future step in evaluating these materials would be to optimize the PSA cycle times in order to better understand their capital requirement. We acknowledge that further optimization of the heat integration would likely lead to even higher calculated efficiencies; however, we note

that even with our simple heat integration techniques the hydroxide PSA cycle is competitive with Selexol. Finally, we showed that 4 of the 5 materials identified using DFT screening result in overall IGCC-CCS efficiencies within 1 percentage point HHV of that of Selexol, with $\text{Fe}(\text{OH})_2$ predicted to be the most efficient.

Chapter 4. Computational Screening of Hg Adsorbents Using DFT

4.1 Introduction

Here we depart from our previous focus on CO₂ in favor of a different coal-derived pollutant, Hg. As we stated in Chapter 1, the main difficulty in identifying a material for Hg capture is not necessarily that it acts efficiently. Rather, the difficulty with Hg is chemical: identifying a material that not only reacts with Hg at the trace concentrations found in the IGCC stream, but is also inert to the other species in the gas stream. In this chapter we use density functional theory (DFT) to screen metallic species, metal oxides, and metal sulfides for their ability to capture Hg.

4.2 Previous Uses of DFT for Hg Capture

In Chapter 1 we described several examples of using DFT for materials screening. Previous work has also focused on more accurate DFT calculations for specific Hg adsorption reactions. Padak et al. used DFT within the Gaussian03 software package to model mercury adsorption onto halogenated activated carbon surfaces[99]. The intended application of these calculations was to quantify the adsorption ability of mercury onto these activated carbons under hot flue gas conditions. A cluster model was used with pyrene as the basis for activated carbon. Various oxygen-containing functional groups were added to the pyrene cluster in an attempt to model the activated carbon surface more effectively. For the DFT calculations, the B3LYP[100–102] functional with the LANL2DZ basis set was used. Although the calculations were limited in that they were performed at room temperature and did not include the presence of other flue gases, they did successfully show the energetic effects of modifying the surface of a sorbent. Cluster models in Gaussian03 have also been performed investigating the adsorption of Hg on surfactants. In this case, Sun et al. used DFT with the B3LYP functional to identify the

mechanism of Hg adsorption on ionized surfactants, a behavior that had been observed experimentally[103].

Other studies of Hg adsorption using DFT abound. Several groups have studied the adsorption of elemental Hg (Hg^0) and HgCl_2 on CaO-based materials at different surface coverages[104–106]. All three studies used GGA methods such as PW91[107] or B3LYP for the energy calculations. Based on the relative magnitudes of the calculated binding energies they concluded that Hg^0 binds via a physisorption mechanism, and the HgCl_2 species bind via a chemisorption mechanism. Finally, Steckel[108] also developed a mercury adsorption model using DFT in the Vienna *ab initio* Simulation Package (VASP)[109]. The purpose of their calculations was to characterize the bonding of mercury to various metal surfaces. Their method employed a periodic lattice model, and LDA and GGA functionals were both used for the DFT calculations. The absolute values of the adsorption enthalpies that they calculated were lower than experiments predicted for the GGA functional used. They did, however, predict the following trend of reactivity: $\text{Ag} < \text{Au} < \text{Cu} < \text{Ni} < \text{Pt} < \text{Pd}$. This trend was verified previously using experiments, with the exception of Cu, which was measured to have the lowest reactivity of the species listed. Therefore, with the exception of mercury adsorption onto copper, they have developed a method to capture trends in the behavior of metals with respect to mercury adsorption ability.

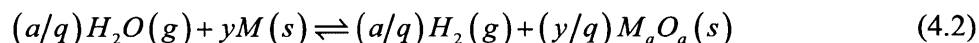
Two important conclusions can be drawn from these previous studies. First, the use of GGA functionals such as PW91, PBE[110], or B3LYP is much more common for energetic calculations with Hg than LDA functionals. Second, most likely due to inaccuracies inherent to DFT calculations, studies calculating *relative* energies are much more common. In other words, the absolute enthalpies of adsorption calculated using DFT may not be correct, but because the systematic error is likely to be the same between two different calculations, one can use DFT to correctly predict which mechanism or adsorbent material results in a lower energy. Both of these results are used in our own calculation method for screening Hg adsorbent materials: our method also uses GGA functionals, and more importantly, because we are interested in increasing the absolute accuracy of the calculations without increasing the computation time, we use experimental data wherever possible.

4.3 DFT Screening of Pure Metals for Hg Adsorption

Following the results of Steckel in investigating pure metals for Hg adsorption, our initial study was high-throughput screening of pure metals as candidates for Hg adsorption. This work was done in collaboration with Anubhav Jain and Gerbrand Ceder, and the details of these calculations can be found in Jain et al[111]. To briefly summarize the method, these calculations centered on identifying pure metal materials M that could react with Hg via the reaction shown in Equation (4.1).



It is worth noting that the reaction shown in Equation (4.1) is a bulk formation reaction—not a surface reaction, which is expected to be the predominant reaction for Hg capture due to factors such as surface effects, particle size, kinetics, and mass transfer limitations. However, the enthalpy of reaction was expected to be among the strongest contributors to the efficacy of a given sorbent material, thereby giving a method to quickly screen candidate materials via simpler bulk DFT calculations. As was stated previously, a successful Hg sorbent would possess two main characteristics: reactivity to Hg and inertness to the other syngas components. In the case of pure metals, it was predicted that the most likely competing reaction for Hg adsorption would be oxidation of the metal via steam, as shown in Equation (4.2).



The electronic energies of the materials were calculated using VASP and crystal structure inputs from the Inorganic Crystal Structure Database (ICSD)[112], [113]. The electronic energies were combined with calculated chemical potentials of Hg and O_2 in the syngas stream to evaluate the relative reactivity to amalgam formation (reaction with Hg) and oxide formation (reaction with steam). These results are summarized in Figure 4.1 below.

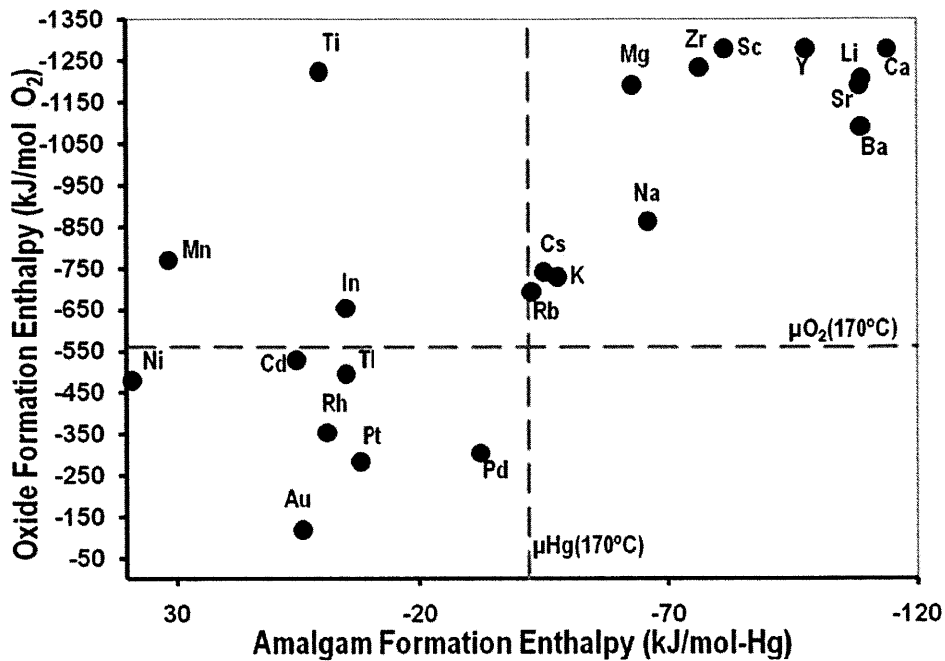


Figure 4.1 Comparison of oxide and amalgam formation enthalpies for pure metal sorbents[111].

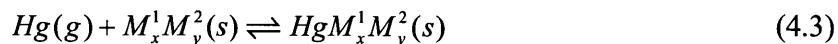
The chemical potentials of Hg and O₂ were calculated based on their typical inlet concentrations (in the case of O₂, the equilibrium concentration based on the amounts of H₂ and H₂O). The temperature of interest, 170°C, was chosen because this temperature is close to dew point of steam in the syngas stream[114], and as the results in Chapter 3 showed, removing pollutants at temperatures above the dew point of steam can increase the efficiency of the IGCC plant.

A promising sorbent would fall into the lower right quadrant of Figure 4.1—above the chemical potential of Hg, but below the chemical potential of O₂. Unfortunately, no metals investigated were found to fall into that desirable material range. However, although the results may be disheartening from an environmental perspective, from an engineering perspective they are quite encouraging. The metal predicted to be the most likely to work in the syngas stream, Pd, has been shown experimentally to capture Hg at temperatures above 170°C[47]. In addition, the use of this computational methodology has led to the successful elimination of many potential materials more rapidly and perhaps more safely than could have been done experimentally. We used these results to expand the calculation method into a larger materials space: binary alloys. These results are discussed in the next section.

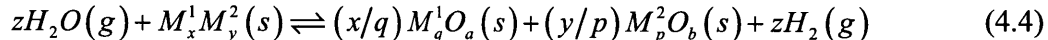
4.4 DFT Screening of Binary Metal Alloys for Hg Adsorption

4.4.1 Calculation Details

The binary alloys for elemental Hg capture generally fall into the type of reaction shown in Equation (4.3) below.



In the above equation, M^1 and M^2 refer to pure metals within some sort of binary alloy with stoichiometric coefficients x and y . Following the method of Jain et al., we computed the bulk enthalpies of reaction for the reactions shown in Equation (4.3) as an indicator of the quality of the adsorbent material. In particular, we used density functional theory (DFT) calculations to compute the reaction energies of 17 different binary alloys whose crystal structures are available in the ICSD[112], [113]. The competing reaction for the binary alloys is very similar to that of Equation (4.2) but is modified slightly to account for the fact that there are two metals present. This competing reaction is shown in Equation (4.4).



In Equation (4.4), $a(x/q) + b(y/p) = z$ in order to conserve the stoichiometry. In the case where the metals have multiple oxide forms (for example, TiO_2 vs. Ti_2O_3), the most stable form of each oxide was selected.

The density functional theory calculations were performed using the Vienna Ab Initio Simulation Package (VASP)[109] using the PW91 functional[107]. Crystal structure data, taken from the ICSD, were used as inputs to the calculations. Atomic positions and cell parameters were relaxed using a conjugate gradient algorithm within the VASP package. Electronic relaxations were considered converged when the energy difference was less than or equal to 10^{-6} eV, and the ionic relaxations were assumed converged when the net force on the atoms were less than or equal to 10^{-4} eV/Å. A final static run using Blöchl's corrected tetrahedron method was performed to obtain the electronic energy.

The plane wave energy cutoff was fixed at 500 eV for all compounds studied due to the fact that a systematic error arises in computing energy differences between compounds that were computed with different energy cutoffs[115]. It is worth noting that this value of 500 eV is much higher than 1.25 times the maximum energy cutoff for each compound for the supplied PAW potentials[116], [117] as was suggested in the VASP documentation for cell relaxation calculations[118], so we expect the values to be well-converged at this cutoff value. An automatic k -point mesh generating program within the Alloy Theoretic Automated Toolkit[119], *ezvasp*, was used to generate a k -point mesh so that the product of the number of k -points and the total number of atoms in the unit cell was greater than or equal to 7500. The k -point convergence was checked by running a small subset of compounds at higher k -point meshes. Those calculations were all converged within 1 kJ/mol, as shown in Table 4.1 below.

Table 4.1 Convergence of electronic energies at different k -point densities for reactions involving binary alloy sorbents.

Compound	Space Group	E^{el} (kJ/mol)	
		$k\text{-points}*\text{atoms} = 7500$	$k\text{-points}*\text{atoms} = 30000$
CuZr	'P m -3 m'	-1197	-1197
EuHgPb	'P 63 m c'	-710	-710
KAs	'P 21 21 21'	-645	-645
PbYb	'P 4/m m m'	-587	-587
SnSr	'C m c m'	-663	-663

4.4.2 Extension of Calculations to Stream Conditions

The VASP calculations compute the electronic energy of a given species at 0 K. However, in order for the calculations to be physically relevant to our system, they needed to be adjusted to the typical temperatures, and partial pressures of components in a syngas stream. The concentration of each species can be widely variable, but the concentrations chosen for this work are shown in Table 4.2. We anticipated that the best location for an adsorption process that involves the use of binary metal alloys would be downstream of the sulfur removal plant in order to inhibit any interference from the sulfur species. As such, the concentrations chosen for this work reflect a syngas stream at this location in the IGCC plant[9]. The Hg concentration was chosen to be 10 ppbv as a typical value for Hg concentration in a syngas stream; the concentration can vary by several orders of magnitude in either direction, depending on the coal type[19].

Table 4.2 Syngas conditions chosen for binary alloy calculations, including volumetric composition of key species.

Stream Parameter	Value
<i>Composition</i>	
H ₂	42%
H ₂ O	26%
Hg	10 ppbv
<i>Pressure</i>	40 bar
<i>Temperature</i>	170°C

The total pressure for our calculations was chosen to be 40 bar, which is typical for IGCC and is the approximate pressure needed for the RTI high-temperature sulfur removal process[24]. The temperature chosen for our calculations was 170°C as in the case of Jain et al.

For the solid-phase species, the electronic energy was estimated to be the dominant source of energy such that the enthalpy of reaction for a reaction between solid species could be calculated using the formula in Equation (4.5).

$$\Delta H_{rxn(s)}^0(T) = \left(H_{HgM_x^1M_y^2(s)}^0 - \left(H_{M_x^1M_y^2(s)}^0 + H_{Hg(s)}^0 \right) \right) \approx \left(E_{HgM_x^1M_y^2(s)}^{el} - \left(E_{M_x^1M_y^2(s)}^{el} + E_{Hg(s)}^{el} \right) \right) \quad (4.5)$$

The heat capacity and PV terms are expected to nearly cancel, assuming the zero point energies are also nearly the same. An added complication, however, is that the syngas stream contains Hg in its gaseous form, not its solid form. Therefore, a representation of the ΔH_{rxn}^0 of interest to this work is shown in Equation (4.6).

$$\Delta H_{rxn-Hg}^0 = \Delta H_{rxn(s)}^0(T) - \Delta H_{Hg,g-s}^0 \quad (4.6)$$

The last term in Equation (4.6) is the enthalpy difference between the solid Hg and gaseous Hg. To compute this last term, we recognize that the enthalpy of gaseous Hg at temperature T can be represented by Equation (4.7).

$$\begin{aligned} H_{Hg(g)}(T) &= H_{Hg(s)}(0K) + \int_0^{T_{melt}} C_{p,solid} dT + \Delta H^{fus}(T_{melt}) \\ &+ \int_{T_{melt}}^{T_{boil}} C_{p,liq} dT + \Delta H^{vap}(T_{boil}) + \int_{T_{boil}}^T C_{p,gas} dT \end{aligned} \quad (4.7)$$

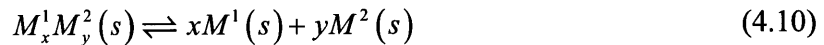
Subtracting off a similar expression for the enthalpy of the solid phase species at temperature T yields the expression in Equation (4.8).

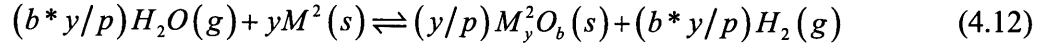
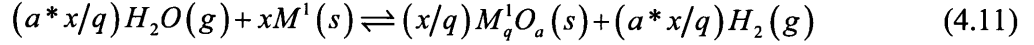
$$H_{Hg(g)}(T) - H_{Hg(s)}(T) = \Delta H_{Hg,g-s}^0 = \Delta H^{fus}(T_{melt}) + \int_{T_{melt}}^{T_{boil}} (C_{p,liq} - C_{p,solid}) dT + \Delta H^{vap}(T_{boil}) + \int_{T_{boil}}^T (C_{p,gas} - C_{p,solid}) dT \quad (4.8)$$

To simplify the calculations, we assumed that the heat capacity differences between the different phases of Hg were small and could be neglected. This assumption is reasonable considering that we expect the heat capacities of the two condensed phases to be similar, and even for the dissimilar vapor and solid phases, the heat capacity of a monatomic ideal gas is $5/2 \cdot R$, while the corresponding high-temperature heat capacity of a solid is $3 \cdot R$. The similar heat capacities between the three phases leads to a final expression for the enthalpy of reaction, shown in Equation (4.9).

$$\Delta H_{rxn-Hg}^0(T) = \left(E_{HgM_x^1M_y^2(s)}^{el} - \left(E_{M_x^1M_y^2(s)}^{el} + E_{Hg(s)}^{el} \right) \right) - \left(\Delta H^{fus}(T_{melt}) + \Delta H^{vap}(T_{boil}) \right) \quad (4.9)$$

The experimental values for the enthalpy of fusion and vaporization for Hg were taken from Bebout[18]. The enthalpy of reaction for the competing reaction with steam was computed in a slightly different manner. If we were to follow the formula of Equation (4.4), we would compute the electronic energies of the binary metal $M_x^1M_y^2$ and its resultant oxides, $M_q^1O_a$ and $M_p^2O_b$. Several problems arise with this strategy, however. First, previous studies have shown that DFT does not correctly predict the oxygen binding strength in metal oxides[120], which would cast doubt on the accuracy of our calculations. Second, many of the metals studied in this work are transition metals. It is well-known that a corrected DFT method such as DFT+U is necessary to more accurately capture the behavior of transition metal oxides[120], [121]; however, DFT+U is not appropriate for metallic species due to their electrons being delocalized[64], meaning that we could not use the same functional for all species in our chemical reactions. This would also lead to significant systematic errors. We eliminated this problem by using experimental data for the metal oxides. The competing reaction shown in Equation (4.4) can actually be broken down into 3 sub-reactions, shown in Equations (4.10) through (4.12).





The enthalpy of reaction of Equation (4.10) can be determined using the electronic energies from DFT, as shown in Equation (4.13).

$$\Delta H_{rxn-metal}^0 \approx xE_{M^1} + yE_{M^2} - E_{M_1^x M_2^y} \quad (4.13)$$

As before, this method assumes that the heat capacities and zero point energies will essentially cancel between different solid species. The enthalpies of reaction of Equations (4.11) and (4.12) can be calculated using experimental data—Kubaschewski et al. for the metals and metal oxides[122], and the NIST Chemistry Webbook for the gaseous species[79]. Therefore, the final expression for the enthalpy of reaction for steam oxidation, $\Delta H_{rxn-steam}^0$, is shown below in Equation (4.14), with the last two terms being determined experimentally.

$$\Delta H_{rxn-steam}^0 = \Delta H_{rxn-metal}^0 + \Delta H_{rxn-M^1 ox}^0 + \Delta H_{rxn-M^2 ox}^0 \quad (4.14)$$

To determine the suitability of a given material for Hg adsorption, it is necessary to use the Gibbs energy of adsorption. Specifically, our chosen metric is the Gibbs energy of reaction, ΔG_{rxn} , calculated at the reaction conditions.

$$\Delta G_{rxn-Hg}(T) = G_{HgM_x^1 M_y^2(s)} - \left(G_{M_x^1 M_y^2(s)} + G_{Hg(g)} \right) \quad (4.15)$$

Because this Gibbs energy of reaction is calculated at the reaction conditions themselves and not at standard state, its value should be equal to 0 if the system is at equilibrium. Therefore, if ΔG_{rxn} is calculated to be less than zero, the adsorption process is favorable, and if it is calculated to be greater than zero then the adsorption process is unfavorable. We note that this metric is slightly different from the method used at Jain et al., which used the chemical potential of Hg and O₂, but because both metrics are strongly related to the Gibbs energy, we predicted that the two metrics would yield equivalent results. We expected that in the Hg adsorption reactions the dominant source of entropy change arose from the Hg atom moving from the vapor phase to the solid phase and that the entropy differences between the solid phases were small. As a result, we

assumed the entropic contributions of the solid-phase species cancel out, resulting in the relationship shown in Equation (4.16).

$$\Delta G_{rxn-Hg}(T) = \Delta H_{rxn-Hg}^0 - T(S_{Hg(s)}^0 - S_{Hg(g)}^0) - RT \ln\left(\frac{P_{Hg}}{P^0}\right) \quad (4.16)$$

The enthalpy of reaction term is identical to that in Equation (4.9). The dominant entropy change for the reaction is represented by the second term in Equation (4.16), which is the entropy difference between the Hg in the solid phase and Hg in the vapor phase. This term was estimated to be the entropy of sublimation between the solid and vapor phases of Hg, calculated by taking our estimate for the enthalpy of sublimation in Equation (4.9) and dividing it by the temperature of interest. The final term in Equation (4.16) is a correction to the Gibbs energy due to the fact that the partial pressure of Hg is not the standard pressure of 1 bar. The final expression for the Gibbs energy of reaction is shown below in Equation (4.17).

$$\Delta G_{rxn-Hg}(T) = \Delta H_{rxn-Hg}^0 + T\Delta S_{Hg}^{sub} - RT \ln\left(\frac{P_{Hg}}{P^0}\right) \quad (4.17)$$

The steam oxidation reaction shown in Equation (4.4) needed to be treated differently because a gaseous species is present on both the reactant and product side of the reaction; as a result, there is no dominant entropy change due to adsorption. However, we expected the entropy change between the solid-phase species shown in Equation (4.10) to be minimal due to the similarity of all the species involved. Therefore, the overall entropy change could again be determined using the experimental values of Equations (4.11) and (4.12). The final expression is shown below in Equation (4.18).

$$\begin{aligned} \Delta G_{rxn-steam} &= \Delta H_{rxn-steam}^0 - T\Delta S_{rxn-steam}^0 + RT \ln\left(\frac{P_{H_2}^z}{P_{H_2O}^z}\right) \\ &= \Delta H_{rxn-steam}^0 - T(\Delta S_{M^1ox}^0 + \Delta S_{M^2ox}^0) + RT \ln\left(\frac{P_{H_2}^z}{P_{H_2O}^z}\right) \end{aligned} \quad (4.18)$$

Again, the entropy expressions in the second term of Equation (4.18) are taken from experimental values, with the entropies of the metals and metal oxides being calculated from

Kubaschewski et al.[122], and the entropies of the gaseous species being calculated from the Shomate equation from the NIST Chemistry Webbook[79].

4.4.3 Accuracy of Enthalpy of Formation Calculations

Unfortunately, due to the paucity of experimental thermodynamic data in the literature, we were unable to compare the enthalpies of formation we determined for the Hg alloy species to their experimental values. However, Jain et al. have shown the enthalpies of formation determined for reactions with Hg and pure metals are accurate to within about 20 kJ/mol (with the exception of Mn-Hg compounds)[111]. Therefore, because the chemical similarity between binary alloys and pure metals, we expected a similar level of accuracy with our calculations.

Because the enthalpy of reaction for the steam oxidation reaction was computed using experimental data for the subreactions of Equations (4.11) and (4.12), the accuracy of our steam oxidation calculations hinged on the accuracy of the reaction in Equation (4.10). Combining this information with the calculation method shown in Equation (4.13) and recognizing the fact that $-\Delta H_{rxn-metal}^0$ is equal to the enthalpy of formation of the binary alloy since, by convention, the enthalpies of formation of pure species are equal to zero, we can generate a comparison between the calculated and experimental values, shown in Figure 4.2.

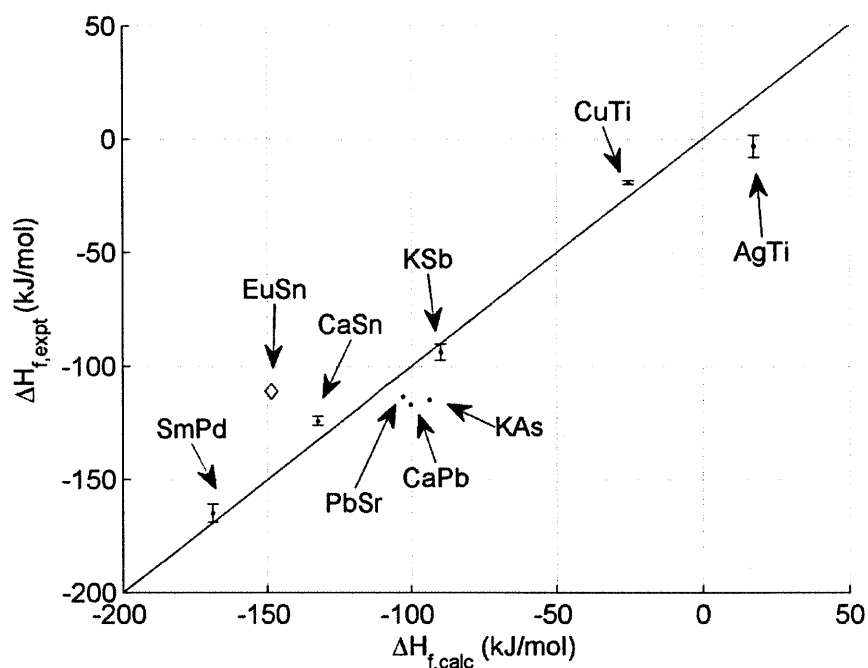
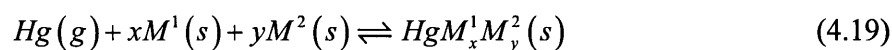


Figure 4.2 Parity plot between experimental and calculated enthalpies of formation at 298 K for binary alloys. The value of EuSn is indicated with a diamond because its experimental value is estimated.

Experimental uncertainties, if available, were included in Figure 4.2. As the calculations show, most binary alloys are reproduced to within 20 kJ/mol. A full listing of all the computed enthalpies of formation for these species can be found in Table 4.10 at the end of this chapter.

Furthermore, because we are confident in the accuracy of our binary alloy formation enthalpies, we can use these calculations to determine the enthalpies of formation of the Hg-containing species. If we subtract Equation (4.10) from Equation (4.3), we get the result shown below.



Therefore, the enthalpy of formation of the Hg species in Equation (4.19) is simply equal to the formula below, where the ΔH_{rxn}^0 term is determined using the electronic energies as described above.

$$\Delta H_{f, \text{Hg}M_x^1M_y^2(s)}^0 = \Delta H_{rxn}^0 + \Delta H_{f, \text{Hg}(g), \text{expt}}^0 \quad (4.20)$$

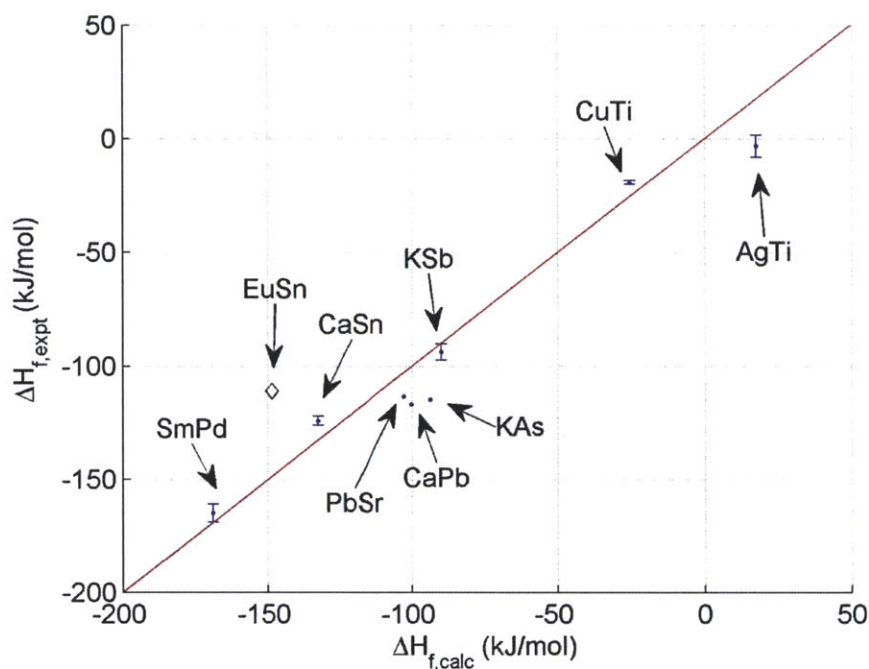


Figure 4.2 Parity plot between experimental and calculated enthalpies of formation at 298 K for binary alloys. The value of EuSn is indicated with a diamond because its experimental value is estimated.

Experimental uncertainties, if available, were included in Figure 4.2. As the calculations show, most binary alloys are reproduced to within 20 kJ/mol. A full listing of all the computed enthalpies of formation for these species can be found in Table 4.10 at the end of this chapter.

Furthermore, because we are confident in the accuracy of our binary alloy formation enthalpies, we can use these calculations to determine the enthalpies of formation of the Hg-containing species. If we subtract Equation (4.10) from Equation (4.3), we get the result shown below.



Therefore, the enthalpy of formation of the Hg species in Equation (4.19) is simply equal to the formula below, where the ΔH_{rxn}^0 term is determined using the electronic energies as described above.

$$\Delta H_{f, \text{Hg}M_x^1M_y^2(s)}^0 = \Delta H_{rxn}^0 + \Delta H_{f, \text{Hg}(g), \text{expt}}^0 \quad (4.20)$$

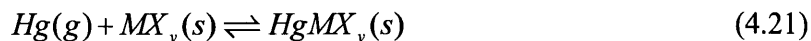
Unfortunately, the Gibbs energies of reaction for their respective steam oxidation reactions are roughly an order of magnitude larger, making it very unlikely that these materials would be stable in a syngas environment. This is logical from a chemical perspective. In either the case of Hg adsorption or steam oxidation, the sorbent metals are likely donating some of their electron density to the Hg atom or the O atom, respectively. Because O is much more electronegative and therefore more likely to be stable upon accepting this electron density, it makes sense that the oxidation reaction is so much more favorable. This phenomenon also appears in the clustering of the data in Figure 4.3. If one attempts to fit a line to the data, there is a weak correlation between O binding affinity and Hg binding affinity; that is, the compounds that tend to oxidize strongly, such as Eu- or Yb-containing compounds, are also those that are predicted to most strongly adsorb Hg.

Three compounds studied, BaTl₂, KAs, and KSb, are all predicted within the uncertainty of our calculations to remain inert to steam oxidation under IGCC conditions. It is possible, therefore, that at higher Hg concentrations or different H₂/H₂O ratios that these compounds could potentially work as Hg sorbents. However, one would expect that Tl- or As-containing compounds may be toxic and therefore undesirable for reasons other than their thermodynamic properties.

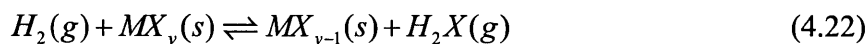
4.5 DFT Screening of Metal Oxides and Metal Sulfides for Hg Adsorption

4.5.1 Calculation Details

In contrast to the work of Jain et al.[111] and the work detailed in Section 4.4, which study materials that capture Hg via amalgamation, the compounds considered in this portion of the thesis capture Hg via oxidation. In other words, the elemental Hg species is initially at an oxidation state of 0, but its oxidation state in the adsorbed product is either +1 or +2. A typical adsorption reaction would take the form shown in Equation (4.21) below.



In the above equation, M refers to a metal capable of reducing its oxidation state (such as $\text{Sn}^{4+}/\text{Sn}^{2+}$), and X usually refers to a common anion like oxide or sulfide. As before, an additional design criterion is the inertness of the sorbent material to the other components in the gas stream. Because the sorbent material is already oxidized, a more likely competing reaction is reduction via the H_2 present in the gas stream, shown in Equation (4.22).



In total, we computed the reaction energies of 23 different oxidative sorbent candidates whose crystal structures were available in the ICSD. A full listing of these compounds can be found in Table 4.12 at the end of this chapter.

The calculation method within VASP is very similar to that of the binary metal alloys described in Section 4.4.1. The density functional theory calculations were again performed with the PW91 functional using VASP. Crystal structure data, taken from the ICSD, were used as inputs to the calculations. Atomic positions and cell parameters were relaxed using a conjugate gradient algorithm within the VASP package. Electronic relaxations were assumed converged when the energy difference was less than or equal to 10^{-6} eV, and the ionic relaxations were assumed converged when the net force on the atoms were less than or equal to 10^{-4} eV/Å. A final static run using Blöchl's corrected tetrahedron method was performed to obtain the electronic energy.

The plane wave energy cutoff was set at 500 eV for reactions involving metal oxides and 350 eV for reactions involving metal sulfides. These values were selected because they are equal to 1.25 times the maximum energy cutoff for oxygen and sulfur for the supplied PAW potentials[116], [117]. The automatic k -point mesh generating program *ezvasp* was again used to generate the k -point mesh so that the product of the number of atoms in the unit cell and the total number of k -points was greater than or equal to 7500. The k -point convergence for these species was checked by running a small subset of compounds at higher k -point meshes. These calculations were all converged within 1 kJ/mol, as shown in Table 4.3 below.

Table 4.3 Convergence of electronic energies at different k -point densities for reactions involving oxidized sorbents.

Compound	Space Group	E^{el} (kJ/mol)	
		$k\text{-points} \times \text{atoms} = 7500$	$k\text{-points} \times \text{atoms} = 15000$
GaS	'P 63/m m c'	-810	-810
HgSrO ₂	'P 32 2 1'	-1803	-1803
CaO ₂	'F 4/m m m'	-1713	-1714
Na ₂ O	'F m -3 m'	-1101	-1101
Hg ₂ I ₂	'I 4/m m m'	-433	-432
Ag ₂ S	'P 1 21/n 1'	-941	-941

For the gaseous species H₂, H₂S, and H₂O, the electronic energies were calculated by placing each species at the center of a large unit cell. The k -point convergence for these species was tested by evaluating their electronic energies at increasing k -point densities until the change in energy was less than 1 kJ/mol when roughly doubling the number of k -points. Where applicable, spin-polarized calculations were conducted using a ferromagnetic or antiferromagnetic initial state (determined from literature sources). DFT+U (as developed by Dudarev et al.[121]) was employed for transition metal oxides Cr₂O₃, CrO₂, FeO, Fe₂O₃, VO₂, and V₂O₅ using the parameters determined by Wang et al[120]. DFT+U was also employed for the transition metal oxides MoO₂ and MoO₃ using the (U - J) value of 6.3 determined by Coquet and Willock[123].

4.5.2 Extension of Calculations to Stream Conditions

We envisioned that the most favorable location in an IGCC plant for Hg removal via a metal oxide or metal sulfide sorbent to be after the water gas shift reactor, but before the sulfur is removed. At this location, the H₂S concentration is still maximized (to inhibit the H₂S-forming competing reaction for sulfur-containing sorbents) and the reactive species, CO, is virtually eliminated. This location is different from that chosen for the metals and binary alloys, and as such the stream conditions changed slightly. The assumed conditions at this location are shown in Table 4.4 below.

Table 4.4 Syngas conditions chosen for oxidative sorbent calculations, including volumetric composition of key species.

Stream Parameter	Value
<i>Composition</i>	
H ₂	44%
H ₂ O	23%
H ₂ S	1%
Hg	10 ppbv
<i>Pressure</i>	40 bar
<i>Temperature</i>	170°C

Following the method described earlier for the investigation of binary alloys, we expected the difference in the electronic energies of the solid-phase species to comprise the majority of the enthalpy of reaction. The heat capacity and PV terms were expected to nearly cancel, assuming the zero point energies were also the same. The final expression for the enthalpy of reaction, modified from Equation (4.9), is shown below.

$$\Delta H_{rxn-Hg}^0(T) = \left(E_{HgMX_{y(s)}}^{el} - \left(E_{MX_{y(s)}}^{el} + E_{Hg(s)}^{el} \right) \right) - \left(\Delta H^{fus}(T_{melt}) + \Delta H^{vap}(T_{boil}) \right) \quad (4.23)$$

Because experimental data was not as readily available in the case of metal oxide and metal sulfide sorbents, the enthalpy of reaction for the competing H₂ reduction reaction was calculated differently from the method outlined in Section 4.4.2. The enthalpy of reaction here follows similar assumptions in which the differences in the electronic energies are approximately equal to the differences in the enthalpies for the solid phase species. This is shown mathematically in Equation (4.24).

$$\Delta H_{rxn-H_2}^0(T) = \left(E_{MX_{y-l(s)}}^{el} - E_{MX_{y(s)}}^{el} \right) + \left(H_{H_2X(g)}(T) - H_{H_2(g)}(T) \right) \quad (4.24)$$

We note that the above expression differs from the form of ΔH_{rxn-Hg}^0 , due to the presence of two gaseous species, H₂ and H₂X. Although their electronic energies were calculated for their gaseous form, we did not necessarily expect that the vibrational and rotational energies for H₂ and H₂X would completely cancel. Because these experimental data are readily available, for completeness we included these contributions to the enthalpy of reaction. The full expression for the enthalpy of reaction is therefore shown in Equation (4.25).

$$\Delta H_{rxn-H_2}^0(T) = \left(E_{MX_{y-1}(g)}^{el} + E_{H_2X(g)}^{el} - \left(E_{MX_y(g)}^{el} + E_{H_2(g)}^{el} \right) \right) + \Delta U_{H_2X-H_2}^{trans} + \Delta E_{H_2X-H_2}^{vib} + \Delta E_{H_2X-H_2}^{rot} \quad (4.25)$$

The translational, vibrational (including zero point energy), and rotational energies were calculated using classical statistical mechanical formulas for polyatomic ideal gases. As such, the difference in the translational energy between H₂X and H₂ is identically equal to 0 because the energy is calculated to be 3/2*RT for all molecules. The statistical mechanics parameters and equations used for each species were taken from the NIST Webbook[79].

As before, the critical metric for the feasibility of a given sorbent was chosen to be the Gibbs energy of reaction. The Gibbs energy of reaction for Hg adsorption was calculated in an identical manner to the method in Section 4.4. Equation (4.17) is repeated here for convenience.

$$\Delta G_{rxn-Hg}(T) = \Delta H_{rxn-Hg}^0 + T\Delta S_{Hg}^{sub} - RT \ln\left(\frac{P_{Hg}}{P^0}\right) \quad (4.17)$$

The competing reaction shown in Equation (4.22) needed to be treated differently because a gaseous species was present on both the reactant and product side of the reaction; as a result, there was no dominant entropy change due to adsorption. This can be seen in Equation (4.26), where the expression for the Gibbs energy of reaction has been rearranged for clarity.

$$\begin{aligned} \Delta G_{rxn-H_2} &= \Delta H_{rxn-H_2}^0 - T\Delta S_{rxn-H_2}^0 + RT \ln\left(\frac{P_{H_2X}}{P_{H_2}}\right) \\ &= \Delta H_{rxn}^0 - T\left(S_{H_2X}^0 - S_{H_2}^0\right) - T\left(S_{MX_{y-1}}^0 - S_{MX_y}^0\right) + RT \ln\left(\frac{P_{H_2X}}{P_{H_2}}\right) \end{aligned} \quad (4.26)$$

The second term in Equation (4.26) was calculated using the entropy values for H₂X and H₂ that are predicted by the Shomate equation using parameters from NIST[79]. The third term was more difficult because thermodynamic data was not readily available for all the species investigated here. To increase the speed of these calculations, the third term was estimated using thermodynamic data that was available for similar species—for example, the entropy difference between BaO₂ and BaO was used for the entropy difference for SrO₂ and SrO.

4.5.3 Accuracy of Enthalpy of Formation Calculations

A comparison of the calculated and experimental enthalpies of formation for Hg-containing species is shown in Figure 4.4. For clarity this figure has been divided into two ranges: $0 \leq |\Delta H_f^0| \leq 500$ kJ/mol, and $600 \leq |\Delta H_f^0| \leq 1100$ kJ/mol.

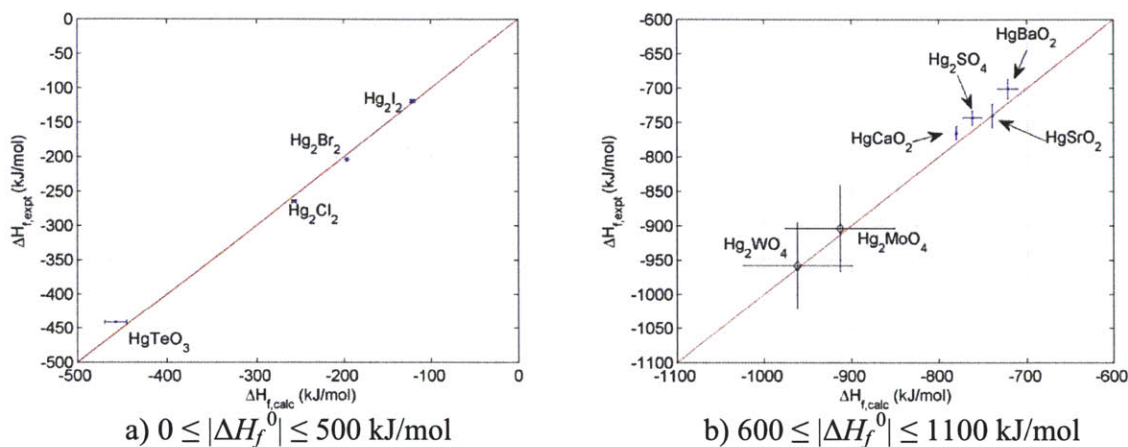


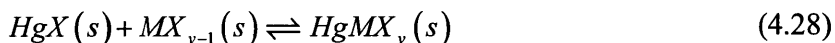
Figure 4.4 Parity plot for enthalpy of formation for Hg species HgMX_y for a) $0 \leq |\Delta H_f^0| \leq 500$ kJ/mol and b) $600 \leq |\Delta H_f^0| \leq 1100$ kJ/mol. Hg_2WO_4 and Hg_2MoO_4 are indicated with diamonds because the experimental values are estimated.

The calculated enthalpy of formation for the HgMX_y species shown in Equation (4.21) was determined using the formula in Equation (4.27) below, where ΔH_{rxn}^0 is calculated using electronic energies as described in the previous sections, and the other enthalpies of formation are taken from experimental values.

$$\Delta H_{f,\text{HgMX}_y}^0 = \Delta H_{rxn-\text{Hg}}^0 + \left(\Delta H_{f,\text{Hg}(expt)}^0 + \Delta H_{f,\text{MX}_y(expt)}^0 \right) \quad (4.27)$$

Any error bars in the calculated enthalpy of formation shown in Figure 4.4 arise from error bars in the experimental enthalpies of formation in Equation (4.27); therefore, the deviations between the data points and the line $y = x$ can be attributed to errors in the VASP calculations of $\Delta H_{rxn-\text{Hg}}^0$. Figure 4.4 shows that these errors are relatively small, with a maximum deviation beyond the error bars being approximately 10 kJ/mol.

It is worth noting that another method for computing the enthalpy of formation of $HgMX_y$ would be to use the reaction and subsequent equation shown in Equations (4.28) and (4.29), respectively.



$$\Delta H_{f,HgMX_y}^0 = \Delta H_{rxn-HgX}^0 + \left(\Delta H_{f,HgX(expt)}^0 + \Delta H_{f,MX_y(expt)}^0 \right) \quad (4.29)$$

The enthalpy of reaction in Equation (4.29) is computed from the electronic energies in a method similar to that in Equation (4.5). It would be our expectation that the enthalpies of formation derived from the two methods would produce similar results. However, as Table 4.5 shows, although the two methods are consistent for the reactions involving sulfides, they are not consistent for most oxides, with only metal peroxides such as BaO_2 yielding results within even 30 kJ/mol of each other.

Table 4.5 Comparison of enthalpies of formation calculated using Equations (4.27) and (4.29). The experimentally-determined enthalpy of formation of $HgBaO_2$ is -701 kJ/mol[124].

Species	Equation (4.27)	$\Delta H_{f,calc}^0$ (kJ/mol)	Equation (4.29)	$\Delta H_{f,calc}^0$ (kJ/mol)
$HgBaO_2$	$Hg + BaO_2 \rightleftharpoons HgBaO_2$	-722	$HgO + BaO \rightleftharpoons HgBaO_2$	-728
$HgSnO_3$	$Hg + 2SnO_2 \rightleftharpoons HgSnO_3 + SnO$	-666	$HgO + SnO_2 \rightleftharpoons HgSnO_3$	-634
HgV_2O_6	$Hg + 2V_2O_5 \rightleftharpoons HgV_2O_6 + 2VO_2$	-1702	$HgO + V_2O_5 \rightleftharpoons HgV_2O_6$	-1661
$HgCr_2O_4$	$Hg + 2CrO_2 \rightleftharpoons HgCr_2O_4$	-1280	$HgO + Cr_2O_3 \rightleftharpoons HgCr_2O_4$	-1240
$HgNa_2S_2$	$Hg + Na_2S_2 \rightleftharpoons HgNa_2S_2$	-442	$HgS + Na_2S \rightleftharpoons HgNa_2S_2$	-453
$HgGa_2S_4$	$Hg + 2Ga_2S_3 \rightleftharpoons HgGa_2S_4 + 2GaS$	-595	$HgS + Ga_2S_3 \rightleftharpoons HgGa_2S_4$	-591
$HgCr_2S_4$	$Hg + 2Cr_2S_3 \rightleftharpoons HgCr_2S_4 + 2CrS$	-540	$HgS + Cr_2S_3 \rightleftharpoons HgCr_2S_4$	-539

This discrepancy between the two techniques casts doubt on the accuracy of our method, at least in the case of metal oxides. Unfortunately, due to the scarcity of experimental thermodynamic data available for these compounds, it is difficult to definitively determine which method is more accurate.

One may be tempted to assume that the enthalpies calculated using Equation (4.29) are more accurate—the oxidation state of each atomic species is constant on either side of the chemical

reaction, making it more likely that any systematic errors would cancel out. However, this assumption may not be correct. Specifically, it has been observed that DFT calculations using GGA functionals tend to err in the energy calculations of metal oxides. An empirical correction of 1.36 eV (130 kJ/mol) has been proposed[120]. However, further studies have shown that this empirical correction, while effective for many types of metal oxides, tends not to accurately reproduce the experimental enthalpies of formation for both noble metal oxides and metal peroxides[111]. This could help to explain the discrepancy we observed, since our calculations involved an unreactive (“noble”) Hg and peroxides (e.g., BaO₂) . The two methods could be consistent for the calculation of HgBaO₂ because one method uses a DFT calculation of a metal peroxide (BaO₂), and the other uses a DFT calculation of an oxide of an unreactive metal (HgO), leading to a systematic error in each method that happens to be of a similar order or magnitude. Further evidence for this is that the experimentally-determined $\Delta H_{f,calc}^0$ for HgBaO₂ is -701 kJ/mol, albeit with an estimated uncertainty of 14 kJ/mol (see the Appendix), showing that both methods, while in relative agreement with each other, are at least somewhat in disagreement with the experimentally-determined value. Because there is no such metal peroxide used in the other metal oxide calculations in Table 4.5, it results in a discrepancy between the two methods.

Numbers computed using Equation (4.27) are reported throughout the remainder of this work. However, we add a caution that the metal oxide enthalpies of formation that we calculate may therefore have additional uncertainties of up to 40 kJ/mol due to the DFT GGA inaccuracy for metal oxides.

A similar series of plots can be made for enthalpies of formation determined using the competing reaction in Equation (4.22). The simplest method of determining the enthalpy of formation is shown in Equation (4.30).

$$\Delta H_{f,MX_y}^0 = \left(\Delta H_{f,H_2X}^0(expt) - \Delta H_{f,H_2}^0(expt) + \Delta H_{f,MX_{y-1}}^0(expt) \right) - \Delta H_{rxn-H_2}^0 \quad (4.30)$$

Although the method shown in Equation (4.30) has good accuracy for some types of compounds (namely those involving Group 1 or Group 2 elements), the accuracy is decreased for transition metal compounds and those in Group 13 through 15. The accuracy is increased if the H₂/H₂X reaction couple is substituted for a pair that is more chemically similar to the species of interest. In the case of transition metal compounds this pair was chosen to be FeO/Fe₂O₃ for oxides and

NiS/NiS₂ for sulfides, and for Groups 13 through 15 it was SnX/SnX₂, where X is either oxygen or sulfur. The ΔH_{rxn}^0 and $\Delta H_{f,MX}^0$ equations can therefore be rewritten in the form of Equations (4.31) and (4.32).

$$\Delta H_{rxn-SnX}^0 = \left(E_{SnX_2}^{el} + E_{MX_{y-1}}^{el} \right) - \left(E_{SnX}^{el} + E_{MX_y}^{el} \right) \quad (4.31)$$

$$\Delta H_{f,MX_y}^0 = \left(\Delta H_{f,SnX_2}^0(expt) - \Delta H_{f,SnX}^0(expt) + \Delta H_{f,MX_{y-1}}^0(expt) \right) - \Delta H_{rxn-SnX}^0 \quad (4.32)$$

Similar equations can also be made for the transition metal reaction pairs. The results with this increased accuracy are shown in Figure 4.5.

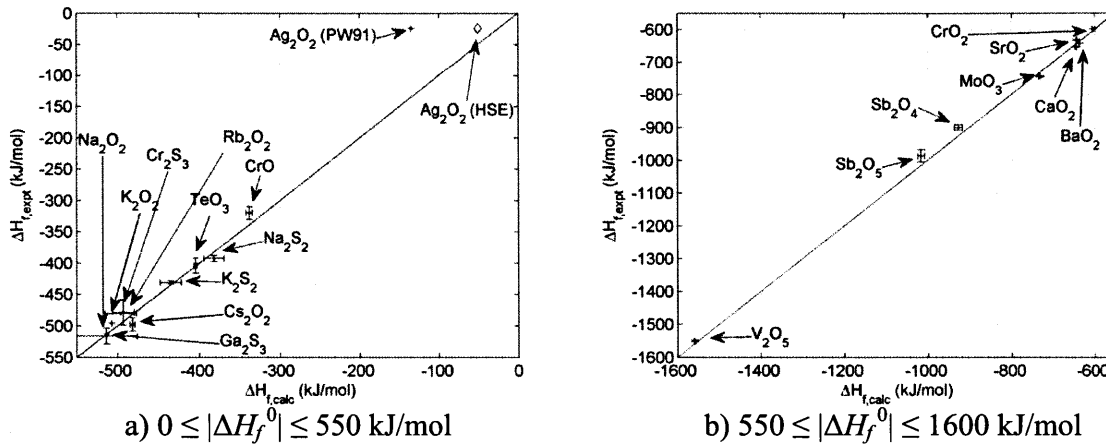


Figure 4.5 Parity plot for enthalpy of formation for MX_y using Equation (4.32) for a) $0 \leq |\Delta H_f^0| \leq 550$ kJ/mol and b) $550 \leq |\Delta H_f^0| \leq 1600$ kJ/mol. The Ag_2O_2 species indicated with a diamond was calculated using the HSE functional. The error bars shown are from the experimental numbers in Equation (4.32); deviations from the parity line bigger than the error bars are likely due to the DFT calculations.

As Figure 4.5 shows, the calculated enthalpy of adsorption is consistent with the experimental enthalpy of adsorption for most compounds, within the estimated uncertainty. The Ag_2O_2 species in Figure 4.5a has the largest deviation from the experimental value: approximately 100 kJ/mol. This is not surprising, based on our earlier discussion of the inaccuracy of certain types of metal oxides; in fact, this particular reaction involves two different oxides of a noble metal. This reaction is unique, however, in that some evidence suggests that the Ag_2O_2 used in the experiments was not a metal peroxide but rather a mixed oxide with Ag ions in both +1 and +3 oxidation states[125]. An oxidation state greater than +1 may imply the need for DFT+U, since the number of *d* electrons may be changing in the different Ag species, or perhaps a hybrid

functional such as HSE[126], [127] that has shown evidence of decreasing the effect of O₂ overbinding in some cases[128]. Because no (*U-J*) parameter was readily available in the literature for Ag species, we elected to recalculate silver oxide species using the HSE functional. This corrected point is shown on Figure 4.5a as a diamond. The HSE functional was then used in the calculations for HgAg₂O₂ in order to keep all silver oxide compounds on a consistent basis.

4.5.4 Gibbs Energy of Reaction Calculations

A comparison of the results obtained via Equation (4.17) and the results obtained experimentally are shown below in Table 4.6.

Table 4.6 Comparison of experimental and calculated Gibbs free energies of reaction.

Reaction	$\Delta G_{rxn,calc}$ (kJ/mol)	$\Delta G_{rxn,expt}$ (kJ/mol)
$Hg + CaO_2 \rightleftharpoons HgCaO_2$	-72	-46
$Hg + HgSO_4 \rightleftharpoons Hg_2SO_4$	-3	8
$Hg + HgBr_2 \rightleftharpoons Hg_2Br_2$	27	14
$Hg + HgCl_2 \rightleftharpoons Hg_2Cl_2$	27	14
$Hg + HgI_2 \rightleftharpoons Hg_2I_2$	38	25
$Hg + Na_2S_2 \rightleftharpoons HgS + Na_2S$	39	35
$Hg + BaO_2 \rightleftharpoons HgO + BaO$	56	47
$Hg + K_2O_2 \rightleftharpoons HgO + K_2O$	110	89

In general, the calculation method reproduces the experimental data quite well, with the average deviation being about 13 kJ/mol and a maximum deviation being 30 kJ/mol. This shows that our assumption that the entropy of the solid phase is cancels out is fairly accurate. Also, it appears that the accuracy of the calculations does not depend on whether one product (i.e., Reaction 1), or two products (i.e., Reaction 6) is formed, showing that the method is applicable to a wider range of adsorption reactions.

The computed Gibbs energy of reaction for the Hg adsorption reaction and the competing H₂ reduction are compared side by side in Figure 4.6.

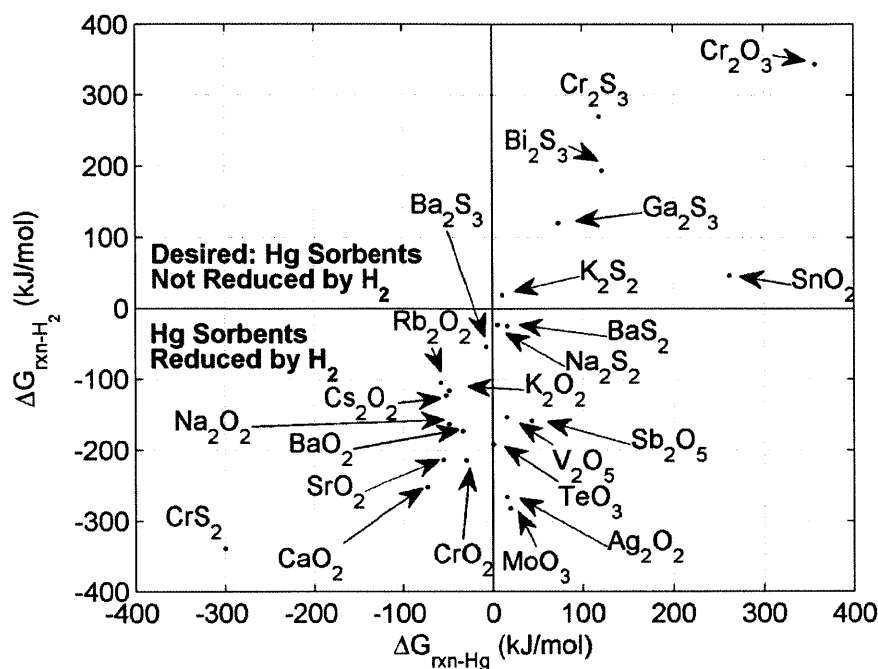


Figure 4.6 Computed Gibbs energy of reaction for Hg adsorption (Equation (4.17)) and H₂ reduction (Equation (4.26)) for the IGCC conditions found in Table 4.4. A full description of each reaction is found at the end of this chapter.

As was described earlier, a negative Gibbs energy of reaction implies that the reaction will move toward the formation of products. In the Hg reactions, this is the HgMX_y species (thereby favoring adsorption), and in the H₂ reactions, this is the MX_{y-1} + H₂X species. We quantitatively compared the relative favorability of each reaction based on the magnitude of each calculated Gibbs energy. Therefore, the compounds that were predicted to be favorable to the Hg adsorption reaction but inert toward H₂ reduction at IGCC conditions were those compounds whose Gibbs energies of reaction lay in the upper left quadrant in Figure 4.6. As Figure 4.6 shows, no compounds were predicted to lie in this quadrant. However, one compound, K₂S₂, *did* have a Gibbs energy of reaction with H₂ greater than 0, and the computed Gibbs energy of reaction of Hg was approximately 10 kJ/mol. Because this 10 kJ/mol difference is well within the 13 kJ/mol average deviation of our calculations, Table 4.6, we feel that this compound is worthy of further study.

Several qualitative trends emerge from the information in Figure 4.6. First, the Group 1 metal peroxides studied here are less favorable to H₂ reduction than their Group 2 counterparts.

Furthermore, most of the compounds that were predicted to be closest to the upper left quadrant of Figure 4.6 are sulfide compounds. This is a logical result; the oxidation of H₂ to H₂O, which occurs in the case of metal oxide materials, is highly exothermic, with an enthalpy difference of approximately -240 kJ/mol at room temperature. By contrast, the enthalpy difference between H₂S and H₂ is merely -20 kJ/mol at room temperature—a full order of magnitude smaller. Because the H₂ to H₂S reaction is far less exothermic, the Hg adsorption reaction has a greater chance to compete. It is worth noting, however, that although metal oxides are predicted to be *thermodynamically* more susceptible to reduction than Hg adsorption, it is possible that *kinetically* the barrier to the H₂ reduction reaction may be quite large.

Finally, we note that although no compounds tested in this work lie in the desired upper left quadrant of Figure 4.6, several compounds are predicted to have strongly negative Gibbs energies of reaction with Hg at syngas conditions. Because this Gibbs energy was predicted to be so large, we briefly investigated their thermodynamic stability in a *flue* gas environment, such as one leaving a typical subcritical pulverized coal power plant. In this oxygen-rich environment, reducing reactions such as those shown in Table 4.4 are not expected to occur. The partial pressure of Hg would considerably lower in this case, however, since the total pressure of the system is approximately 1 atm. In addition, a greater fraction of the Hg present in the gas stream is oxidized[56], and the flue gas is heavily diluted in N₂, making the partial pressure of Hg⁰ even lower. We account for these effects by assuming $p_{\text{Hg}} = 1$ ppbv in the flue gas stream, rather than 10 ppbv, as was assumed above. Table 4.7 shows a comparison of the most promising oxide sorbents at syngas conditions and flue gas conditions.

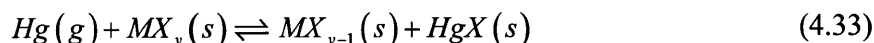
Table 4.7 Comparison of metal oxide sorbents at syngas and flue gas conditions. The temperature of both the syngas and the flue gas streams was assumed to be 170°C.

Compound	$\Delta G_{\text{rxn-Hg}}$ (kJ/mol)	$\Delta G_{\text{rxn-Hg}}$ (kJ/mol)
	Syngas Conditions $p_{\text{Hg}} = 10$ ppbv at 40 bar	Flue Gas Conditions $p_{\text{Hg}} = 1$ ppbv at 1.01 bar
BaO ₂	-33	-11
CaO ₂	-72	-50
CrO ₂	-29	-7
Cs ₂ O ₂	-52	-30
K ₂ O ₂	-49	-27
Na ₂ O ₂	-48	-26
Rb ₂ O ₂	-58	-45
SrO ₂	-54	-32

Clearly, the reactivity with Hg at low partial pressure is not the only requirement of an effective Hg sorbent for flue gas conditions, but this does show that even if these materials are not suitable for IGCC warm syngas conditions, they may still have potential in other applications.

4.5.5 Comparison of Hg and H₂ Reactions Using Experimental Data

As a final note about oxidative sorbents, a key difference between the binary metal alloys and the oxidized sorbent materials is that a significant amount of experimental data exists for the oxidized materials. In particular, one could envision a Hg capture reaction proceeding in a similar mechanism to the H₂ reaction from Equation (4.22).

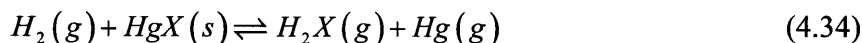


In other words, the reaction shown above in Equation (4.33) differs in that the resulting product is a Hg oxide or a Hg sulfide, not a mixed metal oxide or sulfide (HgMX_y) as proposed in Equation (4.21). At an initial glance this reaction seems to be quite valuable—not only does it provide a wide new array of possible compounds and reactions to investigate, but it also allows the screening to be performed using existing experimental data. Metal oxides (and to a lesser extent, metal sulfides) are traditionally well-studied, and as a result we would expect a significant amount of accurate thermochemical data for both the MX_y and MX_{y-1} compounds in Equation (4.33). However, a quick analysis shows why Equation (4.33) cannot be used as a Hg capture reaction when being compared to the H₂ competing reaction. A summary of the Gibbs energy of reaction as calculated by Equations (4.17) and (4.26) is shown in Table 4.8 below. The source of the experimental data was Binnewies and Milke[129], and the stream conditions were identical to those of Table 4.4.

Table 4.8 Comparison of Gibbs energy of sample Hg and H₂ reactions using experimental data.

Species	Hg Reaction	ΔG_{rxn-Hg} (kJ/mol)	H ₂ Reaction	ΔG_{rxn-H_2} (kJ/mol)
BaO ₂	$Hg + BaO_2 \rightleftharpoons HgO + BaO$	47	$H_2 + BaO_2 \rightleftharpoons H_2O + BaO$	-171
SrO ₂	$Hg + SrO_2 \rightleftharpoons HgO + SrO$	-8	$H_2 + SrO_2 \rightleftharpoons H_2O + SrO$	-226
CrO ₃	$Hg + CrO_3 \rightleftharpoons HgO + CrO_2$	-54	$H_2 + CrO_3 \rightleftharpoons H_2O + CrO_2$	-272
FeS ₂	$Hg + FeS_2 \rightleftharpoons HgS + FeS$	47	$H_2 + FeS_2 \rightleftharpoons H_2S + FeS$	-1
MnS ₂	$Hg + MnS_2 \rightleftharpoons HgS + MnS$	1	$H_2 + MnS_2 \rightleftharpoons H_2S + MnS$	-46
SnS ₂	$Hg + SnS_2 \rightleftharpoons HgS + SnS$	32	$H_2 + SnS_2 \rightleftharpoons H_2S + SnS$	-15

As can be seen in Table 4.8, the H₂ reactions are consistently more exergonic than the Hg reactions. A simple explanation for this phenomenon can be seen in Equation (4.34) below, in which Equation (4.33) has been subtracted from Equation (4.22).



As the above equation shows, the MX_y species completely cancel out, and the comparison of the Gibbs energies of reaction only depend on the relative differences of the H₂-H₂X species and the Hg-HgX species. At the stream conditions shown in Table 4.4, Equation (4.34) will always be exergonic, regardless of the metal species used. Therefore, this serves as an illustration why the Hg capture reaction investigated in this work is the form of Equation (4.21) and not of Equation (4.33): the influence of the MX_y species does not cancel out, and as a result the Hg capture reaction has the potential to be more exergonic than the H₂ reaction.

4.6 Conclusions

In this chapter we extended the screening method developed by Jain et al.[111] to include binary metal alloys, metal oxides, and metal sulfides for elemental Hg capture. Due to the lack of available experimental data, we were unable to compare our calculated thermodynamic parameters with experimental values in the case of Hg adsorption on binary metal alloys; however, following the results of Jain et al., we expect our calculations to be accurate to within

20 kJ/mol. Following from this result, we have calculated the enthalpy of formation for 17 Hg-containing ternary metal alloys and 7 binary metal alloys that to our knowledge were not previously reported in the literature. Based on our results we are able to conclude the binary metal alloys studied do not show much promise as Hg sorbents in the IGCC syngas because the competing reaction of steam oxidation is likely to degrade the sorbents.

With respect to the metal oxide and metal sulfide sorbent calculations, we have been able to predict enthalpies of formation within approximately 10-15 kJ/mol. We also report the first accurate enthalpies of formation of 11 Hg metal oxides and 7 Hg metal sulfides. We also computed the enthalpy of formation of BaS_2 , Ba_2S_3 , BiS , and CrS_2 . Based on our results we are able to conclude that due to a combination of the relative concentrations of the syngas species and the relative exothermicities of the $\text{H}_2\text{-H}_2\text{O}$ reactions vs. the $\text{H}_2\text{-H}_2\text{S}$ reactions, the most promising sorbent materials for IGCC conditions will be metal sulfides. The majority of the metal sulfides surveyed here were not predicted to be favorable at the syngas stream conditions, but K_2S_2 showed promise due to the fact that the Gibbs energy of reaction is actually predicted to be more negative for the Hg adsorption than for the H_2 reduction. In addition, several sorbent materials bind Hg strongly enough to be effective at the lower Hg concentrations present in flue gas streams. The use of this computational screening method has allowed for the selection and rejection of potential sorbents at a much faster time scale than with experiments alone.

4.7 Appendix

Table 4.9 Reactions for Hg capture and steam oxidation for the binary alloys investigation.

Compound	Hg Capture Reaction	Steam Oxidation Reaction
AgTi	$Hg + \frac{1}{2} AgTi \rightleftharpoons \frac{1}{2} Hg_2AgTi$	$\frac{5}{4} H_2O + \frac{1}{2} AgTi \rightleftharpoons \frac{1}{4} Ag_2O + \frac{1}{2} TiO_2 + \frac{5}{4} H_2$
AsK	$Hg + AsK \rightleftharpoons HgAsK$	$2H_2O + AsK \rightleftharpoons \frac{1}{2} As_2O_3 + \frac{1}{2} K_2O + 2H_2$
BaSn	$Hg + BaSn \rightleftharpoons HgBaSn$	$3H_2O + BaSn \rightleftharpoons BaO + SnO_2 + 3H_2$
BaTi ₂	$Hg + \frac{1}{2} BaTi_2 \rightleftharpoons \frac{1}{2} Hg_2BaTi_2$	$H_2O + \frac{1}{2} BaTi_2 \rightleftharpoons \frac{1}{2} Ti_2O + \frac{1}{2} BaO + H_2$
CaPb	$Hg + CaPb \rightleftharpoons HgCaPb$	$2H_2O + CaPb \rightleftharpoons CaO + PbO + 2H_2$
CaSn	$Hg + CaSn \rightleftharpoons HgCaSn$	$3H_2O + CaSn \rightleftharpoons CaO + SnO_2 + 3H_2$
CdTi	$Hg + \frac{1}{2} CdTi \rightleftharpoons \frac{1}{2} Hg_2CdTi$	$\frac{3}{2} H_2O + \frac{1}{2} CdTi \rightleftharpoons \frac{1}{2} CdO + \frac{1}{2} TiO_2 + \frac{3}{2} H_2$
CuTi	$Hg + \frac{1}{2} CuTi \rightleftharpoons \frac{1}{2} Hg_2CuTi$	$\frac{5}{4} H_2O + \frac{1}{2} CuTi \rightleftharpoons \frac{1}{4} Cu_2O + \frac{1}{2} TiO_2 + \frac{5}{4} H_2$
CuZr	$Hg + \frac{1}{2} CuZr \rightleftharpoons \frac{1}{2} Hg_2CuZr$	$\frac{5}{4} H_2O + \frac{1}{2} CuZr \rightleftharpoons \frac{1}{4} Cu_2O + \frac{1}{2} ZrO_2 + \frac{5}{4} H_2$
EuPb	$Hg + EuPb \rightleftharpoons HgEuPb$	$\frac{5}{2} H_2O + EuPb \rightleftharpoons \frac{1}{2} Eu_2O_3 + PbO + \frac{5}{2} H_2$
EuSn	$Hg + EuSn \rightleftharpoons HgEuSn$	$\frac{7}{2} H_2O + EuSn \rightleftharpoons \frac{1}{2} Eu_2O_3 + SnO_2 + \frac{7}{2} H_2$
KSb	$Hg + KSb \rightleftharpoons HgKSb$	$2H_2O + KSb \rightleftharpoons \frac{1}{2} Sb_2O_3 + \frac{1}{2} K_2O + 2H_2$
PbSr	$Hg + PbSr \rightleftharpoons HgPbSr$	$2H_2O + PbSr \rightleftharpoons PbO + SrO + 2H_2$
PbYb	$Hg + PbYb \rightleftharpoons HgPbYb$	$\frac{5}{2} H_2O + PbYb \rightleftharpoons \frac{1}{2} Yb_2O_3 + PbO + \frac{5}{2} H_2$
PdSm	$Hg + PdSm \rightleftharpoons HgPdSm$	$\frac{5}{2} H_2O + PdSm \rightleftharpoons \frac{1}{2} Sm_2O_3 + PdO + \frac{5}{2} H_2$
SnSr	$Hg + SnSr \rightleftharpoons HgSnSr$	$3H_2O + SnSr \rightleftharpoons SrO + SnO_2 + 3H_2$
SnYb	$Hg + SnYb \rightleftharpoons HgSnYb$	$\frac{7}{2} H_2O + SnYb \rightleftharpoons \frac{1}{2} Yb_2O_3 + SnO_2 + \frac{7}{2} H_2$

Table 4.10 Calculated enthalpy of formation of $M_x^1M_y^2$ species. The number indicated with an asterisk(*) is estimated. All values included for the CuTi and CuZr entries are from the same source.

Compound	Space Group	$\Delta H_{f,calc}^0$ (kJ/mol)	$\Delta H_{f,expt}^0$ (kJ/mol)	Reference
EuSn	'C m c m'	-148	-111*	[130]
SnYb	'P 4/m m m'	-126		
BaTi ₂	'P 63/m m c'	-117		
AsK	'P 21 21 21'	-94	-115	[131]
KSb	'P 1 21/c 1'	-90	-94 ± 4	[132]
AgTi	'P 4/m m m'	18	-3 ± 5	[133]
CdTi	'P 4/n m m S'	-12		
			-19	
CuTi	'P 4/n m m S'	-25	-19 ± 1	[134]
			-22 ± 3	
			-49 ± 2	
CuZr	P m -3 m'	-21	-18 ± 2	[134]
BaSn	'C m c m'	-141		
CaPb	'P 4/m m m'	-103	-113	[135]
PbSr	'C m c m'	-108		
PdSm	'C m c m'	-169	-165 ± 4	[136]
EuPb	'P 4/m m m'	-119		
PbYb	'P 4/m m m'	-100	-117	[137]
CaSn	'C m c m'	-133	-124 ± 2	[138]
SnSr	'C m c m'	-138		

Table 4.11 Calculated enthalpy of formation of $HgM_x^1M_y^2$ species. The estimated uncertainty is 20 kJ/mol.

Compound	Space Group	$\Delta H_{f,calc}^0$ (kJ/mol)
Hg ₂ AgTi	'P 4/m m m'	37
HgAsK	'P 63/m m c'	-110
HgBaSn	'P 63/m m c'	-176
Hg ₂ BaTi ₂	'P 42/m n m'	-165
HgCaPb	'P 63/m m c'	-106
HgCaSn	'P 63 m c'	-162
Hg ₂ CdTi	'P 4/m m m'	18
Hg ₂ CuTi	'F -4 3 m'	69
Hg ₂ CuZr	'F -4 3 m'	10
HgEuPb	'P 63 m c'	-164
HgEuSn	'P 63 m c'	-199
HgKSb	'P 63/m m c'	-113
HgPbSr	'P 63 m c'	-142
HgPbYb	'P 63/m m c'	-111
HgPdSm	'P -6 2 m'	-209
HgSnSr	'P 63 m c'	-171
HgSnYb	'P 63 m c'	-169

Table 4.12 Reactions for Hg capture and H₂ reduction for the sorbent materials investigation.

Compound	Hg Capture Reaction	H ₂ Reduction Reaction
Ag ₂ O ₂	$Hg + Ag_2O_2 \rightleftharpoons HgAg_2O_2$	$H_2 + Ag_2O_2 \rightleftharpoons Ag_2O + H_2O$
Ba ₂ S ₃	$Hg + Ba_2S_3 \rightleftharpoons HgBa_2S_3$	$H_2 + Ba_2S_3 \rightleftharpoons 2BaS + H_2S$
BaO ₂	$Hg + BaO_2 \rightleftharpoons HgBaO_2$	$H_2 + BaO_2 \rightleftharpoons BaO + H_2O$
BaS ₂	$Hg + BaS_2 \rightleftharpoons HgBaS_2$	$H_2 + BaS_2 \rightleftharpoons BaS + H_2S$
Bi ₂ S ₃	$Hg + 2Bi_2S_3 \rightleftharpoons HgBi_2S_4 + 2BiS$	$2H_2 + 2Bi_2S_3 \rightleftharpoons 4BiS + 2H_2S$
CaO ₂	$Hg + CaO_2 \rightleftharpoons HgCaO_2$	$H_2 + CaO_2 \rightleftharpoons CaO + H_2O$
Cr ₂ O ₃	$Hg + 2Cr_2O_3 \rightleftharpoons HgCr_2O_4 + 2CrO$	$2H_2 + 2Cr_2O_3 \rightleftharpoons 4CrO + 2H_2O$
Cr ₂ S ₃	$Hg + 2Cr_2S_3 \rightleftharpoons HgCr_2S_4 + 2CrS$	$2H_2 + 2Cr_2S_3 \rightleftharpoons 4CrS + 2H_2S$
CrO ₂	$Hg + 2CrO_2 \rightleftharpoons HgCr_2O_4$	$H_2 + 2CrO_2 \rightleftharpoons Cr_2O_3 + H_2O$
CrS ₂	$Hg + 2CrS_2 \rightleftharpoons HgCr_2S_4$	$H_2 + 2CrS_2 \rightleftharpoons Cr_2S_3 + H_2S$
Cs ₂ O ₂	$Hg + Cs_2O_2 \rightleftharpoons HgCs_2O_2$	$H_2 + Cs_2O_2 \rightleftharpoons Cs_2O + H_2O$
Ga ₂ S ₃	$Hg + 2Ga_2S_3 \rightleftharpoons HgGa_2S_4 + 2GaS$	$2H_2 + 2Ga_2S_3 \rightleftharpoons 4GaS + 2H_2S$
K ₂ O ₂	$Hg + K_2O_2 \rightleftharpoons HgK_2O_2$	$H_2 + K_2O_2 \rightleftharpoons K_2O + H_2O$
K ₂ S ₂	$Hg + K_2S_2 \rightleftharpoons HgK_2S_2$	$H_2 + K_2S_2 \rightleftharpoons K_2S + H_2S$
MoO ₃	$Hg + 2MoO_3 \rightleftharpoons HgMoO_4 + MoO_2$	$2H_2 + 2MoO_3 \rightleftharpoons 2MoO_2 + 2H_2O$
Na ₂ O ₂	$Hg + Na_2O_2 \rightleftharpoons HgNa_2O_2$	$H_2 + Na_2O_2 \rightleftharpoons Na_2O + H_2O$
Na ₂ S ₂	$Hg + Na_2S_2 \rightleftharpoons HgNa_2S_2$	$H_2 + Na_2S_2 \rightleftharpoons Na_2S + H_2S$
Rb ₂ O ₂	$Hg + Rb_2O_2 \rightleftharpoons HgRb_2O_2$	$H_2 + Rb_2O_2 \rightleftharpoons Rb_2O + H_2O$
Sb ₂ O ₅	$Hg + Sb_2O_5 \rightleftharpoons \frac{1}{2}Hg_2Sb_2O_7 + \frac{1}{2}Sb_2O_3$	$H_2 + Sb_2O_5 \rightleftharpoons Sb_2O_4 + H_2O$

Compound	Hg Capture Reaction	H ₂ Reduction Reaction
SnO ₂	$Hg + 2SnO_2 \rightleftharpoons HgSnO_3 + SnO$	$2H_2 + 2SnO_2 \rightleftharpoons 2SnO + 2H_2O$
SrO ₂	$Hg + SrO_2 \rightleftharpoons HgSrO_2$	$H_2 + SrO_2 \rightleftharpoons SrO + H_2O$
TeO ₃	$Hg + TeO_3 \rightleftharpoons HgTeO_3$	$H_2 + TeO_3 \rightleftharpoons TeO_2 + H_2O$
V ₂ O ₅	$Hg + V_2O_5 \rightleftharpoons HgVO_3 + VO_2$	$H_2 + V_2O_5 \rightleftharpoons 2VO_2 + H_2O$

Table 4.13 Calculated enthalpy of formation for MX_y species.

Compound	Space Group	$\Delta H_{f,calc}^0$ (kJ/mol)	$\Delta H_{f,expt}^0$ (kJ/mol)	Reference
Ag ₂ O ₂	'P 1 21/c 1'	-50	-24	[78]
Ba ₂ S ₃	'I 41 m d'	-912		
BaO ₂	'I 4/m m m'	-638	-642	[129]
BaS ₂	'C 1 2/c 1'	-478		
BiS	'B 2 m m'	-35		
CaO ₂	'F 4/m m m'	-645	-653	[139]
Cr ₂ S ₃	'R -3 H'	-496	-480 ± 2	[140]
CrO	'F m -3 m'	-339	-305	[141]
CrO ₂	'P 42/m n m'	-603	-335	[142]
CrS ₂	'C 2/m 1 1'	-109	-598	[129]
Cs ₂ O ₂	'I m m m'	-482	-498 ± 10	[143]
Ga ₂ S ₃	'C 1 c 1'	-514	-516 ± 13	[122]
K ₂ O ₂	'C m c a'	-507	-496	[79]
K ₂ S ₂	'P -6 2 m'	-435	-431 ± 3	[144]
			-448	[145]
MoO ₃	'P b n m'	-732	-745 ± 1	[122]
Na ₂ O ₂	'P -6 2 m'	-514	-513	[79]
Na ₂ S ₂	'P 63/m m c'	-382	-388 ± 5	[146]
			-397	[147]
Rb ₂ O ₂	'I m m m'	-493	-479 ± 20	[143]
Sb ₂ O ₄	'P n a 21'	-936	-907 ± 5	[122]
			-895	[148]
Sb ₂ O ₅	'C 1 2/c 1'	-1022	-1008 ± 5	[122]
			-981	[148]
			-972	[149]
SrO ₂	'I 4/m m m'	-644	-636	[150]
TeO ₃	'R -3 c H'	-405	-416 ± 1	[151]
			-392	[152]
V ₂ O ₅	'P m n m S'	-1559	-1550 ± 2	[122]

Table 4.14 Calculated enthalpy of formation of HgMX_y species. The asterisks (*) refer to compounds whose experimental enthalpy of formation is estimated.

Compound	Space Group	$\Delta H_{f,calc}^0$ (kJ/mol)	$\Delta H_{f,expt}^0$ (kJ/mol)	Reference
Hg ₂ Br ₂	'I 4/m m m'	-197	-204	[122]
Hg ₂ Cl ₂	'I 4/m m m'	-257	-265 ± 2	[122]
Hg ₂ I ₂	'I 4/m m m'	-122	-119 ± 2	[122]
Hg ₂ MoO ₄	'P 1 21/c 1'	-913	-904* ± 63	[153]
Hg ₂ Sb ₂ O ₇	'F d -3 m Z'	-1320		
Hg ₂ SO ₄	'P 1 2/c 1'	-762	-743 ± 10	[122]
Hg ₂ TeO ₃	'P b m 2'	-442		
Hg ₂ WO ₄	'C 1 2/c 1'	-962	-958*±63	[153]
HgAg ₂ O ₂	'P 43 21 2'	-63		
HgAg ₂ S ₂	'P 1 21/c 1'	-66		
HgBa ₂ S ₃	'P n m a'	-995		
HgBaO ₂	'R -3 m H'	-722	-701 ± 14	[124]
HgBaS ₂	'P m c 21'	-537		
HgBi ₂ S ₄	'C 1 2/m 1'	-265		
HgCaO ₂	'R -3 m H'	-780	-765 ± 10	[124]
HgCr ₂ O ₄	'F d -3 m Z'	-1280		
HgCs ₂ O ₂	'I 4/m m m'	-604		
HgGa ₂ S ₄	'I -4'	-591		
HgK ₂ O ₂	'I 4/m m m'	-599		
HgK ₂ S ₂	'P -6 2 m'	-475		
HgNa ₂ O ₂	'I 4/m m m'	-616		
HgNa ₂ S ₂	'P b c a'	-442		
HgRb ₂ O ₂	'I 4/m m m'	-590		
HgSnO ₃	'R -3 c H'	-666		
HgSrO ₂	'P 32 2 1'	-740	-740 ± 17	[124]
HgTeO ₃	'P -1'	-457	-441	[152]
HgV ₂ O ₆	'P b c a'	-1700		
HgVO ₃	'P -1'	-876		

Chapter 5. Experimental Testing of Promising Sorbents for Hg Capture

5.1 Introduction

In the previous chapter we used computational methods to identify promising new materials for Hg capture. Here we test some of the most promising materials experimentally. We describe the construction of the experimental testing apparatus, including the analysis method used and the safety precautions taken. We then evaluate three materials, BaO₂, K₂S₂, and CrO₂, that were predicted by the DFT calculations to be promising for Hg adsorption.

5.2 Construction of Experimental Apparatus

5.2.1 Previous Investigations of Hg Adsorption

There are many examples of experimental measurements of Hg adsorption in the literature. In general, there are three key components to any Hg testing apparatus: Hg generation technique, adsorption system, and Hg analyzer. Granite et al. at NETL have published several articles regarding their experimental testing of Hg sorbents[47], [48], [56]. The Hg was generated in their apparatus using a Hg permeation tube developed by VICI Metronics. The Hg permeation tube consists of a small droplet of Hg inside a polymer membrane. The tube is placed in a constant temperature environment at which the tube has been certified to release a known flow rate of Hg (usually on the order of hundreds of nanograms per minute), assuming the carrier gas flow rate is sufficiently high. In the case of Granite et al., the permeation tube was placed in a glass U-tube and the U-tube assembly was placed in a constant-temperature oil bath. The Hg-laden carrier gas then passed through a quartz tube containing approximately 10 mg of sorbent, all of which being held at a constant temperature inside a furnace. The Hg was analyzed in one of several ways. If the carrier gas was inert, then the outlet Hg concentration was analyzed online using cold vapor atomic fluorescence spectrophotometry (CVAFS). Hg is well-known to

have strong absorbance at approximately 254 nm, and the Hg atoms fluoresce at this wavelength as well. For more complicated carrier gas mixtures, such as simulated syngas, the other gas components were not compatible with CVAFS, and as a result the saturated sorbent was analyzed offline by dissolving the material in solution and analyzing the resulting solution using either atomic absorption spectroscopy (AAS) or inductively-coupled plasma atomic emission spectroscopy (ICP-AES). The sensitivity of the CVAFS was found to be the best, with reported detection limits being as low as 1 ppb.

Lee et al. measured Hg adsorption on activated carbon using a similar method[154]. The Hg was again generated using a certified Hg permeation tube, and the sorbent was placed in a borosilicate glass column, which was placed inside a furnace. In this case, however, the Hg was analyzed using Ontario Hydro impinger tubes. The outlet Hg gas passed through 1 M KCl solution in order to collect the oxidized forms of Hg. The remaining carrier gas then passed through $\text{H}_2\text{O}_2/\text{HNO}_3$ and $\text{KMnO}_4/\text{H}_2\text{SO}_4$ solutions in order to oxidize and capture the elemental Hg (Hg^0). This technique is useful when it is desired to quantify not only total Hg content, but also Hg speciation. The resulting solutions were analyzed using cold vapor atomic absorption spectroscopy (CVAAS).

As a final example, Portzer et al. and RTI used a similar technique for the lab-scale screening of their sorbent materials[51]. Their system also involved the introduction of Hg via a certified Hg permeation tube—in this case, the tube was held constant in a permeation oven designed by VICI Metronics. Their sorbent, typically 200 to 600 mg, was placed in a borosilicate glass tube that was held at constant temperature inside a clamshell furnace. The Hg was analyzed using the spent sorbent bed; the bed was purged of Hg after the experiment was over and fed into a gold amalgam Hg trap in which the Hg was analyzed using CVAAS. Although this method is fairly effective at determining the amount of Hg adsorbed, because the Hg sorbents were measured after the experiment, there was no potential for dynamic adsorption behavior measurements.

5.2.2 Experimental Apparatus Design

We designed our adsorption apparatus based on the experimental systems described in the previous section. By far the most common Hg generation approach we encountered was the use of certified Hg permeation tubes, and as a result that was the method chosen for our system.

Rather than use an oil bath to maintain the permeation tubes in a constant temperature environment, we used a Dynacalibrator 150 permeation oven similar to the one by Portzer et al. The commercial permeation oven was advantageous because it was easier to connect to the rest of the adsorption system (important for the elimination of leaks) and because it was able to maintain a very tight temperature window—less than 0.1°C variation. Throughout the course of these experiments, several different Hg permeation tubes were used, and all were certified to release hundreds of nanograms of Hg per minute at 70°C (for example, 176 ± 2 ng/min, 325 ± 2 ng/min, 362 ± 2 ng/min, and so on). To change the Hg concentration in our carrier gas stream, the carrier gas flow rate could be changed or multiple tubes could be added to the permeation oven. Unfortunately, throughout the course of our experiments we discovered that the permeation rates certified by VICI Metronics were only certified at the time of measurement. In other words, perhaps due to structural changes in the polymer membrane over time, the permeation rate was expected to change over time—sometimes by as much as a factor of 4 in our experiments. We attempted to mitigate this uncertainty by comparing the relative Hg signals achieved between multiple permeation tubes; however, because the apparatus had no other method for determining the absolute concentration of Hg in the carrier gas stream, this uncertainty still had a significant negative impact on our ability to achieve reliable quantitative results.

Our adsorption column was modified slightly from those described in Section 5.2.1. Because many of our experiments were operating at temperatures above 200°C, we did not wish to use traditional borosilicate glass. Although a quartz column would be able to withstand the temperatures of our experiments, the connection between the quartz column and the stainless steel tubing included a polymeric o-ring whose maximum temperature was only 200°C. As a result, our column was eventually selected to be a 1/4" outer diameter (OD) stainless steel tube with Swagelok fittings on either end. The analyzer chosen for our apparatus was an Agilent 5975C quadrupole mass spectrometer detector (MSD) that was outfitted with a Diablo Analytical 5000A Real Time Gas Analyzer (RTGA) interface[155]. We selected a mass spectrometer as our analyzer because it offered the ability to perform dynamic measurements and seemed to be a promising candidate to address the shortcomings of the techniques described in Section 5.2.1. Most of these techniques involved analyzing the saturated sorbent bed at the end of the experiment, thereby eliminating most mechanisms to evaluate time-dependent adsorption

phenomena. Meanwhile, although the CVAFS technique used by Granite et al. was used to perform dynamic experiments in inert gas environments, it was not suitable for a simulated syngas environment. A mass spectrometer is able to perform online analysis of gas samples of variable compositions. Its detection limit is in general higher than the atomic absorption or fluorescence techniques. However, the RTGA interface coupled with the MSD had been previously shown to be able to detect less than 200 parts per billion (ppb) of sulfur compounds[156], which is actually an even lower detection limit because these compounds would likely fragment in the MSD (whereas Hg, an atomic species, would not). Because of this, the detection limit seemed to be suitably low for our applications.

All tubing and connections that were exposed to Hg vapor were 1/16" OD stainless steel. Stainless steel was chosen because previous researchers had used stainless steel and Teflon for their inertness to Hg[47], and Teflon was known to have a nonzero permeability to H₂[157], making it more difficult to perform experiments involving a simulated syngas. Despite its reported inertness, however, other researchers have reported Hg adsorption onto room temperature stainless steel[158], and indeed we also observed this in our own experiments. Two modifications were made to the stainless steel tubing as a result of this information. First, we replaced all tubing exposed to Hg (including that of the 1/4" OD column) with Sulfinert[®] tubing developed by Restek. Although this tubing was designed to be inert to sulfur compounds, not Hg, the manufacturers indicated that it would likely have some inertness to Hg over untreated stainless steel. In addition, all tubing and valves were covered with electrical heating tape and were heated to approximately 40°C using a Variac variable resistor. The packed column itself was placed in a clamshell furnace whose temperature was set by the desired temperature in a given experiment. Through these two modifications, the Hg adsorption onto the tubing was lessened, although not completely eliminated, as will be described in future sections.

A general schematic of the experimental apparatus is shown in Figure 5.1.

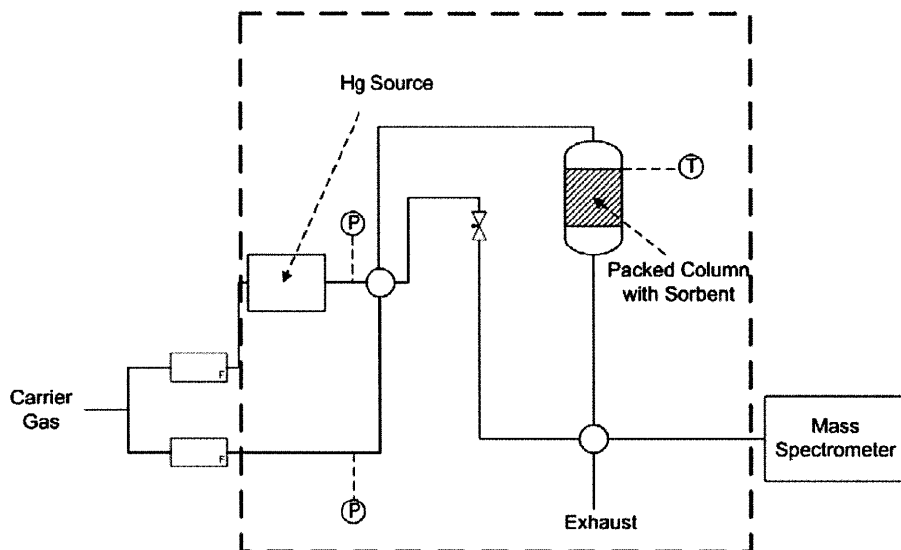


Figure 5.1 General schematic of experimental apparatus. The dotted box refers to the portions of the apparatus contained within the ventilated cabinet, as described in Section 5.2.3.

A carrier gas was introduced and passed through two mass flow controllers: one that directed flow to the Hg permeation oven, and one that remained as pure carrier gas. The Hg permeation oven was set at a constant temperature of 70°C so that the Hg was permeating at a specified mass flow rate (although, as described earlier in this section, this flow rate was not really known as accurately as suggested by the error bars given by VICI Metronics). Both gas streams met at a modified 4-port valve, indicated by a circle in Figure 5.1. From there, the gases could either proceed to the packed column or bypass the column, heading through a needle valve to mimic the pressure drop of the column. Accounting for the column pressure drop was considered to be critical because the signal in the MSD is known to be pressure-dependent, and therefore by mimicking this pressure drop we were able to adjust the Hg signals in both branches of the apparatus to be the same. Both gas streams again met at another 4-port valve, where they proceeded to either the Diablo RTGA and MSD or were sent to the exhaust stream.

5.2.3 Safety Considerations

Arguably the most important design consideration when working with something as dangerous as Hg vapor is safety. Even though our inlet Hg concentration rarely exceeded 200 ppbv, this concentration was still roughly an order of magnitude larger than the exposure recommended by the American Conference of Industrial Hygienists. As a result, the majority of the apparatus,

including the furnace, the column, and the permeation oven, was placed in a ventilated cabinet, as indicated by the blue box in Figure 5.1.

We worked with the Department of Environmental Health and Safety to ensure that the face velocity in the ventilated cabinet was sufficient and that the apparatus configuration met their safety standards. As Figure 5.1 shows, however, due to space considerations the MSD was not placed in the ventilated cabinet. This configuration meant that there were several Swagelok connections (to and from the RTGA interface) that were placed outside the safety of the ventilation cabinet. As a result, two additional safety measures were taken. First, additional ventilation in the form of a small canopy was placed over the MSD to create negative pressure and attract any potential leaks. Second, in addition to leak checking upon installation, periodic leak checking was performed with a portable Jerome Hg Analyzer that we borrowed from the Environmental Health and Safety office or from Michael Strano's lab group.

5.3 Characterization of Experimental Apparatus

5.3.1 Hg Detection in the Mass Spectrometer

The working principle of the MSD is separation (and therefore detection) based on different mass to charge (m/z) ratios. In order to detect Hg, therefore, we needed to focus the detector on the m/z ratios specific to Hg. A listing of the known stable isotopes of Hg is shown below in Table 5.1.

Table 5.1 Natural abundance of stable Hg isotopes.

Isotope	% Abundance
¹⁹⁶ Hg	0.151
¹⁹⁸ Hg	9.978
¹⁹⁹ Hg	16.8710
²⁰⁰ Hg	23.1016
²⁰¹ Hg	13.188
²⁰² Hg	29.8620
²⁰⁴ Hg	6.876

The MSD detected a signal for each isotope; the total mercury concentration was determined either by measuring ^{202}Hg , the most abundant isotope, or by measuring all six major isotopes and adding the signals together (^{196}Hg was not included because its % abundance is small compared to the other isotopes).

In order to improve its sensitivity, the MSD was operated in Selective Ion Monitoring (SIM) mode—in essence, instead of scanning an entire m/z range, it focused on specific m/z ratios that we specified in the MSD. An artifact of operating in SIM mode, however, was that the signal was nonzero even when there was no Hg flowing. In order to subtract this baseline signal, we also monitored the signal at an m/z ratio of 189. We anticipated that no real species with that m/z ratio would exist in our system, and as a result we calculated the “true” Hg signal by subtracting the signal at $m/z = 189$ from the raw Hg signal.

5.3.2 Accounting for Signal Drift

Throughout the course of our experiments we noticed that the Hg signal was not constant over the entire duration of a given experiment, even if the inlet concentration was unchanged. In other words, the Hg signal had the tendency to “drift” lower over time, further complicating our ability to extract quantitative results from our system. An example plot showing the drift in the raw Hg signal over time is shown in Figure 5.2 below.

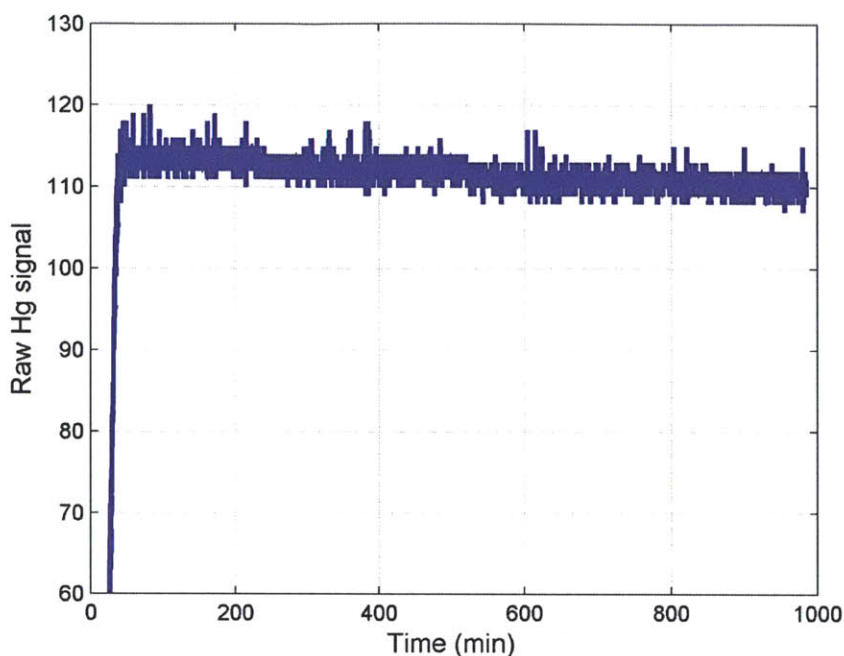


Figure 5.2 Drift associated with raw Hg signal in the mass spectrometer.

The drift in Figure 5.2 is only 3% over about 700 minutes, which, if this drift were constant from experiment to experiment, could likely be taken into account by adjusting the signal accordingly. Unfortunately the drift, although usually approximately the same magnitude between experiments, was not constant, and as a result we needed to find an alternative method to monitor the Hg signal. Discussions with the manufacturer of the Diablo RTGA interface led us to the conclusion that keeping track of the Hg signal *relative* to some internal standard, rather than the *absolute* Hg signal, would probably eliminate the drift. The rationale for this was that if the signal were drifting due to the electron multiplier detector in the MSD becoming “desensitized” over the course of a long experiment, we would expect this drift to be evident in the signals of all species. As a result, we replaced our carrier gas, which was originally pure He, with 500 ppm Ne in He. Ne was chosen as the internal standard due to its inertness and low atmospheric concentration. We then monitored the Hg signal as the ratio between the Hg and Ne raw signals. The data shown in Figure 5.2 adjusted with this new metric is shown in Figure 5.3.

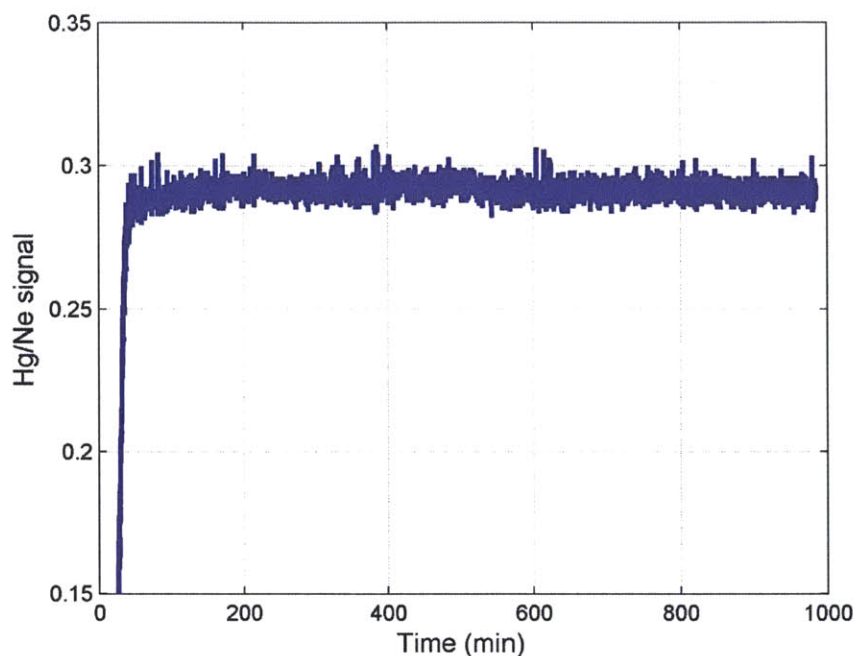


Figure 5.3 Drift reduction using ratio of Hg and Ne signals.

Qualitatively, the drift appears to be greatly reduced using this technique, and in fact, the drift in Figure 5.3 has been reduced to about 0.2% over the same time interval. More importantly, however, is that the magnitude of this drift has shown to be more constant over the course of our experiments. As an added benefit, monitoring the Hg concentration as a relative signal eliminated the effect of the MSD signal being pressure dependent (originally requiring the needle valve shown in Figure 5.1). We expected any changes in pressure to affect both the Hg and Ne signals by the same factor, and therefore any effect to the signal would cancel out with the ratio of the two signals. Therefore our measured Hg concentrations would become much less sensitive to this pressure effect. As a result, this new metric of relative Hg signal was the one that we adopted for our experimental work.

It is worth noting that because Ne is still present in small concentrations in the atmosphere, small errors may arise in the Ne signal. This error tended to be larger when the time between experiments was large, perhaps due to the buildup of atmospheric Ne in the tubing. We attempted to avoid this error by minimizing the time between experiments, but it is important to note that this metric of relative Hg signal is not without its own disadvantages.

5.3.3 Investigation of Detection Limit

As we reported in Section 5.2.2, the Diablo RTGA system has been previously reported to achieve sensitivity to sulfur compounds at concentrations below 200 ppb. Although that sensitivity figure is quite low, we needed our sensitivity to be approximately an order of magnitude below that in order to be suitable for our applications. As we mentioned in Chapter 4, the concentration of Hg in a coal gasification stream can vary widely, but a reasonable average value is approximately 10 ppbv. That means that the partial pressure of Hg in the syngas stream is approximately 400×10^{-9} atm, assuming a total syngas pressure of about 40 atm (this figure can also vary widely, depending on the gasifier type). Because our apparatus was set up to run between 1 and 2 atm of total pressure, the inlet Hg concentration we needed to study was about 200 to 400 ppbv, which is near the lower limit of the demonstrated sulfur sensitivity. As a result, we investigated the Hg sensitivity in the MSD to verify that the MSD could be an effective analyzer. The results are shown in Figure 5.4.

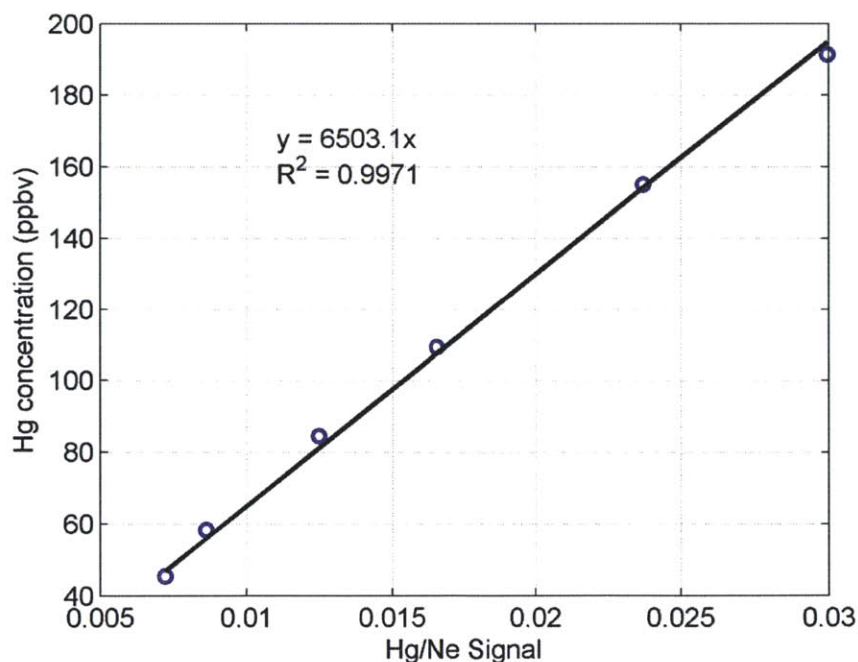


Figure 5.4 Investigation of Hg detection limit in MSD.

The different concentrations of Hg were determined by placing a single Hg permeation tube in the permeation oven at 70°C. At this temperature, the permeation tube used for Figure 5.4 was

certified to release 362.38 ng/min of Hg. In order to change the concentration of Hg, we varied the carrier gas flow rate. Using this method we generated the 6 data points shown in the above figure. The signal reported in Figure 5.4 was a ten-minute average of the measured signal. As Figure 5.4 shows, the MSD maintained good linearity with Hg signal vs. concentration even as low as about 45 ppbv. In addition, if the best-fit line were forced to pass through the origin (as we would expect a concentration vs. signal plot to behave), the linearity still existed with a correlation coefficient of 0.9971. Based on this result, therefore, we concluded that it was a reasonable approximation to extrapolate the linear trend even for Hg concentrations lower than 45 ppbv. We note that the averaging method used to generate the data points in Figure 5.4 can also be used to estimate the detection limit of the MSD. In order to be confident in our measured signal, we expect that the magnitude of the fluctuations in the signal should be no larger than 50% of the magnitude of the average signal. The typical standard deviation of the signal fluctuations corresponded to a fluctuation of 5 ppbv in the calculated concentration; therefore, we estimate that the detection limit of the MSD is approximately 10 ppbv.

This method was of course limited by the fact that we certainly did not know the Hg concentration to the 5 digits of precision specified by the manufacturer (due to the reasons specified in Section 5.2.2). Furthermore, the linear trend did not confirm in any way that the permeation rate was in fact 362.38 ng/min. Equation (5.1) shows the expected relationship between Hg permeation rate and the MSD signal.

$$\frac{F_{Hg}}{F_i} = Ks_i \quad (5.1)$$

Essentially, the signal (s_i) is expected to be related to the Hg mole fraction, designated by the ratio of the mole flow of Hg (F_{Hg}) to the mole flow of carrier gas (F_i), by some constant multiplicative factor (K). The calibration curve in Figure 5.4 was generated by varying F_i and obtaining different values of s_i . Therefore, the slope of the curve in Figure 5.4 only helped to identify the ratio F_{Hg}/K , not the individual value of F_{Hg} .

However, because we did not have any method to independently verify the concentration of Hg, we were forced to assume that this permeation rate was approximately correct. In addition, even if the permeation rate were not correct, it is very reasonable to assume that the rate was constant

over a given experiment—therefore, the linearity of the signal with Hg is still an important result.

5.4 Breakthrough Analyses of Candidate Materials

Our analysis in Chapter 4 identified several materials that were predicted to adsorb Hg at 170°C; of these, only one, potassium disulfide (K_2S_2), was predicted within the error of our calculations to both adsorb Hg and resist reduction via the H_2 present in the syngas. For completeness we also included two other compounds in our testing, barium peroxide (BaO_2) and chromium (IV) dioxide (CrO_2), that were also predicted to adsorb Hg at 170°C (but not resist H_2 reduction).

5.4.1 Sorbent Preparation and Safety Considerations

The three materials were partially chosen due to their ability to be readily purchased from chemical supply companies. All three compounds were purchased from Sigma Aldrich. K_2S_2 unfortunately was not available in pure form and was only available as a component of potassium polysulfide (K_2S_x), in which no less than 42% of it was potassium sulfide (K_2S), and presumably the remaining 60% was a combination of inert fillers, K_2S_2 , K_2S_3 , and so on. This material was determined to be a suitable approximation to K_2S_2 for our experiments because although we would not predict K_2S to react with Hg, the remaining potassium polysulfide components are likely to be more reactive than K_2S_2 and therefore would probably also have some affinity for Hg.

Two additional complications arose with K_2S_x as a sorbent material, however. First, in its purchased form the material consisted of large chunks approximately 1 to 2 cm in diameter, which required grinding the material into smaller pieces using a mortar and pestle. Second, the MSDS indicated that the material was corrosive, had high aquatic toxicity, and was hazardous to mucous membranes, meaning that additional safety precautions were required. All the preparations required for this material were performed in the chemical fume hood on a disposable mat and with the drain covered to prevent emission to the environment. Additional personal protective equipment in the form of an additional pair of rubber gloves and a chemical apron were also used. After this grinding step, only particles approximately 1 mm in diameter

(estimated) were used in order to reduce the entrainment of hazardous dust particles in the system by the carrier gas. The BET surface area was measured to be $4.9 \text{ m}^2/\text{g}$ by Dr. Herui Duo on a Quantachrome Autosorb-iQ.

BaO_2 was purchased from Sigma Aldrich as a greater than 95% pure powder. Its particle size was listed as approximately 325 mesh (approximately $45 \text{ }\mu\text{m}$ in diameter), although due to some of the particles sticking together, sieving analysis showed that approximately 20% of the mass was in particles larger than $250 \text{ }\mu\text{m}$. The main hazard of BaO_2 seemed to be the fact that it is a strong oxidizer, so care was taken to avoid incompatible materials. In addition, the material was also indicated to be toxic (perhaps due the presence of BaO in the mixture), and as a result it was handled using the same personal protective equipment as the K_2S_x solid. The BET surface area of this material was measured by Zan Liu using the Micromeritics ASAP 2020 Surface Analyzer in the Institute for Soldier Nanotechnology at MIT and was determined to be $1.5 \text{ m}^2/\text{g}$.

Finally, CrO_2 was purchased from Sigma Aldrich as Magtrieve™ powder. The mesh size was not given in the documentation, but sieving analysis showed that the particles were between 45 and $250 \text{ }\mu\text{m}$ in diameter, with approximately 70% of the mass in particles between than $150 \text{ }\mu\text{m}$ and $250 \text{ }\mu\text{m}$. This material was not as hazardous as K_2S_x or BaO_2 ; however, in order to minimize exposure to dust the material was handled in the fume hood when possible. The BET surface area, again measured by Zan Liu in the Institute for Soldier Nanotechnology, was determined to be approximately $32.8 \text{ m}^2/\text{g}$.

5.4.2 General Procedure of Breakthrough Experiment

Approximately 30 mg of sorbent material was placed in the 1/4" OD stainless steel column. This material was supported using a quartz wool packing. The sorbent-containing column was reinstalled into the apparatus. The Hg permeation tube, certified to emit 362.38 ng/min of Hg at 70°C was placed in the permeation oven and brought to temperature along with the heating tape on the apparatus overnight. During this overnight operation approximately 250 standard cubic centimeters per minute (SCCM) of the He/Ne mixture was flowing through the permeation oven with the valves configured such that the flow bypassed the sorbent column and went directly to the analyzer. The column had approximately 100 to 150 SCCM of the He/Ne mixture flowing through it during this period. This gas was sent directly to the exhaust. The purpose of this

overnight operation was to allow suitable time for the system to warm up and obtain a constant Hg signal.

Once the Hg signal had stabilized, a calibration curve was generated. Because the Hg signal was not constant in the MSD from experiment to experiment, a calibration curve needed to be generated prior to every experiment. As was the case in Figure 5.4, the temperature in the permeation oven was kept constant at 70°C and the carrier gas flow rate was varied in order to introduce different Hg concentrations. In order to decrease the time required for the experiment, the calibration curve was generally reduced to consist of 2 or 3 data points fit to pass through the origin (in other words, the equation form was $y = m \cdot x$, not $y = m \cdot x + b$). As we described in Section 5.3.3, the inlet Hg concentration should have been about 200 to 400 ppbv to accurately mimic the inlet partial pressure of Hg in a syngas stream. However, because the Hg concentrations are widely variable between different syngas streams, meaning that a lower Hg concentration would allow the material to function in a larger number of syngas streams, and because lower concentrations of Hg were preferable from a safety standpoint, our inlet concentration of Hg was set at about 150 ppbv.

Once the calibration curve was generated the Hg-laden carrier gas was diverted to the sorbent column and the outlet concentration was monitored using the MSD. A simulated breakthrough curve that would be generated by monitoring the outlet concentration is shown in Figure 5.5.

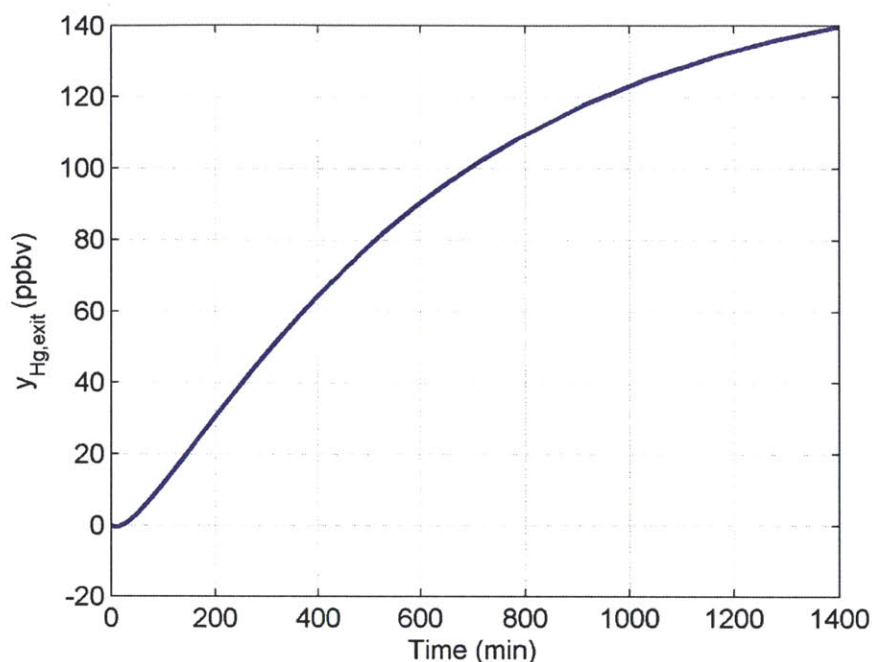


Figure 5.5 Typical form of breakthrough curve.

The capacity of the sorbent bed could then be determined by integrating the area in between the inlet concentration and the breakthrough curve. This is shown mathematically in Equation (5.2) below.

$$q = \frac{1}{m_{sorb}} \int (F_{Hg,in} - F_{Hg,out}) dt \cong \frac{F_{carrier}}{m_{sorb}} \int (y_{Hg,in} - y_{Hg,out}) dt \quad (5.2)$$

The variable F refers to a mole flow rate (in moles per time), and the variable q refers to the sorbent loading in moles of Hg per kg sorbent. The total flow rate is mathematically equal to the sum of the carrier gas flow rate and the Hg flow rate, but because the Hg flow rate is approximately 7 orders of magnitude smaller than the carrier gas flow rate, the total flow rate is essentially constant, and Equation (5.2) is a good approximation. We then reported two figures of merit for a given sorbent material: the Hg adsorbed in 2 hours, and the breakthrough time as defined by the time at which the outlet concentration reached 50% of the inlet concentration. The Hg adsorbed after 2 hours was reported rather than the saturation capacity because the signal drift, although reduced using the method described in Section 5.3.2, was still not completely eliminated, and the longer the experiment, the larger the error associated with the variability in

the Hg signal. Therefore, we attempted to decrease this effect by limiting the quantitative calculations to the first two hours. In addition, although the heating tape in the system decreased the amount of Hg adsorbed on the stainless steel tubing, it did not completely eliminate it. In order to account for this effect, we performed a two hour breakthrough experiment using a blank column packed with quartz wool. The amount of Hg adsorbed in this experiment was subtracted from the calculated amounts in the experiments containing sorbent in an effort to report only the capacity due to the presence of sorbent. Finally, we note that as before, any uncertainty in the permeation rate of in the Hg permeation tube directly affects the measured loading. However, because a different permeation rate simply implies a different mole fraction of Hg, this means that any variations in the Hg permeation rate would simply result in the loading being incorrect by a multiplicative factor. Therefore, even if the absolute loadings that we measured were inaccurate, we would expect the relative loadings to be correct.

5.4.3 *Potassium Polysulfide*

In the first K_2S_x experiments the sorbent column was held at a constant temperature of 170°C, the temperature used in the Hg calculations in Chapter 4. The results of the breakthrough experiment are shown below in Figure 5.6.

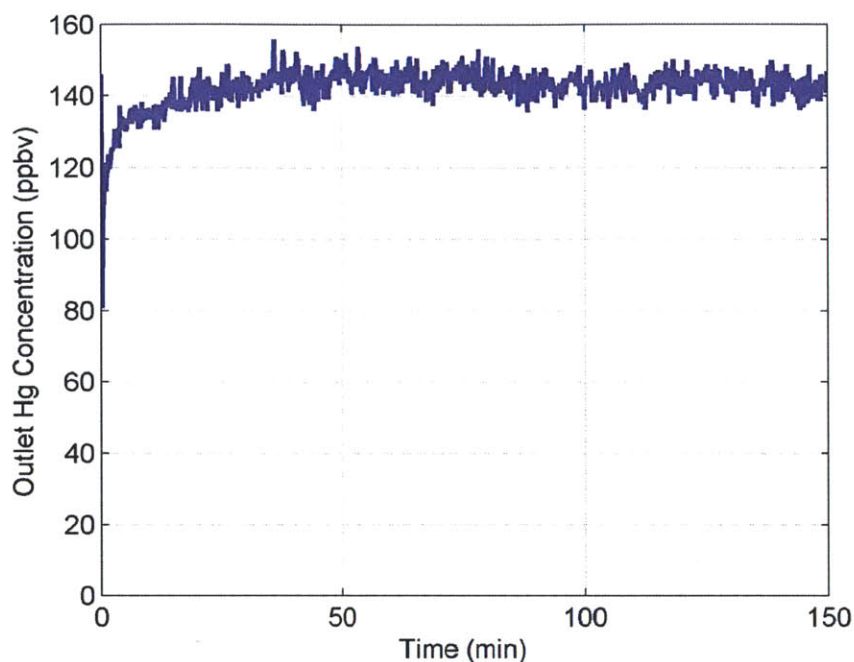


Figure 5.6 Breakthrough experiment of K_2S_x at $170^\circ C$ of 155 ppbv Hg in 260 SCCM He/Ne.

As Figure 5.6 shows, the adsorption on K_2S_x was fairly minimal at $170^\circ C$. The calculated capacity after 2 hours was 3×10^{-4} mol Hg/kg sorbent, and the breakthrough time was less than 1 minute.

Because a small amount of Hg did adsorb, however, we investigated the adsorption behavior at lower temperatures. We placed approximately 110 mg of K_2S_x in the column (a larger amount due to the fact that the experiment itself was longer) and repeated the experiment at various temperatures. Our intention with this experiment was merely to qualitatively investigate whether Hg adsorption occurred at various temperatures. The results are shown in Figure 5.7 below.

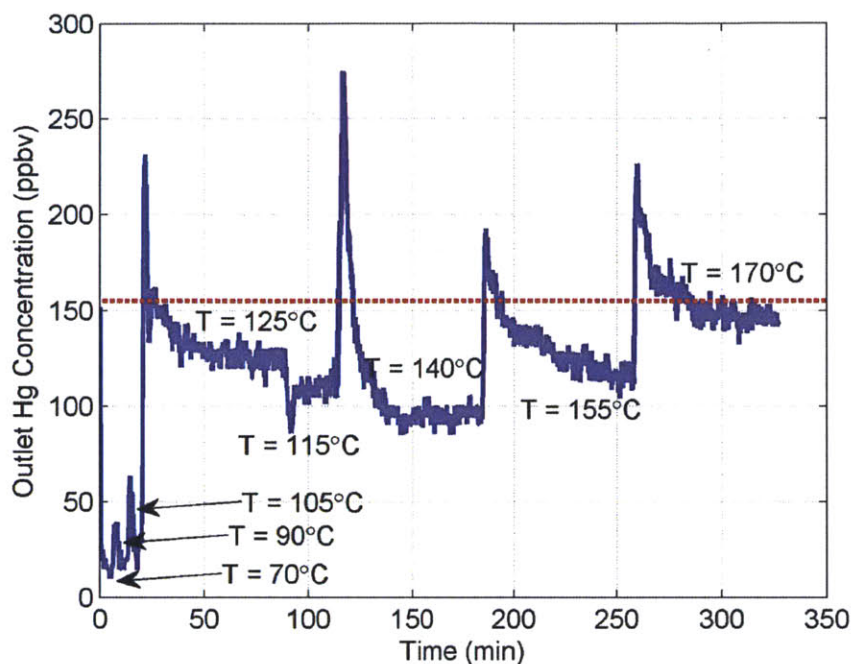


Figure 5.7 Investigation of Hg adsorption on K_2S_x at different temperatures. The red dotted line shows the constant inlet Hg concentration of 155 ppbv.

Each peak in Figure 5.7 refers to a point at which the temperature of the adsorption column was changed. The inlet Hg concentration was always constant at 155 ppbv. As Figure 5.7 shows, a significant amount of Hg adsorption occurred even at temperatures as high as about 155°C, as evidenced by the outlet Hg concentration remaining below the inlet concentration of 155 ppbv. This observation supports our earlier DFT calculations, which predicted that K_2S_2 is a marginal sorbent near 170°C for $p_{Hg} = 0.04$ Pa. It is possible that with alterations to the sorbent surface area or higher inlet Hg concentrations K_2S_x could effectively capture Hg, even at 170°C. However, we limited our investigation in this thesis to these initial experiments for two reasons. First, the toxicity of the K_2S_x material is a significant disadvantage for it to be used in any industrial process. Second, in the course of our investigations we found that K_2S_x is water soluble. Although we initially thought this could be beneficial because it could facilitate dispersing the material on an inert support, it is more likely that this behavior is detrimental to the sorbent's efficacy. Potassium monosulfide (K_2S) does not merely dissolve in H_2O but hydrolyzes according to Equation (5.3)[159].



Because K_2S_2 also dissolves in water, we expect that its mechanism of dissolution is similar to Equation (5.3) above. Unfortunately, because there is a significant amount of steam present in the syngas mixture, we predicted that any K_2S_2 sorbent would degrade during industrial operation, rendering it ineffective as a Hg sorbent.

5.4.4 Barium Peroxide

Our DFT calculations in Chapter 4 predicted that BaO_2 would be thermodynamically capable of adsorbing Hg well above $170^\circ C$. Therefore, in an effort to help overcome any kinetic barriers to Hg adsorption we performed this experiment at a slightly elevated temperature of $200^\circ C$. The results of the breakthrough experiment are shown in Figure 5.8.

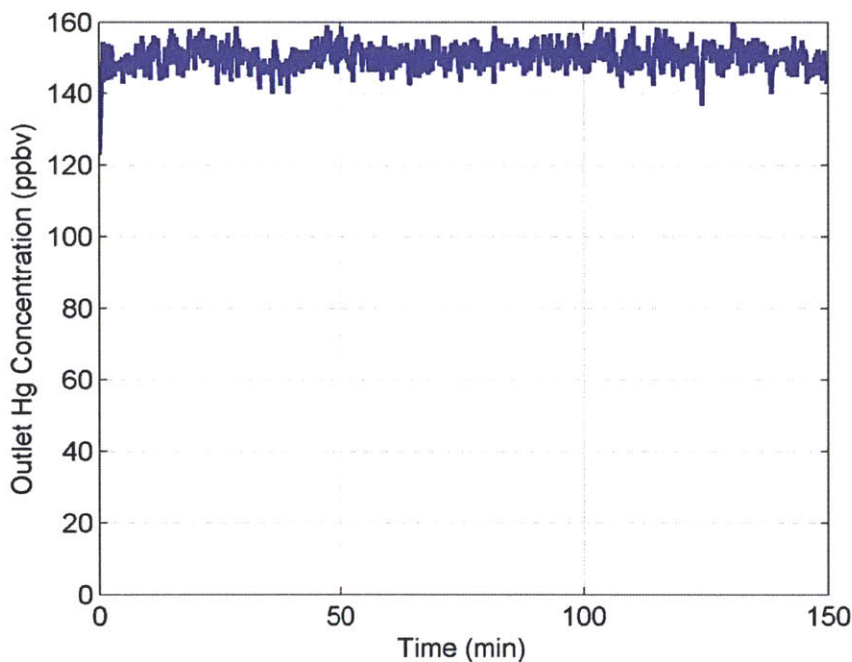


Figure 5.8 Breakthrough experiment of BaO_2 at $200^\circ C$ of 155 ppbv Hg in 260 SCCM He/Ne.

Clearly, virtually no Hg adsorbed during the experiment shown in Figure 5.8. The calculated capacity after 2 hours was 0 mol/kg within the error of our measurements, and the time to 50% breakthrough was again less than 1 minute. We had several hypotheses about the cause of this lack of adsorption. First, although unlikely, the temperature of $200^\circ C$ could be too high for the adsorption to be thermodynamically possible. Second, the temperature of $200^\circ C$ could be too low to overcome any kinetic barriers to adsorption. Finally, the measured surface area of 1.5

m²/g could be too low to observe any Hg adsorption. We tested all three explanations by repeating the experiment with approximately 120 mg of sorbent (increasing the available surface area) and varying the temperature anywhere from 120°C to 385°C. Even with these variations, the adsorption behavior remained virtually unchanged. The fact that no adsorption was observed at temperatures below 170°C suggested that the lack of adsorption was either due to a high kinetic barrier (requiring temperatures greater than 385°C) or the low surface area. Based on the literature for the synthesis procedure of the HgBaO₂ product, our conclusion was that the problem was likely kinetic. The synthesis techniques of HgBaO₂ in the literature involve mixtures of HgO and BaO₂ at 800°C in one case[160] and 700°C and 6000 bar[161] in another case; both of which imply that the barrier to the formation of HgBaO₂ is quite large, and is perhaps too large to be effective at our temperatures of interest. Because our calculations predicted that the H₂ would react with the BaO₂ more readily than the Hg anyway, we did not pursue this compound any further.

5.4.5 Chromium (IV) Oxide

As was the case with BaO₂, our calculations predicted Hg to adsorb onto CrO₂ at temperatures above 170°C. As a result, we performed the breakthrough experiment at a sorbent column temperature of 200°C. The results of the breakthrough analysis are shown in Figure 5.9.

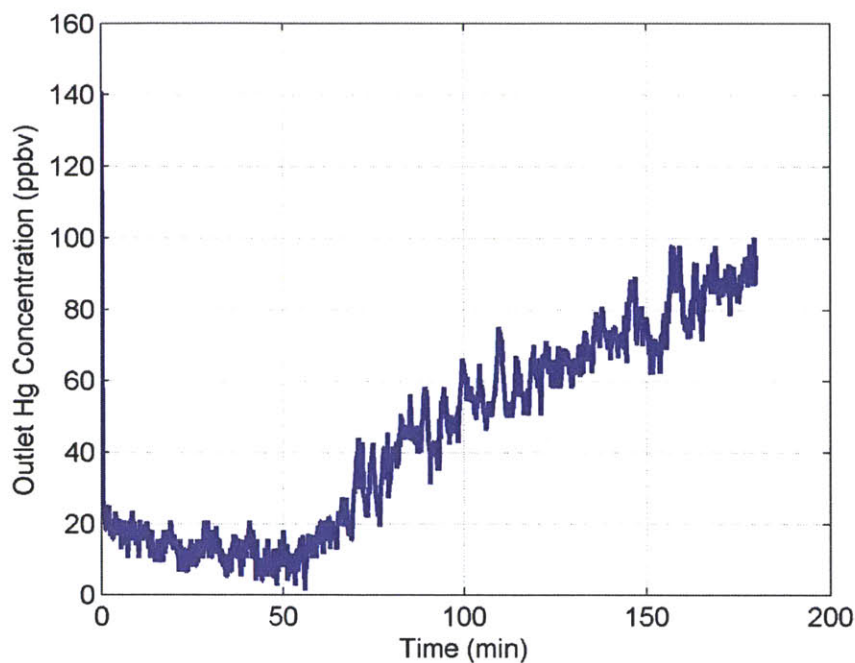


Figure 5.9 Breakthrough experiment of CrO₂ at 200°C of 155 ppbv Hg in 260 SCCM He/Ne.

The CrO₂ sorbent successfully adsorbs Hg at 200°C according to Figure 5.9. The capacity at 2 hours is approximately 6×10^{-3} mol Hg per kg of sorbent, and the breakthrough time is actually slightly longer than 2 hours at about 140 minutes. We calculated a theoretical maximum capacity for surface adsorption based on the measured BET surface area of 32.8 m²/g. A typical unit cell of Cr₂O₄ (according to our calculations, 2 CrO₂ molecules is one site for Hg) is about 4.5 Å x 4.5 Å x 3 Å, so assuming the 4.5 x 4.5 face is on the surface, 32.8 m²/g translates to about 0.3 moles of adsorption sites per kg. This means that roughly 2% of the available sites were occupied at these conditions. The fact that Hg adsorbed was encouraging, so we investigated the reactivity of CrO₂ with other syngas components. The apparatus was modified slightly to include a variety of carrier gases, as shown in Figure 5.10.

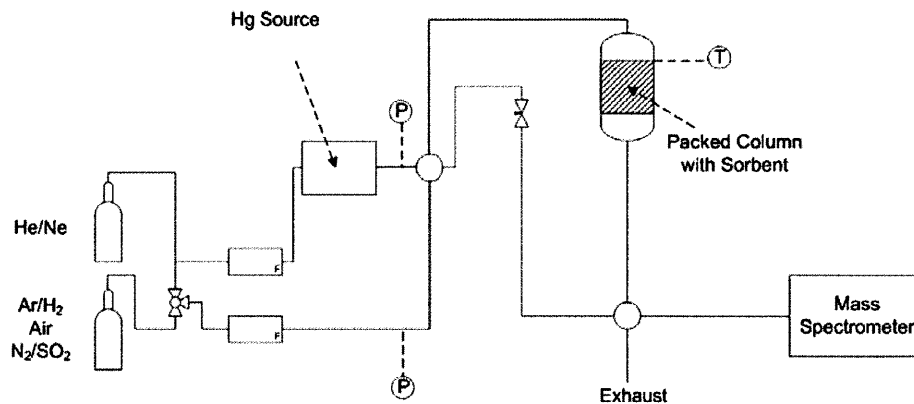


Figure 5.10 Experimental apparatus with modified carrier gas inlet.

The ventilated enclosure (indicted with a blue box in Figure 5.1) was still present in the modified apparatus shown in Figure 5.10; it has been removed from the figure for clarity. Essentially, the carrier gas was modified so that the He/Ne gas mixture could be the sole carrier gas or various gas mixtures such as 2% H₂ in Ar, air, or 5% SO₂ in N₂ could be introduced to the sorbent instead. In order to test the affinity of CrO₂ for H₂, we exposed 30 mg of CrO₂ sorbent to 145 SCCM of the H₂/Ar gas mixture for 3 hours at 200°C. Clearly, 2% H₂ in a gas stream with a total pressure of 1 – 2 atm is much lower than the typical partial pressure of H₂ in a syngas stream (10 – 15 atm). However, we decided to maintain a low H₂ concentration for safety. Therefore, if we saw any change in sorbent behavior at this low H₂ concentration, we would conclude that a real syngas mixture with the appropriate levels of H₂ would cause an equal or larger change. After the CrO₂ was exposed to the H₂ gas mixture for 3 hours, the system was allowed to warm up overnight in the He/Ne carrier gas following the identical procedure to that of Section 5.4.2, and another breakthrough analysis was performed. The results of this analysis are shown in Figure 5.11.

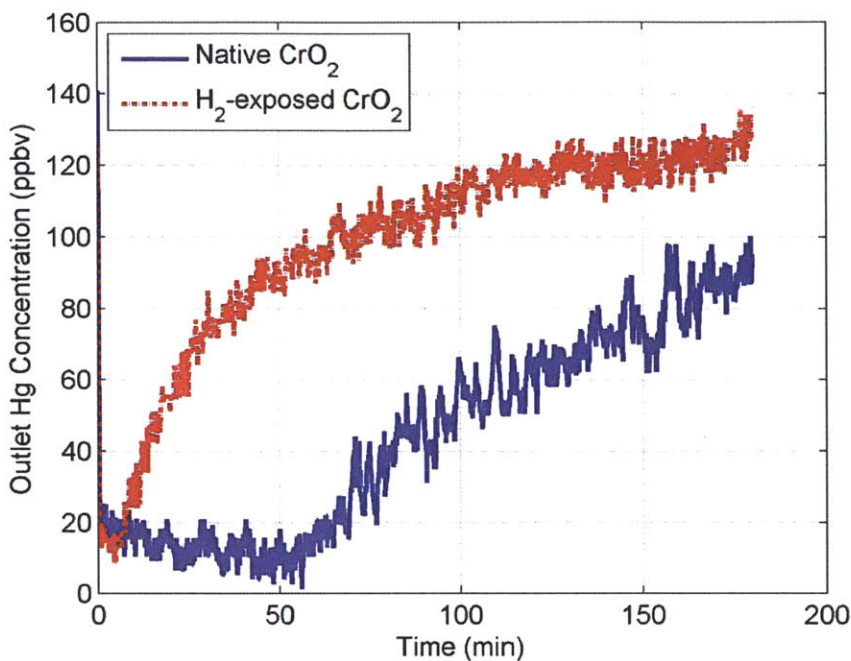


Figure 5.11 Breakthrough experiment of CrO₂ at 200°C of 155 ppbv Hg in 260 SCCM He/Ne after exposure to 145 SCCM 2% H₂ in Ar at 200°C for 3 hours. The results of the breakthrough experiment for native CrO₂ are shown for comparison.

Clearly, the ability to adsorb Hg greatly decreased upon exposure of the sorbent to the H₂ gas mixture. The capacity after two hours was reduced from 6×10^{-3} mol/kg to 3×10^{-3} mol/kg, and the breakthrough time was only about 40 minutes.

Therefore, this experiment provided additional evidence to the validity of the DFT calculations from Chapter 4—our calculations predicted that the CrO₂ material would react with both Hg and H₂, and this behavior was confirmed by our experiments. However, our calculations also predicted that the CrO₂ would bind Hg strongly enough to even capture Hg from flue gas, where the inlet Hg concentration is closer to 1 ppbv in 1 atm total pressure. The sensitivity of our MSD did not allow us to test that low concentration behavior, but we were able to test the affinity of CrO₂ for typical “competing” species found in a flue gas stream. In other words, although H₂ is present in large quantities in the syngas stream, the flue gas stream contains air, steam, and, depending upon the sulfur removal technique, SO₂. Our experimental apparatus was not configured to be able to generate significant amounts of water vapor, but we were able to test the effect of the exposure of the sorbent to air and SO₂. As a result, two additional experiments were

performed using a similar method to that which was described above. In the first experiment, the 2% H₂ in Ar stream was replaced with air, but the experimental method was otherwise identical. In the second experiment, the 2% H₂ in Ar stream was replaced with a 5% SO₂ in N₂ stream. Due to some unreliability in the MSD during this latter experiment, the 5% SO₂ stream was only exposed to the CrO₂ sorbent for 2 hours. Other than this difference, the remainder of the experiment proceeded identically to that involving the H₂/Ar stream. The results of these two experiments are shown in Figure 5.12.

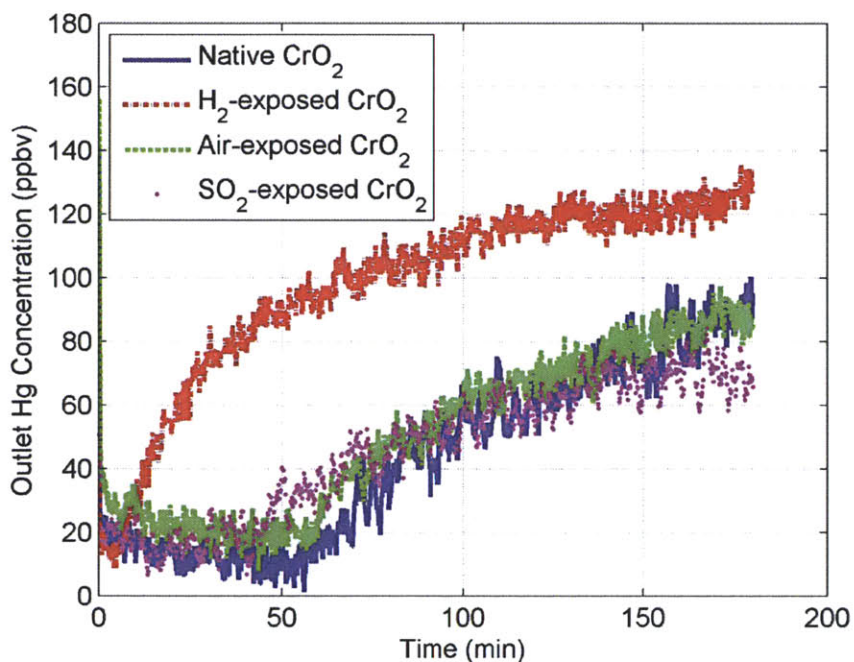


Figure 5.12 Breakthrough experiment of CrO₂ at 200°C of 155 ppbv Hg in 260 SCCM He/Ne after exposure to 145 SCCM 2% H₂ in Ar, 145 SCCM air, and 145 SCCM 5% SO₂ in N₂ at 200°C. The results of the breakthrough experiment for native CrO₂ are shown for comparison.

The Hg adsorbed after 2 hours and breakthrough time for the air-exposed CrO₂ were 6×10^{-3} mol/kg and about 135 minutes, respectively—virtually identical to the behavior of the native sorbent. Because of the unreliability in the MSD during the SO₂ experiment, extra signal averaging was performed, and as a result the data were not as reliable as most of our traces. Qualitatively, however, the shape of the breakthrough curve is very similar to that of the air-exposed and native CrO₂, implying that the presence of SO₂ had little effect on the adsorption capacity. These results indicate that CrO₂ could have potential as a sorbent for Hg capture from

flue gas due to the fact that these common components of a flue gas mixture do not seem to affect the Hg adsorption ability.

5.5 Additional Investigations of Chromium (IV) Oxide

The favorable Hg adsorption characteristics of CrO₂, described in Section 5.4.5, were very encouraging about the potential of CrO₂ as a sorbent for elemental Hg. As a result we performed additional investigations of Hg adsorption on CrO₂ in an effort to better characterize its behavior.

5.5.1 *Cyclic Adsorption of Hg on CrO₂*

Our initial study of Hg on CrO₂ was to evaluate its working capacity as a sorbent material. The experiment involved placing 10 mg of CrO₂ powder in the 1/4" OD column and performing a breakthrough experiment very similar to that described in Section 5.4.2. The Hg and carrier gas flow rates were identical to those of the general breakthrough experiment (155 ppbv in 260 SCCM carrier gas), and the temperature of the column was again held at 200°C. The key difference in this experiment was that instead of stopping the breakthrough experiment after 3 hours, the experiment was instead allowed to proceed overnight. The intention of this longer breakthrough experiment was to completely saturate the CrO₂ with Hg. At this point, the temperature of the column was increased to 230°C at a rate of approximately 5°C/min, and the flow over the column was changed to 190 SCCM of pure He/Ne. The use of 190 SCCM He/Ne rather than 260 SCCM He/Ne likely affected the mass transfer characteristics of the system; however, because we were concerned with the total amount desorbed and not any time-dependent behavior, any effects of changing the mass transfer profile were acceptable. The outlet Hg concentration was monitored using the MSD in an effort to quantify the extent of regeneration that occurred under these conditions. Once the outlet Hg concentration stabilized near zero, the adsorption step was repeated: the temperature was decreased to 200°C, and 155 ppbv Hg in 260 SCCM He/Ne was exposed to the regenerated sorbent. This procedure (He/Ne desorption at 230°C, Hg adsorption at 200°C) was repeated one more time for a total 2 adsorption-desorption cycles. A plot of the mass change over the course of these adsorption-desorption experiments (after the initial overnight adsorption step) is shown in Figure 5.13. The

mass of Hg adsorbed was calculated by integrating the breakthrough curves over the course of the experiments.

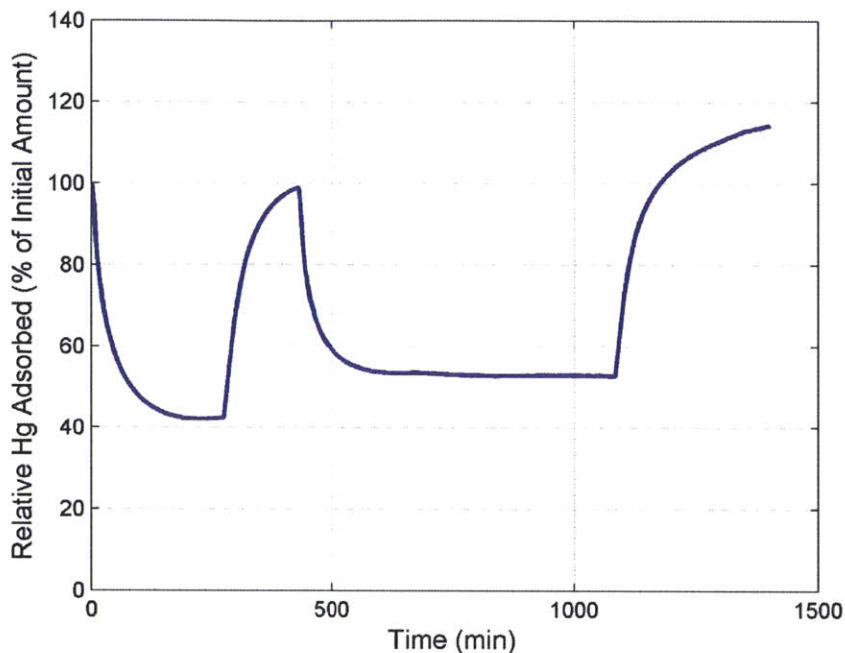


Figure 5.13 Cyclic adsorption of Hg on CrO₂. The regeneration steps were taken at 230°C in 190 SCCM pure He/Ne, and the adsorption steps were taken at 200°C with 155 ppbv Hg in 260 SCCM He/Ne.

Unfortunately, the results of this experiment were again semi-quantitative. As was described in Section 5.3.2, the use of an internal Ne standard in the carrier gas greatly decreased the signal drift over the course of our experiments; however, the signal drift was still present over long experiments, and this experiment spanned multiple days. The calibration curves were shifted over the course of the experiment in an effort to account for the signal drift, but our confidence in the quantitative accuracy of the results decreased as time increased. The results indicate that regeneration at 230°C in 190 SCCM He/Ne did not completely regenerate the sorbent, since the first desorption step only removed about 60% of the adsorbed Hg. This is evidence that at least some of the Hg chemisorbs onto the CrO₂ material, since we would expect a weaker physisorption bond to regenerate more under these conditions. In addition, the amount of Hg adsorbed in the first adsorption step in Figure 5.13 was roughly the same as the amount desorbed earlier, indicating that the desorption step did not dramatically alter the number of available sites

for Hg binding. The second desorption-adsorption pair was less quantitative: the desorption step indicated that less Hg desorbed here than before, but the adsorption step indicated that roughly the same amount of Hg re-adsorbed as it did in the first desorption-adsorption pair. These results do not conclusively determine whether the working capacity decreases from cycle to cycle, but they do at least indicate that any decrease in the Hg working capacity is small.

5.5.2 *Estimation of Enthalpy of Adsorption*

One potential method to determine the enthalpy of adsorption would be to measure the adsorption isotherms at several different temperatures and determine the isosteric heat of adsorption following the formula shown in Equation (5.4).

$$\Delta H_{ads} = R \left(\frac{\partial \ln p}{\partial 1/T} \right)_q \quad (5.4)$$

Unfortunately, the limitations of the apparatus were such that we were unable to reliably measure the necessary isotherms for this method. Similarly, due to the low concentration of Hg present in our gas stream, we did not expect calorimetry to be an effective technique. Therefore, we attempted to estimate the enthalpy of adsorption via alternative methods.

To overcome our limitation of unreliable MSD signals in long breakthrough experiments, we fit the tails of the breakthrough curves to exponential fits and integrated the analytical curve for the adsorption at long times. A sample exponential fit is shown below.

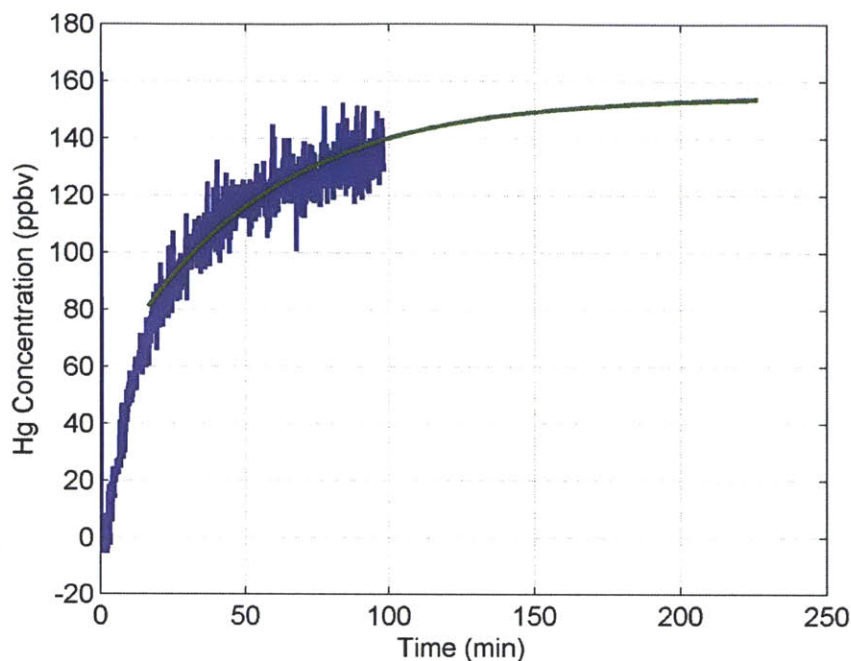


Figure 5.14 Exponential fit of tail of breakthrough curve for $y_{inlet} = 155$ ppbv Hg, $T = 250^{\circ}\text{C}$.

The breakthrough experiment was repeated for a total of 6 data points, which are summarized in Table 5.2 below.

Table 5.2 Summary of breakthrough experiments performed with exponential fit on the tail of the breakthrough curve.

Temperature ($^{\circ}\text{C}$)	Mole Fraction Hg (nominal)	Mole Fraction Hg (adjusted)	Hg Loading (mol/kg)
250	155	143	0.0048
240	155	143	0.0078
230	155	143	0.0103
220	155	143	0.0140
220	267	255	0.0175
220	112	112	0.0091

All breakthrough experiments in Table 5.2 were performed with 260 SCCM He/Ne carrier gas and approximately 10 mg CrO_2 sorbent. The “nominal” Hg mole fraction refers to the calculated mole fraction of Hg based on the Hg permeation rate specified by VICI Metronics. The “adjusted” mole fraction was calculated based on the relative MSD signals of two different permeation tubes: 362.38 ng/min and 261.61 ng/min. The ratio of the two signals was not equal

to the ratio of the two nominal permeation rates, and as a result the permeation rate of the 362.38 ng/min was adjusted to 335 ng/min to make the two ratios consistent with each other. The 261.61 ng/min rate was used as the reference because this tube was relatively new, and as a result it was more likely to perform at its original specified rate.

These 6 data points were then fit to the Langmuir model using a nonlinear fit in MATLAB. The Langmuir model, shown in Equation (5.5), has three fitted parameters: ΔH_{ads} , ΔS_{ads} , and q^{sat} . We assumed during this data fitting that all three parameters were independent of temperature, pressure, and sorbent loading, which are characteristic assumptions of the Langmuir model but probably do not accurately represent a real surface.

$$q = \frac{q^{sat} \exp\left(-\frac{\Delta H_{ads} - T\Delta S_{ads}}{RT}\right) y_{Hg} \frac{p}{p_{ref}}}{1 + \exp\left(-\frac{\Delta H_{ads} - T\Delta S_{ads}}{RT}\right) y_{Hg} \frac{p}{p_{ref}}} \quad (5.5)$$

It was our original intention to use a Henry's Law model rather than a Langmuir model for the adsorption process; the measured capacities in Table 5.2 are significantly smaller than the maximum capacity of about 0.3 mol/kg calculated in Section 5.4.5. However, the three data points at 220°C did not fit Henry's Law behavior, so we decided to use the more general Langmuir model. The fitted isotherms are plotted in Figure 5.15.

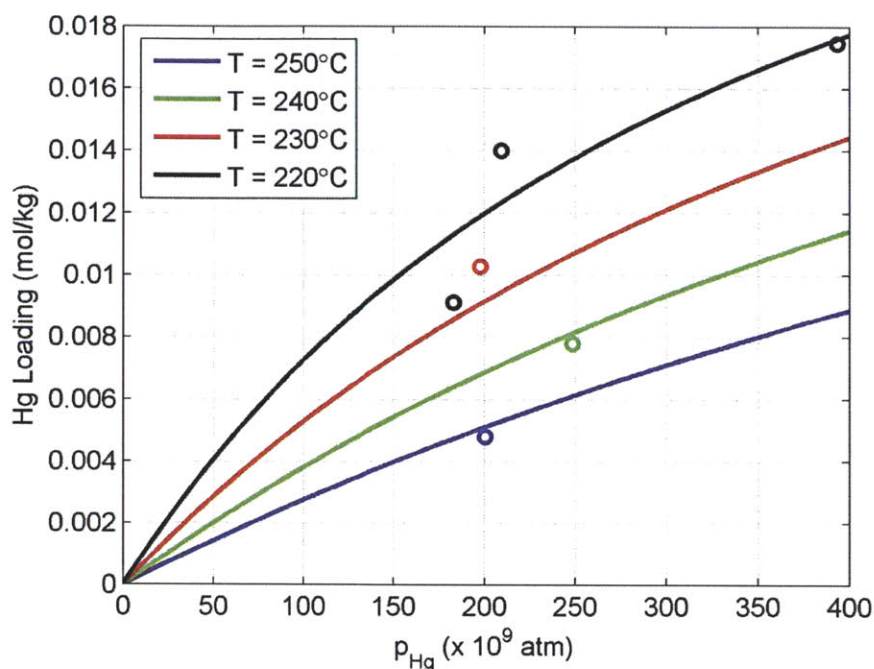


Figure 5.15 Fitted Langmuir isotherms for the data shown in Table 5.2. The solid lines refer to the model predictions and the colored circles refer to the experimental data at the temperatures corresponding to the colors of the model.

Qualitatively, the fit is not very strong, especially for the data at 220°C . However, based on this fit, the calculated enthalpy of adsorption was -80 kJ/mol . The DFT calculations in Chapter 4 predicted the enthalpy of reaction for the bulk species to be about -150 kJ/mol , so this value is considerably lower. Moreover, the predicted entropy of adsorption was approximately -40 J/mol-K —also considerably lower than the -140 J/mol-K estimated by the DFT calculations. However, the DFT calculations were intended to be merely an indicator of Hg-sorbent bond strength, and we would expect the enthalpy of adsorption to be lower than that of the formation of a bulk HgCr_2O_4 crystal, so the fact that these measured values are lower than those of the DFT calculations is expected.

Clearly, however, this method for estimating the enthalpy of adsorption had considerable sources of uncertainty, and as a result we decided to do a separate experiment in order to attempt to confirm our measurement. In this second experiment, we exposed approximately 10 mg of CrO_2 to 155 ppbv (nominal) Hg in 260 SCCM He/Ne at 250°C overnight in order to saturate the sorbent. We then increased the temperature of the column to other discrete temperature levels,

each time measuring the amount that desorbed using the MSD. A key advantage of this method was that because all data points were collected at the same inlet concentration, much of the uncertainty in the true value of this inlet concentration would cancel out as we calculated the enthalpy of adsorption. A disadvantage, however, was that the accuracy of this method hinged on the accuracy of the first data point, the measured capacity at 250°C. Because this data point was measured overnight while the sorbent became saturated, the accuracy of this data point was limited. To avoid this difficulty, we used the initial capacity of 0.0048 mol/kg at 250°C determined by the breakthrough curve fitting in Table 5.2. The results of this experiment are summarized in Table 5.3.

Table 5.3 Summary of desorption experiments based on initial saturation at 250°C.

Temperature (°C)	Change in Hg Loading (mol/kg)	Hg Loading (mol/kg)
250	--	0.0048
265	-0.0010	0.0038
280	-0.0011	0.0028
295	-0.0007	0.0020
310	-0.0005	0.0015
325	-0.0007	0.0008
335	-0.0003	0.0005

The results of fitting these 7 data points to the Langmuir model are shown in Figure 5.16.

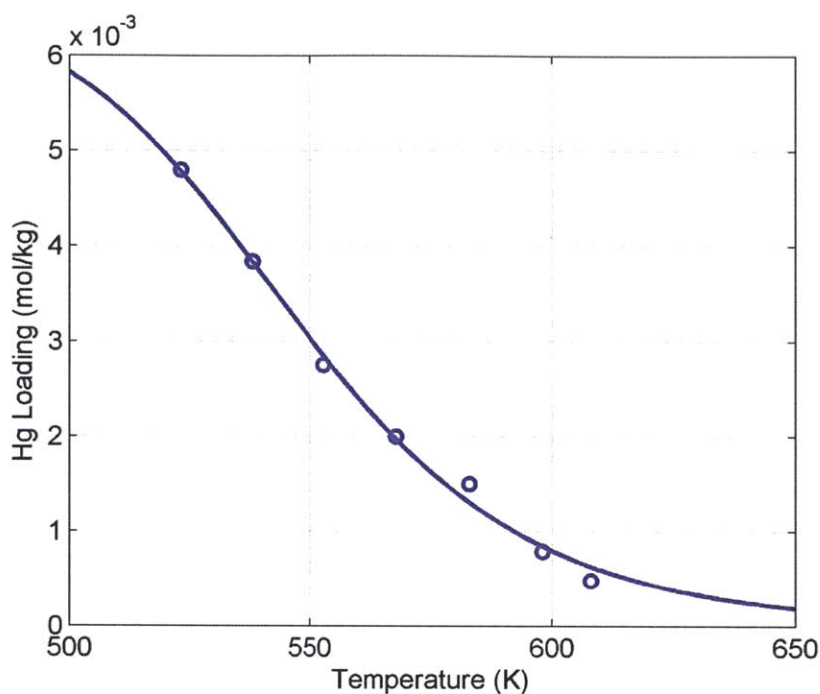


Figure 5.16 Fitted Langmuir isobar at $p_{Hg} = 2.1 \times 10^{-7}$ atm for the data shown in Table 5.3. The solid lines refer to the model predictions and the colored circles refer to the experimental data at the temperatures corresponding to the colors of the model.

The calculated enthalpy of adsorption based on this experiment is -100 kJ/mol. The entropy of adsorption was also correspondingly larger in magnitude, with a calculated value of approximately -60 J/mol-K. We caution, however, that these calculated thermodynamic parameters were very sensitive to the value of the initial saturation capacity. For example, if the saturation capacity were changed from 0.0048 mol/kg to 0.005 mol/kg (a change of roughly 4%), the calculated enthalpy of adsorption dropped to -90 kJ/mol (a change of roughly 10%). Based on these two experiments, our best estimate for the enthalpy of adsorption is -90 kJ/mol, although given the uncertainties in the individual data points and in the appropriateness of the Langmuir model, a confidence interval of at least ± 20 kJ/mol would be necessary.

5.6 Conclusions

In this chapter we detailed the construction of an adsorption apparatus to investigate candidate sorbent materials experimentally. Unfortunately, a significant amount of uncertainty existed in

our measurements due to the presence of signal drift in the MSD analyzer and in the uncertainty of the permeation rate of the Hg permeation tubes. Nevertheless, our experiments showed that K_2S_x has some affinity for Hg, but that affinity was minimal at the temperatures of interest for warm temperature Hg removal. This affinity could likely be increased with an increased surface area of the adsorbent, but because K_2S_x is both unstable in H_2O and toxic, we did not investigate that material further. BaO_2 showed no affinity for Hg in our experiments. This could have been due to its extremely low surface area (approximately $1.5 \text{ m}^2/\text{g}$), but based on synthesis strategies of $HgBaO_2$ found in the literature we anticipated that a large kinetic barrier may also have contributed to the lack of adsorption observed. CrO_2 did show affinity for Hg in our experiments. We calculated the capacity after 2 hours to be about $6 \times 10^{-3} \text{ mol/kg}$. This capacity was greatly reduced upon exposure of the sorbent to H_2 gas, which served as a confirmation of our DFT calculations. However, the sorbent was minimally affected by exposure to common flue gas components such as air or SO_2 .

Further investigations of CrO_2 indicated that regeneration in pure carrier gas at a temperature increase of 30°C did not fully regenerate the sorbent material. We were unable to conclusively determine whether the working capacity diminished in subsequent adsorption-desorption cycles, but if any decrease in capacity occurred, the decrease was likely small. Finally, we estimated the enthalpy of adsorption of Hg on CrO_2 using two different methods. Based on the results of these methods, we estimated the enthalpy of adsorption to be -90 kJ/mol , but we caution that a significant amount of uncertainty exists in this value.

Chapter 6. Recommendations for Future Work

6.1 Introduction

In this thesis we have demonstrated our work in the development of pressure swing adsorption models for CO₂ capture with metal oxides and hydroxides, the integration of those models into process simulations in Aspen Plus, the use of density functional theory to aid in the identification of novel materials for Hg capture, and the evaluation of the more promising materials experimentally. Throughout the course of this work we have identified many areas for further study. Here we present our recommendations for those areas we feel are the most promising.

6.2 Development of Carbon Dioxide Adsorption Model

6.2.1 Model Equations

In Chapter 2 we developed both adiabatic and isothermal models for CO₂ adsorption on metal oxides and metal hydroxides. In Chapter 3 we showed that isothermal operation tends to outperform adiabatic operation in terms its effect on the overall efficiency of the IGCC process, showing a reasonable upper bound on the potential efficiency gains. However, because true isothermal operation is difficult to achieve in an industrial-scale, fixed bed reactor, it could be worthwhile to add some form of heat transfer, perhaps of the form of Equation (2.15), in order to obtain a more realistic picture of the potential benefits of heat transfer. An alternative method to increase the heat transfer could be to redesign the adsorption column into less traditional designs, such as the transport reactor used by Eastman Chemical and RTI for their warm sulfur removal process[24]. The modification to the model equations and the MATLAB code would obviously be much more extensive in this case, however. Another interesting modification to the model equations would be to calculate the linear driving force rate constant (k_{LDF}), rather than choosing a suitably large value to approximate equilibrium conditions. Our sensitivity analysis showed that the effect of the rate constant can be small, but it may be useful to investigate the effect of

this rate constant at all parameter values, not just those investigated in the sensitivity study. Furthermore, although the main focus of our analyses in this thesis was on the process efficiency, the economics of any CO₂ capture process is also extremely important in determining the best technology going forward. A better understanding of the rate of adsorption and the corresponding PSA cycle times would be very beneficial in helping to estimate the capital costs and operating costs of each PSA process.

6.2.2 Modifications to PSA Cycle

A key difference between the metal oxide and metal hydroxide PSA models was the nature of the rinse step. In the metal oxide process, we used high-pressure steam as the purge gas during the rinse step, and in the metal hydroxide process, we used high-pressure CO₂ as the purge gas. At the project's outset, this seemed to be a logical choice. The use of CO₂ as a purge gas increases the amount of CO₂ that needs to be compressed for sequestration, since the purge CO₂ is compressed, recycled back to the PSA unit, produced at lower pressure, and compressed again. Because CO₂ adsorption on metal oxides is pressure-dependent, the regeneration is favored at lower pressures, thereby increasing this CO₂ compression effect. The use of steam in the rinse step does not result in a simple process, however. Because steam condenses at the inlet conditions of the rinse step, one is forced to either use high-temperature steam (removing more heat from the steam cycle of the IGCC plant) or multiple depressurization steps so that the pressure is lowered before the rinse step. Therefore, despite the potential disadvantages of using CO₂ as a rinse gas for the metal oxide case, the relative ease of its operation makes it worthwhile to simulate the metal oxide process using a CO₂ rinse to see if the simulations confirm our initial predictions of its efficiency penalties. In addition, further modifications to the PSA cycle, such as the addition of pressure equalization steps, could reduce the compression energy required for the PSA process and increase its overall efficiency.

6.3 Process Simulations of IGCC Systems Using CO₂ Adsorption Models

In Chapter 3 we computed the HHV efficiency of the IGCC-CCS plant using both metal oxide and metal hydroxide sorbents. In each case we used simple heat integration techniques that resulted in a plant where steam usage is far from optimized. However, previous researchers have shown that optimizing global variables like the water gas shift temperatures or the different steam temperatures in the steam power section can significantly increase the overall efficiency of the power plant[95], [162]. In fact, the potential gains in efficiency are as large as 2 percentage points HHV—larger than any potential gains we observed from simply using warm CO₂ capture. As a result, it would be very valuable to perform a more rigorous heat integration optimization to see the potential gains that would result. One particular example is shown in Figure 6.1.

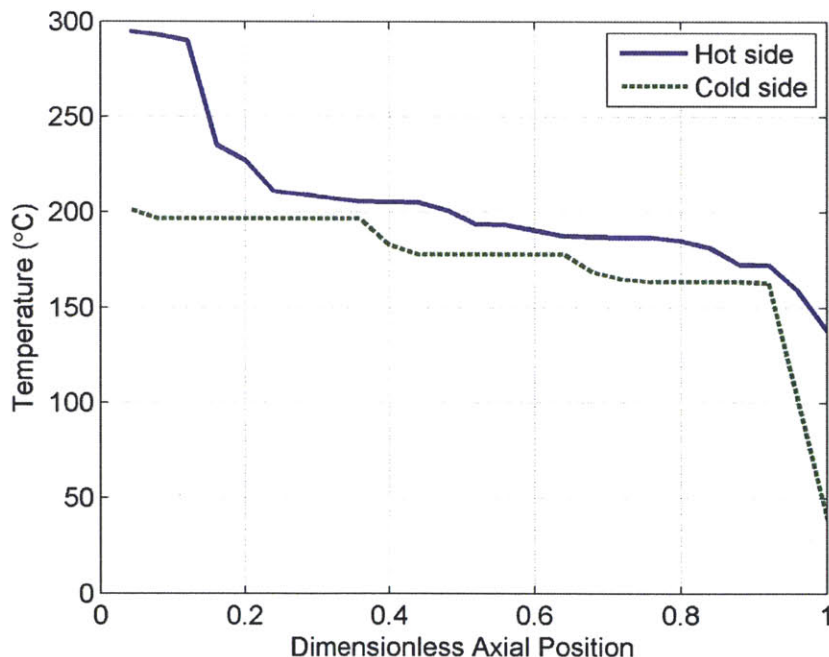


Figure 6.1 Heat exchanger profile for generation of sweep steam in metal hydroxide process simulation. In this example, $|\Delta H_{ads}| = 25$ kJ/mol and $p_{regen} = 23$ atm.

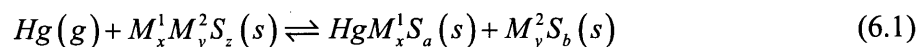
The above plot shows the generation of sweep steam for the metal hydroxide process simulation. The hot streams are primarily the H₂ and CO₂ product streams, and the cold side is liquid water that was boiled at 3 different pressures. The use of 3 different pressures helped to better match

the hot and cold side temperature profiles, but as Figure 6.1 shows, there are still regions with very large temperature differences. Improving the heat integration here could have a potentially large impact on the overall IGCC efficiency.

6.4 Computational Screening of Hg Adsorbents Using DFT

6.4.1 Expansion of Parameter Space

In Chapter 4 we used DFT to screen dozens of materials as candidates for Hg adsorption. An interesting way to expand this work would be to expand the material types considered in the calculations. One interesting example could be through mixed metal oxides or sulfides. A sample reaction could be the type shown in Equation (6.1), which is very similar to that of CO₂ reacting with Li₂ZrO₃ to form Li₂CO₃ and ZrO₂.



In the above equation, $z = a + b$ in order to preserve the stoichiometry. These reactions could show promise if the metal sulfide product adds stability to the Hg reaction and is not formed by the H₂ competing reaction.

The parameter space could also be expanded to look at Hg sorbents for flue gas capture in greater depth. One of the downsides of flue gas capture is that the Hg partial pressure is considerably lower, meaning that there is a smaller window of operating conditions in which the material could be regenerated. However, in many cases the Hg sorbent is disposable, meaning that regeneration is not a concern. In addition, many of the sorbent materials identified in Chapter 4 show strong enough affinity for Hg that they are predicted to bind Hg even at the lower partial pressures of a flue gas stream. Therefore, an interesting expansion of this project could be to look at typical flue gas species, such as HCl, H₂O, or SO₂, to see if any of them are competitive with Hg adsorption.

Finally, the parameter space could be expanded to investigate the capture of other metallic pollutants present in coal gas streams, such as Cd, Pb, or As. The discovery of materials for Hg capture is a key component in the development of warm syngas cleanup, but for the cleanup

technology to be effective, similar warm temperature methods need to be developed for all pollutant species.

6.4.2 Expansion of Calculation Methods

Several materials were identified in Chapter 4 that were predicted to capture Hg at elevated temperatures but react more strongly with H₂ or H₂O. However, the fact that a reaction is to occur thermodynamically does not mean that it is also favored kinetically. Therefore, it could be interesting to perform more detailed calculations such as transition state calculations for surface reactions, in order to determine whether a kinetic barrier to the competing H₂ or H₂O reactions is too high, allowing Hg adsorption to occur. Because these calculations are much more computationally intensive, they should be limited only to those materials identified by the screening method to be favorable to Hg adsorption.

6.5 Experimental Testing of Promising Sorbents for Hg Capture

6.5.1 Modifications to Apparatus

The experiments in Chapter 5 showed semi-quantitative evidence that CrO₂ can be an effective sorbent for elemental Hg capture, even at temperatures above 200°C. However, many of the reasons that the evidence was semi-quantitative, rather than fully quantitative, were caused by limitations in the experimental apparatus. First of all, as was described in Chapter 5, a significant amount of uncertainty existed in the Hg concentration because the Hg generation rate from the Hg permeation tubes was not well-known. Therefore, a key improvement to the experimental apparatus would be to have some sort of independent method of determining the absolute partial pressure of Hg. One possible technique could be to install a second Hg analyzer such as the Ontario Hydro method (described in greater detail in Chapter 5). The Hg permeation tube would heat up and reach steady-state, and then flow would be directed to the Ontario Hydro impingers for a set amount of time. After the solutions were analyzed, one could calculate the absolute amount of Hg absorbed and back-calculate the Hg flow rate. This example technique is cumbersome, and additional error would be introduced via the Ontario Hydro analysis method. Furthermore, additional safety concerns would be present due to the presence of aqueous Hg.

In Chapter 5 we also indicated that despite the presence of heating tape, Hg still likely adsorbed on the sides of the tubing that connected the apparatus together. One possible modification to the apparatus, therefore, would be to put as much of the apparatus as possible in a constant temperature oven, such as a GC oven. With this modification, the tubing and the adsorption column would all be at the same temperature, further decreasing the amount of Hg adsorbed on the tubing. As an added benefit, eliminating the heating tape would remove a potential electric safety risk of the heating tape shorting out due to age or to the interference from foreign bodies.

The MSD is an effective Hg analyzer, but the Hg signal tends to drift over the course of long experiments. Therefore, if we could incorporate an offline method to analyze the saturated sorbent, such as digesting the sorbent and analyzing it using ICP-AES or CVAAS, we would likely increase the reliability of our thermodynamic measurements.

Finally, as we mentioned in Chapter 5, H₂O is a common component of both syngas and flue gas, and as a result it would be beneficial to test candidate materials that had been exposed to H₂O vapor. Therefore, installing some type of H₂O bubbler to saturate the carrier gas could allow us to learn more about the efficacy of various materials. The MSD is not equipped to handle large amounts of H₂O, however, since H₂O is known to adsorb on the surfaces in the chamber. Therefore, an additional H₂O removal unit, such as a membrane, would need to be installed immediately upstream of the MSD to remove the H₂O in order to preserve the instrument's lifetime.

6.5.2 Additional Experiments

With the modifications to the apparatus described in the previous section, a greater number of experiments would be possible. For example, it would be interesting to first determine the thermodynamic parameters, and then perform several breakthrough experiments while varying temperature and inlet concentration in an effort to determine the time-dependent parameters of adsorption (either the mass transfer coefficient or the kinetics). It could also be worthwhile to perform breakthrough experiments in a simulated syngas or flue gas which Hg, H₂, and H₂O (or H₂S) are introduced to the sorbent material simultaneously. The presence of H₂O or H₂S could serve to inhibit the H₂ reduction reaction via Le Chatelier's Principle, and performing breakthrough experiments in this manner would allow us to quantify that effect.

In addition, all of the experiments performed in this thesis were performed on powdered sorbents with measured BET surface areas no larger than 40 m²/g. It would therefore be interesting to investigate dispersing these materials on some sort of porous support to increase the surface areas by at least an order of magnitude and see how the capacities are affected. It could also be worthwhile to investigate incorporating these materials into more sophisticated architectures, such as carbon nanotubes or fullerenes. Some of these methods have been shown to alter the thermodynamics of the supported substrate[163], [164], and as a result the competing H₂ or H₂O reactions may be inhibited in this manner.

Finally, the use of a different experimental technique, such as zero length column desorption experiments, could be used as a separate method to verify the equilibrium and kinetic parameters determined using the breakthrough curves. Therefore, due to the unreliability associated with Hg measurements, it would be worthwhile to include these types of measurements in order to provide more confidence in the calculated results.

Bibliography

- [1] H. Schulz, "Short History and Present Trends of Fischer-Tropsch Synthesis," *Applied Catalysis A: General*, vol. 186, pp. 3-12, 1999.
- [2] P. J. A. Tijm, F. J. Waller, and D. M. Brown, "Methanol Technology Developments for the New Millenium," *Applied Catalysis A: General*, vol. 221, no. 1-2, pp. 275-282, 2001.
- [3] *State Clean Energy Technical Forum: Integrated Gasification Combined Cycle (IGCC) Background and Technical Issues*. US Environmental Protection Agency, 2006.
- [4] O. Maurstad, "An Overview of Coal based Integrated Gasification Combined Cycle (IGCC) Technology," Massachusetts Institute of Technology, Laboratory for Energy and the Environment, Cambridge, MA, 2005.
- [5] J. A. Ratafia-Brown, L. M. Manfredo, J. W. Hoffman, and M. Ramezan, *Major Environmental Aspects of Gasification-Based Power Generation Technologies: Final Report*. US Department of Energy, 2002.
- [6] G. S. Samuelsen and A. D. Rao, "System Analyses of Advanced Brayton Cycles for High Efficiency Zero Emission Plants," University of California--Irvine, Irvine, CA, 2006.
- [7] J. Katzer et al., *The Future of Coal*. Massachusetts Institute of Technology, 2007.
- [8] *International Energy Outlook*. Energy Information Administration, DOE/EIA-0484, 2010.
- [9] *Cost and Performance Baseline for Fossil Energy Plants: Bituminous Coal and Natural Gas to Electricity Final Report*. U. S. Department of Energy, Office of Fossil Energy, NETL, DOE/NETL-2007/1397, 2010.
- [10] *Environmental Footprints and Costs of Coal-Based Integrated Gasification Combined Cycle and Pulverized Coal Technologies*. US Environmental Protection Agency, 2006.
- [11] "U.S. Environmental Protection Agency: National Ambient Air Quality Standards (NAAQS)," 2011. [Online]. Available: www.epa.gov/air/criteria.html. [Accessed: Sep-2011].
- [12] P. Tans and R. Keeling, "Trends in Atmospheric Carbon Dioxide," *NOAA Earth System Research Laboratory*, 2011. [Online]. Available: <http://www.esrl.noaa.gov/gmd/ccgg/trends/>. [Accessed: Sep-2011].
- [13] B. Metz, O. R. Davidson, P. R. Bosch, R. Dave, and L. A. Meyer, Eds., "IPCC, 2007: Summary for Policymakers," in *Climate Change 2007: Mitigation. Contribution of Working Group III to the Fourth Assessment Report of the Intergovernmental Panel on Climate Change*, Cambridge, UK and New York, USA: Cambridge University Press, 2007.
- [14] "Clean Air Mercury Rule," 2005. [Online]. Available: <http://www.epa.gov/air/mercuryrule/basic.htm>.
- [15] "U.S. Environmental Protection Agency: Mercury," 2011. [Online]. Available: <http://www.epa.gov/mercury>. [Accessed: May-2011].
- [16] T. W. Clarkson and L. Magos, "The Toxicology of Mercury and Its Chemical Compounds," *Critical Reviews in Toxicology*, vol. 36, pp. 609-662, 2006.
- [17] "Materials Safety Data Sheet: Mercury." Bethlehem Apparatus Company, Inc.
- [18] D. C. Bebout, "Mercury: Inorganic and Coordination Chemistry," *Encyclopedia of Inorganic Chemistry*. pp. 1-15, 2006.
- [19] M. G. Klett, R. C. Maxwell, and M. D. Rutkowski, "The Cost of Mercury Removal in an IGCC Plant." US Department of Energy, 2002.

- [20] E. Shuster, "Tracking New Coal-Fired Power Plants." Office of Strategic Energy Analysis & Planning, NETL, 2011.
- [21] U. Koss and H. Schlichting, "Lurgi's MPG Gasification Plus Rectisol Gas Purification--Advanced Process Combination for Reliable Syngas Production," in *Gasification Technologies Conference*, 2005.
- [22] B. Trapp, N. Moock, and D. Denton, "Coal Gasification: Ready for Prime Time," *Power*, 2004.
- [23] "Metal Prices," 2011. [Online]. Available: <http://www.metalprices.com>. [Accessed: Sep-2011].
- [24] J. Schlather and B. Turk, "Comparison of a New Warm-Gas Desulfurization Process versus Traditional Scrubbers for a Commercial IGCC Power Plant," in *Gasification Technologies Conference*, 2007.
- [25] R. P. Gupta, B. S. Turk, J. W. Portzer, and D. C. Cicero, "Desulfurization of Syngas in a Transport Reactor," *Environmental Progress*, vol. 20, no. 3, pp. 187-195, 2001.
- [26] T. L. Ward and T. Dao, "Model of Hydrogen Permeation Behavior in Palladium Membranes," *Journal of Membrane Science*, vol. 153, no. 2, pp. 211-231, 1999.
- [27] S. E. Nam, S. H. Lee, and K. H. Lee, "Preparation of a Palladium Alloy Composite Membrane Supported in a Porous Stainless Steel by Vacuum Electrodeposition," *Journal of Membrane Science*, vol. 153, no. 2, pp. 163-173, 1999.
- [28] D. J. Edlund, "Hydrogen-Permeable Metal Membrane and Method for Producing the Same," U.S. Patent 6152995, 2000.
- [29] A. Li, W. Liang, and R. Hughes, "The Effect of Carbon Monoxide and Steam on the Hydrogen Permeability of a Pd/Stainless Steel Membrane," *Journal of Membrane Science*, vol. 165, no. 1, pp. 135-141, 2000.
- [30] T. A. Peters, M. Stange, H. Klette, and R. Bredeesen, "High Pressure Performance of Thin Pd--23% Ag/Stainless Steel Composite Membranes in Water Gas Shift Gas Mixtures; Influence of Dilution, Mass Transfer and Surface Effects on the Hydrogen Flux," *Journal of Membrane Science*, vol. 316, no. 1-2, pp. 119-127, 2008.
- [31] B. D. Morreale, M. V. Ciocco, B. H. Howard, R. P. Killmeyer, A. V. Cugini, and R. M. Enick, "Effect of Hydrogen-Sulfide on the Hydrogen Permeance of Palladium--Copper Alloys at Elevated Temperatures," *Journal of Membrane Science*, vol. 241, no. 2, pp. 219-224, 2004.
- [32] D. Jack, D. Anderson, C. Evenson, M. Mundschau, and R. Mackay, "CO₂ Capture Using Dense Hydrogen Transport Membranes," in *6th Annual Conference on Carbon Capture and Sequestration*, 2007.
- [33] M. Dolan, R. Donelson, and N. Dave, "Performance and Economics of a Pd-based Planar WGS Membrane Reactor for Coal Gasification," *International Journal of Hydrogen Energy*, vol. 35, pp. 10994-11003, 2010.
- [34] P. Chiesa, T. G. Kreutz, and G. G. Lozza, "CO₂ Sequestration From IGCC Power Plants by Means of Metallic Membranes," *Journal of Engineering for Gas Turbines and Power*, vol. 129, pp. 123-134, 2007.
- [35] J. D. Figueroa, T. Fout, S. Plasynski, H. McIlvried, and R. D. Srivastava, "Advances in CO₂ Capture Technology - The U.S. Department of Energy's Carbon Sequestration Program," *International Journal of Greenhouse Gas Control*, vol. 2, no. 1, pp. 9-20, 2008.
- [36] W. Koros, "Gas Separation Membranes: Needs for Combined Materials Science and Processing Approaches," in *Macromolecular Symposia*, 2002, vol. 188, no. 1.

- [37] I. Taniguchi, S. Duan, S. Kazama, and Y. Fujioka, "Facile Fabrication of a Novel High Performance CO₂ Separation Membrane: Immobilization of Poly (Amidoamine) Dendrimers in Poly (Ethylene Glycol) Networks," *Journal of Membrane Science*, vol. 322, no. 2, pp. 277-280, 2008.
- [38] J. Zou and W. S. W. Ho, "CO₂-Selective Polymeric Membranes Containing Amines in Crosslinked Poly(Vinyl Alcohol)," *Journal of Membrane Science*, vol. 286, pp. 310-321, 2006.
- [39] R. Bredeesen, K. Jordal, and O. Bolland, "High-Temperature Membranes in Power Generation with CO₂ Capture," *Chemical Engineering & Processing*, vol. 43, no. 9, pp. 1129-1158, 2004.
- [40] R. Yang, *Gas Separation by Adsorption Processes*. London: Imperial College Press, 1997.
- [41] C. Gauer and W. Heschel, "Doped Lithium Orthosilicate for Adsorption of Carbon Dioxide," *Journal of Materials Science*, vol. 41, pp. 2405-2409, 2006.
- [42] C. S. Martavaltzi and A. A. Lemonidou, "Development of New CaO-Based Sorbent Materials for CO₂ Removal at High Temperature," *Microporous and Mesoporous Materials*, vol. 110, pp. 119-127, 2008.
- [43] H. T. J. Reijers, S. E. A. Valster-Schier-Meier, P. D. Cobden, and R. W. van den Brink, "Hydrotalcite as CO₂ Sorbent for Sorption-Enhanced Steam Reforming of Methane," *Industrial & Engineering Chemistry Research*, vol. 45, pp. 2522-2530, 2006.
- [44] Z. Yong, V. Mata, and A. E. Rodrigues, "Adsorption of Carbon Dioxide at High Temperature--a Review," *Separation and Purification Technology*, vol. 26, pp. 195-205, 2002.
- [45] R. V. Siriwardane, C. Robinson, M. Shen, and T. Simonyi, "Novel Regenerable Sodium-Based Sorbents for CO₂ Capture at Warm Gas Temperatures," *Energy & Fuels*, vol. 21, no. 4, pp. 2088-2097, Jul. 2007.
- [46] R. V. Siriwardane and R. W. Stevens, "Novel Regenerable Magnesium Hydroxide Sorbents for CO₂ Capture at Warm Gas Temperatures," *Industrial & Engineering Chemistry Research*, vol. 48, no. 4, pp. 2135-2141, Feb. 2009.
- [47] E. J. Granite, C. R. Myers, W. P. King, D. C. Stanko, and H. W. Pennline, "Sorbents for Mercury Capture from Fuel Gas with Application to Gasification Systems," *Industrial & Engineering Chemistry Research*, vol. 45, pp. 4844-4848, 2006.
- [48] S. Poulston et al., "Metal Sorbents for High Temperature Mercury Capture from Fuel Gas," *Fuel*, vol. 86, pp. 2201-2203, 2007.
- [49] E. J. Granite and T. O'Brien, "Review of Novel Methods for Carbon Dioxide Separation From Flue and Fuel Gases," *Fuel Processing Technology*, vol. 86, pp. 1423-1434, 2005.
- [50] G. Alptekin, J. Lind, R. Amalfitano, and R. Copeland, "Sorbents for Mercury Removal from Coal-Derived Synthesis Gas," in *29th International Technical Conference on Coal Utilization and Fuel Systems*, 2004.
- [51] J. W. Portzer, J. R. Albritton, C. C. Allen, and R. P. Gupta, "Development of Novel Sorbents for Mercury Control at Elevated Temperatures in Coal-Derived Syngas: Results of Initial Screening of Candidate Materials," *Fuel Processing Technology*, vol. 85, pp. 621-630, 2004.
- [52] R. Gupta, B. Turk, M. Lesemann, J. Schlather, and D. Denton, "Status of RTI/Eastman Warm Gas Clean-up Technology and Commercialization Plans," in *Gasification Technologies Conference*, 2008.

- [53] "High Temperature Syngas Cleanup Technology Scale-Up and Demonstration Project," *NETL: Gasification--Gas Separation*, 2011. [Online]. Available: <http://www.netl.doe.gov/technologies/coalpower/gasification/projects/gas-clean/00489.html>. [Accessed: Oct-2011].
- [54] J. J. P. Biermann, B. Higgins, J. O. L. Wendt, C. L. Senior, and D. Wang, "Mercury Reduction in a Coal Fired Power Plant at Over 2000°F using MinPlus Sorbent through Furnace Sorbent Injection," in *Electric Utilities Environmental Conference*, 2006.
- [55] T. Wajima et al., "Material Conversion from Paper-Sludge Ash in NaOH, KOH, and LiOH Solutions," *American Mineralogist*, vol. 92, pp. 1105-1111, 2007.
- [56] E. J. Granite, H. W. Pennline, and R. A. Hargis, "Novel Sorbents for Mercury Removal from Flue Gas," *Industrial & Engineering Chemistry Research*, vol. 39, pp. 1020-1029, 2000.
- [57] A. M. Ribeiro, C. A. Grande, F. V. S. Lopes, J. M. Loureiro, and A. E. Rodrigues, "A Parametric Study of Layered Bed PSA for Hydrogen Purification," *Chemical Engineering Science*, vol. 63, pp. 5258-5273, 2008.
- [58] M. W. Biddulph, "Multicomponent Distillation Simulation -- Distillation of Air," *AIChE Journal*, vol. 21, no. 2, pp. 327-335, 1975.
- [59] M. Amelio, P. Morrone, F. Gallucci, and A. Basile, "Integrated Gasification Gas Combined Cycle Plant with Membrane Reactors: Technological and Economical Analysis," *Energy Conversion and Management*, vol. 48, no. 10, pp. 2680-2693, 2007.
- [60] D. Grainger and M. B. Hägg, "Techno-Economic Evaluation of a PVAm CO₂-Selective Membrane in an IGCC Power Plant with CO₂ Capture," *Fuel*, vol. 87, no. 1, pp. 14-24, 2008.
- [61] S. Ito and H. Makino, "Carbon Dioxide Separation from Coal Gas by Physical Adsorption at Warm Temperature," in *Greenhouse Gas Control Technologies Conference, Interlaken, Switzerland*, 1998.
- [62] M. Vasiliu, K. Guynn, and D. A. Dixon, "Prediction of the Thermodynamic Properties of Key Products and Intermediates from Biomass," *The Journal of Physical Chemistry C*, pp. 15686-15702, 2011.
- [63] E. M. Mindrup and W. F. Schneider, "Computational Comparison of the Reactions of Substituted Amines with CO₂," *ChemSusChem*, vol. 3, no. 8, pp. 931-8, Aug. 2010.
- [64] A. Jain et al., "A High-Throughput Infrastructure for Density Functional Theory Calculations," *Computational Materials Science*, vol. 50, no. 8, pp. 2295-2310, Jun. 2011.
- [65] R. Armiento, B. Kozinsky, M. Fornari, and G. Ceder, "Screening for High-Performance Piezoelectrics Using High-Throughput Density Functional Theory," *Physical Review B*, vol. 84, no. 1, pp. 1-13, Jul. 2011.
- [66] K. C. Kim, A. D. Kulkarni, J. K. Johnson, and D. S. Sholl, "Large-Scale Screening of Metal Hydrides for Hydrogen Storage from First-Principles Calculations Based on Equilibrium Reaction Thermodynamics," *Physical Chemistry Chemical Physics: PCCP*, vol. 13, no. 15, pp. 7218-29, Apr. 2011.
- [67] E. Ochoa-Fernández, H. Rusten, H. Jakobsen, M. Rønning, A. Holmen, and D. Chen, "Sorption Enhanced Hydrogen Production by Steam Methane Reforming Using Li₂ZrO₃ as Sorbent: Sorption Kinetics and Reactor Simulation," *Catalysis Today*, vol. 106, no. 1-4, pp. 41-46, Oct. 2005.
- [68] J. R. Hufton, R. J. Allam, R. Chiang, P. Middleton, E. L. Weist, and V. White, "Development of a Process for CO₂ Capture from Gas Turbines Using a Sorption

- Enhanced Water Gas Shift Reactor System,” in *7th International Conference on Greenhouse Gas Control Technologies*, 2005.
- [69] J. D. Seader and E. J. Henley, *Separation Process Principles*. Hoboken: John Wiley and Sons, 1998, pp. 778-871.
- [70] D. Ruthven, *Pressure Swing Adsorption*. New York: VCH Publishers, Inc., 1994.
- [71] *Current and Future Technologies for Gasification-Based Power Generation, Volume 2: A Pathway Study Focused on Carbon Capture Advanced Power Systems R&D Using Bituminous Coal*. U. S. Department of Energy, Office of Fossil Energy, NETL, DOE/NETL-2009/1389, 2009.
- [72] D. Ruthven, *Principles of Adsorption and Adsorption Processes*. New York: John Wiley and Sons, 1984.
- [73] M. Suzuki, *Adsorption Engineering*. New York: Elsevier, 1990, pp. 125-186.
- [74] H. Du, A. D. Ebner, and J. A. Ritter, “Pressure Dependence of the Nonequilibrium Kinetic Model That Describes the Adsorption and Desorption Behavior of CO₂ in K-Promoted Hydrotalcite Like Compound,” *Industrial & Engineering Chemistry Research*, pp. 412-418, 2011.
- [75] E. Glueckauf, “Theory of Chromatography: Part 10--Formulae for Diffusion into Spheres and Their Application to Chromatography,” *Transactions of the Faraday Society*, vol. 51, pp. 1540-1551, 1955.
- [76] S. Sircar and J. Hufton, “Why Does the Linear Driving Force Model for Adsorption Kinetics Work?,” *Adsorption*, vol. 6, pp. 137-147, 2000.
- [77] A. Gorbach, M. Stegmaier, and G. Eigenberger, “Measurement and Modeling of Water Vapor Adsorption on Zeolite 4A--Equilibria and Kinetics,” *Adsorption*, vol. 10, pp. 29-46, 2004.
- [78] D. Lide, “CRC Handbook of Chemistry and Physics.” CRC Press/Taylor and Francis, Boca Raton, FL, 2009.
- [79] “NIST Chemistry Webbook,” *National Institute of Standards and Technology*, 2011. [Online]. Available: <http://webbook.nist.gov>.
- [80] R. Zhang and J. A. Ritter, “New Approximate Model for Nonlinear Adsorption and Diffusion in a Single Particle,” *Chemical Engineering Science*, vol. 52, no. 18, pp. 3161-3172, 1997.
- [81] M. Simo, C. J. Brown, and V. Hlavacek, “Simulation of Pressure Swing Adsorption in Fuel Ethanol Production Process,” *Computers and Chemical Engineering*, vol. 32, pp. 1635-1649, 2008.
- [82] S. Ergun, “Fluid Flow Through Packed Columns,” *Chemical Engineering Progress*, vol. 48, pp. 89-94, 1952.
- [83] R. B. Bird, W. E. Stewart, and E. N. Lightfoot, *Transport Phenomena*, 2nd ed. New York: John Wiley and Sons, 2002.
- [84] A. E. Rodrigues, C. Costa, R. Ferreira, J. Loureiro, and S. Azevedo, “Design Aspects of Catalytic Reactors and Adsorbers,” in *NATO Advanced Study Institute on Zeolites: Science and Technology*, F. R. Ribeiro, A. E. Rodrigues, L. D. Rollman, and C. Naccache, Eds. Alcabideche, Portugal: Martinus Nijhoff Publishers, 1983, pp. 423-489.
- [85] S. Patankar and D. Spalding, “A Calculation Procedure for Heat, Mass and Momentum Transfer in Three-Dimensional Parabolic Flows,” *Journal of Heat and Mass Transfer*, vol. 1, pp. 1787-1806, 1972.

- [86] S. V. Patankar, "A Calculation Procedure for Two-Dimensional Elliptic Situations," *Numerical Heat Transfer, Part A: Applications*, vol. 4, no. 4, pp. 409-425, Oct. 1981.
- [87] M. S. A. Baksh and C. E. Terbot, "Pressure Swing Adsorption Process for the Production of Hydrogen," U.S. Patent 6503299, 2003.
- [88] A. Wright, V. White, J. Hufton, E. V. Selow, and P. Hinderink, "Reduction in the Cost of Pre-combustion CO₂ Capture through Advancements in Sorption-Enhanced Water-Gas-Shift," *Energy Procedia*, vol. 1, no. 1, pp. 707-714, Feb. 2009.
- [89] B. E. Poling, G. H. Thomson, D. G. Friend, R. L. Rowley, and W. V. Wilding, "Physical and Chemical Data," in *Perry's Chemical Engineers' Handbook*, 8th ed., D. W. Green, Ed. New York: McGraw Hill, 2008.
- [90] R. T. Jacobsen, S. G. Penoncello, and E. W. Lemmon, *Thermodynamic Properties of Cryogenic Fluids*. New York: Plenum Press, 1997.
- [91] J. B. Kitto and S. C. Stultz, Eds., "Thermodynamics of Steam," in *Steam: its Generation and Use*, 41st ed., Babcock and Wilcox Company, 2005, pp. 2-1 through 2-27.
- [92] J. W. Tester and M. Modell, *Thermodynamics and Its Applications*, 3rd ed. Upper Saddle River: Prentice Hall PTR, 1997.
- [93] U. Das and W. H. Green, "Computational Screening of CO₂ Sorbents," *In preparation*.
- [94] R. P. Field and R. Brasington, "Baseline Flowsheet Model for IGCC with Carbon Capture," *Industrial & Engineering Chemistry Research*, vol. 50, pp. 11306-11312, 2011.
- [95] D. Bhattacharyya, R. Turton, and S. E. Zitney, "Steady-State Simulation and Optimization of an Integrated Gasification Combined Cycle Power Plant with CO₂ Capture," *Industrial & Engineering Chemistry Research*, vol. 50, pp. 1674-1690, 2011.
- [96] D. Brdar and R. Jones, *GE IGCC Technology and Experience with Advanced Gas Turbines*. GE Power Systems, GER-4207, 2000.
- [97] J. Portzer, B. Turk, and S. Gangwal, *Durability Testing of the Direct Sulfur Recovery Process*. Research Triangle Institute, 1996.
- [98] W. DePriest and R. Gaikwad, *Economics of Lime and Limestone for Control of Sulfur Dioxide*. Sargent and Lundy, LLC, 2003.
- [99] B. Padak, M. Brunetti, A. Lewis, and J. Wilcox, "Mercury Binding on Activated Carbon," *Environmental Progress*, vol. 25, no. 4, pp. 319-326, 2006.
- [100] A. D. Becke, "A New Mixing of Hartree-Fock and Local Density Functional Theories," *Journal of Chemical Physics*, vol. 98, p. 1372, 1993.
- [101] C. Lee, W. Yang, and R. G. Parr, "Development of the Colle-Salvetti Correlation-Energy Formula into a Functional of the Electron Density," *Physical Review B*, vol. 37, p. 785-789, 1988.
- [102] P. J. Stephens, F. J. Devlin, C. F. Chabalowski, and M. K. Frisch, "Ab Initio Calculation of Vibrational Absorption and Circular Dichroism Spectra Using Density Functional Force Fields," *Journal of Physical Chemistry*, vol. 98, p. 11623-11627, 1994.
- [103] X. Sun, J.-Y. Hwang, and S. Xie, "Density Functional Study of Elemental Mercury Adsorption on Surfactants," *Fuel*, vol. 90, no. 3, pp. 1061-1068, Mar. 2011.
- [104] E. Sasmaz and J. Wilcox, "Mercury Species and SO₂ Adsorption on CaO(100)," *Journal of Physical Chemistry C*, vol. 112, no. 42, pp. 16484-16490, Oct. 2008.
- [105] B. G. Kim, X. Li, and P. Blowers, "Adsorption Energies of Mercury-Containing Species on CaO and Temperature Effects on Equilibrium Constants Predicted by Density Functional Theory Calculations," *Langmuir*, vol. 25, no. 5, pp. 2781-9, Mar. 2009.

- [106] P. Blowers and B. G. Kim, "The Adsorption of Mercury-Species on Relaxed and Rumbled CaO (0 0 1) Surfaces Investigated by Density Functional Theory," *Journal of Molecular Modeling*, vol. 17, no. 3, pp. 505–514, 2011.
- [107] J. Perdew and Y. Wang, "Accurate and Simple Analytic Representation of the Electron-Gas Correlation Energy," *Physical Review B*, vol. 45, no. 23, pp. 244-249, 1992.
- [108] J. Steckel, "Density Functional Theory Study of Mercury Adsorption on Metal Surfaces," *Physical Review B*, vol. 77, no. 11, pp. 1-13, Mar. 2008.
- [109] G. Kresse and J. Furthmueller, "Efficiency of Ab Initio Total Energy Calculations for Metals and Semiconductors Using a Plane-Wave Basis Set," *Computational Materials Science*, vol. 6, p. 15, 1996.
- [110] J. P. Perdew, K. Burke, and M. Ernzerhof, "Generalized Gradient Approximation Made Simple," *Physical Review Letters*, vol. 77, no. 8, pp. 3865-3868, 1996.
- [111] A. Jain, S.-A. Seyed-Reihani, C. C. Fischer, D. J. Couling, G. Ceder, and W. H. Green, "Ab Initio Screening of Metal Sorbents for Elemental Mercury Capture in Syngas Streams," *Chemical Engineering Science*, vol. 65, no. 10, pp. 3025-3033, May 2010.
- [112] "ICSD: Inorganic Crystal Structure Database, FIZ Karlsruhe." FIZ Karlsruhe.
- [113] G. Bergerhoff, "The Inorganic Crystal-Structure Data-Base," *Journal of Chemical Information and Computer Sciences*, vol. 23, no. 2, pp. 66-69, 1983.
- [114] W. Bakker, "Materials Guidelines for Gasification Plants," *Topical report TR-110507, EPRI, Palo Alto, CA*, no. 1998, 1998.
- [115] D. Sholl and J. A. Steckel, *Density Functional Theory: A Practical Introduction*. New York: John Wiley and Sons, 2009, p. 180.
- [116] G. Kresse and D. Joubert, "From ultrasoft pseudopotentials to the projector augmented-wave method," *Physical Review B*, vol. 59, p. 1758, 1999.
- [117] P. E. Blöchl, "Projector Augmented-Wave Method," *Physical Review B*, vol. 50, no. 24, pp. 17953-17979, 1994.
- [118] G. Kresse, M. Marsman, and J. Furthmueller, "VASP the Guide." 2011.
- [119] A. Vandewalle, M. Asta, and G. Ceder, "The Alloy Theoretic Automated Toolkit: A User Guide," *Calphad*, vol. 26, no. 4, pp. 539-553, Dec. 2002.
- [120] L. Wang, T. Maxisch, and G. Ceder, "Oxidation Energies of Transition Metal Oxides Within the GGA+U Framework," *Physical Review B*, vol. 73, no. 19, p. 195107, 2006.
- [121] S. L. Dudarev, G. A. Botton, S. Y. Savrasov, C. J. Humphreys, and A. P. Sutton, "Electron-Energy-Loss Spectra and the Structural Stability of Nickel Oxide: An LSDA+U Study," *Physical Review B*, vol. 57, no. 3, pp. 1505-1509, 1998.
- [122] O. Kubaschewski, C. B. Alcock, and P. J. Spencer, "Thermochemical Data," in *Materials Thermochemistry*, Pergamon Press, 1993, pp. 257-322.
- [123] R. Coquet and D. J. Willock, "The (010) Surface of alpha-MoO₃, a DFT + U Study.," *Physical Chemistry Chemical Physics : PCCP*, vol. 7, no. 22, pp. 3819-28, Nov. 2005.
- [124] D. Mikhailova, V. A. Alyoshin, E. V. Antipov, and J. Karpinski, "Thermogravimetric Study of MHgO₂ (M=Ca, Sr, Ba) under Controlled Oxygen and Mercury Partial Pressures and Related Thermodynamics," *Journal of Solid State Chemistry*, vol. 146, no. 1, pp. 151-156, Aug. 1999.
- [125] D. Tudela, "Silver(II) Oxide or Silver(I,III) Oxide?," *Journal of Chemical Education*, vol. 85, no. 6, p. 863, Jun. 2008.
- [126] J. Heyd, G. E. Scuseria, and M. Ernzerhof, "Hybrid Functionals Based on a Screened Coulomb Potential," *The Journal of Chemical Physics*, vol. 118, no. 18, p. 8207, 2003.

- [127] J. Heyd and G. E. Scuseria, "Efficient Hybrid Density Functional Calculations in Solids: Assessment of the Heyd-Scuseria-Ernzerhof Screened Coulomb Hybrid Functional," *The Journal of Chemical Physics*, vol. 121, no. 3, pp. 1187-92, Jul. 2004.
- [128] J. Da Silva, M. Ganduglia-Pirovano, J. Sauer, V. Bayer, and G. Kresse, "Hybrid Functionals Applied to Rare-Earth Oxides: The Example of Ceria," *Physical Review B*, vol. 75, no. 4, pp. 19-24, Jan. 2007.
- [129] M. Binnewies and E. Milke, *Thermochemical Data of Elements and Compounds*. New York: WILEY-VCH Verlag Weinheim, 2002.
- [130] L. Liu, C. Li, F. Wang, Z. Du, and W. Zhang, "Thermodynamic Assessment of the Eu-Sn System," *Journal of Alloys and Compounds*, vol. 379, no. 1-2, pp. 148-153, Oct. 2004.
- [131] J. Sangster and A. D. Pelton, "The As-K (Arsenic-Potassium) System," *Journal of Phase Equilibria*, vol. 14, no. 2, pp. 234-237, 1993.
- [132] G. F. Voronin, N. T. Shiu, N. M. Mukhamedzhanova, and Y. I. Gerasimov, "Thermodynamic Properties of Potassium-Antimony Compounds," *Russian Journal of Physical Chemistry*, vol. 41, no. 11, pp. 1604-1606, 1967.
- [133] S. Meschel and O. Kleppa, "Thermochemistry of Some Binary Alloys of Noble Metals (Cu, Ag, Au) and Transition Metals by High Temperature Direct Synthesis Calorimetry," *Journal of Alloys and Compounds*, vol. 350, no. 1-2, pp. 205-212, 2003.
- [134] G. Ghosh, "First-Principles Calculations of Structural Energetics of Cu-TM (TM=Ti, Zr, Hf) Intermetallics," *Acta Materialia*, vol. 55, no. 10, pp. 3347-3374, Jun. 2007.
- [135] B. Predel, "Ca-Pb (Calcium-Lead)," in *Landolt-Börnstein - Group IV Physical Chemistry: Numerical Data and Functional Relationships in Science and Technology*, O. Madelung, Ed. .
- [136] Q. Guo and O. J. Kleppa, "Standard Enthalpies of Formation for Some Samarium Alloys, Sm+ Me (Me= Ni, Rh, Pd, Pt), Determined by High-Temperature Direct Synthesis Calorimetry," *Metallurgical and Materials Transactions B*, vol. 29, no. 4, pp. 815-820, 1998.
- [137] R. A. Shiffman, "Thermodynamics of the Ytterbium-Lead System by Simultaneous Weight-Loss--Mass-Spectrometry Knudsen Effusion," *Journal of Physical Chemistry*, vol. 86, pp. 3855-3861, 1982.
- [138] R. Arróyave and Z.-K. Liu, "Intermetallics in the Mg-Ca-Sn Ternary System: Structural, Vibrational, and Thermodynamic Properties from First Principles," *Physical Review B*, vol. 74, no. 17, pp. 1-15, Nov. 2006.
- [139] G. K. Moiseev and N. A. Vatolin, "Thermodynamic Functions of BaO₂, Ba₂O, and CaO₂ Oxides," *Zhurnal Fizicheskoi khimii*, vol. 74, no. 6, pp. 986-988, 2000.
- [140] T. A. Stolyarova, "Thermochemistry of Chromium Sulfides," *Geokhimiya*, no. 11, pp. 1240-1242, 2003.
- [141] N. I. Shirokov, "Thermodynamic Properties of Chromous Oxide," *Russian Metallurgy*, no. 2, pp. 73-74, 1973.
- [142] A. A. Plyshevskii, V. Y. Belogurov, and M. M. Shakirov, "Thermodynamic Characteristics of Solid Chromium(II) Oxide," *Izvestiya Vysshikh Uchebnykh Zavedenii, Chernaya Metallurgiya*, no. 12, pp. 5-7, 1976.
- [143] R. Lamoreaux and D. Hildenbrand, "High Temperature Vaporization Behavior of Oxides. I. Alkali Metal Binary Oxides," *Journal of Physical and Chemical Reference Data*, vol. 13, pp. 151-173, 1984.

- [144] J. M. Letoffe, R. D. Joly, J. Thourey, G. Perachon, and J. Bousquet, "Determination of Enthalpy of Formation of Potassium Polysulfides," *Journal de Chimie Physique et de Physico-Chimie Biologique*, vol. 71, no. 3, pp. 427-430, 1974.
- [145] D. Lindberg, R. Backman, M. Hupa, and P. Chartrand, "Thermodynamic Evaluation and Optimization of the (Na+K+S) System," *The Journal of Chemical Thermodynamics*, vol. 38, no. 7, pp. 900-915, Jul. 2006.
- [146] J. M. Letoffe, J. Thourey, G. Perachon, and J. Bousquet, "Determination of Standard Enthalpies of Formation of Sodium and Lithium Polysulfides," *Bulletin de la Société Chimique de France*, no. 3-4, pp. 424-426, 1976.
- [147] J. P. Toscano, C. A. Deakynne, and J. F. Liebman, "Paradigms and Paradoxes: Energetics of Aqueous Oxyanions of Nonmetals and Metalloids," *Structural Chemistry*, vol. 14, no. 3, pp. 315-320, 2003.
- [148] "Knovel Critical Tables (2nd Edition)." Knovel, 2008.
- [149] P. Patnaik, *Handbook of Inorganic Chemicals*. McGraw Hill, 2003.
- [150] D. Risold, "The Strontium-Oxygen System," *Calphad*, vol. 20, no. 3, pp. 353-361, Sep. 1996.
- [151] A. S. Pashinkin and V. A. Dolgikh, "Some Problems of Chemistry and Thermodynamics of Oxygen Compounds of Tellurium in Relation to Telluride Oxidation," *Zhurnal Neorganicheskoi Khimii*, vol. 42, no. 2, pp. 190-195, 1997.
- [152] R. Diehl and B. I. Noläng, "Dry Oxidation of $Hg_{1-x}Cd_xTe$: Calculation of Predominance Area Diagrams of the Oxide Phases," *Journal of Crystal Growth*, vol. 66, no. 1, pp. 91-105, 1984.
- [153] D. E. Wilcox and L. A. Bromley, "Computer Estimation of Heat and Free Energy of Formation for Simple Inorganic Compounds," *Industrial & Engineering Chemistry*, vol. 55, no. 7, pp. 32-39, 1963.
- [154] J.-Y. Lee, Y. Ju, S.-S. Lee, T. C. Keener, and R. S. Varma, "Novel Mercury Oxidant and Sorbent for Mercury Emissions Control from Coal-fired Power Plants," *Water, Air, & Soil Pollution: Focus*, vol. 8, no. 3-4, pp. 333-341, Oct. 2007.
- [155] "The Diablo Analytical 5000A Real-Time Gas Analyzer," 2009. [Online]. Available: www.diab.com/mssensor/index.htm. [Accessed: Oct-2011].
- [156] R. Firor, "Chemical Analysis in Fuel Cell Systems: Applications of the Agilent 5000A Real-Time Gas Analyzer for Monitoring Low-Level Sulfur." Agilent, Inc., 2002.
- [157] J. Dobson and M. Taylor, "The Permeability of Gases through PFTE and other Membranes at 25°C," *Electrochimica Acta*, vol. 31, no. 2, pp. 231-233, 1986.
- [158] R. S. Daniels and D. C. Wigfield, "Gas-Phase Adsorptional Losses of Elemental Mercury in Cold-Vapor Atomic Absorption Spectrometry," *Analytica Chimica Acta*, vol. 248, pp. 575-577, 1991.
- [159] A. F. Holleman, E. Wiberg, N. Wiberg, M. Eagleson (trans), W. Brewer (trans), and B. J. Aylett (rev), *Inorganic Chemistry*. New York: Academic Press, 2001, pp. 520-521.
- [160] S. N. Putilin, S. M. Kazakov, and M. Marezio, "On the Alkali-Earth Mercurates, $MHgO_2$," *Journal of Solid State Chemistry*, vol. 109, pp. 406-409, 1994.
- [161] M. Soll and H. Müller-Buschbaum, "Das Erste Bariumoxomercurat: $BaHgO_2$. Synthese und Kristallstruktur," *Journal of the Less Common Metals*, vol. 162, pp. 169-174, 1990.
- [162] B. B. Botros and J. G. Brisson, "Targeting the Optimum Steam System for Power Generation with Increased Flexibility in the Steam Power Island Design," *Energy*, vol. 36, no. 8, pp. 4625-4632, Aug. 2011.

- [163] M. A. Gómez-García, V. Pitchon, A. Kiennemann, M. Corrias, P. Kalck, and P. Serp, "Sorption– Desorption of NO_x from a Lean Gas Mixture on H₃PW₁₂O₄·6H₂O Supported on Carbon Nanotubes," *Topics in Catalysis*, vol. 30/31, no. 2, pp. 229-233, 2004.
- [164] B. Gao, J.-X. Zhao, Q.-H. Cai, X.-G. Wang, and X.-Z. Wang, "Doping of Calcium in C₆₀ Fullerene for Enhancing CO₂ Capture and N₂O Transformation: a Theoretical Study," *The Journal of Physical Chemistry A*, vol. 115, no. 35, pp. 9969-76, Sep. 2011.